

N° d'ordre : **40958**

UNIVERSITE LILLE 1 – SCIENCES ET TECHNOLOGIES

ECOLE DOCTORALE SCIENCES DE LA MATIERE, DU
RAYONNEMENT ET DE L'ENVIRONNEMENT

THESE

présentée par

Jhon Jhon QUIROZ TORRES

pour l'obtention du

TITRE DE DOCTEUR EN MOLECULES ET
MATIERE CONDENSEE

intitulée

FORMALDEHYDE CATALYTIC OXIDATION OVER MESOPOROUS

MANGANESE BASED MATERIALS

Soutenue **le 18 décembre 2012** devant le jury d'examen :

Directeur de thèse: **Jean-François LAMONIER**, Professeur, Université
Lille 1

Rapporteurs : **Sébastien ROYER**, Maître de Conférences,
Université de Poitiers
Véronique PITCHON, Directeur de Recherche
CNRS, Université de Strasbourg

Membres : **Jean-Marc GIRAUDON**, Maître de Conférences,
Université Lille 1
Anne PONCHEL, Professeur, Université d'Artois
Antonella GERVASINI, Professeur, Université de
Milan

Titre en Français:

OXYDATION CATALYTIQUE DU FORMALDEHYDE SUR DES MATERIAUX MESOPOREUX A BASE DE MANGANESE

Résumé :

La qualité de l'air intérieur est une préoccupation majeure de notre société. Le formaldéhyde (HCHO) est un polluant atmosphérique important et présent dans divers environnements intérieurs comme la maison, le bureau et l'industrie. L'oxydation catalytique complète du formaldéhyde est une voie prometteuse pour convertir ce polluant en produits inoffensifs. Les catalyseurs à base d'oxydes de métaux de transition sont décrits comme les plus prometteurs. Parmi ces oxydes, ceux à base d'oxydes de manganèse sont peu coûteux, non toxiques et peuvent être efficaces pour convertir le formaldéhyde à basse température. Ce travail vise à développer des catalyseurs mésoporeux à base d'oxydes de manganèse pour l'élimination catalytique à basse température du formaldéhyde. Des oxydes de manganèse mésoporeux contenant des teneurs variables en cérium ont tout d'abord été obtenus par activation chimique (traitement acide). L'optimisation de la synthèse du matériau mésoporeux sous atmosphère contrôlée a ensuite conduit à l'obtention d'une mésostructure lamellaire d'oxyde de manganèse. Le délaminage de cet oxyde, après calcination, a produit un oxyde de manganèse ayant des propriétés texturales très intéressantes et redox grandement améliorées. Le catalyseur le plus actif a pu oxyder complètement HCOH en CO₂ et H₂O à 110 °C. Finalement, des hydrotalcites à base de Mg, Mn et Al, activées par ultrasons, ont été synthétisées pour être employées en tant que précurseurs d'oxydes mixtes de manganèse de grandes surfaces spécifiques. L'effet de l'apport des ultrasons et de la composition en éléments du matériau (Mg/Mn) sur les propriétés structurales, texturales, basiques et catalytiques des oxydes mixtes a plus particulièrement été étudié.

Mots-clés : Composés Organiques Volatils (COV), Oxydation Catalytique, Formaldéhyde, Oxydes de Manganèse, Matériaux Mésoporeux, Pollution Intérieur.

Title in English:

FORMALDEHYDE CATALYTIC OXIDATION OVER MESOPOROUS MANGANESE BASED MATERIALS

Abstract:

Indoor air quality is currently a societal concern. Formaldehyde is an important air pollutant in various indoor environments, including houses, offices and industries. The catalytic complete oxidation of formaldehyde is a promising way to convert this pollutant into harmless products. Transition metal oxides based catalysts are described as the most promising catalysts. Among these oxides, manganese oxide based materials are promising, cheap, non-toxic and effective catalysts to convert formaldehyde at low temperature. The present work aims to develop a novel mesoporous manganese oxide based catalyst for low temperature formaldehyde catalytic removal. Mesoporous manganese oxides containing variable amounts of cerium were first obtained by chemical activation (acid treatment). The optimization in the synthesis of mesoporous manganese oxide under controlled atmosphere produces a layered mesostructure manganese oxide. The delamination of this layered mesostructure oxide, after calcination, produces high surface area manganese oxides with improved redox properties and the most active catalyst completely oxidizes HCHO into CO₂ and H₂O at 110 °C. Finally, Mg Mn and Al hydrotalcites based compounds, activated by ultrasound, are employed as precursors to obtain high surface area mixed manganese oxide. The effect of ultrasound contribution and the elemental composition of the material (Mg / Mn) on the structural, textural, basic and catalytic properties of the resulting mixed oxides have been particularly studied.

Keywords: Volatile organic compound (VOC), Catalytic Oxidation, Formaldehyde, Manganese Oxides, Mesoporous Material, Indoor Pollution.

Laboratoire :

Unité de Catalyse et Chimie du Solide (UCCS), UMR 8181

Boulevard Paul Langevin

59655 VILLENEUVE D'ASCQ Cedex

France

Acknowledgments

First of all, I would like to express my sincere gratitude to my advisor, Prof. Jean-François Lamonier, from University of Lille 1 for the continuous support to my work and for his motivation, inspiration, enthusiasm, and valuable expertise. His important guidance helped in my progress during the different phases of the work, from the understanding of the subject to the interpretation of results.

I would like to show all my gratitude to Dr. Jean-Marc Giraudon, from University of Lille 1 whose encouragement, guidance and support helped me during all activities carried out. His insights were very important for the achievement of the work.

I am extremely grateful to Prof. María Josefina Pérez Zurita de Scott, from Central University of Venezuela for her motivation and encouragement to prepare my PhD studies.

I would like to thank heartily the members of the jury, Dr. Sébastien Royer, from University of Poitiers, Dr. Véronique Pitchon, from University of Strasbourg, Prof. Anne Ponchel, from University of Artois, and Prof. Antonella Gervasini, from the University of Milan, for their time and dedication spent in the examination of the thesis, and their valuable contribution with insightful comments and questions.

I am extremely thankful to the financial support from FUNDAYACUCHO (Caracas, Venezuela) and French Embassy, essential for the accomplishment of this work.

I am grateful to Prof. Lionel Montagne director of Unité de Catalyse et Chimie du Solide (UCCS) laboratory and in particular I would like to thank the technical and administration staff of the laboratory for all the support during the accomplishment of this work.

I would like to express all my gratitude to Dr. Jean-Philippe Dacquin and Dr. Simon Dasset for fruitful discussions about the topic and for sharing their friendship and sympathy.

My sincere thanks also go to all my colleagues and friends from the UCCS: Manuel, Alexia, Andres, Alejandro, Orianne, Minh Tuan, Yihao, Duy Luan, Rémy, Jeremy, Pierre, Guillaume, Lishil, Dayane and Selva for supporting me with their friendship and important insights.

I would like to thank all my family, and in special my parents, Nelida Maria Torres de Quiroz and Juan Bautista Quiroz Herrera, my sister Dayahana Quiroz Torres and my grandmother Celina Torres for supporting me throughout my life.

I want to express my kind regards to my partner Bianca Pinheiro for always supporting me during the period of achievement of this work.

Finally, I would like to show my gratitude to everyone who helped me in different ways to offer me a wonderful and unforgettable time in France.

TABLE OF CONTENTS

Introduction	1
Chapter 1 : Volatile organic compounds and formaldehyde as a primary indoor pollutant	7
1.1 Volatile organic compounds (VOCs) general description	9
1.1.1 Definition, sources, environmental and health impact	9
1.1.2 Indoor emissions of VOCs	10
1.1.3 Sources of indoors VOCs	11
1.2 Formaldehyde: General aspect	12
1.2.1 Introduction	12
1.2.2 Physicochemical properties and reactivity of formaldehyde	13
1.2.3 Production of formaldehyde	14
1.2.4 Technical products	15
1.2.5 Formaldehyde application	15
1.3 Formaldehyde in the environment: Formaldehyde as a primary indoor pollutant	17
1.3.1 Outdoor sources	17
1.3.2 Indoor sources	18
1.4 Exposures and human risk	23
1.4.1 Calculation of the daily intake	23
1.4.2 Non carcinogenic exposures	23
1.4.3 Formaldehyde as a human carcinogen	24
1.5 References	26

Chapter 2 : Formaldehyde removal techniques and formaldehyde complete catalytic oxidation	31
2.1 Formaldehyde removal techniques	31
2.1.1 General aspects	31
2.1.2 Adsorption	32
2.1.3 Photocatalytic oxidation	34
2.1.4 Catalytic oxidation	36
2.2 Catalytic oxidation for formaldehyde removal	37
2.2.1 Heterogeneous catalytic oxidation: general aspects of oxidation of VOCs	37
2.3 Formaldehyde complete catalytic oxidation	40
2.3.1 Supported noble metal catalysts	40
2.3.2 Noble metals supported on Manganese oxide and mixed manganese oxide catalyst	46
2.3.3 Transition metal oxide catalysts: Manganese oxide based catalyst for HCOH total catalytic oxidation	48
2.4 Objectives of the thesis	57
2.5 References	60
Chapter 3: Background to experimental techniques	67
3.1 Powder X-ray diffraction	67
3.2 Surface area determination by physisorption analysis	68
3.3 Raman spectroscopy	70
3.4 Transmission Electron Microscopy	71
3.5 Scanning electron microscopy (SEM)	72
3.6. X-ray Photoelectron Spectroscopy (XPS)	72
3.7 Thermal gravimetric analysis (TGA) and Differential thermal analysis (DTA)	76
3.8 Temperature programmed reduction (TPR)	77
3.9 Formaldehyde catalytic oxidation model test	79

3.10 Determination of surface basicity by pulse technique using benzoic acid as a probe molecule	84
3.10 References	87

Chapter 4: Formaldehyde total oxidation over chemically activated mesoporous MnO_x and MnO_x-CeO₂ catalyst 85

4.1 Synthesis and characterization of chemically activated mesoporous manganese oxide and their application to formaldehyde oxidation 91

4.1.1 Introduction 91

4.1.2 Experimental procedure 92

4.1.2.1 Materials preparation 92

4.1.3 Results and Discussions 93

4.1.3.1 Characterization of the materials 93

4.1.3.2 Catalytic activity test 111

4.2 Influence of the cerium incorporation to the system: MnO_x-CTAB 116

4.2.1 Introduction 116

4.2.2 Experimental procedure 116

4.2.2.1 Materials preparation 116

4.2.3 Results and Discussions 117

4.2.3.1 Characterization of the materials 117

4.2.3.2 Catalytic activity test 127

4.2.3.3 Formaldehyde adsorption and surface reaction experiments 131

4.3 Conclusions 139

4.4 References 141

Chapter 5: Optimized synthesis of mesostructure manganese oxides and their impact on formaldehyde removal performances 145

5.1 Introduction	145
5.2 Experimental	146
5.2.1 Experimental setting developed for the preparation	146
5.2.2 Synthesis of mesostructure manganese oxides	146
5.3 Results and discussions	147
5.3.1 Parameters evaluated in the obtention of hybrid manganese oxide inorganic-organic materials	147
5.3.1.1 Washing procedure	147
5.3.1.2 Influence of the OH/Mn ratio	152
5.3.1.3 Influence of surfactant concentration	154
5.3.1.4 Influence of Cerium incorporation	159
5.3.2 Calcined Precursor: Characterization and their Application to Formaldehyde Oxidation	163
5.4 Conclusions	173
5.5 References	174

Chapter 6: Sono-assisted preparation of Mg-Mn-Al Hydrotalcite like compounds and their application to formaldehyde removal

6.1 Introduction	177
6.2 Experimental section	178
6.2.1 Description of the experimental setup used for the preparation of hydrotalcites precursor using ultrasound (US)	178
6.2.2 Synthesis of hydrotalcites precursors	178
6.3 Results and discussions	179
6.3.1 Characterization of the as made hydrotalcites (HT)	180
6.3.2 Calcined Precursor: Characterization	184
6.3.3 Catalytic activity of calcined hydrotalcites precursors	190
5.4 Conclusions	200
5.5 References	201

INTRODUCTION

INTRODUCTION

1. GENERAL INTRODUCTION

The high solubility of formaldehyde in water causes rapid absorption in respiratory and gastro-intestinal tracts. The primary effects of acute exposure to formaldehyde are mucosal irritations in the upper respiratory tract and eyes irritations. The International Agency for Research on Cancer (IARC) therefore classified this substance as human carcinogen in June 2004 [1]. This classification is based on information regarding the relationship between nasopharyngeal cancer and leukaemia related to human exposure to formaldehyde. In the European Union, formaldehyde is classified as Category 3 compound, *i.e.* a suspected carcinogen (Directive 2001/58/ CEE) [2]. An overview of guideline values for the exposure to formaldehyde was recently given. The maximum acceptable values for the exposure to formaldehyde in indoor air are very low, from 3 ppb to 0.1 ppm over an average period of 8-hour, depending on the country-specific legislation in consideration. This molecule is then a priority pollutant to eliminate in many countries, as recently highlighted in France [3], for instance.

Industrially, formaldehyde is produced by the selective catalytic oxidation of methane or methanol [4]. Formaldehyde is commonly purchased as a 37 wt.% solution in water, with 10 wt.% methanol added as stabilizer. More than 65% of the total formaldehyde is used to synthesize resins. Between the years 1900 and 1930, formaldehyde-based resins found extensive uses in the industry, especially as adhesives for wood and wood composites. Since 1950, particle boards have become an attractive alternative to solid wood for the manufacturing of furniture. Particle boards and derived wood-based panels were subsequently used for the construction of houses. Nevertheless, formaldehyde also finds applications in the manufacture of antiseptics, disinfectants, artificial silk, dyes, explosives, glass mirrors and textiles. Formaldehyde in our environment (air or water) also comes from natural sources and sources related to human activity [5]. The combustion of plants is the main source of the so-called “natural” formaldehyde. Exhaust gases from motor vehicles (diesel and gasoline) generate most of the emissions from human activities. Although the overall associated quantities of formaldehyde are small, the use of wood stoves, cigarette smoke, and some cooking methods constitute sources of indoor air contamination. Moreover, the degradation and degassing of products containing formaldehyde, such as particle board, can increase its

concentration in indoor air. Consequently, high concentrations of formaldehyde were measured in indoor air of residences containing urea formaldehyde foam insulation in the 80s. Once the resins used for the manufacture of these construction materials were modified, formaldehyde emission rates dropped significantly. Nevertheless, indoor contamination is in average 10 times higher than that of outdoor contamination, justifying recent research efforts for proposing efficient technologies for its removal.

For lowering the concentration of formaldehyde in indoor environments, different techniques have been developed. Photocatalytic oxidation (PCO) systems for formaldehyde removal have recently become popular [6]. Wall paints equipped with modified TiO_2 are frequently recommended, but their efficiency was not yet proved. In addition, some authors showed that under the influence of light, photocatalytic wall paints could produce undesired secondary products, having toxicity as high as formaldehyde [6]. Adsorption of formaldehyde, over activated carbon and other adsorbents (including microporous zeolitic materials), is also proposed as an efficient way of emission control [7]. However, competitive adsorption occurs when both water (present in ambient air) and formaldehyde molecules are present. As a consequence, the adsorption of formaldehyde is significantly reduced when the relative humidity increases [6]. In addition, this process alone suggests the step of adsorbent regeneration, and consequently a final degradation step of formaldehyde is needed. Therefore, complete catalytic oxidation (CCO) of formaldehyde was evinced as an attractive alternative with respect to the previous proposed processes, due to the high effectiveness in achieving total conversion of HCOH into harmless CO_2 and H_2O . Then, the development of new catalysts (preferably free of noble metals for low cost), exhibiting high catalytic activity for HCHO complete oxidation at low temperatures, is actually of high relevance due to the recent consideration of formaldehyde effects on human health by many governments.

The main objective of the present study is to develop the synthesis of manganese based materials with improved textural, structural and redox properties devoted to formaldehyde catalytic oxidation.

2. STRUCTURE OF THE DISSERTATION

In the first two chapters, a literature review is presented comprising initially a brief description of formaldehyde as a primary indoor pollutant and the corresponding human exposure risks (Chapter 1). In Chapter 2, a short introduction of the formaldehyde removal by

adsorption and photocatalytic oxidation technologies and a short survey of general aspects of VOCs catalytic oxidation process are presented. Additionally, a review of formaldehyde catalytic oxidation is given: (i) over noble metals; (ii) transition metal-supported noble metals; (iii) manganese oxides, and (iv) manganese containing mixed-oxide structures.

The following chapters concern the experimental work. Chapter 3 comprises the experimental procedures for catalyst characterization and the description of the experimental setup used for formaldehyde catalytic oxidation. Chapter 4 concerns the synthesis characterization and catalytic properties in formaldehyde oxidation of chemically activated mesoporous manganese oxide catalyst. In the first part of this chapter, the synthesis and characterization of pure mesoporous MnO_x oxides by surfactant assisted wet-chemistry route and their activation by acidic treatment are described. Different characterization techniques were employed to investigate the effects of the chemical activation in the structure, specific surface area, redox properties and average oxidation state of manganese. The application of these materials in the formaldehyde oxidation is also studied, focusing on the effect of the acidic treatment in the materials. In the second part, the effect of cerium addition to the pure manganese oxide system is investigated; the effect of chemical activation in the mixed MnO_x - CeO_2 catalysts with different Mn/Ce ratios prepared by surfactant assisted wet-chemistry route is also studied. The third part concerns the study of formaldehyde adsorption and transformation on the MnO_x based catalyst surface; a mechanistic approach by surface reaction experiments using TPD, FTIR and XPS analyses of formaldehyde adsorption is proposed.

Chapter 5 includes the optimization in the synthesis of mesoporous manganese oxide. Herein, we present a novel synthetic route under controlled atmosphere that permits $[\text{Mn}(\text{OH})_6]^{4-}$ octahedral clusters to be stabilized. The interaction of these inorganic precursors with surfactant molecules will be discussed. Additionally, several important factors that influence the accomplishment of mesostructure phase are considered, comprising, for instance, the surfactant concentration, the OH/Mn ratio, and the addition sequence. The application of the resulting materials in formaldehyde catalytic oxidation is also considered.

Chapter 6 concerns the results obtained within two collaboration projects: (1) ECOS-Nord France-Colombia, developed in conjunction with the National University of Colombia, and (2) PHC-Galilée France-Italy, accomplished in association with the University of Milan. In this chapter, the preparation of Mg-Mn-Al HT using ultrasound (US) is attempted. The

effects of US on the structural, textural, redox and basic properties of the resulting manganese mixed oxides and their performance in formaldehyde catalytic oxidation are discussed.

Finally, the general conclusion will highlight the most important results obtained and the perspectives in this research will be proposed.

References

¹IARC. "IARC classifies formaldehyde as carcinogenic to humans" press release no.153; International Agency for Research on Cancer: Lyon, 2004.

² Directive 2001/58/ CEE : <http://www.ineris.fr/aida>

³ 2ème Plan National Santé Environnement (PNSE 2) 2009-2013, <http://www.developpement-durable.gouv.fr/IMG/pdf/01-22.pdf>

⁴H.R. Gerberich, G.C. Seaman in *Encyclopedia of Chemical Technology, Vol. 11*, John Wiley & Sons, New York, **2004**, pp. 929–951.

⁵R. Koppmann, J. Wildt in *Volatile Organic Compounds in the Atmosphere*, Blackwell Publishing, Oxford, **2007**

⁶ J. Mo, Y. Zhang, Q. Xu, J.J. Lamson, R. Zhao, *Atmos. Environ.* **2009**, *43*, 2229.

⁷ H. Rong, Z. Ryu, J. Zheng, Y. Zhang, *J. Colloid Interface Sci.* **2003**, *261*, 207.

CHAPTER 1

Chapter 1: Volatile organic compounds and formaldehyde as a primary indoor pollutant

1.1 Volatile organic compounds, general description.

1.1.1 Definition, sources, environmental and health impact

Volatile organic compounds VOCs belong to the group of main air pollutants, together with sulphur oxides, nitrogen oxides, carbon monoxide, ammonia and particulate matter (PM). Definitions of VOC may vary depending on the country and legislation in question. For instance, different definitions are based on vapour pressure, boiling points and reactivity of organic species [1].

According to the European Solvent Emission Directive's definition, VOCs shall mean any organic compound having at 293.15 K a vapour pressure of 0.01 kPa or more, or having a corresponding volatility under the particular conditions of use [2].

In the legislation of the U.S. Environmental Protection Agency (EPA) Volatile organic compounds (VOC) mean any compound of carbon, excluding carbon monoxide, carbon dioxide, carbonic acid, metallic carbides or carbonates, and ammonium carbonate, that participates in atmospheric photochemical reactions [3]. The participation in atmospheric photochemical reaction is also mentioned in the VOC definition of VOC Protocol of United Nations Economic Commission for Europe (UNECE) and VOC definition of Canadian Authorities [4].

In general, VOCs have been reported to cause eye, nose and throat irritation, headaches, loss of coordination, nausea but also more problematic issues like damage in the central nervous system. Some of the VOCs are highly toxic and some have unknown health effects, some are carcinogenic and some of them are genotoxic. The time and level of exposure affect the extent of a health effect [5].

Ozone is a particular gas present in the Earth upper atmosphere and at ground level. There are two distinct types of ozone: the Ground-level Ozone (or bad ozone) and the Stratospheric Ozone (or good ozone).

Ground-level Ozone (GOL) is located in the troposphere, close to the Earth's surface. It is the main component of urban smog that originates in emissions from industrial facilities and electric utilities, motor vehicle exhaust, gasoline vapours, and chemical solvents. GOL is

created by chemical reactions between oxides of nitrogen (NO_x) and VOCs in the presence of sunlight. This reaction disturbs a natural balance of formation and destruction of ozone in the troposphere and its accumulation. The accumulation of ozone in the troposphere has very serious climate repercussion. It has been calculated that doubling the concentration of ozone in the troposphere could increase the average air temperature of about 1 °C [5].

VOCs and particularly chlorinated VOCs are involved directly in global warming. These compounds contribute to the depletion of stratospheric ozone. Their presence in the high atmospheric layers would lead to a warming of the temperature from 2 °C to 5 °C, affecting seriously the climate [5].

VOCs are emitted into the atmosphere from anthropogenic and biogenic sources. Moreover, these compounds may also be formed in situ in the atmosphere as products of the atmospheric transformations of other VOCs. On a worldwide basis, emissions of VOCs from biogenic sources dominate over those from anthropogenic sources by a factor of 10. Nevertheless, in urban areas anthropogenic VOCs often dominate. These anthropogenic emission sources can be further divided into two categories namely stationary (point and area sources) and mobile sources. Stationary sources include for example industrial processes. Mobile sources are related to road and off-road traffic, marine transport, among others [1].

In addition to outdoor emissions, the indoor emissions of VOCs have been subject of recent consideration from many governments around the world. In fact, the extensive use of new products and materials in our days has resulted in increased concentrations of indoor pollutants, especially of volatile organic compounds.

1.1.2 Indoor emissions of VOCs

Indoor air quality (IAQ) has become an important community concern due to the increased amount of personal time spent in indoor environment. Nowadays, people generally spend more than 80% of their time in an indoor environment such as home, office, car and shopping centre. Some studies showed that the level of pollutants in indoor environment is actually higher than that in outdoor environment. Furthermore, pollutant sources are more varied and exposures are more important than those found in outdoor environments [6,7].

Hundreds of VOCs are found in a typical indoor environment. Many of these compounds are aromatic hydrocarbons, alkenes, alcohols, aliphatic hydrocarbons, aldehydes, ketones, esters, glycols, glycolethers, halocarbons, cycloalkanes, and terpenes. Moreover,

amines like nicotine, pyridine, 2-picoline, 3-ethenylpyridine and myosmine are also widespread, especially in smoking microenvironments. Additionally, low molecular weight carboxylic acids, siloxanes, alkenes, cycloalkenes and Freon 11 are frequently encountered in typical nonindustrial indoor air [6,7].

1.1.3 Sources of indoors VOCs

VOCs are omnipresent in indoor environments. They are widespread in household and consumer products, furnishing and building materials, office equipment, air fresheners, paints, household solvents and in microorganisms found in indoor environments. In addition, humans and their indoor activities such as cooking, cleaning, building renovation and tobacco smoking generate high levels and wide varieties of VOCs. Apart from these indoor sources, intrusions of VOCs from outdoor traffic as well as biogenic and industrial emissions contribute significantly to indoor VOC levels. Furthermore, indoor air reactions are now recognized as sources of indoor VOCs, as exemplified by the reaction of ozone with 4-phenylcyclohexene contained in carpets and latex paints to generate appreciable amounts of aldehydes. While some common indoor VOCs originate exclusively from indoor sources, others have multiple indoor and outdoor sources. Consequently, the indoor level of a particular VOC is the summation of the contributions of its different indoor and outdoor sources. Table 1 presents the main source of typical indoors VOC sources together with the major VOC chemical classes associated with the sources [6,7].

Table1.1. Indoors VOC sources and released chemical class associated.

Sources of indoor COV	Chemical classes
Outdoor sources : -Traffic -Industry	-Aliphatic and Aromatic Hydrocarbon -Aldehydes - Ketones -Esters
Building material: -Insulation -Paint -Plywood -Adhesives	-Aliphatic and aromatic hydrocarbons -Aldehydes -Alcohols -Ketones -Esters
Furnishing material: -Furniture -Floor/wall coverings	-Aliphatic and aromatic hydrocarbons -Alcohols -Halocarbons -Aldehydes -Ketones -Ethers -Esters
Garage and combustion appliances: -Vehicle emission -Tobacco smoking -Candles	-Aliphatic and aromatic hydrocarbons -Aldehydes -Amines

Consumer products: -Cleaning -Personal care products	-Aliphatic and aromatic hydrocarbons -Alcohols -Halocarbons -Aldehydes -Ketones -Terpenes -Ethers -Esters
Equipment: -Laser printers -Photocopiers -Computers -Other office equipment	-Aromatic hydrocarbons -Aldehydes -Ketones -Esters
Indoor activities: -Cooking -Tobacco smoking -Use of water and solvents	-Amines -Aliphatic and aromatic hydrocarbons -Aldehydes -Halocarbons
Ventilation systems: -Filters of heating -Ventilation and air-conditioning systems	-Aliphatic and aromatic hydrocarbons -Alcohols -Halocarbons -Aldehydes -Ketones -Terpenes -Ethers -Esters
Biological sources: -Humans -Moulds -Bacteria -Plants	-Terpenes -Glycoesters -Alcohols -Esters -Aldehydes

1.2 Formaldehyde: General aspect

1.2.1 Introduction

From 1900 to 1930, formaldehyde based resins found extensive uses in the industry, especially as adhesives for wood and wood composites. From 1950, particle boards have become an attractive alternative to solid wood for the manufacturing of furniture. Particle boards, and derived wood panels, were subsequently used for house constructions. In the mid-1960, complaints from residents were first reported, especially irritation of the eyes and upper airways. Formaldehyde emissions from particle boards bonded with urea formaldehyde resin were soon identified as the cause of these complaints. As a consequence, the health communities in Europe and United States have established criteria for the limitation and regulation of formaldehyde emissions from wood based materials [8].

Over the years, the resins used in the manufacture of constructions materials were modified. Therefore, the release of formaldehyde from building products has been decreasing. For this reason, formaldehyde slipped out of the primary focus of indoor research in the 1990s. However, in 2004, formaldehyde discussions were generally taken up again when

formaldehyde was considered as carcinogenic for humans. As a consequence, various authorities and institutions have proposed new indoor air guidelines, giving values that are nearly universal. Although a prioritized ranking of chemicals and exposures that cause concern is difficult and uncertain, the Scientific Committee on Health and Environmental Risks (SCHER) states that formaldehyde (like carbon monoxide, nitrogen dioxide, benzene, naphthalene, environmental tobacco smoke (ETS), radon, lead, and organophosphate pesticides) is a compound of concern in the indoor environment [8].

Occupational exposure to formaldehyde has become a centre of attention of indoor research in the last years due to the higher concentration of the pollutant in the workplace. The Committee on Health and Safety Work (CSST) considers formaldehyde to be a causal agent for occupational asthma. In the case of occupational exposure over several years, formaldehyde has been related to cause cancer of the nasopharynx [8].

1.2.2 Physicochemical properties and reactivity of formaldehyde

Formaldehyde (Chemical Abstracts Service Registry (CAS) number 50-00-0) is the first of the series of aliphatic aldehydes and is a gas at room temperature. Its molecular structure is presented in Figure 1.1. For its reactivity and versatility, it is considered as a chemical intermediate. It readily undergoes polymerization, is highly flammable, and can form explosive mixtures with air. It decomposes at temperatures above 150°C [9].

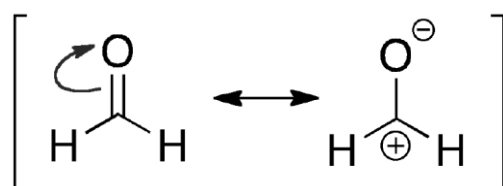


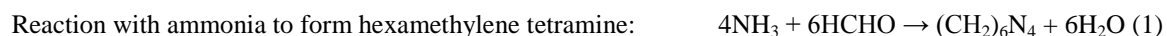
Figure 1.1. Chemical structure of formaldehyde.

At room temperature, pure formaldehyde is a colourless gas with a strong, pungent, suffocating, and highly irritating odour. Formaldehyde is readily soluble in water, alcohols, ether, and other polar solvents. A synopsis of its physicochemical properties is given in Table 1.2.

Table 1.2. Physical and chemical properties of formaldehyde [9,10].

International Union for Pure and applied Chemistry (IUPAC) name	Formaldehyde
Synonyms	Methanal, methyl aldehyde, methyl oxide, oxymethylene, oxomethane
Chemical Abstracts Service Registry (CAS) number	50-00-0
Molecular formula	HCOH, CH ₂ O
Molecular weight	30.03 g/mol
Melting point	-92°C
Boiling point	-21°C
Dipole moment	2.33D
Solubility	Soluble in water, ethanol, ether, acetone, benzene
Density	Gas: 1.067 (air=1) Liquid: 0.815 g/ml at -20°C
Vapor pressure	3.883 mmHg at 25°C
Henry's law constant	2.5 x 10 ³ M/Atm at 25°C
Conversion factor (293K, 1013mbar)	0.1 ppm = 124.84 µg/m ³ 1 µg/m ³ = 0.815 ppb

Formaldehyde has a dipolar resonance structure (see Figure 1.1), which makes the molecule a typical electrophile. According to Roffael [11], the most important reactions apart from polymerization are as follows:



In the atmosphere, HCOH can undergo different reaction pathways. Atkinson [12] has calculated formaldehyde lifetimes in the atmosphere (τ) with respect to photolysis ($\tau = 4$ h), reaction with the OH radical ($\tau = 1.2$ days), reaction with the NO₃ radical ($\tau = 80$ days), and reaction with O₃ ($\tau > 4.5$ years).

1.2.3 Production of formaldehyde

Formaldehyde has been produced commercially since 1889 by the catalytic oxidation of methanol. Various specific methods were used in the past, but only two are widely used currently: the silver catalyst process and the metal oxide catalyst process [10].

For the silver catalyst process, also called the BASF process, partial oxidation and dehydrogenation of methanol is conducted with air in the presence of silver crystals at 680-720 °C and atmospheric pressure. The methanol conversion reaches 97-98%, carbon monoxide, carbon dioxide, methyl formate and formic acid are the by-products [10].

In the metal oxide (Formox) process, methanol is oxidized with air in excess, the presence of a modified iron–molybdenum–vanadium oxide catalyst at 250-400 °C and atmospheric pressure (methanol conversion: 98-99%). By-products are carbon monoxide, dimethyl ether and small amounts of carbon dioxide and formic acid [10].

In a recent review article, Tang *et al.*[13] estimate a global output of 32 million tons of formaldehyde in 2006, with the highest producers being China (34%), the United States (14%), and Germany (8%). More than 65% of the total formaldehyde is used to synthesize resins.

1.2.4 Technical products

Formaldehyde is most commonly available commercially as a 30–50% (by weight) aqueous solution, commonly referred to as ‘formalin’. In dilute aqueous solution, the predominant form of formaldehyde is its monomeric hydrate, methylene glycol [$\text{CH}_2(\text{OH})_2$]. In more concentrated aqueous solutions, oligomers and polymers that are mainly polyoxymethylene glycols [$\text{H}(\text{CH}_2\text{O})_n\text{OH}$] are formed and may predominate. Methanol and other substances (e.g. various amine derivatives) are usually added to the solutions as stabilizers, in order to reduce intrinsic polymerization [9,10].

Paraformaldehyde, a solid polymer of formaldehyde, consists of a mixture of poly-(oxymethylene) glycols [$\text{HO}-(\text{CH}_2\text{O})_n-\text{H}$; $n = 8-100$]. The formaldehyde content is 90-99 wt. %, depending on the degree of polymerization, the value of n and product specifications; the rest is bound or free water. As a convenient source of formaldehyde for certain applications, paraformaldehyde is prepared commercially by the concentration of aqueous formaldehyde solutions under vacuum in the presence of small amounts of formic acid and metal formates [9,10].

1.2.5 Formaldehyde application

Formaldehyde is a chemical feedstock for numerous industrial processes. It is also used as a preservative, disinfectant, and biocide. As far as the indoor environment is concerned, its use as a component of thermosetting adhesives is of particular significance.

Urea-formaldehyde (UF) adhesives (so-called aminoplasts) are still the most commonly used products in the manufacturing of wood-based materials and furniture due to their rapid curing, compatibility with additives, and low price. In the first step, mono-, di-, and trimethylolurea are formed from formaldehyde and urea in a Mannich reaction followed by condensation. This is followed by condensation reactions to build up the polymer (see Eqs. 1 and 2, Figure 1.2). UF adhesives have poor water resistance: the presence of water results in a hydrolysis of the C-N bond and, as a consequence, the release of formaldehyde [8].

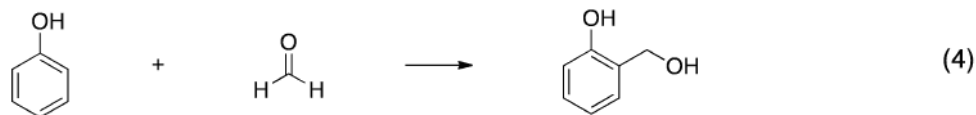
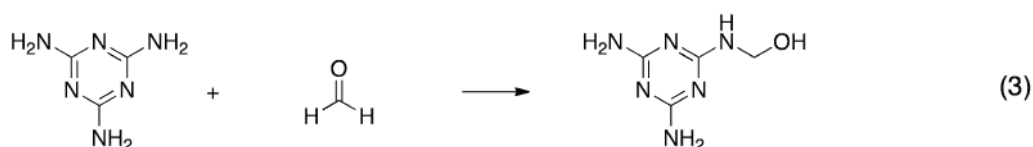
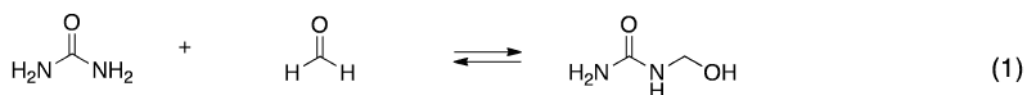


Figure 1.2. Chemical reactions for production of formaldehyde based resins. Urea formaldehyde (equations 1 and 2), melamine urea formaldehyde (equation 3) and phenol formaldehyde (equation 4).

Melamine-urea-formaldehyde (MUF) adhesives are similar to UF adhesives. They are produced by mixing portions of UF and melamine-formaldehyde (MF) or by condensation of all monomers in one batch. Equation 3 (Figure 1.2) shows the first step of the melamine-formaldehyde reaction [8].

Phenol-formaldehyde (PF) adhesives (so-called phenoplasts) are made by electrophilic substitution to methylol phenol in the first step, as shown in Eq. 4. PF adhesives are very stable and water-resistant and have a high adherence to wood. In the past, plastics made of PF resins were used as coverings for telephones, radios, etc [8].

Melamine-urea-phenol-formaldehyde (MUPF) adhesives are used for the production of moisture-proofed wood based products and for construction materials. Like MUF

adhesives, they are produced by the addition of small amounts of phenol [8]. Figure 1.3 provides an overview of the industrial utilization of formaldehyde.

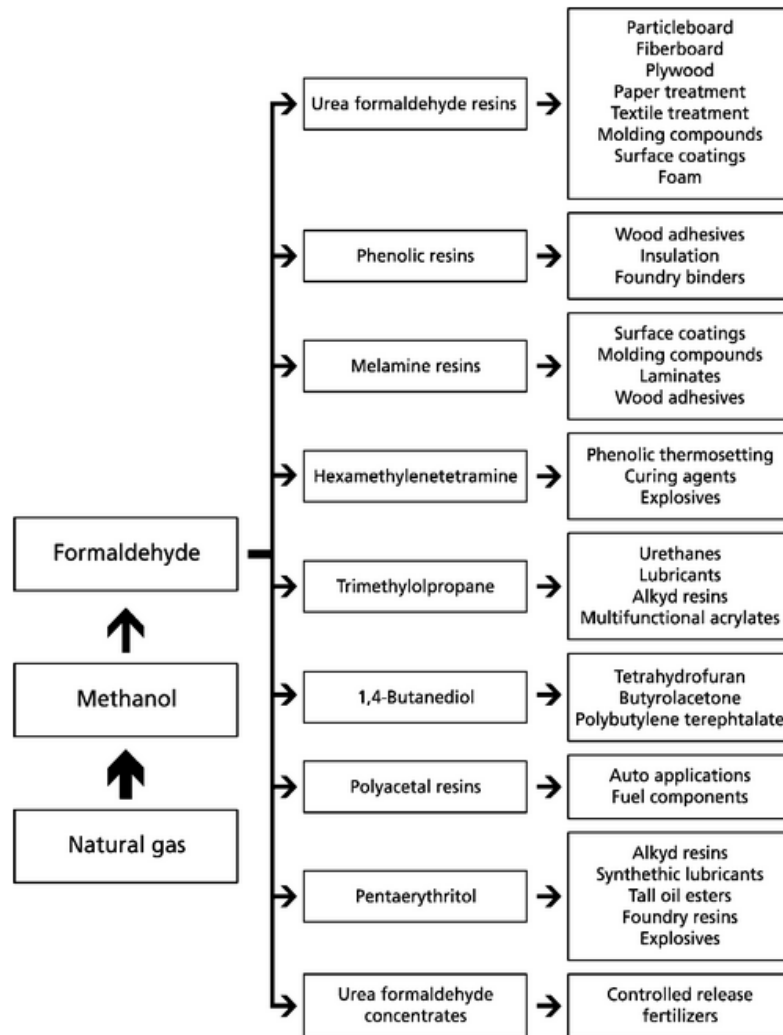


Figure 1.3. Survey of formaldehyde industrial application and formaldehyde products [8].

1.3 Formaldehyde in the environment: Formaldehyde as a primary indoor pollutant

1.3.1 Outdoor sources

Formaldehyde as a Natural Compound

Formaldehyde is omnipresent in the environment, like other VOCs, and it is a biogenic compound and part of plant physiological and plant atmosphere exchange processes. The combustion of plants is the main source of “natural” formaldehyde. In 1927, Freudenberg and Harder identified formaldehyde as a decomposition product of lignin [14]. Muuller *et al.* [15] found formaldehyde within and above a coniferous forest in Germany. Trapp *et al.* [16]

mention formaldehyde as a degradation product of isoprene in a eucalyptus forest in Portugal. Carter and Atkinson [17] proposed a scheme for the formation of formaldehyde from isoprene via reaction with OH and NO. Kesselmeier *et al.* [18] have measured several parts per billion (ppb) of formaldehyde in a remote forest site in central Amazonia.

Atmospheric Reactions

Thousands of organic compounds are released into the atmosphere from biogenic and anthropogenic sources. These organic compounds include isoprene, monoterpenes, and a number of oxygenated compounds. In the troposphere, they react with hydroxyl (OH) radicals, nitrate (NO₃) radicals, and ozone (O₃), and they play an important role in the chemistry of the lower troposphere [12].

Relatively high formaldehyde outdoor concentrations can be found in the urban air of extremely polluted megacities. Here, HCHO is directly released into the atmosphere or produced by photochemical gas-phase reaction of hydroxyl radicals with nonmethane hydrocarbons (NMHC)[12].

Outdoor Combustion

A major source of formaldehyde in urban air is incomplete combustion of hydrocarbon fuels, especially from vehicle emissions. Combustion processes account directly or indirectly for most of the formaldehyde that enters the atmosphere, particularly from engines that are not equipped with catalytic converters. For instance, in USA and Mexico the formaldehyde emission was decreased in 30% after the introduction of the catalytic converter. In contrast, emissions of formaldehyde from automobile exhaust have been reported to increase again with the introduction of oxygenated fuels [10]. Machado *et al.* [19] and also Guarieiro *et al.* [20] have shown that carbonyl emissions are dependent on the biodiesel content and that the biodiesel ester molecules are probably the source of these carbonyls.

The combustion of wood is also a natural source of formaldehyde. Hedberg *et al.* [21] have studied birch combustion and report formaldehyde emission rates of 180-710 mg/kg wood. This is in accordance with data by Schauer *et al.* [22] for oak (759 mg/kg), pine (1165 mg/kg), and eucalyptus (599 mg/kg).

1.3.2 Indoor sources

In general, ambient levels of formaldehyde in outdoor air are significantly lower than those measured in the indoor air of residences or workplaces. Salthammer *et al.* [8] present a thorough review of formaldehyde sources and levels found in the indoor environment. They

used the diagram shown in Figure 1.4 to summarize data they found on the range of formaldehyde air concentrations (in ppb) in different environments, indoor and outdoor.

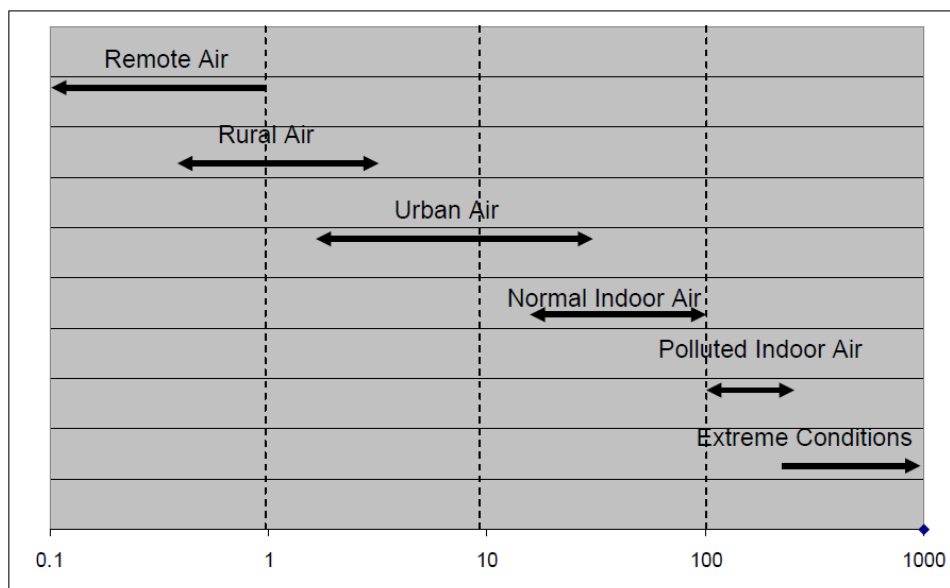


Figure 1.4. Range of formaldehyde air concentrations (ppb) in different environments [8].

The concentrations in residences depend on the sources of formaldehyde that are present, the age of the source materials, ventilation, temperature and humidity. In general, the major indoor air sources of formaldehyde can be described in two ways: (1) those sources that have the highest emissions when the product is new with decreasing emission over time, including volatilization from pressed wood products, carpets, fabrics, insulation, permanent press clothing, latex paint etc.; and (2) those sources that are reoccurring or frequent such as emissions from gas burners, kerosene heaters, and cigarettes [23].

Indoor chemistry: general aspects

Indoor chemistry is an important source of formaldehyde. Wolkoff *et al.* [24] stated that reactions between unsaturated VOCs and ozone can form irritants that may be responsible for many reported symptoms. In 1992, Weschler *et al.* [25] reported the emission of formaldehyde and other aldehydes from carpeting in the presence of ozone, while concentrations of unsaturated compounds such as 4-phenylcyclohexene (PCH), 4-vinylcyclohexene (VCH), and styrene decreased.

In the indoor environment, we have a situation in which ozone concentrations are lower, as compared with the outdoor environment, while concentrations of unsaturated compounds such as terpenes are in contrast distinctly higher. Many terpenoids present in

indoor air, such as limonene (k_{O_3}) $200 \times 10^{-18} \text{ cm}^3 \text{ molecule}^{-1} \text{ s}^{-1}$), myrcene (k_{O_3}) $470 \times 10^{-18} \text{ cm}^3 \text{ molecule}^{-1} \text{ s}^{-1}$), and terpinolene (k_{O_3}) $1880 \times 10^{-18} \text{ cm}^3 \text{ molecule}^{-1} \text{ s}^{-1}$), exhibit high gas-phase reaction constants with ozone. Terpene/ozone reaction rates in indoor and outdoor air can therefore be of the same order of magnitude. It has been shown recently that many household products contain terpenes and can rapidly react with ozone under indoor-related conditions [26].

Indoor combustion: general aspects

Residential cooking activities were identified as formaldehyde sources. In developed countries, cigarette smoke is the primary combustion source indoors. Baek and Jenkins [27] measured an average formaldehyde concentration of $234 \mu\text{g m}^{-3}$ when six cigarettes were smoked in a 30 m^3 chamber under almost static conditions. In the study by Singer *et al.* [28] distinctly higher formaldehyde emission rates of 950-1310 μg per cigarette smoked were measured. According to Baker *et al.* [29] formaldehyde is mainly generated from the pyrolysis of saccharides used as tobacco ingredients.

Other sources

Cosmetic products that contain formaldehyde, formalin and/or paraformaldehyde may come into contact with hair (e.g. shampoos and hair preparations), skin (deodorants, bath products, skin preparations and lotions), eyes (mascara and eye make-up), oral mucosa (mouthwashes and breath fresheners), vaginal mucosa (vaginal deodorants) and nails (cuticle softeners, nail creams and lotions). Use of aerosol products (e.g. shaving creams) may result in potential inhalation of formaldehyde [30].

Formaldehyde occurs naturally in foods, and foods may be contaminated as a result of fumigation (e.g. grain), cooking (as a combustion product) and release from formaldehyde resin-based tableware. It has been used as a bacteriostatic agent in some foods, such as cheese. Fruit and vegetables typically contain 3–60 mg/kg, milk and milk products contain about 1 mg/kg, meat and fish contain 6–20 mg/kg and shellfish contain 1–100 mg/kg. Drinking-water generally contains $< 0.1 \text{ mg/L}$ [30].

Formaldehyde can also be emitted into indoor air during the cooking of fish. Free formaldehyde was found in fish at levels ranging from 1.4 to 40.3 ppm (1.7 to 49.6 mg/m^3); the high levels were attributed to the processes used to freeze fish products. When cooking oils are heated to high temperatures (240 – $280 \text{ }^\circ\text{C}$) that are typical of Chinese wok cooking, several volatile mutagenic organic compounds are released, including formaldehyde.

Emissions of formaldehyde from several cooking oils (rapeseed, canola, soya bean, peanut) ranged from 23 to 71 µg/L [30].

Formaldehyde exposure in the workplaces

Formaldehyde emissions in the workplaces could be more important than in residential environments and it can occur via three main scenarios [23]:

- The production of aqueous solutions of formaldehyde (formalin) and their use in the chemical industry (e.g., for the synthesis of various resins, as a preservative in medical laboratories and embalming fluids and as a disinfectant).
- Release from formaldehyde-based resins in which it is present as a residue and/or through their hydrolysis and decomposition by heat (e.g. during the manufacture of wood products, textiles, synthetic vitreous insulation products, and plastics). In general, the use of phenol-formaldehyde resins results in much lower emissions of formaldehyde than those of urea- based resins.
- The pyrolysis or combustion of organic matter (e.g., in engine exhaust gases or during fire fighting) (IARC, 2006).

Industries with the greatest potential for exposure include health services, business services, printing and publishing, manufacture of chemicals and allied products, manufacture of apparel and allied products, manufacture of paper and allied products, personal services, machinery, transport equipment, and furniture and fixtures. A summary of indoor workplaces formaldehyde emissions data is provided in Table 1-3.

Table 1.3. Summary of indoor workplaces formaldehyde emissions data [31].

Sector of economic activity	Use of formaldehyde	Exposure determinant	Maximum measured concentration (ppm)	Exposure range of workers (ppm)		Controlling the exposure
				Average 8h	Ceiling	
Manufacture of chipboard	Urea-formaldehyde resins as adhesives	- Types of resins (UF, MF, MUF) - Process conditions - Efficiency of the ventilation	<0.3 to >2.0	<0.3	<0.3 - >2.0	-Substitution with isocyanate based products, used of resins with lower emission rate. -Confinement of formaldehyde emissions. -Improve ventilation
Manufacture of wood products	Urea-formaldehyde resins as adhesives	- Types of resins (UF, MF, MUF) - Process conditions - Efficiency of the ventilation	<0.3 to >2.0	<0.3 - 0.9	<0.3- 1.7	-Substitution with isocyanate based products, used of resins with lower emission rate. -Confinement of formaldehyde emissions. -Improve ventilation

Manufacture of wood furniture	Varnishes containing aminated resins	-Types of varnishes -Process conditions -Efficiency of the general ventilation	<0.3 to >2.0	<0.3 - 0.9	<0.3 - >2.0	-Substitution: Different types of formaldehyde free coatings exist. -Confinement of formaldehyde emissions. -Improve general ventilation -Wearing personal protective equipment.
Manufacture of formaldehyde and formaldehyde based-resins	Production of formaldehyde	- Conditions of the piping and equipment - Presence and efficiency of collection system at source -Efficiency of the general ventilation	<0.3 to 1.4	<0.3	<0.3- 1.4	-Confinement of formaldehyde emissions -General ventilation. -Prevention procedures wearing personal protective equipment
Foundries	Formaldehyde based resins	-Types of binders and percentage of free formaldehyde - Types of production - Presence and efficiency of collection system at source - Efficiency of the general ventilation	<0.3 to >2.0	<0.3	>2.0	-Substitution: Not use binder containing formaldehyde - Use of resins with lower emissions -Confinements of formaldehyde emissions -General ventilation. -Prevention procedures wearing personal protective equipment
Pathology laboratories	Formaldehyde solutions	-Concentration of the formaldehyde solution -Work method - Presence and efficiency of collection system at source - Efficiency of the general ventilation	1.0 -2.0	<0.3	0.5 to >2.0	-Substitution:Different substitution products are mentioned but none is subject of consensus -Use of less concentrated formaldehyde solution -Modification of work procedures -General ventilation. -Prevention procedures wearing personal protective equipment
Funeral service industry	Formaldehyde solutions	-Concentration of the formaldehyde solution -Work method - Presence and efficiency of collection system at source - Efficiency of the general ventilation	0.4 to >2.0	<0.3-0.4	0.4- >2.0	-Substitution:Different substitution products are mentioned but none is subject of consensus -Use of less concentrated formaldehyde solution -Modification of work procedures -General ventilation. -Prevention procedures wearing personal protective equipment
Textile finishing industry	Cellulose fiber-based fabrics	-Type of processes and products used -Presence of local collection system at source -Efficiency of the general	<0.3 to >2.0	<0.3	<0.3- >2.0	-Substitution: Formaldehyde-free finished exist. -Ventilation at source -General ventilation - Prevention procedures wearing personal protective equipment

		ventilation				
Plastic processing industry	Uses of phenolic or aminated resins	-Type of process and resins used -Presence of local collection system at source -Efficiency of the general ventilation	<0.3 to >2.0	<0.3-1.5	<0.3- >2.0	-Confinement of the formaldehyde emission steps -Improve general ventilation - Prevention procedures wearing personal protective equipment

1.4 Exposure and human risk

1.4.1 Calculation of the daily intake

Although outdoor air contributes adversely to indoor air quality, it was believed that human exposure to formaldehyde mainly originates in the indoor environment rather than the ambient environment. Two parameters are of major importance in the evaluation of indoor exposure to formaldehyde: (a) the concentration in air and (b) the time spent indoors. The overall mean time of 15.7 h per day is in line with results from the United States and Canada. Approximations made by the U.S. EPA have been widely applied to calculate the daily intake of formaldehyde. The EPA indicated an inhalation rate of $0.63 \text{ m}^3 \text{ h}^{-1}$ and 10 h per day for residential exposure. The total daily intake (DI) for an individual moving in n different environments can be computed from Eq. 5, where C_j , IR_j , and t_j represent the concentration, inhalation rate, and time spent in the environment j , respectively [8].

$$DI = \sum_{j=1}^n (C_j IR_j t_j) \quad 5$$

The World Health Organization (WHO) calculated probabilistic estimations of 24 h time-weighted average concentrations of formaldehyde in air on the basis of five Canadian studies. The results indicate that one in two persons would be exposed to concentrations of $24\text{-}29 \mu\text{g m}^{-3}$, while 1 in 20 persons would be exposed to $80\text{-}94 \mu\text{g m}^{-3}$. It should, however, be pointed out that, for a respiratory tract irritant, the time weighted average concentration and especially the peak exposure are more important than the daily intake [8].

1.4.2 Short-term and long-term exposure (Noncancer)

Acute (short-term) human exposure to formaldehyde causes discomfort, irritation of the eyes, nose, and throat, lachrymation, sneezing, coughing, nausea, and finally death. In the INDEX report [32], studies of humans under controlled conditions are summarized as

follows: “critical exposures to air concentrations ranging from 0.5 mg m⁻³ to 3.7 mg m⁻³ induce reversible eye, nose, and throat irritation, produce changes in nasal lavage fluid contents (indicative of irritation of the nasal epithelium), do not consistently or markedly affect pulmonary function variables in most individuals.”

Studies of irritation in humans have been reviewed by Paustenbach *et al.* [33]. These authors concluded that irritation starts at levels around 1 ppm. Lang *et al.* [34] examined the possible occurrence of sensory irritation and subjective symptoms in human volunteers exposed to formaldehyde concentrations relevant to the workplace. They concluded that sensory eye irritation is the most sensitive parameter and obtained a non-observed effect level (NOEL) of 0.5 ppm.

Formaldehyde is a well-known skin sensitizer, but its interrelationship with asthma has been debated for many years. In a recent review focusing on the effects of residential formaldehyde levels, Arts *et al.* [35] evaluated the data available, especially for children. They concluded that the question is still open whether there is a causal relationship between formaldehyde and allergic asthma, or whether formaldehyde induces airway irritation resembling asthmatic reactions.

In occupational and residential environments, long-term exposure to increased levels of formaldehyde results in irritation of the upper and lower airways and eyes. Most studies related to chronic effects refer to the working environment, where formaldehyde is frequently used. The predominant effect of formaldehyde is sensory irritation at low concentrations, which will progress to cytotoxic irritation with cell destruction at higher concentrations. These effects are concentration- and not time-dependent. The threshold concentrations for sensory and cytotoxic irritation are therefore very similar for serious and chronic exposures. Concentrations not leading to sensory irritation after critical exposures are not expected to result in adverse effects after prolonged exposures [8].

1.4.3. Formaldehyde as a human carcinogen

The classification of formaldehyde as a known human carcinogen by IARC is based on group mortality studies of workers exposed to formaldehyde with an increased incidence of nasopharyngeal cancer [36]. However; the evaluation by IARC has been questioned by several authors. Marsh and Youk [37] pointed out that their reanalysis of the available data provided little evidence for a causal association between formaldehyde exposure and mortality and they recently provided evidence that the increased incidence of nasopharyngeal

cancer might be related to exposures to several suspected risk factors for upper respiratory system cancer (e.g., sulphuric acid mists, mineral acid, metal dusts, and heat) in the metal industries of that area.

The German Federal Institute for Risk Assessment (BfR) and other institutions have stated that results from recent epidemiological studies support a possible causal relationship between inhalation exposure to formaldehyde and nasopharyngeal cancer [38].

According to the evaluation by IARC, the epidemiologic evidence was strong but not sufficient to conclude that formaldehyde exposure causes leukaemia in humans. Moreover, a probable mechanism has not been identified as a cause of how leukaemia may be induced after formaldehyde inhalation. Since the discussion is mainly driven by the National Cancer Institute (NCI) study [39], the observation of Marsh and Youk [37] is relevant in the sense that the increasing trend noted in the NCI study is produced by a deficit of leukaemia cases among the unexposed and low exposed workers. Their reanalysis provided little evidence to support NCI's suggestion of a causal association between formaldehyde exposure and mortality from leukaemia.

For the risk assessment approach with regard to carcinogens, the mode of action is of crucial importance. For genotoxic chemicals that lead to tumours by mutations of the DNA, it is generally accepted that a threshold cannot be defined and linearized mathematical models are used to define an exposure with acceptable risk as regard socioeconomic considerations. A different approach is applicable to nongenotoxic carcinogens that lead to tumours by a threshold mechanism, such as, for example, chronic irritation. Exposures below this threshold are not expected to have a carcinogenic effect. In 2000, the German MAK commission concluded that, at low exposure, concentrations without an increase of cell proliferation genotoxicity “play no or at most a minor part, so that no significant contribution to human cancer risk is expected”[8].

1.5 References

- ¹ S. Ojala, S. Pitkaaho, T. Laitinen, N. Niskala, S. Paivarinta, C. Hirsman, T. Nevanpera, M. Riihimaki, M. Pirila. *Topic on Catal.* **2011**, *54*, 1224.
- ² Council Directive 1999/13/EC of 11 March 1999 on the limitation of emissions of volatile organic compounds due to the use of organic solvents in certain activities and installations (1999) Off J Eur Union.
- ³ United States Environmental Protecting Agency. Definition of volatile organic compounds (VOC) as of 3/31/2009 40 CFR 51.100(s) definition volatile organic compounds (VOC).
- ⁴ Environment Canada (2010) Volatile organic compound definition.
<http://www.ec.gc.ca/cov-voc/default.asp?lang=En&n=10A29F5-1>.
- ⁵ N. Bunce. Environmental Chemistry. Wuerz Publishing Ltd. 1991, pp. 1–115.
- ⁶ G. A. Ayoko; *The Handbook of Environ. Chem.* **2004**, Vol. 4, 1.
- ⁷ S. Wang; H.M. Ang; M. O. Tade. *Environ. Int.* **2007**, *33*, 694.
- ⁸ T. Salthammer; S. Mentese; R. Marutzky. *Chemical. Review.* **2010**, *110*, 2536.
- ⁹ G. Reuss; W. Disteldorf; A.O. Gamer; A. Hilt, Formaldehyde. In: Ullmann's Encyclopedia of Industrial Chemistry. Ed. Wiley-VCH Verlag GmbH &Co. **2003**, Vol. 15, 1.
- ¹⁰ H.R. Gerberich, & G.C. Seaman. Formaldehyde. In: *Encyclopedia of Chemical Technology*, 5th Ed., New York, John Wiley & Sons. **2004**, Vol. 11, 929.
- ¹¹ E. Roffael. Formaldehyde Release from Particleboard and Other Wood Based Panel; Forest Research Institute Malaysia: Kuala Lumpur, **1993**.
- ¹² R. Atkinson. *Atmos. Environ.* **2000**, *34*, 2063.
- ¹³ X. Tang; Y. Bai; A. Duong; M. T. Smyth; L. Li; L. Zhang. *Environ. Int.* **2009**, *35*, 1210.
- ¹⁴ K. Freudenberg, M. Harder. Lignin. II. Formaldehyde as a cleavage product of lignin. *Ber. Dtsch. Chem. Ges. (A and B Ser.)* **1927**, *60*, 581.
- ¹⁵ K. Muller, S. Haferkorn, W. Grabmer, A. Wisthaler, A. Hansel, J. Kreuzwieser; C. Cojocariu, H. Rennenberg, H. Herrmann. *Atmos. Environ.* **2006**, *40*, 81.
- ¹⁶ D. Trapp, K. M. Cooke, H. Fischer, B. Bonsang, R. U. Zitzelsberger, R. Seuwen, C. Schiller, T. Zenker, U. Parchatka, T. V. Nunes, C. A. Pio, A. C. Lewis, P. W. Seakins, M. Pilling. *Chemosphere.* **2001**, *3*, 295.
- ¹⁷ W. P. L. Carter, R. Atkinson. *Int. J. Chem. Kinet.* **1996**, *28*, 497.
- ¹⁸ J. Kesselmeier, U. Kuhn, A. Wolf, M. O. Andreae, P. Ciccioli, E. Brancaleoni, M. Frattoni, A. Guenther, J. Greenberg, P. De Castro Vasconcellos, T. de Oliva, T. Tavares, P. Artaxo. *Atmos. Environ.* **2000**, *34*, 4063.
- ¹⁹ S. Machado Correa, G. Arbilla. *Atmos. Environ.* **2008**, *42*, 769.
- ²⁰ L. L. N. Guarieiro, P. A. Pereira, E. A. Torres, G. O. da Rocha, J. B. de Andrade. *Atmos. Environ.* **2008**, *42*, 8211.

-
- ²¹ E. Hedberg, A. Kristensson, M. Ohlsson, C. Johansson, P.-Å. Johansson, E. Swietlicki, V. Vesely, U. Wideqvist, R. Westerholm. *Atmos. Environ.* **2002**, *36*, 4823.
- ²² J. J. Schauer, M. J. Kleeman,; G. R. Cass,; B. R. T. Simoneit. *Environ. Sci. Technol.* **2001**, *35*, 1716.
- ²³ US Environmental Protection Agency (EPA) Toxicological Review of Formaldehyde Inhalation Assesment. Washinton DC. **2010**
- ²⁴ P. Wolkoff, P. A. Clausen, B. Jensen, G. D. Nielsen, C. K. Wilkins. *Indoor Air.* **1997**, *7*, 92.
- ²⁵ C. J. Weschler, A. T. Hodgson, J. D. Wooley. *Environ. Sci. Technol.* **1992**, *26*, 2371.
- ²⁶ R. B. Lamorena, W. Lee. *J. Hazard. Mater.* **2008**, *158*, 471.
- ²⁷ S. O. Baek, R. A. Jenkins. *Atmos. Environ.* **2004**, *38*, 6583.
- ²⁸ B. C. Singer, A. T. Hodgson, W. W. Nazaroff. *Atmos. Environ.* **2003**, *37*, 5551.
- ²⁹ R. R. Baker. *Food Chem. Toxicol.* **2006**, *44*, 1799.
- ³⁰ M. Maroni, B. Seifert, T. Lindvall. Eds.; Indoor Air Quality; Elsevier: Amsterdam. **1995**
- ³¹ N. Goyer, D. Begin, G. Carrier, IRSST Prevention Guide: Formaldehyde in the Workplace. www.irsst.qc.ca.
- ³² D. Kotzias, K. Koistinen, S. Kephelopulos, C. Schlitt, P. Carrer, M. Maroni, M. Jantunen, C. Cochet, S. Kirchner, T. Lindvall, J. McLaughlin, L. Molhave, E. de Oliveira Fernandez, B. Seifert. The INDEX project - Critical appaisal of the setting and implementation of indoor exposure limits in the EU; EUR-21590-EN; EC-JRC;Ispra. **2005**
- ³³ D. Paustenbach, Y. Alarie, T. Kulle, N. Schachter, R. Smith, J. Swenberg, H. Witschi, S. B. Horowitz. *J. Toxicol. Environ. Health, Part A.* **1997**, *50*, 217.
- ³⁴ I. Lang, T. Bruckner, G. Triebig. *Regul. Toxicol. Pharmacol.* **2008**, *50*, 23.
- ³⁵ J. H. E. Arts, H. Muijser, F. C. Kuper, R. A. Woutersen. *Regul. Toxicol. Pharmacol.* **2008**, *52*, 189.
- ³⁶ M. Hauptmann, J. H. Lubin, P. A. Stewart, R. B. Hayes, A. Blair. *Am. J. Epidemiol.* **2004**, *159*, 1117.
- ³⁷ G. M. Marsh, A. O. Youk. *Regul. Toxicol. Pharmacol.* **2005**, *42*, 275.
- ³⁸ D. McGregor, H. Bolt, V. Cogliano, H.-B. Richter-Reichhelm. *Crit. Rev. Toxicol.* **2006**, *36*, 821.
- ³⁹ M. Hauptmann, J. H. Lubin, P. A. Stewart, R. B. Hayes, A. Blair. *J. Natl. Cancer Inst.* **2003**, *95*, 1615.



CHAPTER 2

Chapter 2: Formaldehyde removal techniques and formaldehyde complete catalytic oxidation

2.1 Formaldehyde removal technologies

2.1.1 General Aspect

For lowering the concentration of formaldehyde in the indoor environment different techniques have been developed. Among these techniques, surface treatment by use of reactive or diffusion resistant coatings, and fumigation with ammonia, could be applied for the treatment of very high concentration of formaldehyde in the 1980 and 1990s. The reaction with ammonia which yields hexamethylene tetramine was consequently used in prefabricated houses [1]. The design of intelligent housing construction and ventilation systems has been proposed to reduce pollutant levels [2]. From time to time, it is reported that plants can act as air cleaners, but the literature data on this topic is contradictory, even if capacity of removal of plants remains very low.

In general, three methods are suggested to improve the indoor air quality: source control, increase ventilation, and air cleaning. Source control is the most effective way to reduce formaldehyde and other pollutants in indoor air. However, source control it is often uncontrollable and mandatory in metropolis and industry. The feasibility of source removal will sometimes depend on the circumstances. It could be easy in the case of furniture, but it could be more complicated in the case of a built structure or industry [3].

Nowadays, people are exposed to lower formaldehyde concentrations in indoor environments, and it is more convenient to reduce pollutant levels by use of intelligent housing construction and ventilation in the case of residential exposure [4,5]. However, in industries the substitution of formaldehyde by less contaminant pollutant is still a challenge, which in some particular cases seems even very difficult to achieve.

When increasing ventilation or controlling the source becomes hard, the air cleaning technologies to remove the pollutant during or after their application can be the most feasible option to improve the indoor air quality. Traditional pollution control methods, such as adsorption by activated carbon, only transfer pollutants from gaseous to solid phase. Catalytic and photocatalytic oxidation come to the attention of indoor research in the last decades since

pollutants can be oxidized to H₂O and CO₂. In the next section, a general survey of these air cleaning technologies will be presented.

2.1.2 Adsorption

Traditional pollution control methods, such as adsorption by activated carbon (AC), basically transfer pollutants from gaseous to solid phase; this process suggests steps of adsorbent regeneration and final degradation of pollutants. The majority of studies available in the literature deals with the adsorption of formaldehyde on activated carbon [6,7,8]. These studies show that the efficiency of the adsorbent strongly depends on the carbon surface chemistry, while the pore size and geometry also play an important role. Virote *et al.* [6] prepared activated carbons from coffee residues and investigated their formaldehyde adsorption at high concentration (13,767–74,216 ppm). The authors found that activated carbon treated by ZnCl₂ and activated under nitrogen, presenting surface area and pore volume of 470 m²/g and 0.454 cc/g respectively, exhibited the highest adsorption capacity (245 mg/g of carbon). However, the activated carbon derived from coffee treated with ZnCl₂ and activated under carbon dioxide, yields the highest surface area (914 m²/g) and total pore volume (1.010 cc/g) but adsorbs less formaldehyde 130 mg/g of carbon. Therefore, the surface chemical properties of activated carbon significantly affect the adsorption capacity. Moreover, changes in surface properties of the adsorbent can significantly increase the performance. The presence of functionalized groups, oxygenated [9] or amino [10], can increase the affinity of formaldehyde with the adsorbent surface. Song *et al.* [8] studied low concentration (20 ppm) formaldehyde adsorption behavior over various AC prepared from different precursors. Among the AC investigated, polyacrylonitrile (PAN)-based AC showed the best formaldehyde adsorption capacity, which might be originating from the abundant surface nitrogen-containing groups, especially pyrrolic or pyridonic nitrogen, pyridinic nitrogen, and quaternary nitrogen-containing groups, which might promote the adsorption of formaldehyde. The breakthrough time and formaldehyde adsorption amount at saturation were 361 min and 0.478 mmol/g, respectively, for a material presenting surface area of 378 m²/g and pore volume of 0.22 cc/g.

A major limitation encountered in adsorption process is the effect of water partial pressure. Indeed, the adsorption capacity of AC decreases abruptly when the relative humidity increases from 30 to 80% (Figure 2.1) [11]. For example, when the relative humidity of mixture gas (containing 20 ppm of formaldehyde balanced with N₂) increased from 30% to 80%, the breakthrough times of formaldehyde, decreased from 6.39 min to 1.35 min

respectively, for AC derived from coconut shell. This effect is explained by the hydrophilic nature of formaldehyde, and therefore the adsorption competition between water and formaldehyde. However, it is possible to limit the effect of water by functionalizing the adsorbent surface with hydrophobic functions (such as organosilane type functions). The same authors reported that for modified AC derived from coconut shell, functionalized with organosilane surface groups, the breakthrough times of formaldehyde decreased from 8.28 min to 4.47 min at 30% and 80% relative humidity, respectively (Figure 2.1). This shows that the amount of formaldehyde adsorbed on the modified activated carbon was larger than that on the original activated carbon at higher relative humidity, and thereby that the use of organosilane compounds to modify surface of the activated carbon can greatly enhance its adsorption selectivity toward formaldehyde. Examples of breakthrough curves of formaldehyde over activated carbon are presented in Figure 2.1.

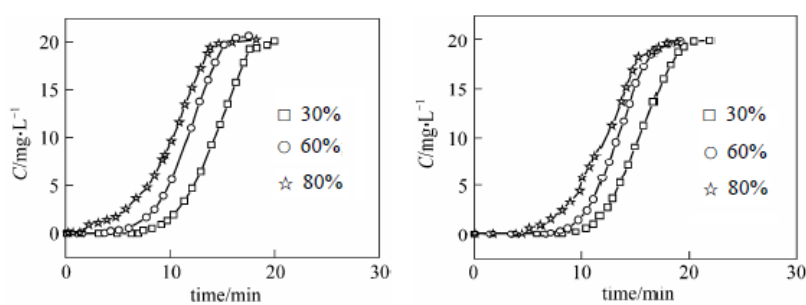


Figure 2.1. Effects of relative humidity on formaldehyde breakthrough curves a) unmodified activated carbon and b) organosilane modified activated carbon. From reference [11].

In addition to the adsorption over microporous carbon, several types of inorganic solids, including microporous zeolites, mesoporous silica, phosphates and alumino-silicates, have been envisaged. Mesoporous silicas functionalized with amine groups are proving to be excellent adsorbents, with capacities up to three times higher than those measured on activated carbon [12]. Then, adsorption capacities up to 1200 mg/g are achieved over the functionalized mesoporous supports, while the carbon reference presented exhibits adsorption capacity of only 250 mg/g. Few recent studies have also shown that zeolites of FAU and LTA type are also good candidates for application in formaldehyde adsorption [13,14,15]. Indeed, FAU-type zeolite is able to adsorb formaldehyde up to 72 mg/g. In addition, the strong affinities of formaldehyde with the surface of the microporous supports allow the formaldehyde removal at low concentrations in effluent (< 100 ppm). Recently, adsorption of formaldehyde by polyamine-intercalated α -zirconium phosphate was studied [16]. The

intercalation compounds are used as a reaction field of self oxidation-reduction of formaldehyde (Cannizzaro reaction in the interlayer space) and also as adsorbents of formaldehyde.

2.1.3 Photocatalytic oxidation

Photocatalysis is also an emerging and promising technology for indoor air purification. Photocatalytic method is effective in the case of high pollutant concentrations; however, its wide application in indoor air purification is limited due to the low level of contaminants generally encountered. The air purification technique by photocatalytic oxidation (PCO) commonly uses nanosemiconductor catalysts and ultraviolet (UV) light to convert organic compounds into benign and odorless constituents such as water vapor (H_2O) and carbon dioxide (CO_2) [17]. Several investigations have found that different inlet pollutant concentrations lead to different reaction rates [17]. Thus, it is necessary to investigate the photocatalytic performances at a low pollutant level. Most PCO reactors use nano-titania (TiO_2) as catalyst that is activated by UV light. Figure 2.2 illustrates schematically the UV-PCO process of VOCs using TiO_2 as catalyst. An electron in an electron-filled valence band (VB) is excited by photo irradiation to a vacant conduction band (CB), leaving a positive hole in the VB. These electrons and positive holes drive reduction and oxidation, respectively, of compounds adsorbed on the surface of the photocatalyst [18].

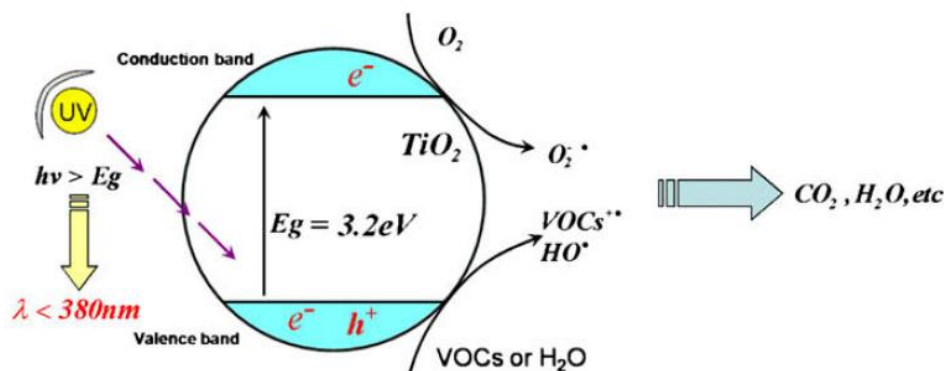


Figure 2.2. Schematic representation of TiO_2 UV photocatalytic oxidation process of VOCs From reference [17].

PCO process for formaldehyde removal has recently become popular. Some authors showed that formic acid and carbon monoxide were identified as intermediate for formaldehyde photocatalytic oxidation [19,20]. Sun *et al.* [21] studied the adsorption and

photocatalytic oxidation of formaldehyde on pure TiO₂ under dry and humid conditions by *in situ* diffuse reflectance Fourier transform infrared spectroscopy (DRIFTS). The authors found that formaldehyde is adsorbed on the hydroxyl groups of the catalyst surface *via* hydrogen bonding. The humidity has consequently a positive effect on the photocatalytic oxidation of formaldehyde. The reason is that the introduction of water results in an accumulation of the hydroxyl radical OH• on the catalyst surface. The hydroxyl radicals OH• are extremely powerful oxidants due to their high redox potential. As a result, the formation rates of formate molecules as intermediates, as well as of CO₂ and H₂O final oxidation products, are significantly increased (Figure 2.3b). In addition to the oxidation of formaldehyde through OH• radicals, some other oxygen species as superoxide (Figure 2.3a) can oxidize formaldehyde.

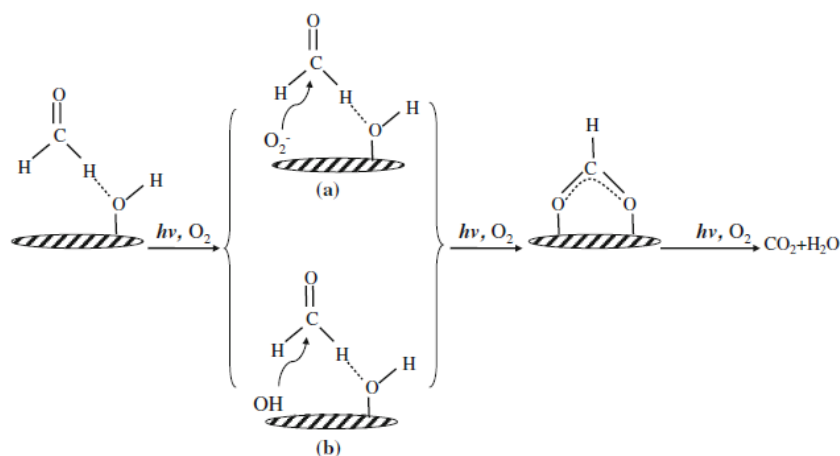


Figure 2.3. Reaction scheme of formaldehyde photocatalytic oxidation over TiO₂ (a) superoxide radical anion O₂^{•-} as oxidant; (b) hydroxyl radical OH• as oxidant. From reference [22].

The effect of activated carbon adsorption on the photocatalytic removal of formaldehyde was investigated by Lu *et al.* [22]. The authors evaluated the photocatalytic performance over the nanosized TiO₂ particles immobilized on the surface of activated carbon (AC). It is observed that the photocatalytic reaction rate increased since AC is able to formaldehyde oxidation from the diluted air stream. The effect is then the generation of an increased concentration on the active catalyst surface. Therefore, the combination of photocatalytic technology with AC adsorptive technology might be a valid pathway to purify indoor HCHO (with the main characteristic to remain at low level of pollutant concentration).

Nano-structured TiO₂, Ag-doped TiO₂ and Ce-doped TiO₂ thin films, prepared by sol-gel method, were also used for the HCOH photo-catalytic decomposition [23]. The effects of

humidity, O₂ concentration, HCOH initial concentration, UV light intensity, and photocatalyst amount on the HCHO decomposition rate under TiO₂/UV conditions were analyzed simultaneously. Byproducts were identified, and a mechanism of HCHO degradation over these catalysts was proposed. The results showed that Ag or Ce dopants enhance the photocatalyst activity. The degradation rate measured was in the sequence Ce/TiO₂ > Ag/TiO₂ > TiO₂. 35% was the optimal humidity for the photo-catalyst process under the experimental conditions. The increase in oxygen concentration is beneficial for the HCHO removal rate, while photocatalytic degradation rate decrease with the increase in HCHO initial concentration. Clay-TiO₂ nanocomposites have also been proposed as suitable alternative photocatalysts in environmental applications. Recently, Kibanova *et al.* [24] have synthesized hectorite-TiO₂ composite (hecto-TiO₂). This material was evaluated for the adsorption and photocatalytic removal of formaldehyde with respect to the reference Degussa P25 TiO₂ catalyst, under controlled conditions of relative humidity, UV irradiation and residence time. The results showed that formaldehyde uptake over hectorite-TiO₂ were 4.1 times higher than over P25. Under irradiation with different UV sources, removal efficiencies were proportional to the titanium content. These results evidenced that clay-TiO₂ composites can enter the formulation of paints, coatings, pavement and cement, as pollution-removing active ingredients including formaldehyde.

2.1.4 Catalytic oxidation

Due to the high effectiveness in achieving total conversion of HCOH into harmless CO₂ and H₂O molecules, Complete Catalytic Oxidation (CCO) formaldehyde was recently demonstrated as an attractive alternative to the two previously presented processes. However, the low concentration of formaldehyde in indoor air requires a catalyst exhibiting high activity, preferably at ambient temperature to ensure a limited energy demand. Supported noble metals (including platinum, palladium...) are considered as promising catalysts for this process, due to their ability to activate VOCs at low temperature. However, the catalyst deactivation occurring at ambient temperature, in the case of formaldehyde, is important [25]. Moreover, the CCO of formaldehyde in the presence of inhibitors (including water) has not been enough studied. Therefore, the development of new catalysts (free of noble metal for low cost), exhibiting high catalytic activity for HCHO complete oxidation at low temperatures and presenting strong resistance to water adsorption (and other inhibitors) is still of high relevance.

2.2 Catalytic oxidation for formaldehyde removal

2.2.1 Heterogeneous catalytic oxidation: general aspects of oxidation of VOCs

Heterogeneous catalytic oxidation is a well-studied process due to its industrial relevance. Moreover, partial and complete catalytic oxidations are important processes for reactions such as partial oxidation of ethylene and propylene, maleic anhydride production, production of sulfuric acid and oxidation of hydrocarbons in automotive exhaust gas depollution, among others. The majority of oxidation catalysts and catalytic oxidation processes have been developed for the commercialization of these industrially important reactions [26].

Unfortunately, considerable differences exist between conditions applied for commercial processes and the complete catalytic oxidation of VOCs at trace concentration in air. Indeed, industrial catalytic oxidation reactions are often carried out at high reactant concentrations. In contrast to these industrial reactions, catalytic oxidation of VOCs in air is carried out at low reactant concentration (ppm level, and below) but with very large stoichiometric excess of oxygen. Since oxidation is an exothermic reaction, industrial reactions are usually net producer of heat at high reactant concentrations. When the reactant concentration is low, the processes are net consumers of heat and the entire gas stream must be heated at elevated temperatures to achieve consequent conversions. Therefore, complete catalytic oxidation of VOCs is economically attractive if the reaction proceeds at low temperature. Thus, highly active and nonselective catalysts are required [26].

Two major classes of catalysts can be distinguished for the complete oxidation of VOCs: supported noble metals and supported or unsupported transition metal oxides. In the next section, a general description of the complete catalytic oxidation mechanism for both types of catalyst will be succinctly introduced.

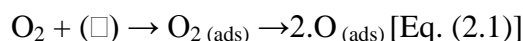
Noble metals catalysts

Precious metals are recognized as the most active phases for the oxidation of VOCs. For these applications, Pt, Pd, Ag, and Au are usually supported on an inert oxide such as alumina or silica. In most practical systems, only Pt and Pd are used since the high temperatures employed for oxidation applications can cause sintering, loss and irreversible oxidation for the

other active phases. As a result, most of the reported researches deal with supported Pt and Pd catalysts, even if these systems can also present deactivation in reaction [26].

A general mechanism for complete total oxidation of VOCs over noble metals cannot be given. The oxidation of CO over noble metals has been extensively studied, and despite the extensive research on this specific reaction, it is difficult to extend the obtained results over this molecule to the oxidation of organic compound [26]. However, literature concerning the complete oxidation of organic compounds over noble metals shows the following general trends:

- Oxidation over noble metals may follow two different mechanisms: the Langmuir-Hinshelwood mechanism, in which the reaction occurs between the adsorbed oxygen species and the adsorbed reactant; or the Eley-Rideal mechanism in which the reaction proceeds between adsorbed oxygen species and reactant molecule in gas phase.
- The mechanism of oxidation over noble metals is thought to involve the dissociative adsorption of oxygen



Where (\square) represents a “surface site” and (ads) refers to surface adsorbed species. The oxygen adsorption / activation step is then followed by reaction of the gaseous organic reactant with the active oxygen adsorbed species. The reactant may however be weakly adsorbed on the surface before reaction.

Due to high and fluctuating cost and scarcity of precious metals, attention has been focused on metal oxide catalysis for combustion of VOCs. Indeed, some of metal oxide phases were highlighted as very powerful systems for low temperature oxidation reactions. This is for example the case of copper and cobalt oxide species in the case of CO oxidation reaction [27] for which oxidation can be performed below the ambient temperature.

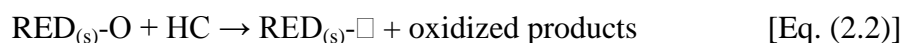
Metal oxides catalysts

Transition metal oxides represent one of the most important and widely employed classes of solid catalyst, either as active phase or as support. Metal oxides are used for their acid-base and redox properties [28].

Oxides of transition metals, mainly Cr, Mn, Co, Ni, Fe, Cu, and V, are employed for the oxidation of organic compounds. Deep oxidation reactions over these metal oxides are

considered to be catalyzed by lattice oxygen [26,28]. A common feature of these materials is the presence of multiple oxidation states of transition metal in the structure, resulting in the ability of the cation to undergo reversible oxidation and reduction under reaction. Occurrence of vacancies in the structure during these redox cycles is then strongly suspected. Some of these aspects, as well as the redox mechanisms developed by Mars and van Krevelen [29], are discussed below.

The oxide catalyst, under given reaction conditions, and undergoing reduction and reoxidation simultaneously by giving out the surface lattice oxide ions and taking in oxygen from the gas phase, can be called “redox” catalyst. Catalytic redox processes on metal oxides are often described in terms of a general redox mechanism, consisting in two successive steps:

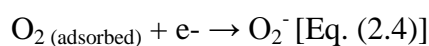


According to this mechanism, the oxide catalyst surface ($\text{RED}_{(s)\text{-O}}$) is reduced when oxidation reaction with the hydrocarbon (HC) proceed [Eq. (2)]. The so-formed reduced site ($\text{RED}_{(s)\text{-}\square}$) can return to its initial state by reoxidation by gas phase oxygen consumption, as described in the second step of the mechanism [Eq. (3)] or by diffusion of oxygen ions from the bulk to the surface. The two step reaction is a cyclic reaction in which transfer of oxygen from the solid to the gas phase occurs. In the majority of redox reactions occurring on the surface of oxide catalysts, the source of oxygen (*i.e.* consumed for the oxidation reaction) is coming from the surface of the oxidized metal oxide. Nucleophilic surface oxygen species in these reactions attack electron deficient centers of the adsorbate molecules [28].

The activity of the catalyst for deep oxidation depends on the type of oxygen involved in the reaction. Numerous oxygen species may be present on the metal oxide surfaces: O_2 (adsorbed molecule), O (adsorbed neutral atom), O_2^- (superoxide), O_2^{2-} (peroxide), O_3^- (ozonide), or O^- (ion radical). Depending on the nature, oxidation state of the metal ion and its environment, the metal-oxygen bound may be more or less polarized and therefore the oxygen ion may exhibit electrophilic or nucleophilic properties [28]. The stability of the oxygen species and the type of active oxygen species also determine the selectivity in the oxidation reaction. There is evidenced in the literature that nucleophilic O^{2-} species are capable of carrying out selective oxidation. Lattice oxygen is extracted and oxygen vacancies are created. At the opposite, active surface species lead to complete combustion products

(electrophilic reactions) [30,31]. Nucleophilic oxygen species then include saturated species such as terminal oxygen groups M=O, or μ -oxo bridging groups M-O-M. Electrophilic oxygen species however comprise electron deficient adsorbed species such as peroxide O_2^- , peroxide O_2^{2-} , and ion radical species O^- [28].

The chemisorption of molecular oxygen on the surface of a metal oxide involves different steps: (i) coordination to the metal center, (ii) electron transfer from the solid to the adsorbed molecule, (iii) dissociation into atomic species, and (iv) incorporation into the oxide lattice. With the participation of valence band electron, the possible detailed scheme for the reinsertion of oxygen in the solid can be written as follow:



When the metal oxide is a *n*-type semiconductor, the oxygen uptake is limited, due to the increased repulsion between the negatively charged adsorbed species and the mobile electrons. For the same reason, the adsorbed species which are preferentially formed are O_2^- , O_2^{2-} and O^- , while the formation of the O^{2-} species and its incorporation into the lattice is less favored. On *p*-type semiconductors, the molecular oxygen picks up electrons that are left by positive holes. In this case, lowered electrostatic repulsion is developed and electron furnishing to oxygen species can proceed up to the formation of the O^{2-} species, and its incorporation into the lattice to replenish an oxygen vacancy (defect) generated by oxygen consumption occurring during oxidation reaction [32].

2.3 Formaldehyde complete catalytic oxidation

2.3.1 Supported noble metals catalysts

Complete catalytic oxidation of formaldehyde on supported noble metals was first reported by Imamura *et al.* [33]. The authors reported a study of the noble metal nature effect on the catalytic properties when supported over ceria. Authors reported the following activity order at 90% formaldehyde conversion: Ru/CeO₂ > Pd/CeO₂ > Rh/CeO₂ > Pt/CeO₂. Ruthenium was the most active catalyst, and it completely oxidized formaldehyde at 200 °C to produce only CO₂ and H₂O in the reaction conditions used. FT-IR analyses indicated that

formaldehyde decomposed on the catalyst surface at RT to produce different intermediate species such as methoxide (CH_3O), poly(oxymethylene) (CH_2O) and dioxymethylene (H_2CO_2). *In situ*-XPS analyses show that Ru is initially present as RuO_2 before formaldehyde adsorption. After formaldehyde adsorption, and heating at 100°C , XPS allows the detection of metallic Ru phase. It evidenced that ruthenium oxide easily loses its lattice oxygen, which can explain the high activity of this metal. The same intermediate species were identified over silver supported on CeO_2 catalyst [34]. High activity appeared and 100% conversion was attained at 300°C for all silver-cerium composite catalysts regardless of their composition. For this kind of catalyst, the activity was partly attributed to the high dispersion of active silver species over the CeO_2 support. Vannice *et al.* [35] also studied silver based catalyst for HCOH oxidation. Ag dispersed on both high surface area alumina and silica was investigated. These catalysts were active below 200°C , but significant deactivation occurs at low temperature ($T < 200^\circ\text{C}$). This deactivation was related to (i) formaldehyde polymerization progressively covering the Ag active surface, (ii) poisoning of active sites by strongly bound species or (iii) pore blockage by polymerization products.

One problem, not well described, is the deactivation of the catalysts at low temperature by water vapor, due to capillary condensation and slow water desorption. Chuang *et al.* [25] developed an original technology to limit the deactivation phenomenon. They loaded platinum active phase on a hydrophobic support. The support used by the authors is a fluorinated carbon (surface area = $340 \text{ m}^2/\text{g}$) coated over 6 mm ceramic Raschig ring. The support, being water repellent, limits the active phase deactivation by water, which is also a product of the VOC oxidation reaction. The hydrophobic supported catalyst exhibits excellent catalytic activity, with HCHO conversion starting at only 63°C . At $[\text{HCHO}] < 100 \text{ ppm}$ in the gas phase, 100% conversion is achieved at temperatures slightly above 150°C . In addition, the reaction temperature increase results in increased selectivity toward CO_2 , with a decreased production of HCOOH intermediate.

The use of titania (TiO_2 , anatase form) as support for noble metals was recently investigated. He *et al.* [36,37] have compared the performances of TiO_2 supported noble metal for formaldehyde total oxidation. The following activity sequence is obtained: $\text{Pt}/\text{TiO}_2 \gg \text{Rh}/\text{TiO}_2 > \text{Pd}/\text{TiO}_2 > \text{Au}/\text{TiO}_2$. Then, under the reaction conditions, 1 wt.% Pt over titania is able of complete formaldehyde oxidation at 20°C , while the other noble metals exhibit very limited activity. An important feature to explain the good performance of the Pt/TiO_2 catalyst is the high dispersion and the small size of the platinum particles ($\sim 1 \text{ nm}$).

The same activity trend was obtained by Wang *et al.* [38], whose reports superior activity of Pt/TiO₂ for the HCOH total oxidation reaction. The authors also compared different supports. The following activity sequence for 0.6 wt.% Pt with respect to the support was proposed TiO₂ > SiO₂ > Ce_{0.8}Zr_{0.2}O₂ > Ce_{0.2}Zr_{0.8}O₂. The performances of the materials are related to the dispersion of platinum on the different supports rather than properties of the supports. The different activities of the noble metals in the HCHO oxidation were related to their ability to form formate species and to decompose them into CO adsorbed species on the catalyst surface. In the presence of O₂, the CO adsorbed species is oxidized to CO₂ [36,37]. Based on *in situ* DRIFTS studies, a simplified mechanism for the catalytic oxidation of HCOH over TiO₂ supported noble metal was proposed (Figure 2.4).

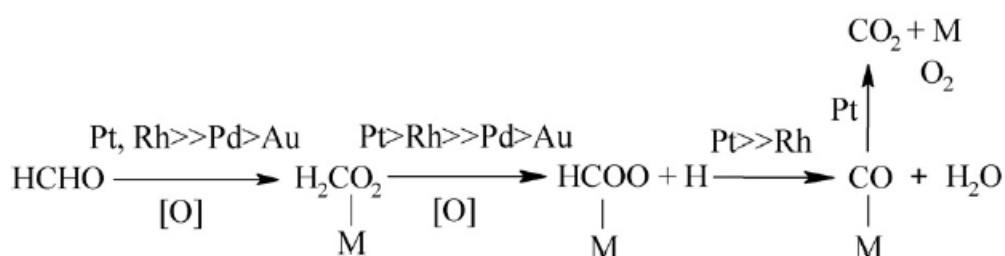


Figure 2.4. Simplified reaction scheme of the catalytic oxidation of HCOH on noble metal/TiO₂ Catalyst at room temperature.[36,37].

Theoretical study of formaldehyde catalytic oxidation at ambient temperature has been done for Pt/TiO₂ catalyst [39]. This study showed that predicted and experimental data are in excellent agreement [40], validating the theoretical approach and confirming the experimental results. In these studies, no by-product was detected in effluent gases, which indicates that CO₂ and H₂O were the only products of oxidation. Although supported Pt catalyst has been evidenced to be effective for HCOH oxidation at low temperature, high loading of Pt is generally needed, which greatly limits its application due to the price of platinum. One alternative is to improve the catalytic activity in order to lower the platinum loading in Pt/TiO₂ catalyst. Recently, Leung *et al.* [41] demonstrated that TiO₂ supported Pt catalysts containing only 0.1 wt.% are highly active for the catalytic oxidation of formaldehyde at RT; a stable formaldehyde conversion close to 100% can be achieved under the applied conditions (10 ppm HCOH). The influences of oxidation state, support nature and platinum particle size were also investigated. An important feature is that nearly 100% HCOH conversion was obtained on the reduced Pt/TiO₂ catalyst at RT, while it was less than 25% over the oxidized catalyst. It is however well known that the oxidation state of noble metals is an important factor controlling the catalytic activity [42]. In another work [43], the same authors studied in

detail the effect of the reduction procedure on the structural properties of the platinum final nanoparticles, and its consequence on the performance for the oxidation of HCOH. Well-dispersed and negatively charged Pt nanoparticles with very small and homogeneous size and rich chemisorbed oxygen can be obtained after reduction treatment during the preparation. For instance, sodium borohydride reduced Pt/TiO₂ catalysts, even with 0.1% Pt loading, showed nearly complete oxidation of HCHO at R.T. These features can explain the high catalytic activities measured. Very recently, Zhang *et al.* [44] studied the effect of alkali metal addition (Li, Na, K) on the performances of Pt/TiO₂ catalyst. The authors reported that addition of Na ions to Pt/TiO₂ is a promising way to strongly promote the activity of Pt-containing catalysts for the HCHO oxidation. A new low-temperature reaction pathway (denoted Direct Formate Oxidation) is facilitated in the presence of the alkali metal dopant (M): $\text{HCOO-M} + \text{OH-M} \rightarrow \text{H}_2\text{O} + \text{CO}_2 + 2\text{M}$. Catalytic activity improvement is related to the stabilization of hydroxyl species in close proximity of the Na-O-Pt sites. OH groups are suggested to be regenerated by the H₂O vapor contained in the stream.

Gold-based catalysts were also evidence to be active for formaldehyde oxidation. Particularly, Au/CeO₂ exhibits high activity for HCOH oxidation at temperature ranging between 80 and 100°C [45,46,47]. A series of catalysts containing gold at loading below 0.85 wt.% deposited over CeO₂ and calcined at 300°C were able to transform HCHO into CO₂ and H₂O at ~100°C. The activity of the catalyst is related to the crystal structure of gold nanoparticles in the catalyst. Highly dispersed and poorly crystallized metallic gold showed superior catalytic activity for HCOH oxidation than large and well crystallized particles obtained at higher calcination temperatures [45]. In more recent works [46,47], a new synthetic route was developed to obtain three dimensionally ordered macroporous (3DOM) Au/CeO₂ catalyst (0.56 wt.% Au). The 3DOM CeO₂ support was prepared via template-directed synthesis by using colloidal crystal polystyrene (PS) spheres as templates. Au nanoparticle incorporation on 3DOM CeO₂ supports was carried out by a gas bubbling-assisted deposition precipitation approach. SEM images of 3DOM CeO₂ support and TEM images of the resulting Au/3DOM-CeO₂ catalyst are presented in Figure 2.5.

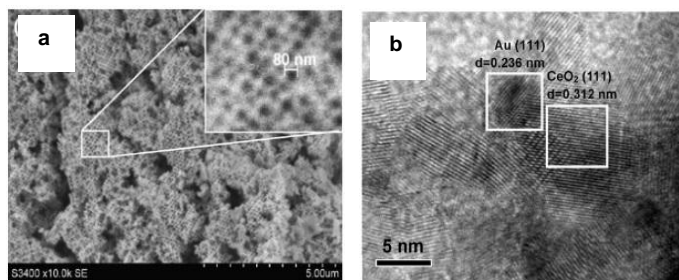


Figure 2.5: (a) SEM image of 3DOM-CeO₂ support and (b) TEM image of the resulting Au/3DOM-CeO₂ catalyst. Adapted from references [46,47].

This material shows enhanced catalytic performance for formaldehyde oxidation compared to reference Au/CeO₂ catalyst: 100% conversion is reached at 75°C, while for previously reported Au/CeO₂ catalysts without porous structure, a temperature of 100°C is needed. Characterizations reveal that the weak CO₂ adsorption ability of the catalyst and the coexistence of two different Au active species, Au³⁺ and Au⁰, are responsible for the high catalytic activity (schematized in Figure 2.6). Based on FT-IR characterization, a mechanism was proposed by the authors (Figure 2.6), describing the role of the ceria support and of each gold active species.

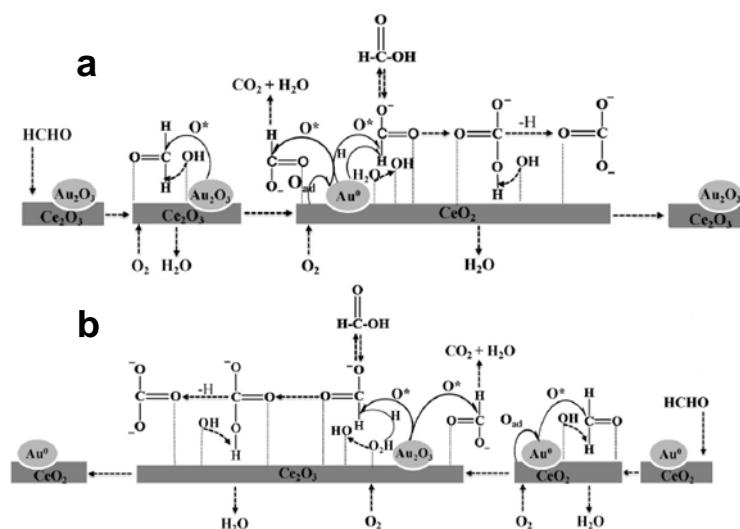


Figure 2.6. Proposed catalytic mechanism for 3DOM Au/CeO₂ catalyst by a) Au³⁺ and b) Au⁰ [46,47].

Gold (< 0.85 wt.%) loaded onto ZrO₂ was also studied [48]. The transformation of formaldehyde into formate species has been proposed to occur on the Au/ZrO₂ surface, while Au⁰ and Au³⁺ were suggested to be the active sites for the oxidation reaction. For Au/ZrO₂, the best catalytic result (100% of HCHO conversion) was obtained at 60°C for a gold loading

of 4 wt.% [49]. Gold/iron binary oxide catalyst was also investigated by Zhu *et al.* [50]; complete HCHO oxidation was achieved at 80°C for a catalyst containing 7 wt.% of gold. The high activity was attributed to the high dispersion of gold on the iron oxide support.

Precious metals like Pt [51] and Ag [52,53] supported over Fe₂O₃ and Al₂O₃, SiO₂ (MCM-41 and SBA-15 type silicas) were also tested for the HCHO oxidation. Among these systems, Pt/Fe₂O₃ seems to be the most promising catalyst since this solid, activated at 200°C, is able to transform HCHO at RT. The interaction between the noble metal particle and the transition metal oxide support seems to be preponderant for the catalytic oxidation at low temperature. The strong interaction was evidenced by a considerable decrease in the reduction temperature of iron oxide in the TPR profile. The reducibility modification could originate from the diffusion of a small amount of Pt oxide species into iron oxide lattice, resulting in the formation of Pt–O–Fe bonds. As a consequence, more easy spillover of atomic hydrogen from Pt to the oxide surface can occur. Regarding the silver-supported catalyst, a novel Ag/SBA-15 prepared by post-grafting method and exhibiting improved metal dispersion and smaller silver particle size, is reported as highly efficient for HCOH oxidation (100% conversion at about 100°C) [53]. A review of conditions usually applied for HCOH total oxidation is summarized in Table 2.1.

2.3.2 Noble metals supported on Manganese oxide and mixed manganese oxide catalyst

Manganese oxide is a widely used transition metal oxide as dopant of noble metal catalysts for HCHO removal. Alvarez-Galvan *et al.* [54,55] investigated the activity of Al₂O₃-supported MnO_x catalysts (with and without Pd) for formaldehyde and methanol oxidation reactions. In the case of formaldehyde oxidation, the light off temperature decreased from 220°C to 90°C when only 0.1 wt.% Pd was added to a support constituted of 18.2 wt.% equivalent Mn on Al₂O₃. The improved activity of the Pd-Mn bimetallic catalyst is attributed to the synergy between manganese and palladium phases. Increase in activity is then associated to the ability of the metal oxide (MnO_x) to release oxygen, thereby facilitating the formation of the PdO active phase. It is suggested that a fraction of PdO is reduced into Pd⁰ under reaction, which provides surface sites for decomposition of organics.

Shen *et al.* [56,57] also reported that when Ag or Pt were supported over MnO_x-CeO₂, the obtained catalysts exhibited excellent catalytic activity for the oxidation of HCOH at low temperature. Over the Ag/MnO_x-CeO₂ catalyst, complete oxidation was achieved at

Table2.1: Survey of Formaldehyde total catalytic oxidation condition in noble metal catalysts.

Catalyst	Quantity of Catalyst	Reaction Mixture	T ₅₀ (°C)	GHSV (h ⁻¹)	Reference
Ru/CeO ₂	1ml	HCOH= 900ppm	<150	20000	[33]
Pd/CeO ₂		CH ₃ OH= 160ppm	<150		
Rh/CeO ₂		H ₂ O= 18%	<150		
Pt/CeO ₂		Air= 82%	<150		
Ir/CeO ₂			207		
Ru/ZrO ₂			188		
Ru/Al ₂ O ₃			198		
Ru/zeolite			210		
Ru/TiO ₂			212		
CeO ₂			238		
Ag/ CeO ₂ 50/50)	1ml	HCOH= 0.42%	<150	21000	[34]
Ag/ CeO ₂ (20/80)		CH ₃ OH= 0.074%	<150		
Ag/ CeO ₂ (10/90)		H ₂ O= 19.9%	<150		
Ag/ CeO ₂ (5/95)		N ₂ = 62.7%	<150		
Ag ₂ O		O ₂ =16.9%	<150		
CeO ₂			150		
Ag/SiO ₂	50mg	HCOH= 1.2%	N.A	7000	[35]
Ag/Al ₂ O ₃	1g	O ₂ = 14.8%		1000	
Pt/Hydrophobic carbon	16g	Balanced with He HCOH= <300ppm	<100	1120	[25]
Pt/TiO ₂	N.A.	Balanced with Air HCOH= 100ppm	RT	50000	[36,37]
Rh/TiO ₂		O ₂ = 20%	50	100000	
Pd/TiO ₂		Balanced with He	70	200000	
Au/TiO ₂			90		
Pt/TiO ₂	0.25g	HCOH=100ppm	R.T	300000	[38]
Pd/TiO ₂		O ₂ =22%	80		
Rh/TiO ₂		Balanced with N ₂	90		
Pt/SiO ₂			60		
Pt/Ce _{0.8} Zr _{0.2} O ₂			>120		
Pt/Ce _{0.2} Zr _{0.8} O ₂			>120		
Pt/TiO ₂	N.A.	HCOH=100ppm	RT	50000	[40]
		O ₂ =20%		100000	
		Balanced with He		200000	
Pt/TiO ₂	0.5g	HCOH= 10ppm	RT	80000	[41]
		H ₂ O vapor= 50%			
		Air balanced			
Pt/TiO ₂	0.5g	HCOH= 10ppm	RT	120000	[43]
		H ₂ O vapor= 50%			
		Air balanced			
Na/Pt/TiO ₂	N.A.	HCOH= 600ppm	RT	120000	[44]
		O ₂ =20%		300000	
		Balanced with He			
		H ₂ O vapor= 50%			
		Air balanced			
Au/CeO ₂	0.2g	HCOH= 0.06%	90	32000	[45]
		Air balanced			
Au/CeO ₂	0.2g	HCOH= 0.06%	<50	66000	[46]
		Air balanced			
Au/CeO ₂	0.2g	HCOH= 0.06%	N.A.	66000	[47]
		Air balanced			
Au/ZrO ₂	0.2g	HCOH= 90ppm	120	52000	[48]
		Air Balance			
Au/Fe-O	0.2g	HCOH= 6.25ppm	<50	54000	[50]
		Air balance			
Pt/Fe ₂ O ₃	0.2g	HCOH= 100-500ppm	RT	60000	[51]
		20%O ₂			
		N ₂ balance			
Ag/SBA-15	0.2g	HCOH= 1000ppm	50	15000	[53]
		O ₂ = 15%			
		He balance			

temperature as low as 100°C. The catalytic activity was explained by the effective activation of molecular oxygen, through the consecutive transfer of oxygen from CeO₂ to Ag₂O through MnO_x sites, as shown in Figure 2.7.

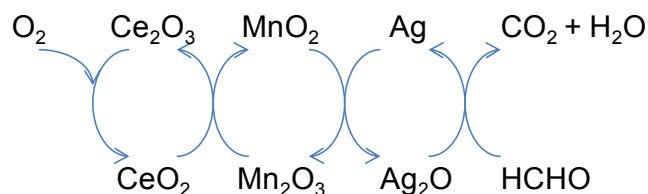


Figure 2.7. Activation of molecular oxygen over a Ag/MnO_x-CeO₂ catalyst. Taked from [57].

Pt/MnO_x-CeO₂ catalyst allows the complete oxidation of formaldehyde at RT [57]. The promoting effect of Pt was ascribed to the presence of active sites for HCOH adsorption on the metal particle surface, and the effective activation of dioxygen molecule on the MnO_x-CeO₂ surface. Cryptomelane-type manganese oxide doped with cerium and platinum were also investigated for the formaldehyde oxidation reaction [58]. Cryptomelane is a square tunnel structure of manganese oxide. Total HCOH oxidation was achieved at 120°C for cryptomelane alone. The Pt doping is observed to be beneficial for the activity at low temperature which is observed to increase. However, the 100% conversion temperature is similar with or without platinum. Cerium doping however resulted in less interesting performance. Changes in the cryptomelane structure due to mismatch of the cerium cation size are suggested to be at the origin of the limited activity measured over this material [58]. Very recently, Pt/MnO₂ nanostructured catalysts were studied for the oxidative decomposition of formaldehyde [59]. Pt nanoparticles were deposited on three MnO₂ nanomaterials, exhibiting different morphologies (cocoon, urchin and nest-like MnO₂).

Table 2.2. Catalytic performance of Pt/MnO₂ catalysts at 20 °C, temperature for HCHO Complete Conversion T100 and BET surface area of MnO₂ Nanostructures.

MnO ₂ Nanostructure	Pt loading Wt (%)	Conversion at 20°C (%)	T100 (°C)	BET area (m ² /g)
Cocoon	0	0	>200	247.6
	2	24.3	90	-
Urchin	0	0	>200	62.3
	2	30.9	80	-
Nest-like	0	0	200	56.9
	2	41.6	70	-

Comparison of the catalyst performances at different Pt loading revealed that 2 wt.% is an optimal loading for the activity. Table 2.2 listed the catalytic activities of three Pt/MnO₂

catalysts and the initial MnO₂ nanomaterials. For 2 wt % Pt/nest-like MnO₂, the temperature at which the HCHO conversion reaches 100% is 70 °C. For comparison, the platinum free MnO₂ material present a complete oxidation at only 200 °C, showing the important effect of platinum on the activity. However, no correlation between the activity of the oxide and its accessible surface can be drawn. The formation of highly dispersed nanoparticles of platinum, and the synergy between Pt atoms and MnO₂ nanostructures were considered to be at the origin of the excellent catalytic activities measured for these materials. TEM images of three Pt/MnO₂ catalysts (Figure 2.8) show that Pt nanoparticles are highly dispersed on the surface. The Pt nanoparticles sizes range from 1.0 to 3.5 nm for the three Pt/MnO₂ catalysts, suggesting that dispersion is independent on the MnO₂ initial morphology.

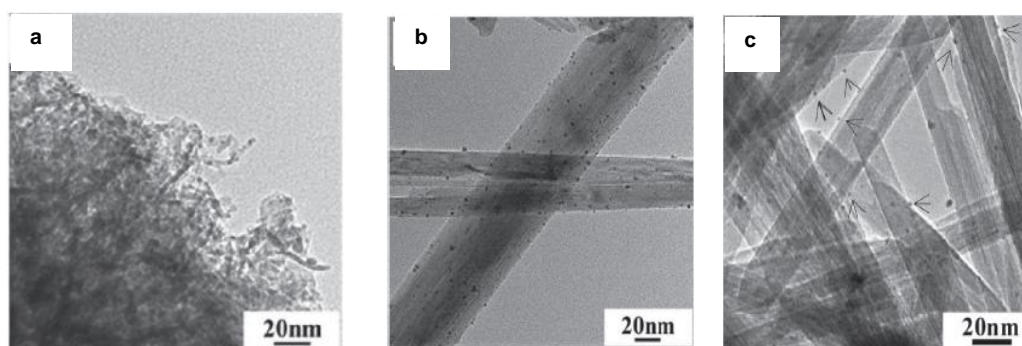


Figure 2.8. TEM images of Pt nanoparticles in (a) 2 wt % Pt/cocoon-like MnO₂ (b)) 2 wt % Pt/urchin-like MnO₂ and (c) 2 wt % Pt/nest-like MnO₂ catalysts. Adapted from reference [59].

Huang *et al.* [60] presented recently the fabrication of single-atom silver chains by thermal processing from supported silver nanoparticles on Hollandite-type manganese oxide nanorods. Single-atom Ag catalyst showed high activation ability to both lattice and molecular oxygen species. Due to the high oxygen mobility in the catalyst, excellent activities for the HCOH oxidation at low temperature are measured. Then, complete conversion can be achieved below 80°C. A review of conditions usually applied for HCOH total oxidation in noble metal manganese oxide catalysts are summarized in Table 2.3.

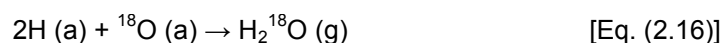
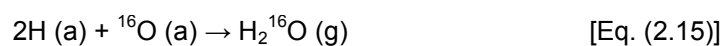
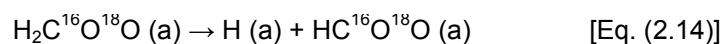
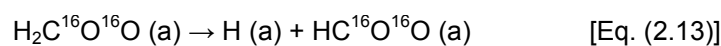
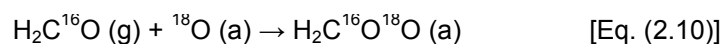
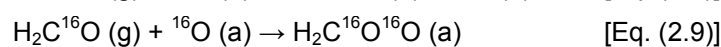
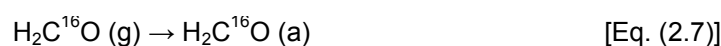
2.3.2 Transition metal oxide catalysts: Manganese oxide based catalyst for HCOH total catalytic oxidation

The high and fluctuating cost and limited resources in noble metals is a limitation to their extensive use. The development of cheaper but effective catalysts, without noble metals, for HCHO catalytic oxidation at low temperature is then a real challenge. Foster and Masel [61] were, to our knowledge, the first that reported total formaldehyde catalytic oxidation to

Table 2.3. Survey of Formaldehyde total catalytic oxidation condition in noble metal manganese oxide catalysts.

Catalyst	Quantity of Catalyst	Reaction Mixture	T ₅₀ (°C)	GHSV (h ⁻¹)	Reference
Mn/Al ₂ O ₃ Mn= 3.9 to 18.2wt.% PdMn/Al ₂ O ₃ Pd= 0.1 to 1.0 wt. %	100mg	HCOH= 0.5% CH ₃ OH= 0.2% H ₂ O= 0.7% N ₂ = 75.6% O ₂ =23%	60	-	[54,55]
Ag/MnO _x -CeO ₂ (50/50)	200mg	HCOH= 580ppm O ₂ = 18% Balanced with He	70	30000	[56]
Pt/MnO _x -CeO ₂ (50/50)	200mg	HCOH= 580ppm O ₂ = 20% Balanced with He	RT	30000	[57]
OMS-2 Pt/Ce/OMS-2	200mg	HCOH= 500ppm O ₂ = 10% Balanced with N ₂	100	30000	[58]
Pt/MnO ₂ Pd= 0.1 to 1.0 wt. %	100mg	HCOH= 460ppm Balanced with Air	40	20000	[59]
Ag/Hollandite Ag= 10 wt. %	200mg	HCOH= 400ppm O ₂ = 10% Balanced with N ₂	<80	-	[60]

carbon dioxide and water over metal oxide. Nickel oxide catalyst has been selected due to its excellent properties in catalyzing the oxidation of CO. It was then highlighted in this work that nickel oxide is an effective active phase for the catalytic combustion of formaldehyde. However, the combustion process is complex; it was then evidenced that the CO₂ produced during oxidation can react with the nickel oxide substrate to form carbonate site. Copper oxide was also proposed as a catalyst for this reaction. The oxidation mechanism was studied using labeled molecules. Then, HC¹⁶OH oxidation by adsorbed ¹⁸O was studied on Copper (110) surface by temperature programmed reaction spectroscopy [62]. The following mechanism for the oxidation of H₂C¹⁶O on the Cu(110) surface was proposed by the authors:



Formaldehyde is observed to exchange its oxygen with adsorbed surface ^{18}O species upon adsorption to yield $\text{H}_2\text{C}^{18}\text{O}_{(\text{a})}$ and $^{16}\text{O}_{(\text{a})}$ [Eq. (2.7) and (2.8)] products, both adsorbed on the copper surface. Formaldehyde was then further oxidized into H_2COO [Eq. (2.9) to (2.12)]. H_2COO adsorbed species subsequently released one hydrogen atoms to form formate species, HCOO [Eq. (2.13) and (2.14)]. The formate adsorbed species were observed to be stable, and undergo dissociation only at temperature above $150\text{ }^\circ\text{C}$ to produce H_2O and CO_2 [Eq. (2.15) to (2.19)]. The proposed mechanism over $\text{Cu}(110)$ then involves the formation of HCOO species as intermediates. The transformation of formaldehyde into formate can be regarded as a Lewis acid-base reaction, in which adsorbed oxygen species acts as a Lewis base that strongly interacts with the acidic carbon atom from the adsorbed HCOH molecule to generate formate species.

Among the different metal oxides, MnO_x was studied by many research groups, due to its low volatility and low toxicity. Manganese oxides assume a wide range of stoichiometries and crystal phases ($\beta\text{-MnO}_2$, $\gamma\text{-MnO}_2$, $\alpha\text{-Mn}_2\text{O}_3$, $\gamma\text{-Mn}_2\text{O}_3$, $\alpha\text{-Mn}_3\text{O}_4$, and Mn_5O_8). Manganese atoms can be found in various oxidation states (+II, +III, +IV). When heated under air, MnO_x undergoes phase transitions. At low temperature, MnO_2 can be easily stabilized. In the temperature range from 500 to 600°C , MnO_2 is converted into Mn_2O_3 , whereas MnO_2 is converted to Mn_3O_4 by heating above 890°C [63]. Manganese atoms, depending on their environment, can assume low or high oxidation states. Ability to switch oxidation states together with the possibility of the structure to support defect formation give rise to properties of the manganese oxides in oxygen mobility and oxygen storage [64].

To our knowledge, formaldehyde catalytic oxidation over manganese oxide was first reported by Sekine *et al.* [65]. The authors developed a board-like air-cleaning material consisting of activated carbon particles and manganese oxides. The material allows the HCHO conversion into carbon dioxide even at RT. The board not only reduced indoor HCHO concentration from 0.21 ppm to 0.04 ppm, but also enhanced the loss of HCHO gas from building materials in apartments. This effect was explained by a mass transfer of VOC between bulk air and the material surface. The performance of the board was evaluated in newly constructed multi-family houses in Japan from May 1998 to January 1999, with promising results. After this result, Sekine [66] tested the HCOH removal efficiencies of several metal oxides under static conditions. Among the metal oxides studied, Ag_2O , PdO , CoO , MnO_2 , TiO_2 , CeO_2 and Mn_3O_4 showed relatively high HCHO removal efficiencies. Products of complete oxidation are detected for MnO_2 , Fe_2O_3 , CeO_2 and Mn_3O_4 . However,

MnO₂ showed the highest reactivity. The effect of the surface area is also reported using two different MnO₂ Materials. With no surprise, the results show that MnO₂ having the highest surface area (163 m²/g) exhibits a significantly higher activity than MnO₂ with lower surface area (63 m²/g).

Shen *et al.* prepared and tested uniform manganese oxide octahedral molecular sieves [with the cryptomelane type structure (OMS-2)] [67]. Complete conversion of HCHO into CO₂ and H₂O can be achieved at 80°C over OMS-2, while the same conversion is obtained at only 100°C over MnO_x reference powder under the same conditions. This result demonstrates that the catalytic activity is closely related to the morphology and structure of the material. The OMS-2 nanorod-type catalyst showed higher activity than the supported precious metals (a Pt/TiO₂ material containing 0.4 wt.% Pt), showing again that this reaction can be efficiently performed without expensive noble metal. The effect of the manganese oxide morphology on the catalytic performance was further studied by He *et al.* [68]. Authors developed a simple approach for the preparation of mesoporous hollow and honeycomb nanospheres of layered MnO₂ (Figure 2.9). K_xMnO₂ honeycomb nanospheres were prepared by mixing KMnO₄ aqueous solution with oleic acid forming a steady emulsion. Brown-black products were collected and washed. Finally, the products were dried under a vacuum at 60°C for 10 h. For the synthesis of K_xMnO₂ hollow nanospheres the same procedure was performed. However, different proportion of KMnO₄ and oleic acid were employed, SEM and TEM images of the resulting materials are presented in Figure 2.9.

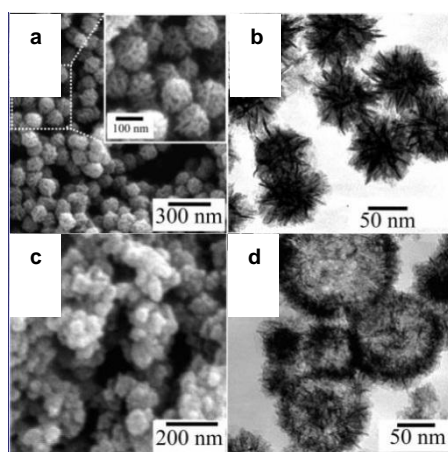


Figure 2.9. SEM (a) and TEM (b) images of honeycomb K_xMnO₂ nanospheres and SEM (c) and TEM (d) images of hollow K_xMnO₂ nanospheres. From reference [68].

The HCHO conversion obtained on the hollow K_xMnO₂ nanospheres reached 100% at 80°C, whereas 85°C is needed for the honeycomb nanospheres. The catalytic activities were

also comparable to those of previously reported MnO₂ OMS-2 nanorods, MnO_x powders, and Mn-Pd/Al₂O₃ catalysts.

As previously mentioned, manganese oxide can be found in many forms, and are classified into one-dimensional tunnel structures, two-dimensional layer phases and three-dimensional spinels [69]. Among them, considerable attentions have been paid to the tunnel-type structure, due to their excellent catalytic performances for the oxidation reaction [70]. Typically, three kinds of square tunnel structures of manganese oxide amongst pyrolusite, cryptomelane and todorokite can be distinguished (structures presented in Figure 2.10). The structure frameworks consist in {MnO₆} octahedral units shared by vertices or/and edges. In pyrolusite, single chains of edge-sharing {MnO₆} octahedral share corners with neighboring chains to form a framework structure containing tunnels of ca. 0.23 x 0.23 nm². The crystal structure of cryptomelane consists in two double edge-sharing {MnO₆} octahedral chains [71], which are corner-connected to form one-dimensional tunnels of ca. 0.46 x 0.46 nm². Todorokite exhibits the largest tunnel structure among the three structures. The structure consists in triple chains of edge-sharing {MnO₆} octahedral that form tunnels of ca. 0.69 x 0.69 nm² [71].

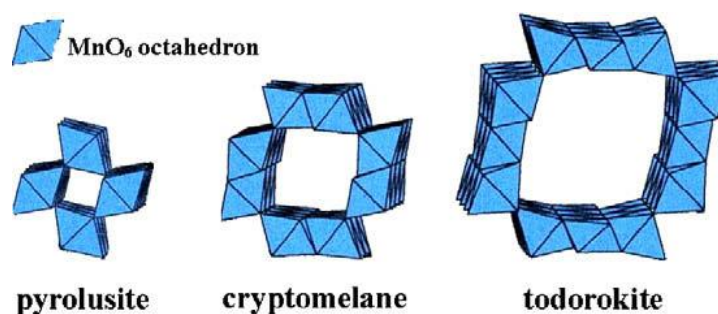


Figure 2.10: Crystal structure models of three manganese oxides with different square tunnel sizes.

Pyrolusite, cryptomelane and todorokite-type manganese oxides, having then different square tunnel sizes (Figure 2.10), were studied for the formaldehyde oxidation reaction by Hao *et al.* [72]. The results of catalytic test revealed that cryptomelane structure presents much higher catalytic activity than pyrolusite and todorokite. 100% HCHO conversion into H₂O and CO₂ can be achieved at 140 °C over cryptomelane. For comparison, pyrolusite and todorokite structures present 100% HCOH conversion at 180° and 160°, respectively. Characterization results showed that surface area, reducibility and average oxidation state of

manganese are not the major factors that govern the catalytic activity. Consequently, the tunnel structure of manganese oxide is proposed by the authors to govern the catalytic activity. More recently, Tiang *et al.* [73] confirm the important effect of the material morphology. Activity was measured for K-OMS-2 with two different morphologies, *i.e.* nanoparticles and nanorods. Authors showed that K-OMS-2 nanoparticles provided much higher catalytic activity than K-OMS-2 nanorods. This difference in activity was explained by the formaldehyde accessibility into the channel. The adsorption and diffusion of HCHO molecules seem to be favored in the inner surface of the pore channels.

It is then observed that manganese oxide structure and morphology greatly influence the catalytic performance of the material for HCHO oxidation. Therefore, the synthesis of manganese based materials with novel morphologies and elevated surface areas have become an attractive research field. In a recent work, Zhou *et al.* [74] reported a simple hydrothermal synthesis method to achieve formation of flower-like MnO₂ particles. The effects of the synthesis conditions including hydrothermal time (6h, 12h, 18h, and 24h), hydrothermal temperature (120°C, 150°C and 180°C), pH value (0.3, 0.6, 0.9 and 1.3), and kind of compensating anions (PO₄³⁻, NO₃⁻, and SO₄²⁻) on the morphology, crystalline form and particle size is reported. The advantages of the flower-like particles are their hierarchical structure, large surface area (95 m²/g), and large overall size, which are proposed to be favorable for the diffusion of reactants. Different crystalline structures of manganese oxide were obtained. Authors reported that the cryptomelane-type MnO₂ presents higher catalytic activity (Figure 2.11). It is expected that the high surface area MnO₂ prepared by this way may offer potential applications in pollutant elimination when doped with noble metal.

Tian *et al.* [75] studied the synthesis of Birnessite-type manganese oxides using a microemulsion process, in order to produce materials having high surface areas (up to 154 m²/g). The morphology, surface area, pore size, and surface reducibility of these materials were controlled via the synthesis temperature (80°C, 100°C, 120°C and 140°C). The most active manganese catalyst, prepared at 120°C, showed 100% HCHO conversion at 100 °C. The catalytic performances of the materials were related to the morphology, surface area and surface reducibility in the solids. Then, the best properties were obtained for a flake-type morphology. This material is also presenting higher reducibility at low temperature. A review of conditions usually applied for HCOH total oxidation over transition metal oxide catalysts are summarized in Table 2.4.

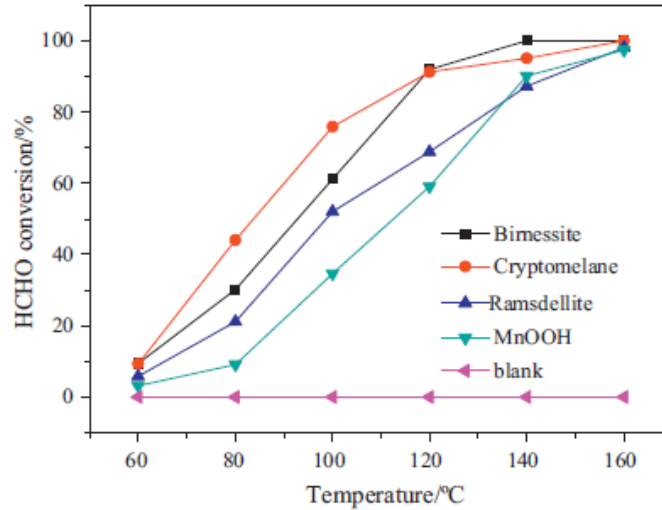


Figure 2.11: HCHO conversion on different crystalline structures of manganese oxide.

Table 2.4. Survey of Formaldehyde total catalytic oxidation condition over transition metal oxide.

Catalyst	Quantity of Catalyst	Reaction Mixture	T ₅₀ (°C)	GHSV (h ⁻¹)	Reference
Activated carbon	-	HCOH= ppm level	N.A.	-	[65]
MnO ₂	500mg	Air balanced	N.A.	-	[66]
Ag ₂ O		HCOH= ppm			
PdO		Air balance			
CuO					
CoO					
ZnO					
Fe ₂ O ₃					
TiO ₂					
La ₂ O ₃					
WO ₃					
CeO ₂					
V ₂ O ₅					
MnO ₂					
Cryptomelane (OMS-2)	200mg	HCOH= 0.01% O ₂ = 20%	70	-	[67]
Hollow MnO ₂	50-70mg	Balanced with He HCOH= 100ppm	50	50000	[68]
Honeycomb MnO ₂		O ₂ = 20%	70		
Pyrolusite	200mg	Balanced with He HCOH= 400ppm	150	18000	[72]
Cryptomelane		O ₂ = 10%	110		
Todorokite		Balanced with N ₂	140		
Cryptomelane	100mg	HCOH= 460ppm	80	20000	[73]
Cryptomelane		Balanced with Air			
Birnessite	50mg	HCOH= 100ppm	95	50000	[74]
Cryptomelane		O ₂ = 20%	90		
Ramsdellite		Balanced with He	100		
MnOOH	100mg	HCOH= 460ppm Balanced with Air	115	30000	[75]
Birnessite			80		
MnO _x -CeO ₂ (50/50)	200mg	HCOH= 580ppm O ₂ = 18%	80	21000	[77]
CeO ₂	200mg	Balanced with He HCOH= 580ppm	225	-	[78]
CeMn10		O ₂ = 20%	150		
CeMn30		Balanced with N ₂	125		
CeMn50			100		
CeMn80			80		
MnO _x			75		
MnO _x -SnO ₂ (50/50)	200mg	HCOH= 400ppm O ₂ = 10%	150	30000	[79]
		Balanced with N ₂			

Mixed manganese oxides

Combination of MnO_x with other oxides generally results in increased catalytic performance at low temperature. Recent studies revealed that when MnO_2 is placed in the proximity of La_2O_3 or CeO_2 , the oxygen mobility in the MnO_x structure is strongly affected [76]. In the Mn–Ce mixed oxide, ceria provides oxygen to manganese sites at low temperature and, in contrast, withdraws oxygen mobility at elevated temperatures (>773 K). Thus, ceria allows increasing the activity of MnO_x during the oxidation process at low temperature, and decreases it at high reaction temperature [76].

MnO_x – CeO_2 mixed oxides were also studied in the complete oxidation of formaldehyde [77]. The structure features and catalytic behaviors of the MnO_x – CeO_2 mixed-oxides ($\text{Mn}/(\text{Mn} + \text{Ce}) = 0.5$, molar ratio) strongly depend on the synthesis conditions. MnO_x – CeO_2 mixed oxides were prepared by different methods:

1. *Sol–gel method (citrate complexation procedure)*: from $\text{Mn}(\text{NO}_3)_2 \cdot 6\text{H}_2\text{O}$, $(\text{NH}_4)_2\text{Ce}(\text{NO}_3)_6$ and citric acid (citric acid/ $(\text{Mn} + \text{Ce}) = 1.0$, molar ratio).
2. *Coprecipitation method*: using 2 KOH to precipitate $\text{Mn}(\text{NO}_3)_2 \cdot 6\text{H}_2\text{O}$ and $(\text{NH}_4)_2\text{Ce}(\text{NO}_3)_6$ precursors in water.
3. *Modified coprecipitation method*: precipitation procedure similar than before, but with $\text{Mn}(\text{NO}_3)_2 \cdot 6\text{H}_2\text{O}$, KMnO_4 and $(\text{NH}_4)_2\text{Ce}(\text{NO}_3)_6$ precursors with a molar ratio of 3:2:5 used.

The catalyst prepared using the modified coprecipitation method exhibited much higher catalytic activity than those prepared by sol–gel and coprecipitation methods. 100% formaldehyde conversion is then achieved at a temperature as low as 100°C in the case of the most active materials. Temperatures of 180°C and 160°C are however necessary to achieve complete conversion over the sol-gel and precipitated materials, respectively. Characterization by XPS revealed that oxidation state of manganese and lattice oxygen species concentration on the surface caused by the formation of a MnO_x – CeO_2 solid solution are determinant parameters to achieve high catalytic activity at low temperature ($< 120^\circ\text{C}$).

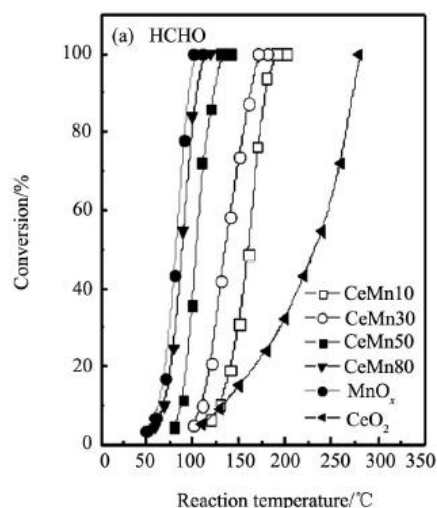


Figure 2.12. HCHO oxidation over MnO_x-CeO₂ catalysts.

Liu *et al.* [78] also studied the properties of MnO_x-CeO₂ mixed-oxides for HCHO and CO oxidation reactions. Mixed-oxides with different molar fractions were prepared by coprecipitation method, using KMnO₄, Mn(NO₃)₂ and Ce(NO₃)₃ precursors. The light-off curves for formaldehyde oxidation over MnO_x-CeO₂ are presented in Figure 2.12. HCHO oxidation can be strongly enhanced by the addition of manganese into ceria. Single MnO_x and CeMn80 composite present the highest catalytic activities. The authors affirm that CeO₂ was not directly involved in the HCHO oxidation, and the enhancement of reactivity could be ascribed to the easier activation of the lattice oxygen in MnO_x species by the addition of ceria.

The effect of Sn doping in MnO_x-SnO₂ catalysts, with molar ratio of Mn/(Mn + Sn) = 0.5, was also studied. Materials were synthesized by two methods: redox co-precipitation and conventional co-precipitation [79]. Catalytic activity is also affected by the synthesis method. The catalyst synthesized by the redox co-precipitation method exhibited much higher catalytic activity, with a 100% HCHO conversion into H₂O and CO₂ at 180°C (400 ppm HCHO, GHSV = 30,000 h⁻¹). The material obtained by conventional co-precipitation method reached HCHO complete oxidation at only 220°C. Differences in catalytic activity are attributed by the authors to the differences in manganese oxidation state, formation of solid solution between MnO_x and SnO₂, and the redox capability of the material. Then, when prepared by redox coprecipitation, the solid present higher reducibility and higher oxidation state of the Mn species are measured. As a consequence, the catalytic activity is higher over this solid than over the material prepared by coprecipitation.

2.4 Objectives of the thesis

In chapter 1 it was demonstrated that Formaldehyde is an important air pollutant in various indoor environments, including houses, offices and industries, and a long term exposure to this pollutant can cause serious health problems, making this molecule a main pollutant to eliminate. Several regulations are bringing new challenges and efficient removal technologies have to be developed. In this chapter, it was evidenced that catalytic oxidation is a promising technology to remove formaldehyde from polluted air at low temperatures. The bibliographic review clearly presents the advantage of using engineered transition metal containing nanomaterials, whose are sometimes found as active as noble metal containing materials. The replacement of these last materials in environmental process is also challenging, due to the well-known limitation of the use of these elements, e.g. high price and limited resource. It was also stated that manganese oxide based nanomaterials are promising, cheap, nontoxic and effective catalysts able to convert formaldehyde at low temperatures. Moreover, it was evidenced that the specific surface area, porosity and surface reducibility greatly influence the catalytic performance of the nanomaterials for HCHO oxidation. *Therefore, the present work aimed to develop the synthesis of manganese based materials with improved textural, structural and redox properties devoted to formaldehyde catalytic oxidation.*

The chemical activation of manganese oxides using acidic medium seems to be a promising route to obtain higher oxidation state of manganese species that was previously found to be preferable for oxidation reactions [80]. Brenet *et al.* [81] studied the chemical activation of manganese oxide in acidic medium using sulphuric acid: the resulting material showed higher oxidation state, high electrochemical properties and improved catalytic activity. More recently, Sinha *et al.* [82,83] have synthesized manganese oxide mesoporous materials by using template assisted method followed by chemical activation under acidic treatment. These materials have a great surface area and enhanced ability to remove volatile organic compounds (acetaldehyde, toluene and n-hexane) at low temperatures. *Therefore, one of the objectives of this work was to develop the synthesis of mesoporous manganese oxide and their chemical activation using acidic treatment. The study was extended to account for the effect of chemical activation in the mixed MnOx-CeO₂ catalyst with different Mn/Ce ratios prepared by surfactant assisted wet-chemistry route.*

Manganese mesostructures seems to be promising catalyst to formaldehyde oxidation. Suib *et al.* [84] have prepared manganese oxide mesoporous structures by oxidation of

Mn(OH)₂ in the presence of cetyltrimethyl-ammonium bromide (CTAB); the solids obtained showed ordered mesoporous structures and exceptional thermal stability (1000°C). *Based on this study, the optimization of mesostructure manganese oxide synthesis and application to formaldehyde oxidation were additional objectives of this thesis.*

The use of hydrotalcites (HT) as precursor is an interesting way to obtain high surface area mixed oxides. Hydrotalcites are naturally occurring minerals with chemical composition Mg₆Al₂(OH)₁₆CO₃·4H₂O exhibiting layered crystal structure, comprised of positively charged hydroxide layers and interlayers composed of carbonate anions and water molecules [85]. Hydrotalcites have three important characteristics that make them interesting for various applications. Firstly, HTs have a good anion-exchange capacity and, therefore, are used as ion-exchangers, adsorbents or sensors. Secondly, most of them, depending on the composition, behave as solid bases and hence have been widely studied and successfully used as basic catalysts. Thirdly, hydrotalcites can be prepared with several bivalent and trivalent cations; for example, Co, Cu, Ni, Fe, Zn, **Mn**, Ru, Cr or Ga, and even V and Li cations, can enter into the composition of HTs, serving as precursors for the preparation of different mixed oxides, active for oxidation and hydrogenation/dehydrogenation reactions [86].

The most common method applied for preparation of hydrotalcite-like compounds is coprecipitation, which is based on the reaction of a solution containing M²⁺ and M³⁺ metal nitrates added slowly and simultaneously at a fixed pH under stirring, followed by a long ageing time or hydrothermal treatment (1 day). By controlled thermal decomposition (calcination), HTs are converted into mixed oxides, which exhibit unique properties like homogeneous dispersion of the elements, high specific surface area and strong basic properties.

Ultrasound has attracted much attention in the synthesis of inorganic and organic materials, owing to its specific effects on material processing. It is widely recognized that the effects caused by ultrasound can be mainly attributed to: (1) rapid movement of fluids due to variation of sonic pressure, which accelerates mass transfer; (2) formation and collapse of microbubbles (cavitation), creating localized high-temperature and high-pressure conditions; and (3) micro-streaming, in which a large amount of vibrational energy is applied to small volumes with little heating [87]. Several studies show that sonication enhances the dissolution process, chemical reactions, and nucleation and growth of precipitates in some inorganic powder syntheses [88,89]. Kooli *et al.* [90] used ultrasound to promote anion exchange in

HTs. The hypothesis of the crystal quality improvement of HTs by ultrasound was suggested, although they did not study its effects extensively. The application of ultrasound (US) irradiation during the synthesis of hydrotalcites was not extensively studied. Seida *et al.* [91] applied sonication for the HTs synthesis and during the ageing step. The authors found that the HTs present smaller crystallites and higher BET surface areas in comparison with conventionally prepared samples. More recently, the same trend was observed by Perez *et al.* [92] for the synthesis Co/Mg HTs using ultrasound during ageing. Moreover, Climent *et al.* [93] have synthesized Mg/Al HT under sonication during the precipitation step. They found that the sample prepared under sonication presents further homogeneous morphology and highly dispersed particles. *The final objective of this work comprises the preparation of Mg/Mn/Al hydrotalcites using ultrasound (US) as precursors for high surface area mixed manganese oxide and their application in total formaldehyde catalytic oxidation.*

2.4 References

- ¹ E. Roffael in *Formaldehyde Release from Particleboard and Other Wood Based Panel*; Forest Research Institute Malaysia, Kuala Lumpur **1993**.
- ² M. Hayashi, H. Osawa, *Build. Environ.* **2008**, *43*, 329.
- ³ Wang S.; Ang H.M.; Tade M.O. Volatile organic compounds in indoor environment and photocatalytic oxidation: State of the art. *Environment International*. *33* (2007) 694–705
- ⁴ Hayashi, M. ; Enai, M. ; Hyrokawa, Y. Annual characteristics of ventilation and indoor air quality in detached houses using a simulation method with Japanese daily schedule model. *Build. Environ.* 2001, *36*, 721-731.
- ⁵ Hayashi, M. ; Osawa, H. The influence of the concealed pollution sources upon the indoor air quality in houses. *Build. Environ.* 2008, *43*, 329-336.
- ⁶ B. Virote, S. Srisuda, T. Wiwut, *Sep. Purif. Technol.* **2005**, *42*, 159.
- ⁷ L. Krisztina, *Microporous Mesoporous Mater.* **2005**, *80*, 205.
- ⁸ Y. Song, W. Qiao, S.H. Yoon, I. Mochida, Q. Guo, L. Liu, *J. Appl. Polym. Sci.* **2007**, *106*, 2151.
- ⁹ W. Shen, Z. Li, Y. Liu, *Recent Pat. Chem. Eng.* **2008**, *1*, 27.
- ¹⁰ S. Tanada, N. Kawasaki, T. Nakamura, M. Araki, M. Isomura, *J. Colloid Interface Sci.* **1999**, *214*, 106.
- ¹¹ J. Li, Z. Li, Q. Xia, H. Xi, *Chin. J. Chem. Eng.* **2008**, *16*, 871.
- ¹² S. Srisuda, B. Virote, *J. Environ. Sci.* **2008**, *20*, 379.
- ¹³ T. Okachi, M. Onaka, *J. Am. Chem. Soc.* **2004**, *126*, 2306.
- ¹⁴ A.M.D.C. Cazorla, M. Grutzeck, *Ceram. Trans.* **2006**, *176*, 3-13.
- ¹⁵ I. Hideyuki, O. Yasunori, S. Tsuneji, *J. Antibact. Antifungal Agents.* **2005**, *33*, 453.
- ¹⁶ H. Nakayama, A. Hayashi, T. Eguchi, N. Nakamura, M. Tsuhako, *Solid State Sci.* **2002**, *4*, 1067.
- ¹⁷ J. Mo, Y. Zhang, Q. Xu, J.J. Lamson, R. Zhao, *Atmos. Environ.* **2009**, *43*, 2229.
- ¹⁸ B. Ohtani, *Chem. Lett.* **2008**, *37*, 217.
- ¹⁹ C.H. Ao, S.C. Lee, J.Z. Yu, J.H. Xu, *Appl. Catal., B.* **2004**, *54*, 41.
- ²⁰ H.M. Liu, Z.W. Lian, X.J. Ye, W.F. Shangguan, *Chemosphere.* **2005**, *60*, 630.
- ²¹ S. Sun, J. Ding, J. Bao, C. Gao, Z. Qi, C. Li, *Catal. Lett.* **2010**, *137*, 239.
- ²² Y. Lu, D. Wang, C. Ma, H. Yang, *Build. Environ.* **2010**, *45*, 615.
- ²³ W. Liang, J. Li, Y. Jin, *Build. Environ.* **2012**, *51*, 345.

-
- ²⁴ D. Kibanova, M. Sleiman, J. Cervini-Silva, H. Destailats, *J. Hazard. Mater.* **2012**, 211, 233.
- ²⁵ K. T. Chuang, B. Zhou, S. Tong, *Ind. Eng. Chem. Res.* **1994**, 33, 1680.
- ²⁶ Spivey J. *Ind. Eng. Chem. Res.* **1987**, 26, 2165.
- ²⁷ S. Royer, D. Duprez, *ChemCatChem.* **2011**, 3, 24.
- ²⁸ J.L.G. Fierro in *Metal oxide Chemistry and Applications*. Taylor and Francis Group. **2006**
- ²⁹ P. Mars, D.W. Van Krevelen, *Chem. Eng. Sci.* **1954**, 3, 41.
- ³⁰ R.K. Grasselli, J.D. Burrington, *Adv. Catal.* **1981**, 30, 133.
- ³¹ P.J. Gellings, H.J.M. Bouwmeester, *Catal. Today.* **2000**, 58, 1.
- ³² P. Arpentnier, F. Cavani, F. Triforo in *The technology of catalytic oxidation*, Edition TECHNIP. Paris, **2001**, pp. 67-114.
- ³³ S. Imamura, Y. Uematsu, K. Utani, T. Ito, *Ind. Eng. Chem. Prod. Res. Dev.* **1991**, 30, 18.
- ³⁴ S. Imamura, D. Uchihori, K. Utani, *Catal. Lett.* **1994**, 24, 377.
- ³⁵ C.-F. Mao, M.A. Vannice, *J. Catal.* **1995**, 154, 230.
- ³⁶ C. Zhang, H. He, K. Tanaka, *Appl. Catal., B.* **2006**, 65, 37.
- ³⁷ C. Zhang, H. He, *Catal. Today.* **2007**, 126, 345.
- ³⁸ J. Peng, S. Wang, *Appl. Catal., B.* **2007**, 73, 282.
- ³⁹ R. Dewil, K. Everaert, J. Baeyens, *Catal. Commun.* **2005**, 6, 793.
- ⁴⁰ C. Zhang, H. He, K.-I Tanaka, *Catal. Commun.* **2005**, 6, 211.
- ⁴¹ H. Huang, D. Y.C. Leung, *J. Catal.* **2011**, 280, 60.
- ⁴² H. Yoshida, Y. Yasawa, T. Hattori, *Catal. Today.* **2003**, 87, 19.
- ⁴³ H. Huang, D. Y. C. Leung, D. Ye. *J. Mater. Chem.* **2011**, 21, 9647.
- ⁴⁴ C. Zhang, F. Liu, Y. Zhai, H. Ariga, N. Yi, Y. Liu. K. Asakura, M. Flytzani-Stephanopoulos, H. He. *Angew. Chem., Int. Ed.* **2012**, 51, 1.
- ⁴⁵ Y. Shen, X. Yang, Y. Wang, Y. Zhang, H. Zhu, L. Gao, M. Jia, *Appl. Catal., B.* **2008**, 79, 142.
- ⁴⁶ J. Zhang, Y. Jin, C. Li, Y. Shen, L. Hanb, Z. Hu, X. Di, Z. Liu, *Appl. Catal., B.* **2009**, 91, 11.
- ⁴⁷ B. Liua, C. Li, Y. Zhang, Y. Liu, W. Hu, Q. Wang, L. Han, J. Zhang, *Appl. Catal., B.* **2012**, 111-112, 467.
- ⁴⁸ Y. Zhang, Y. Shen, X. Yang, S. Sheng, T. Wang, M. F. Adebajo, H. Zhu, *J. Mol. Catal. A: Chem.* **2010**, 316, 100.
- ⁴⁹ Y.-C. Hong, K.-Q. Sun, K.-H. Han, G. Liu, B.-Q. Xu, *Catal. Today.* **2010**, 158, 415.

-
- ⁵⁰ C. Li, Y. Shen, M. Ji, S. Sheng, M. O. Adebajo, H. Zhu, *Catal. Commun.* **2008**, *9*, 355.
- ⁵¹ N. An, Q. Yu, G. Liu, S. Li, M. Jia, W. Zhang, *J. Hazard. Mater.* **2011**, *186*, 1392.
- ⁵² D. Chen, Z. Qu, S. Shen, X. Li, Y. Shi, Y. Wang, Q. Fu, J. Wu, *Catal. Today.* **2011**, *175*, 338.
- ⁵³ Z. Qu, S. Shen, D. Chen, Y. Wang, *J. Mol. Catal. A: Chem.* **2012**, *356*, 171.
- ⁵⁴ M.C. Álvarez-Galván, B. Pawelec, V.A. de la Peña O'Shea, J.L.G. Fierro, P.L. Arias, *Appl. Catal., B.* **2004**, *51*, 83.
- ⁵⁵ V.A. de la Peña O'Shea, M.C. Alvarez-Galvan, J.L.G. Fierro, P.L. Arias, *Appl. Catal., B.* **2005**, *57*, 191.
- ⁵⁶ X. Tang, J. Chen, Y. Li, Y. Li, Y. Xu, W. Shen, *Chem. Eng. J.* **2006**, *118*, 119.
- ⁵⁷ X. Tang, J. Chen, X. Huang, Y. Xu, W. Shen, *Appl. Catal., B.* **2008**, *81*, 115.
- ⁵⁸ R. Wang, J. Li, *Catal. Lett.* **2009**, *131*, 500.
- ⁵⁹ X. Yu, J. He, D. Wang, Y. Hu, H. Tian, Z. He, *J. Phys. Chem. C.* **2012**, *116*, 851.
- ⁶⁰ Z. Huang, X. Gu, Q. Cao, P. Hu, J. Hao, J. Li, X. Tang. *Angew. Chem., Int. Ed.* **2012**, *51*, 4198.
- ⁶¹ J. Foster, R. Masel, *Ind. Eng. Chem. Prod. Res. Dev.* **1986**, *25*, 563.
- ⁶² I. E. Wachs, R. J. Madix, *Surf. Sci.* **1979**, *84*, 375.
- ⁶³ A.H. Reidies, in *Ullmann's Encyclopedia of Industrial Chemistry, 5th ed.* Vol. A16, VCH: New York, **1986**, pp. 123-129.
- ⁶⁴ Y. Chang, J.G. McCarty, *Catal. Today.* **1996**, *30*, 163.
- ⁶⁵ Y. Sekine, A. Nishimura, *Atmos. Environ.* **2001**, *35*, 2001.
- ⁶⁶ Y. Sekine, *Atmos. Environ.* **2002**, *36*, 5543.
- ⁶⁷ X. Tang, X. Huang, J. Shao, J. Liu, Y. Li, Y. Xu, W. Shen, *Chin. J. Catal.* **2006**, *27*, 97.
- ⁶⁸ H. Chen, J. He, C. Zhang, H. He, *J. Phys. Chem. C.* **2007**, *111*, 18033.
- ⁶⁹ Q. Feng, H. Kanoh, K. Ooi, *J. Mater. Chem.* **1999**, *9*, 319.
- ⁷⁰ J. Luo, Q. Zhang, A. Huang, S. Suib, *Microporous Mesoporous Mater.* **2000**, *36*, 209.
- ⁷¹ S. Brock, N. Duan, Z. Tian, O. Giraldo, H. Zhou, S. Suib, *Chem. Mater.* **1998**, *10*, 2619.
- ⁷² T. Chen, H. Dou, X. Li, X. Tang, J. Li, J. Hao, *Microporous Mesoporous Mater.* **2009**, *122*, 270.
- ⁷³ H. Tian, J. He, X. Zhang, L. Zhou, D. Wang, *Microporous Mesoporous Mater.* **2011**, *138*, 118.
- ⁷⁴ L. Zhou, J. Zhang, J. He, Y. Hu, H. Tian, *Mater. Res. Bull.* **2011**, *46*, 1714.

-
- ⁷⁵ H.Tian, J. He, L. Liu, D. Wang, Z. Hao, C. Ma, *Microporous Mesoporous Mater.* **2012**, *151*, 397.
- ⁷⁶ S. Imamura, M. Shono, N. Okamoto, A. Hamada, S. Ishida, *Appl. Catal., A.* **1996**, *142*, 279.
- ⁷⁷ X.Tang, Y.Li, X.Huang, Y.Xu, H.Zhu, J.Wang, W.Shen, , *Appl. Catal., B.* **2006**, *62*, 265.
- ⁷⁸ X. Liu, J. Lu, K. Qian, W. Huang, M. Luo, *J. Rare Earths.* **2009**, *27*, 418.
- ⁷⁹ Y. Wen, X. Tang, J. Li, J. Hao, L Wei, X.Tang, *Catal. Commun.* **2009**, *10*, 1157.
- ⁸⁰ F. Kapteijn, L. Singoredjo, A. Andreini. *Appl. Catal., B.* **1994**, *3*, 173.
- ⁸¹ J. Brenet, M. Beley, *Electrochim. Acta.* **1973**, *18*, 1003.
- ⁸² A.Sinha, K.Suzuki, M.Takahara, H.Azuma, T.Nonaka, N.Suzuki, N.Takahashi, *J. Phys. Chem. C.* **2008**, *112*, 16028..
- ⁸³ A. Sinha, K. Susuki, M. Takahara, H. Azuma, T. Nonaka, K. Fukumoto, *Angew. Chem., Int. Ed.* **2007**, *46*, 891.
- ⁸⁴ Z. Tian, W. Tong, J. Wang, N. Duan, V. Krishnan, S. Suib, *Science.* **1997**, *276*, 926.
- ⁸⁵ F. Kovandaa, D. Kolouseka, Z. Cilova, V. Hulinsky. *Appl. Clay Sci.* **2005**, *28*, 101.
- ⁸⁶ D. P. Debecker, E. M. Gaigneaux, G. Busca. *Chem. Eu. J.* **2009**, *15*, 3920.
- ⁸⁷ T.J. Mason. *Sonochemistry: The Uses of Ultrasound in Chemistry.* The Royal Society of Chemistry, Cambridge, **1990** 157 pp.
- ⁸⁸ Y. Fang., D.M. Roy, P.W. Brown, *J. Mater. Res.* **1992**, *7*, 2294.
- ⁸⁹ J. Hu., K. Agrawa, Y. Fang, R. Roy, *J. Mater. Sci.* **1993**, *28*, 5297.
- ⁹⁰ F. Kooli, W. Jones, V. Rieves, M.A. Ulibarri, *J. Mater. Sci. Lett.* **1997**, *16*, 27.
- ⁹¹ Y. Seida, Y Nakano, Y Nakamura. *Clays Clay Miner.* **2002**, *50*, 525.
- ⁹² A. Perez, J.-F. Lamonier, J.-M. Giraudon, R. Molina, S. Moreno. *Catal. Today.* **2011**, *176*, 286.
- ⁹³ M.J. Climent, A. Corma, S. Iborra, K. Epping, A. Velty. *J. Catal.* **2004**, *225*, 316.



CHAPTER 3

Chapter 3: Background to experimental techniques

3.1 Powder X-ray diffraction

X- Rays irradiating a crystal are scattered in a specular fashion by atoms in lattice planes of the crystal. X-rays scattered from successive crystallographic planes (hkl) will interfere constructively if the path length difference is equal to an integer multiple of the wavelength. The path difference between two waves undergoing constructive interference is given by $2d\sin\theta$, as illustrated in Figure 3.1. This leads to Bragg's law in the form:

$$n\lambda = 2d_{hkl}\sin\theta \quad (\text{Eq. 3.1})$$

where λ is the wavelength of the X-ray and θ is the incidence angle and d_{hkl} the characteristic interplanar spacing of a set of planes with hkl Miller index.

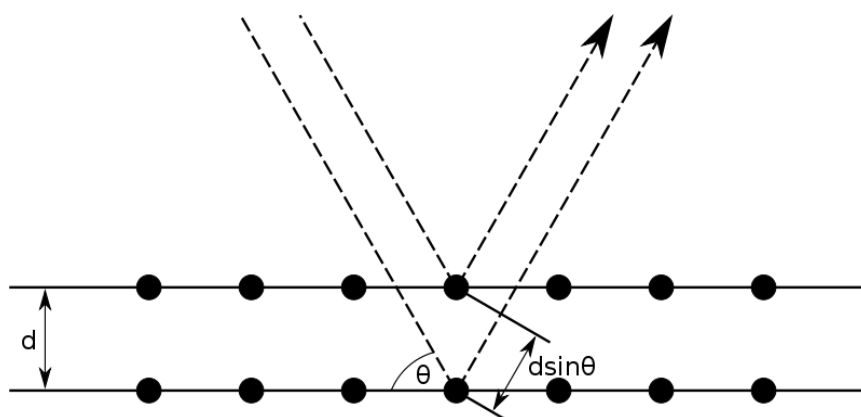


Figure 3.1. Bragg's diffraction.

Diffracted X-ray beams make an angle of 2θ with the incident beam. Because the crystallites can lie in all directions while still maintaining the Bragg condition, the reflections lie on the surface of cones whose semi-apex angles are equal the reflection angles 2θ . The diffraction pattern of a powder sample is taken in automatic diffractometer that use scintillation or CCD detectors to record angle and intensity of the diffracted beams.

The X-ray powder diffraction of a compound provides a convenient and characteristic fingerprint which can be used in qualitative analysis. Values of d_{hkl} spacings line intensities can be compared with those listed in the Powder Diffraction File, which contains entries for more than 500,000 inorganic compounds over 400,000 organic compounds, up to year 2010 [1]. The lattice parameters are readily obtained from d_{hkl} -spacings with the help of computer programs that have been developed for this purpose. Powder X-ray diffraction data are also

useful in the analysis of the relative concentration of different phases in a mixture and in the elucidation of phase diagrams. The phases of a mixture can be identified using the procedure describe above, and their proportions can be determined by comparing the intensities of the characteristic lines from each phase to those from a standard. Additionally when phases are soluble in each other, the solubility limits can be determined by following the shifts of the cell parameters.

3.1.1 Wide angle X-ray diffraction equipments and conditions

Powder X-ray diffraction (XRD) patterns were recorded on a Bruker D8 X-ray diffractometer at room temperature with $\text{CuK}\alpha$ radiation ($\lambda = 1.5418 \text{ \AA}$). The diffractograms were recorded for 2θ values comprised between 5 and 80° using a 0.02° step with an integration time of 4 s . The diffraction patterns have been indexed by comparison with the Joint Committee on Powder Diffraction Standards (JCPDS) files.

High temperature X-ray diffraction patterns were performed on a Bruker D8 diffractometer equipped with a special chamber HTK1200N. The radiation used was the same $\text{CuK}\alpha$ and the conditions were $2\theta = 5 - 80^\circ$, $\text{step} = 0.02^\circ$.

3.1.2 Low angle X-ray diffraction equipments and conditions

Low angle X-ray diffraction was performed on a Bruker AXS D5005 diffractometer using the $\text{CuK}\alpha$ radiation ($\lambda = 1.5418 \text{ \AA}$) as an X-ray source. The diffractograms were recorded for 2θ values comprised between 0.5 and 10° using a 0.02° step with an integration time of 10 s .

3.2 Surface area determination by physisorption analysis.

When a surface is formed from a bulk material chemical bonds are broken. The formation of new bonds with gas phase species gives rise to chemisorption. However, even in the absence of specific chemical interactions, a gas will in general adsorb on the solid surface of a material due to weak Van der Waals type interactions. The volume of adsorbed gaseous species will depend on both pressure and temperature as well as the surface area of the solid. After saturation of the first monolayer of adsorbate, further adsorption may occur on the top of this layer, but typically with a lower heat of adsorption.

Surface area determination by gas adsorption involves determination of the volume of an inert gas (typically nitrogen) adsorbed on a solid surface at low temperatures as a function of increasing pressure. When pressure is reduced back to zero, any possible hysteresis is

revealed by also recording adsorbed volume. Six standard types of adsorption isotherm defined by IUPAC are shown in Figure 3.2. The Type I isotherm is typical of systems where there is strong chemisorption which saturates at one monolayer coverage. This type of isotherm may also be observed for microporous solids. Type II isotherms are typical of physisorption on finely divided non-porous solids where multilayers may build on top of the first adsorbate monolayer. Type III and type V isotherms are characteristics of adsorption where the heat of adsorption onto the adsorbate (nitrogen) itself exceeds the heat of adsorption onto the substrate (the solid), as found with water on hydrophobic materials. Type VI and V isotherms feature a hysteresis loop generated by the capillary condensation of the adsorbate in the mesopores of the solid. Finally, the rare type VI step-like isotherm is shown by nitrogen adsorption on some carbonaceous materials [2].

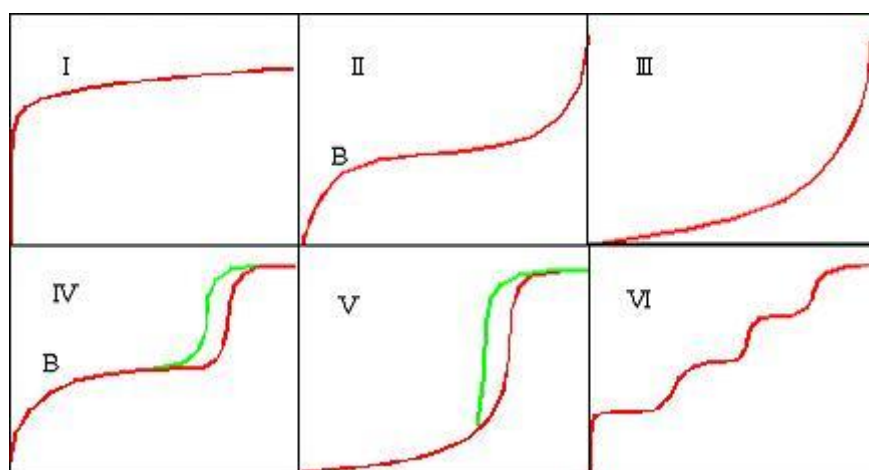


Figure 3.2. Six standard types of adsorption isotherm defined by IUPAC.

If adsorption saturates at monolayer coverage, the surface area is easily determined from the Langmuir adsorption isotherm, which assumes that equilibrium coverage is achieved when rates of adsorption and desorption are equal [3]. However, the most common method of measuring the surface area of powder is that developed by Brunauer, Emmett and Teller using the so called BET method [4]. In essence, the BET isotherm is an extension of the Langmuir isotherm that also considers multilayer adsorption. As in the Langmuir approach the heat of adsorption for the first monolayer is assumed to be independent of coverage. The heat of adsorption for layers other than the first is assumed to be equal to the heat of liquefaction of the adsorbed gas. Summation over an infinite number of adsorbed layers gives the final expression

$$\frac{P}{V(P_0 - P)} = \frac{1}{V_m C} + \frac{(C - 1)P}{V_m C P_0} \quad (\text{Eq. 3.2})$$

where V is the volume of gas adsorbed at pressure P , V_m is the volume of the monolayer, P_0 is the saturation pressure of the adsorbate, and C is a constant related exponentially to the heats of adsorption and liquefaction of the adsorbate as

$$C = e^{(q_1 - q_L)/RT} \quad (\text{Eq. 3.3})$$

where q_1 is the heat of adsorption of the first layer and q_L is the heat of liquefaction of the adsorbate. In general the higher the value of C the more the isotherm approaches the type II form and the more accurate the surface area can be determined.

According to the BET equation (Eq. 3.2) defined above, plots of $P/V(P_0 - P)$ versus P/P_0 should give straight lines whose slope and intercept can be used to evaluate V_m and C . From volume of the monolayer (V_m) and the cross-section area of the adsorbate, the total surface area of the adsorbent can be estimated. Additionally, from the adsorption-desorption isotherm, pore size distributions were obtained applying the Barrett-Joyner-Halenda (BJH) equation to the desorption branch of the isotherm. Total pore volume was estimated from the N_2 uptake at a P/P_0 value of 0.995.

3.2.1 Equipments and conditions for surface area determination

N_2 adsorption-desorption isotherms were recorded at -196°C using an automated ASAP2010 and TRISTAR II instrument from Micromeritics. Before each run, a known mass of sample was heated at 150°C under vacuum for 3 h for degassing and remove the adsorbed species. Specific surface areas were calculated from the linear part of the Brunauer-Emmett-Teller line.

3.3 Raman spectroscopy

The Raman process involves the inelastic scattering of light by matter. A photon may lose energy by electronic, vibrational or (for gases) rotational excitation to give rise to so-called Stokes structure; or photons may gain energy from thermally excited states to give anti-Stokes structure. There is always a strong elastically scattered Rayleigh line. The technique is applied most often to study vibrational excitations. The frequency distribution of the scattered light constitutes the Raman spectrum of a species. Owing to the low cross sections for inelastic light scattering an intense radiation source is required, typically a laser operating in the visible region.

In Stokes scattering the incident electric fields produce an oscillating polarisation in the scattering medium, which then re-emits radiation at the incident frequency minus a vibrational frequency. Raman activity is governed by the *polarisability tensor*, which relates the dipole induced in x, y and z directions to electric fields E_x , E_y and E_z .

$$\begin{pmatrix} \mu_x \\ \mu_y \\ \mu_z \end{pmatrix} = \begin{pmatrix} \alpha_{xx} & \alpha_{xy} & \alpha_{xz} \\ \alpha_{yx} & \alpha_{yy} & \alpha_{yz} \\ \alpha_{zx} & \alpha_{zy} & \alpha_{zz} \end{pmatrix} \begin{pmatrix} E_x \\ E_y \\ E_z \end{pmatrix}$$

The components of the polarisability tensor transform like x^2 , y^2 , xy , xz etc. or linear combinations of them. Since xy and yx , xz and zx and yz and zy have the same transformation properties, there are 6 components of the polarisability tensor to worry about. One component is always totally symmetrical, whilst the other 5 components behave like the d orbitals. Raman active modes must transform as one component of the polarisability tensor and in centrosymmetric systems Raman active modes are therefore of gerade symmetry. This contrasts with infrared spectroscopy which probes ungerade modes transforming like x, y or z.

3.3.1 Raman spectroscopy equipment and conditions

The Raman spectra of the samples, were recorded at room temperature using a Raman microprobe (Labram infinity), equipped with a photodiode array detector. The exciting light source was the 532 nm line of an Nd:Yag laser and the wavenumber accuracy was $\pm 4 \text{ cm}^{-1}$. Laser power was 12 mW and acquisition time was between 2 to 4min. The Raman spectrometer was calibrated using the silicon line at 521 cm^{-1} .

3.4 Transmission Electron Microscopy

Electron microscopy exploits the short wavelength of high energy electrons to achieve spatial resolution superior to that of optical microscopy. In transmission electron microscopy (TEM) electrons generated by thermionic emission are accelerated to a kinetic energy of around 100 keV or greater and pass through a thin slice of sample. The de Broglie wavelength at 100 keV is about 0.037 \AA . Electrons are scattered by the atomic potentials of the atoms in the specimen and form a diffraction pattern. TEM exploits three different interactions of electron beam-specimen: unscattered electrons (transmitted beam), elastically scattered electrons (diffracted beam) and inelastically scattered electrons. The transmission of unscattered electrons is inversely proportional to the specimen thickness. These electrons are subsequently magnified by electron optics to produce a bright-field image. The scattered electrons can be collated using magnetic lenses to form a pattern of spots; each spot

corresponding to a specific atomic spacing (a plane). This pattern can then give information about the orientation, atomic arrangements and phases present in the examined area. Inelastically scattered electrons can be utilized in two ways; Electron Energy Loss Spectroscopy (EELS) and Kikuchi Bands.

3.4.1 Transmission electron microscopy equipment

The TEM images were taken on a TECNAI electron microscope operating at an accelerating voltage of 200 kV. Prior to TEM observations, samples were deposited from ethanolic solution onto holey-carbon copper grids.

3.5 Scanning electron microscopy (SEM)

In a typical SEM, an electron beam is thermionically emitted from an electron gun fitted with a tungsten filament cathode, which typically has an energy ranging from 0.2 keV to 40 keV. In scanning electron microscopy visual inspection of the surface of a material utilizes signals of two types, secondary and backscattered electrons. Secondary electrons are a result of the inelastic collision and scattering of incident electrons with specimen electrons. They are generally characterized by possessing energies of less than 50 eV [1]. They are used to reveal the surface structure of a material with a resolution of ~10 nm or better [1]. Backscattered electrons are a result of an elastic collision and scattering event between incident electrons and specimen nuclei or electrons. Backscattered electrons can be generated further from the surface of the material and help to resolve topographical contrast and atomic number contrast with a resolution of >1 micron. While there are several types of signals that are generated from a specimen under an electron beam the x-ray signal is typically the only other signal that is used for scanning electron microscopy. The x-ray signal is a result of recombination interactions between free electrons and positive electron holes that are generated within the material. The X-ray signal can originate from further down into the surface of the specimen surface and allows for determination of elemental composition through EDS (energy dispersive X-ray spectroscopy) analysis of characteristic X-ray signals.

3.5.1 Scanning electron microscopy equipment

The Scanning Electron Microscope (SEM) images were taken on a Hitachi 4100 S equipped with micro-analysis (Energy-Dispersive X-ray Spectroscopy, EDS) and a field emission gun. The working voltage was 20 kV.

3.6. X-ray Photoelectron Spectroscopy (XPS)

X-ray photoelectron spectroscopy (XPS) is a quantitative spectroscopic technique that measures the elemental composition, empirical formula, chemical state and electronic state of

the elements that exist within a material. XPS spectra are obtained by irradiating a material with a beam of X-rays while simultaneously measuring the kinetic energy and number of electrons that escape from the top 1–10 nm of the material being analyzed.

X-ray photoelectron spectroscopy (XPS) is a technique based on the photoelectric effect, as enunciated by Einstein in 1905. Whereby an atom absorbs a photon of energy, $h\nu$, after which a core or valence electron with binding energy E_b is ejected with kinetic energy expressed by equation 3.4

$$E_k = h\nu - E_b - \phi \quad (\text{Eq 3.4})$$

Where E_k is the kinetic energy of the photoelectron, h is the Planck's constant, ν is the frequency of the of the exciting radiation, E_b is the binding energy of the photoelectron with respect to the Fermi level and ϕ is the work function of the spectrometer. [5].Physical principles of photoemission process are demonstrated by Figure 3.3.

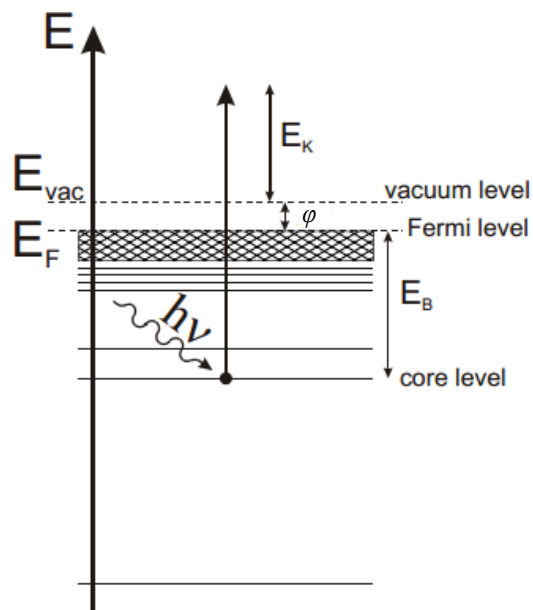


Figure 3.3. Schematic diagram of a core-level-photoelectron emission process.

As shown in figure 3.3 an incident X-ray photon is absorbed and a photoelectron emitted. A measurement of its kinetic energy allows the binding energy of the photoelectron to be calculated. The atom stays behind as an unstable ion with a hole in one of the core levels.

The basic elements of an XPS instrument are a light source, an electron energy analyser and an electron detector as it is drawn on Figure 3.4.

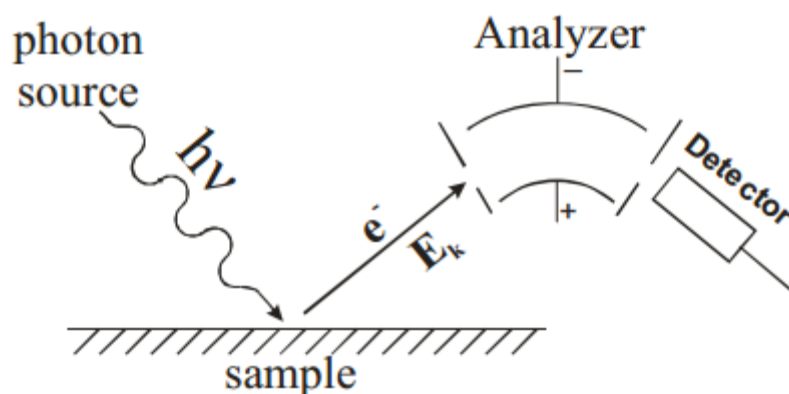


Figure 3.4. Basic elements of XPS experiment.

With photon energies in the ultraviolet region of the electromagnetic spectrum only roughly bound valence band electrons can be ionized, but under irradiation with soft X-rays both core and valence levels are accessible. Laboratory based x-ray photoelectron spectroscopy (XPS) experiments are commonly carried out using Al $K\alpha$ or Mg $K\alpha$ lines, with photon energies of 1486.6 eV and 1253.6 eV respectively. Core level binding energies are essentially characteristic of an element so that core XPS provides a means of chemical analysis.

Soft X-rays may penetrate several hundreds of nanometres into a solid, so that photoelectrons are generated with a significant flux quite deep into the bulk of the solid. However, the electrons may be inelastically scattered as they propagate toward the surface. The electron mean free path λ is a measure of the mean distance that an electron travels before suffering an inelastic scattering event inside a solid. Figure 3.5 shows the electron mean free path λ as a function of kinetic energy for a few selected materials [6]. It can be seen that in the kinetic energy range of interest in XPS measurements (5 eV to 1500 eV) the mean free path of electrons varies from about 5 Å to 15 Å. This means that the peaks in X-ray photoelectron spectra are due to those electrons generated within the first few atomic layers of the material. This gives rise to the characteristic surface sensitivity of XPS when applied to solids.

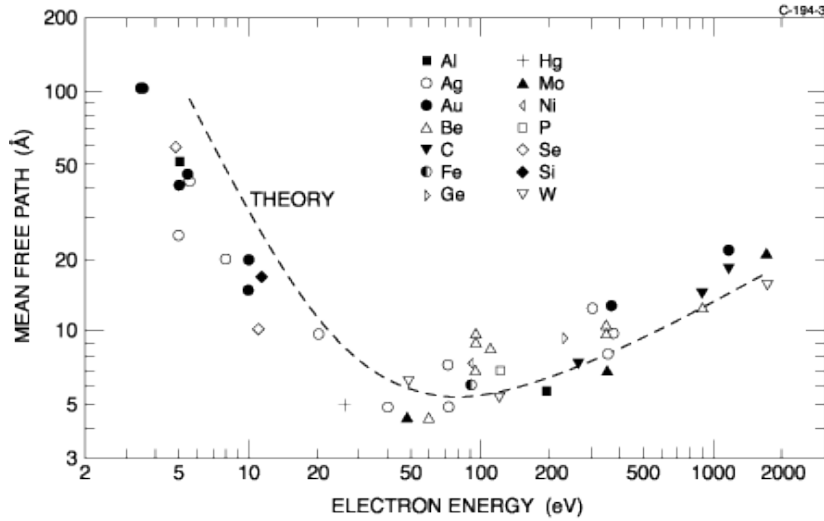


Figure 3.5. Mean-free paths in different elements as a function of kinetic energy.

The stoichiometry of the sample surface can be estimated from the area ratio of XPS peaks. The general formula for the XPS peak area is:

$$I = nF\sigma\lambda AT \sin \theta \quad (\text{Eq 3.5})$$

where I is the intensity of the XPS peak, n is the atomic concentration of the element, F is the X-ray flux, σ is the photoelectronic cross-section for the atomic orbital of interest, θ is the angular efficiency factor for the instrumental arrangement, λ is the mean free path of the photoelectrons in the sample, A is the area of the sample from which photoelectrons are detected, T is the detection efficiency for electrons emitted from the sample.

The atomic composition, N_A / N_B , between A and B atoms is derived from the equation 3.6:

$$\frac{N_A}{N_B} = \frac{I_A}{I_B} \times \left(\frac{E_{CA}}{E_{CB}} \right)^{-0.23} \times \frac{\sigma_A}{\sigma_B} \quad (\text{Eq. 3.6})$$

where σ is the cross section, EC kinetic energy and I is the intensity of the peak.

An X-ray photoelectron spectrum of a solid-state sample always contains a background, which is formed by inelastically scattered photoelectrons. To estimate the peak shape and the stoichiometry from an experimental spectrum first the background should be subtracted. Different models of background shape are in use. A simple linear-type background can be used for fast spectra analysis, while for more accurate line shape and stoichiometry analysis more complicated background types should be used. D.A. Shirley suggested the

background shape on the assumptions of a constant energy spectrum of scattered photoelectrons and a constant scattering probability in the peak region [19].

3.6.3 XPS equipment and conditions

XPS experiments were performed using an AXIS Ultra DLD Kratos spectrometer equipped with a monochromatised aluminium source (Al K α = 1486.69 eV) and charge compensation gun. All binding energies were referenced to the C 1s core level at 285 eV. Simulation of the experimental photopeaks was carried out using a mixed Gaussian/Lorentzian peak fit procedure according to the software supplied by CasaXPS. Semi-quantitative analysis accounted for a nonlinear Shirley background subtraction.

3.6.4 In situ XPS equipment and conditions

In situ XPS analysis were performed using a Vacuum Generators Escalab 220 XL spectrometer equipped with a monochromatised aluminium source (Al K α = 1486.6 eV) and a special catalytic cell, set up near the analysis chamber. This special cell allows the treatment of the sample under different reactionnel stream (H₂, CO, NO, O₂) for controlled pressure and until T=500°C, then transfer in situ towards the chamber of analysis of the spectrometer. In situ XPS analysis were made in a previously HCOH saturated catalyst. A little part of this solid was placed in the special cell, where it was heated up to 200°C (2°C/min) by steps of 25°C under a flow of argon. The XPS analyses were made each 25°C.

3.7 Thermal gravimetric analysis (TGA) and Differential thermal analysis (DTA)

Thermogravimetry is a technique in which the mass of the sample is monitored against time or temperature while the temperature of the sample, in a specified atmosphere, is programmed. In order to enhance the steps in the thermogravimetric curve, the derivative thermogravimetric (DTG) trace is frequently drawn.

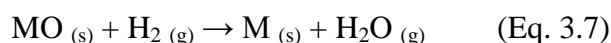
Differential thermal analysis (DTA) is a technique in which the difference in temperature between the sample and a reference material is monitored against time or temperature while the temperature of the sample, in a specified atmosphere is programmed. The DTA curve is generally a plot of the difference of temperature (ΔT) as the ordinate against the temperature (or time) as the abscissa.

3.7.1 TGA-DTA equipment and conditions

Thermal gravimetric analysis (TGA) and differential thermal analysis (DTA) were carried out using TA Instrument SDT-2960 simultaneous TGA-DTA instrument. Clean alumina sample pans were tared on the microbalance arms prior to use. The sample and the reference were heated from 25°C to 1000°C at a rate of 10°C/min. The atmosphere used during the analysis depends of the study, typically air or nitrogen was employed. Thermal events were characterized according to the position of endotherms and exotherms in relation to mass loss. Mass loss and onset calculations were performed by standard methods.

3.8 Temperature programmed reduction (TPR)

Temperature-Programmed Reduction (TPR) determines the number of reducible species present on the catalyst surface and reveals the temperature at which the reduction of each species occurs. The basic reaction during H₂-TPR test is shown in the following equation 3.7:



where MO is the metal oxide and M the metal. However, most of time the metal oxide is not reduced to metal but to lower oxidation states species.

The TPR analysis begins by flowing an analysis gas (typically hydrogen in an inert carrier gas such as nitrogen or argon) through the sample, usually at ambient temperature. While the gas is flowing, the temperature of the sample is increased linearly with time and the consumption of hydrogen by adsorption/reaction is monitored. Changes in the concentration of the gas mixture downstream from the reaction cell are determined. This information yields the volume of hydrogen uptake.

3.8.1 TPR equipment and conditions

Temperature-programmed reduction (H₂-TPR) measurements were performed on a Micromeritics AutoChem apparatus. H₂-TPR was performed in a quartz microreactor (9mm). The experimental conditions of the TPR analysis (sample preparation, pre-treatment, and acquisition of experimental data) affect the obtained results. In particular, experimental parameters such as: hydrogen concentration in the gas mixture, temperature increase rate, total flow rate, sample weight and contact time; influence the analytical profiles and have also effects on the detector sensitivity.

There are two parameters, K and P, which standardize the TPR data. The parameter K represent the sensitivity and is represented as follow:

$$K = \frac{S_0}{VC_0} \quad (55 < K(s) < 150) \quad (\text{Eq. 3.8})$$

Where S_0 is the amount of initial reducible species in the sample (μmol) and VC_0 is the molar flow rate ($\mu\text{mol/s}$) of the reactive gas.

The second parameter P representing the shape and the resolution is expressed as follow:

$$P = K\beta \quad (20 < P (^{\circ}\text{C}) < 50) \quad (\text{Eq. 3.9})$$

Where β is the linear rate of temperature increase ($^{\circ}\text{C}/\text{min}$)

A numerical example used for planning a TPR experiment is presented:

Sample: MnOx

W_{MnO} : 0.005g

mol_{MnO} : 6.3 E-5

Analytical conditions:

Gas mixture: $\text{H}_2/\text{Ar} = 5\%$

Flow rate: 15ml/min ($0.111\text{E-}4 \text{ mol/s}$)

β : $10^{\circ}\text{C}/\text{min}$ (0.133°C/s)

$$K = S_0/(VC_0) \quad (\text{Eq. 3.10})$$

$$K = \frac{6.310^{-5}}{0.111 \cdot 10^{-4} * 0.053} = 115s$$

$$P = K\beta$$

$$P = 115 * 0.133 = 16^{\circ}\text{C}$$

The H_2 -TPR was made in two stages.

1. Degassing treatment to remove the adsorbed species: The sample was heated from room temperature to 300°C ($30^{\circ}\text{C}/\text{min}$) under an argon flow ($50\text{ml}/\text{min}$). The sample was then maintained at 300°C for 1h and cooled to room temperature under argon atmosphere.
2. Reduction process: The reduction mixture containing 5%v/v H_2 in argon was send to the sample at room temperature, the flow was $50\text{ml}/\text{min}$. After a short stabilization process the temperature was increased from room temperature to 800°C (with $10^{\circ}\text{C}/\text{min}$ heating rate). Finally the sample was cooled to room temperature under argon.

3.9 Formaldehyde catalytic oxidation model test

As discussed in Chapter 2 total formaldehyde catalytic oxidation with environmental application is generally carried out in the following conditions:

Table 3.1: Typical conditions used for formaldehyde catalytic oxidation.

Temperature (°C)	20-400
Pressure (Atm)	1
GHSV	20000-60000
HCOH concentration (ppm)	100-1000
Oxidant	O ₂ /Air O ₂ /He O ₂ /N ₂
Oxidant concentration (vol %)	5-21
Mass of catalyst (mg)	100-500

The activity of catalysts is typically compared using light off curves, where the reactant mixture passes through a catalyst bed while the temperature is increased by a selected heating program. The resulting S-shaped curves give an idea about the activity of different catalysts as well as total conversion temperature. In the next section, the conception of formaldehyde system to perform catalytic test will be described. The formaldehyde catalytic set up have been manufacture in the laboratory at the beginning of my PhD.

3.9.1 Catalytic activity system

The formaldehyde catalytic set up is presented in Figure 3.6.

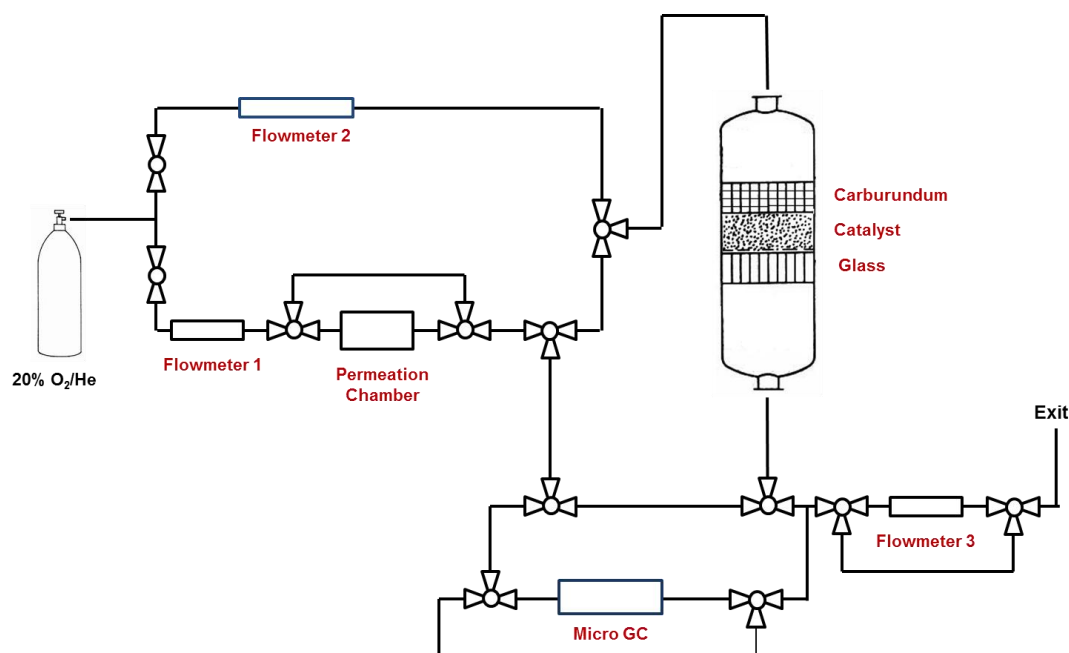


Figure 3.6. Formaldehyde catalytic oxidation set up.

Table 3.2. Description of the different components of HCOH catalytic oxidation set up.

Component	Description
20% O ₂ /He	Mark: Praxair Characteristics: Calibration mixture 20% vol O ₂ balanced with Helium. Exit pressure regulated at 8 bars.
Flowmeter 1	Mark: Bronkhorst Model: EL-Flow Operation: The heart of the thermal mass flow meter is the sensor that consists of a stainless steel capillary tube with resistance thermometer elements. A part of the gas flows through this bypass sensor, and is warmed up by heating elements. Consequently the measured temperatures T1 and T2 drift apart. The temperature difference is directly proportional to mass flow through the sensor.
Permeation Chamber	Mark: VICI Metronics Dynacalibrator Model: 150 Operation: It is a constant temperature system designed to generate precise ppm concentrations of chemical compounds in a gas stream, using permeation devices as the gas source. The basic requirement is to maintain the permeation device at a constant temperature in a known carrier flow.
MicroGC	Mark: Varian Model: 4900 CP Operation: The 4900 CP is a compact GC analyser equipped with two independent channel systems. Each channel equipped with thermal conductivity detector, injector and column. For channel 1 the column is a 1 m COX for analysis of permanent gas, for channel 2 an 8 m CP-Sil 5 CB column is used for the analysis of formaldehyde CO ₂ and incomplete oxidation by-products.
Flowmeter 2	Mark: Brooks Instruments Model: Rotameter Operation: A rotameter is a device that measures the flow rate of liquid or gas in a closed tube. A rotameter is typically made of glass with a 'float' inside that is pushed up by the drag force of the flow and pulled down by gravity. Drag force for a given fluid and float cross section is a function of flow speed squared only, according to the drag equation.
Flowmeter 3	Mark: Hellew-Packard Model: Soap flow meter Operation: The travelling time of the soap film through a fixed volume marked on the glass tube is determined by the calibrated chronometer.

3.9.2 Composition of the reaction mixture

The gaseous formaldehyde was generated using Dynacal permeation tubes containing reagent grade paraformaldehyde in solid phase. Dynacal permeation devices are small, inert capsules containing a pure chemical compound in two phase equilibrium between its gas phase and its liquid or solid phase, as shown in Figure 3.7. Release of the chemical fill occurs by permeation through the wall of the polytetrafluoroethylene PTFE tube for the entire length

between the impermeable plugs. A wide range of rates can be achieved by varying the length and thickness of the tube, with typical rates ranging from 5 ng/min to 50,000 ng/min.

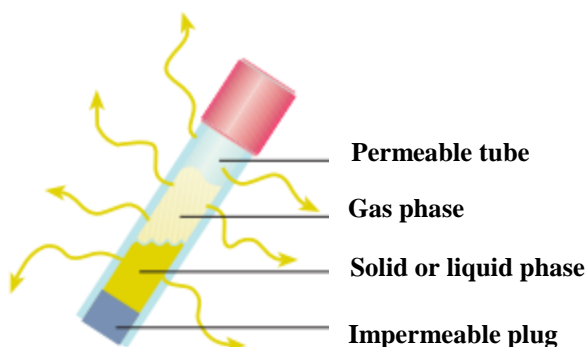


Figure 3.7. Dynacal permeation tubes (taken from VICI Analytical Components and Systems [7]).

The dynacal permeation tubes are placed in the VICI Metronics dynacalibrator. A passivated glass-coated permeation chamber houses the permeation tube(s), with carrier gas passing through the chamber. The temperature controller maintains the chamber temperature at a set point with an accuracy of $\pm 0.01^\circ\text{C}$. Figure 3.8 shows a schematic representation of dynacalibrator device.

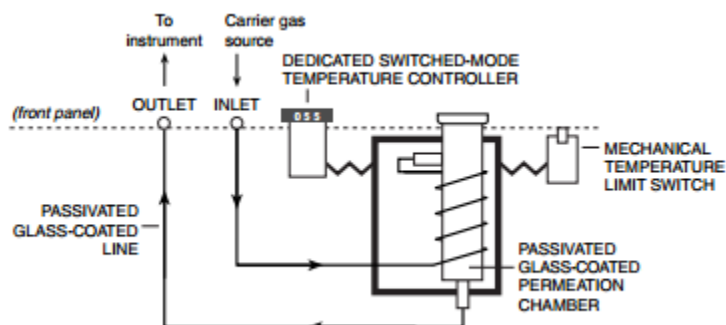


Figure 3.8. Schematic representation of Dynacalibrator used to produce gaseous formaldehyde [8].

Formaldehyde concentration in the reaction mixture is determined using the following equation given by VICI Metronics:

$$[\text{HCOH}] = \frac{K * P}{F} \quad (\text{Eq. 3.11})$$

Where: $[\text{HCOH}]$ = Formaldehyde concentration in ppm

$K = 24.45/\text{Molecular weight of gas}$

P = Permeation rate in ng/min (information included with the permeation device)

F = Chamber carrier flow (ml/min)

For formaldehyde permeation device with a permeation rate 10400 ng/min at 100°C and carrier flow of 100 ml/min a sample calculation, considering two permeation devices, is done:

$$[HCOH] = \frac{\left(\frac{24.45}{30 \text{ g.mol}^{-1}} \right) * (2 * 10400 \text{ ng.min}^{-1})}{100 \text{ ml.min}^{-1}}$$

$$[HCOH] = 170 \text{ ppm}$$

Two different reactions mixture were employed for HCOH catalytic test: high and low formaldehyde content. The composition of this two mixture are presented in Table 3-3

Table 3.3: Compositions of the reaction mixture.

Mixture	[HCOH] (ppm)	[O ₂] (% vol)	Balance
1	500	20	He
2	170	20	He

3.9.3 Analysis of reaction products

As discussed in chapter 2, HCOH complete catalytic oxidation produce only CO₂ and H₂O. However, sometimes incomplete oxidation products as CO, HCOOH, and CH₃OH among others could be obtained in the reaction. To control the activity and selectivity of different catalyst, analysis of reaction products is important. To achieve this MicroGC Varian described in Table 3.2 was employed. Quantification is performed by calibration of peak areas and for each compound linear regression is used to determine the response factors. The response factors of main products detected in HCOH oxidation are listed in table 3.4.

Table 3.4: Response factor of main products.

Product	Response factor Channel 1 (ppm/μV*s)	Response factors Channel 2 (ppm/μV*s)
HCOH	0.37	-
CO ₂	0.35	1.57
CO	-	2.34

The formaldehyde conversion was estimated using the following equation:

$$X_{HCOH}(\%) = \left(1 - \frac{[HCOH]}{[HCOH] + [CO_2] + [CO] + [\dots]} \right) \times 100 \quad (Eq. 3.12)$$

The selectivity towards products was estimated by the following equation:

$$S_{P1}(\%) = \frac{[P1]}{[P1] + [P2] + [P3] + [\dots]} \times 100 \quad (Eq. 3.13)$$

3.9.4 Catalytic test procedure

The catalytic test protocol is schematically represented in Figure 3.9. The formaldehyde catalytic oxidation was performed in a fixed bed reactor (i.d. 8-10mm). In each test, 200 mg of the catalyst were loaded in the reactor. The total flow rate was 100 ml/min and the gas hourly space velocity was 30,000 ml/g_{cat} h.

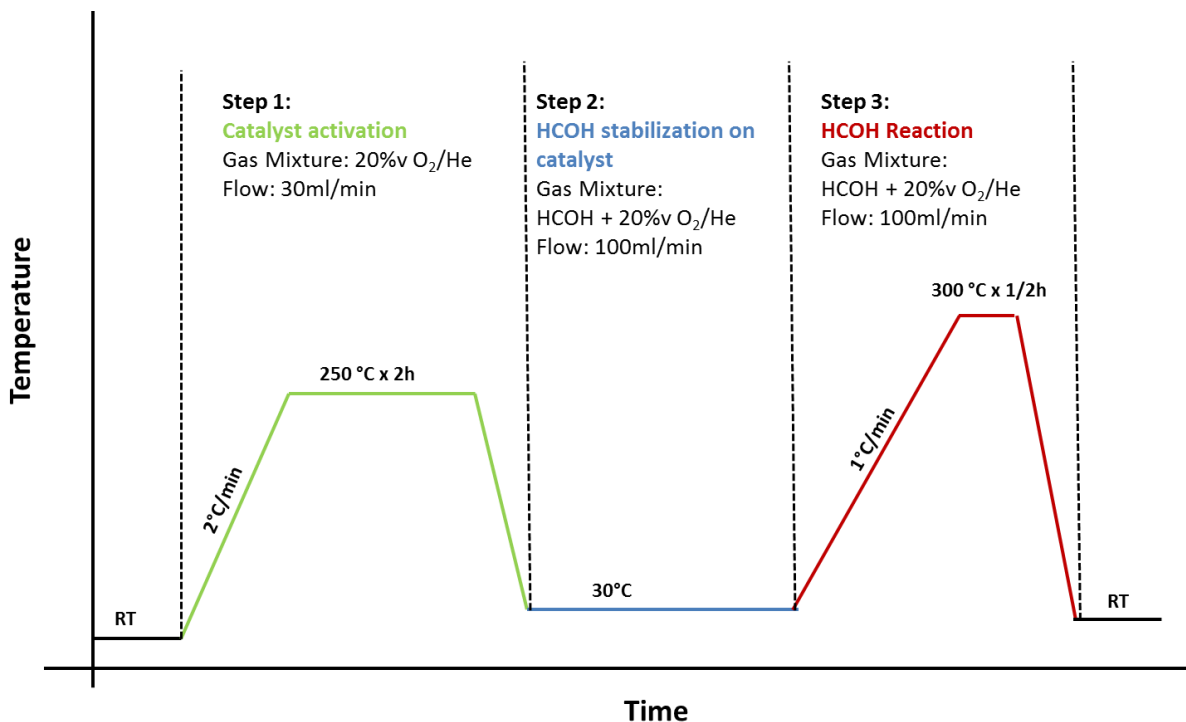


Figure 3.9. Schematic representation of catalytic test protocol.

Step 1: Catalyst activation is the first step of the catalytic test. The aim of this activation process is to clean the catalyst surface and remove physisorbed or chemisorbed water and surface impurities eventually present on the catalyst.

Step 2: Formaldehyde stabilization on solids is done until saturation to control the adsorption capacity of the materials. During the stabilization process the reactant mixture passes through the catalyst bed, formaldehyde concentration was monitored by using on line MicroGC analyser every ten minutes. This step also allows us to control the HCOH concentration at the beginning of the reaction.

Step 3: The formaldehyde catalytic oxidation start, the temperature is increased and the effluent gas from the reactor was analysed by using on line MicroGC analyser, injections were made every five minutes to better control the reaction evolution.

3.10 Determination of surface basicity by pulse technique using benzoic acid as a probe molecule

This technique is based on the interaction / adsorption of a probe molecule (benzoic acid BA) with the basic sites on the surface of the test sample. The acid character of this molecule was used in order to determine, in liquid phase, the amount and the strength of basic sites of the materials.

The experiments were performed using a liquid chromatograph (HPLC) comprised by a pump Waters model 510, an injector Rheodyne 7725 and a UV detector Waters model 2487 coupled to a computer for the collection and processing of data. The tube containing the sample replaces the chromatographic column of HPLC. A diagram of the configuration is shown in Figure 3.10.

The solid is placed in a sample holder comprising a steel tube (1/8 inch) length 12 cm. The sample is held at the middle of the tube using wool silica and acid washed sand sea. This tube is purged using an aprotic solvent (cyclohexane). A solution with a well-known concentration of BA is prepared and then is injected by pulses of 20 μ L through the sample. Figure 3.11 shows an example of the results obtained after integration of chromatographic peaks. The quantification of total acid sites is performed in the first injection cycle of BA. After the first cycle the sample is purged with cyclohexane (0.5 mL min⁻¹) for one hour to remove weakly adsorbed BA molecules on the surface of the sample (second cycle). A third injection cycle of BA determines the number of BA molecules previously removed during the purge and therefore the amount of weak sites. Quantification of strong acid sites is obtained by the difference between total sites, titrated in the first cycle, and the number of weak sites, titrated in the third cycle.

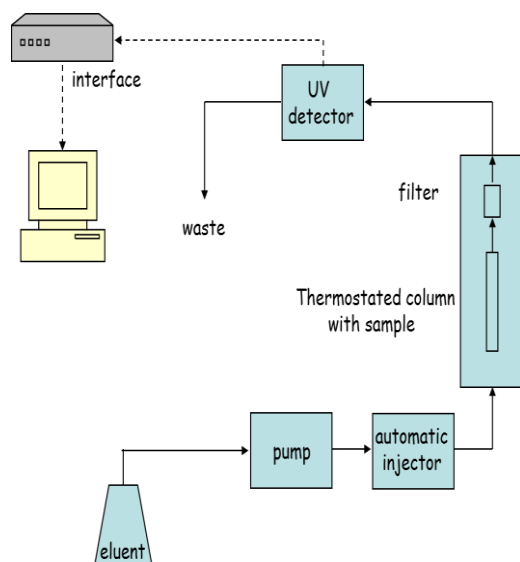


Figure 3.10. Schematic representation of the system to determine surface basicity by pulse technique using benzoic acid as a probe molecule.

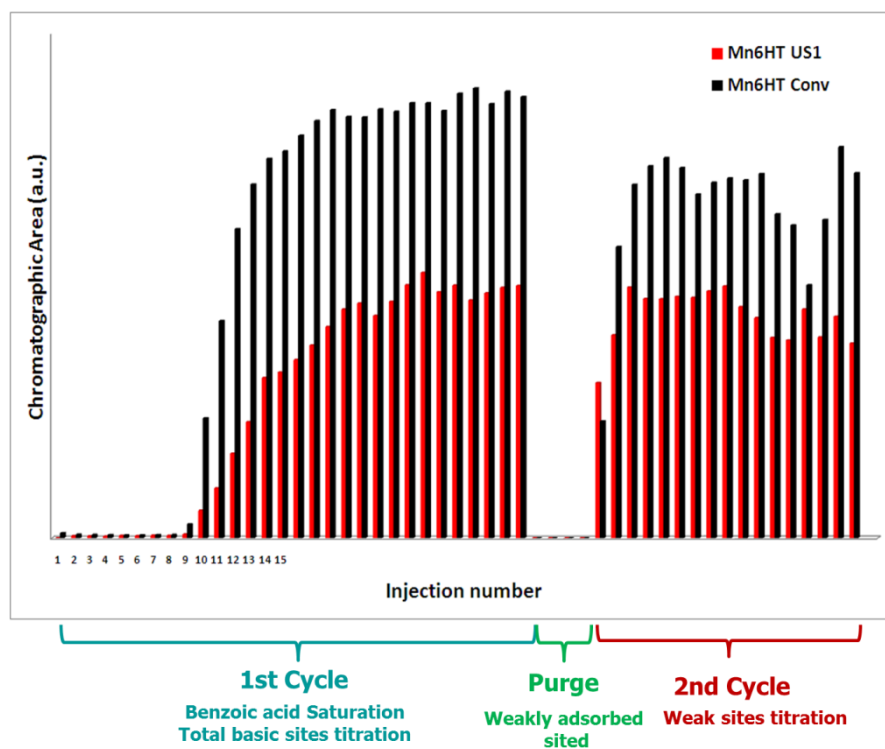


Figure 3.11. Example of the results obtained after integration of chromatographic peaks.

The amount of benzoic acid (BA) adsorbed on the sample after i pulses can be calculated by the following equation 3.14:

$$\text{Adsorbed acid}_i (\text{mequiv} \cdot \text{g}^{-1}) = \left(\frac{VC}{w}\right) \frac{(A-A_i)}{A} \quad (\text{Eq 3.14})$$

Where: V: pulse volume (mL), C: concentration of the benzoic acid solution (M), W: sample weight (g) A: area of the peak in the state of saturation A_i : is the area of the peak corresponding to the i^{th} pulse.

Assuming a stoichiometry of adsorption 1 (benzoic acid): 1 (basic site), the total number of basic sites is actually the total amount of benzoic acid adsorbed on the solid surface (equation 3.15).

$$\text{Basic sites (mequiv} \cdot \text{g}^{-1}) = \sum_i (\text{quantity of BA adsorbed})_i \text{ (mequiv} \cdot \text{g}^{-1}) \quad (\text{Eq 3.15})$$

3.10 References

- ¹ Asahi, R.; Taga, Y.; Mannstadt, W.; Freeman, A. J. *Physical Review B* 2000, 61, 7459.
- ² Cheetham, A. K. In *Solid State Chemistry. Techniques*; Cheetham, A. K., Day, P., Eds.; Oxford University Press: Oxford, 1988.
- ³ Satterfield, C. N. *Heterogeneous catalysis in practice*; McGraw-Hill: Boston, 1980.
- ⁴ Brunauer, S.; Emmett, P. H.; Teller, E. *Journal of the American Chemical Society* 1938, 60, 309.
- ⁵ Wertheim, G. K. In *Solid State Chemistry. Techniques*; Cheetham, A. K., Day, P., Eds.; Oxford University Press: Oxford, 1988.
- ⁶ Hüfner, S. *Photoelectron Spectroscopy: principles and applications*; Third edition ed.; Springer: Berlin, 2003.
- ⁷ <http://www.vici.com/calib/permtube.pdf>
- ⁸ Vici Metronics Dynacalibrator Instruction Manual



CHAPTER 4

Chapter 4: Formaldehyde total oxidation over chemically activated mesoporous MnO_x and MnO_x-CeO₂ catalysts

4.1 Synthesis and characterization of chemically activated mesoporous manganese oxides and their application to formaldehyde oxidation

4.1.1 Introduction

In Chapter 2 it was evidence that transition metal oxides and their combination such as MnO_x, Co₃O₄, CeO₂ and MnO_x-CeO₂ were found as active as the supported precious metals catalyst in deep HCOH oxidation reaction [1,2]. It was also stated that among transition metal oxides, MnO_x has been reported to be the most efficient for catalytic oxidation of volatile organic compounds (VOCs) [3,4,5]. Moreover, among the manganese oxide containing catalysts, highest oxidation state of manganese species was previously found to be preferable for oxidation reactions. Kapteijn *et al.* [6] have investigated the reduction of NO by NH₃ over pure manganese oxides and found that the NO conversions decreased in the order MnO₂ > Mn₅O₈ > Mn₂O₃ > Mn₃O₄. Consequently, for this application it is crucial to generate high-valent manganese oxide materials to improve redox properties at low temperature. Brenet *et al.* [7] studied the chemical activation of manganese oxide in the form of hausmannite phase (Mn₃O₄) by treatment in acidic medium using sulphuric acid; the influence of various factors such as acid concentration and temperature has been specified, and the manganese oxide obtained showed higher oxidation state, high electrochemical properties and improved catalytic activity. Askar *et al.* [8] have prepared high electrochemical active manganese dioxide by chemical processes. In this work, hausmannite phase was activated using hydrochloric and sulphuric acids under various reaction conditions, and the influence of the acid concentration on the type and crystal structure of the manganese dioxide obtained was specified. More recently, Sinha *et al.* [9,10] have synthesized manganese oxide mesoporous materials by using template assisted method followed by chemical activation under acidic treatment. These materials have a great surface area and enhanced ability to eliminate volatile organic compounds at room temperature. Suib *et al.* [11] have prepared manganese oxide mesoporous structures by oxidation of Mn(OH)₂ in the presence of cetyltrimethyl-ammonium bromide (CTAB); the solid obtained showed ordered mesoporous structures and exceptional thermal stability (1000°C).

Thus, in the present chapter, synthesis and characterization of mesoporous MnO_x oxides by high concentration surfactant assisted wet-chemistry route and their activation by acidic treatment are described. The techniques of X-ray diffraction (XRD), nitrogen adsorption-desorption isotherms, Raman spectroscopy, transmission electron microscopy (TEM), X-ray photoelectron spectroscopy (XPS), and temperature-programmed reduction (H_2 -TPR) were employed for catalyst characterization. The application of these materials in the formaldehyde oxidation was also studied taking into account the effect of the acidic treatment of the materials. Finally, a mechanistic approach by surface reaction experiments using TPD, FTIR and XPS analysis of formaldehyde adsorption is proposed.

4.1.2 Experimental procedure

4.1.2.1 Materials preparation

Manganese oxides were prepared by precipitation from aqueous solution of nitrate involving the cetyltrimethylammonium bromide surfactant in the process. In a specific synthesis appropriate quantities of $\text{Mn}(\text{NO}_3)_2 \cdot 6\text{H}_2\text{O}$ were dissolved in 15 mL of H_2O followed by the addition of a solution of NaOH (0.48 g NaOH in 5 mL of H_2O). The resulting manganese hydroxide precipitated solution was added to an aqueous solution of cetyltrimethylammonium bromide (6,7 g in 15 mL of H_2O). The resulting mixture was heated to 75 °C and then stirred for 1 h. The final gel obtained in a sealed beaker was transferred to an oven and heated for 12 h at 75°C. The solid residue was filtered, washed with water, dried in air and finally calcined at 500°C for 6 h (1°C min^{-1}). The calcined sample was treated with an aqueous solution of H_2SO_4 (120 mL - 10 mol L^{-1}) by stirring in a beaker for 1 h. The final product was filtered, and the residue was washed with water and dried at 105°C. The obtained solids were denoted MnO_xSC and $\text{MnO}_x\text{SC_TA}$, calcined and acid treated, respectively.

For comparison, manganese oxide was also prepared without surfactant using the same procedure described previously. The resulting samples were denoted MnO_xC and $\text{MnO}_x\text{C_TA}$.

4.1.3 Results and discussions

4.1.3.1 Characterization of the materials

4.1.3.1.1 Bulk structure and specific surface area

The wide angle powder XRD patterns of the solids after each step of the synthesis, (1) solid dried in air, (2) calcined and (3) treated with sulphuric acid are displayed in Figure 4.1.

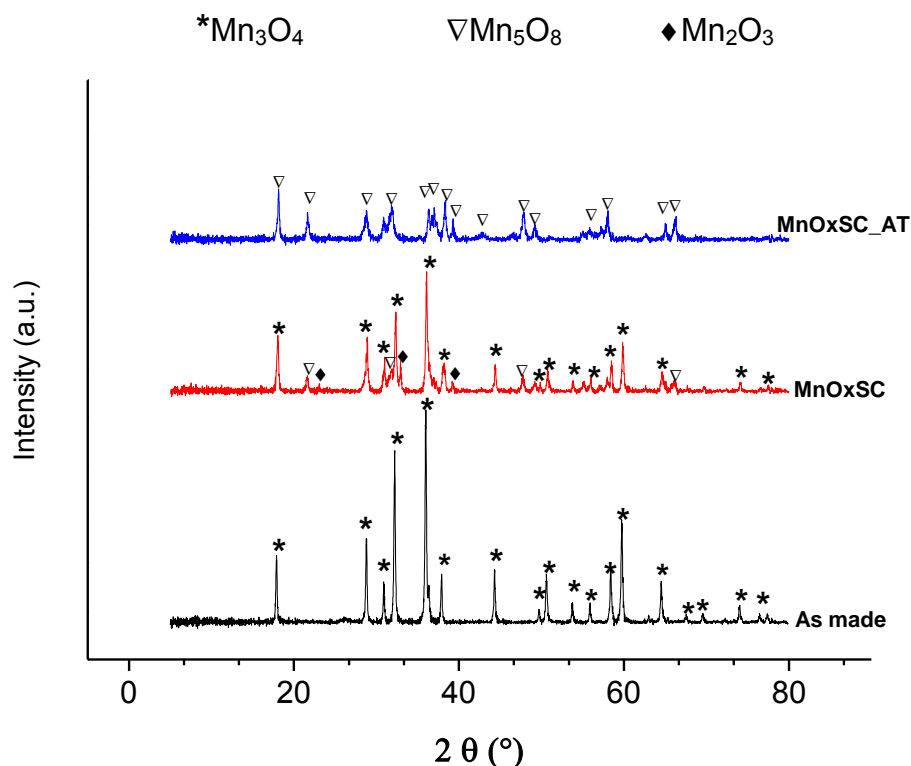


Figure 4.1. XRD patterns of the solid prepared using surfactant after each step of the synthesis.

The brown solid obtained (as made) showed diffraction peaks that could be attributed to the crystalline phase hausmanite Mn₃O₄ (JCPDS 071841). After calcination (MnOxSC), the solid turned black and showed diffraction peaks due to the hausmanite phase and also peaks of lower intensity ascribed to the Mn₅O₈ (JCPDS 391218) phase and bixbyite Mn₂O₃ phase (JCPDS 070856). The oxidative atmosphere used at the beginning of the synthesis provides a pathway to oxidize some Mn²⁺ present in Mn(OH)₂ to Mn³⁺ and Mn⁴⁺. During the calcination step, the Mn³⁺ ions of the Mn₃O₄ are partially oxidized into Mn⁴⁺ ions to give Mn₅O₈ (Mn₂²⁺Mn₃⁴⁺)O₈⁻². This is probably due to the generation of hot spot by carbon based template exothermic decomposition, which can enhance the transformation of Mn₃O₄ into Mn₅O₈. The

existence of Mn_2O_3 is related to the phase transformation of Mn_5O_8 , in which the divalent and tetravalent ions synproportionate to yield Mn_2O_3 [12].

After acidic treatment (MnOxSC_TA), the peaks due to the hausmanite phase disappeared and only peaks due to the monoclinic phase Mn_5O_8 were observed. The crystal structure of Mn_5O_8 , as determined previously by Oswald *et al.*[13], was isostructural to monoclinic $\text{Cd}_2\text{Mn}_3\text{O}_8$, having a compositional formula $\text{Mn}_2^{2+}\text{Mn}_3^{4+}\text{O}_8$. As shown in Figure 4.2, the compound is composed of 2D octahedral sheets of $[\text{Mn}_3^{4+}\text{O}_8]$ consisting of Mn^{4+} ions in the bc planes separated by Mn^{2+} layers.

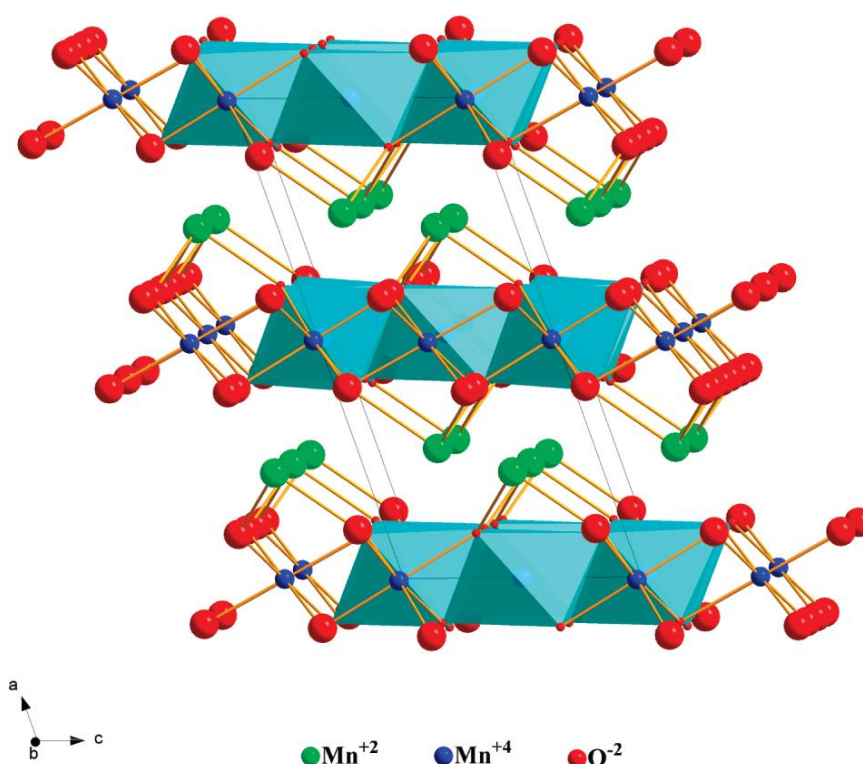


Figure 4.2. Polyhedral representation of the crystal structure of Mn_5O_8 . From reference [14].

Brenet *et al.* [7] showed that Mn^{2+} and Mn^{3+} can be transformed in the presence of sulphuric acid according to the following dismutation reaction:



In accordance with this reaction, the phase resulting from complete transformation of Mn_3O_4 in the presence of sulphuric acid should be MnO_2 , although the monoclinic phase

Mn_5O_8 was obtained in our experiments. Therefore, it seems that a partial amount of Mn^{3+} can be oxidized leading to Mn_5O_8 monoclinic phase, which stabilizes the divalent Mn^{2+} ions inherited from Mn_3O_4 . Digestion time and acid concentration could explain this discrepancy [7]. In agreement with reaction (1), one part of the manganese dissolves to form Mn^{+2} . It was verified by a change of colour in the solution from colourless to pink at the end of the acid treatment.

Figure 4.3 presents the wide angle powder XRD patterns of the solids prepared without surfactant after each step of the synthesis, showing (1) solid dried in air, (2) calcined and (3) treated with sulphuric samples. It could be seen that the samples underwent similar phase transitions Mn_3O_4 (dried in air), $Mn_3O_4 + Mn_5O_8$ (calcined) and Mn_5O_8 (acid treated). However, a higher proportion of Mn_5O_8 phase seems to be produced in the calcined sample when surfactant is employed (Figure 4.1). Moreover, for the calcined sample the Mn_2O_3 phase was not detected, it seems that the oxidation pathway is different when surfactant is employed. Finally, after acidic treatment, it can be observed (Figures 4.1 and 4.3) that higher crystallinity of the Mn_5O_8 phase was obtained when surfactant was employed, the full width at half maximum (FWHM) of the diffraction peak of Mn_5O_8 ($2\theta = 22^\circ$), given by 0.19° and 0.25° for the samples $MnOxSC_TA$ and $MnOxC_TA$, respectively, supports this statement.

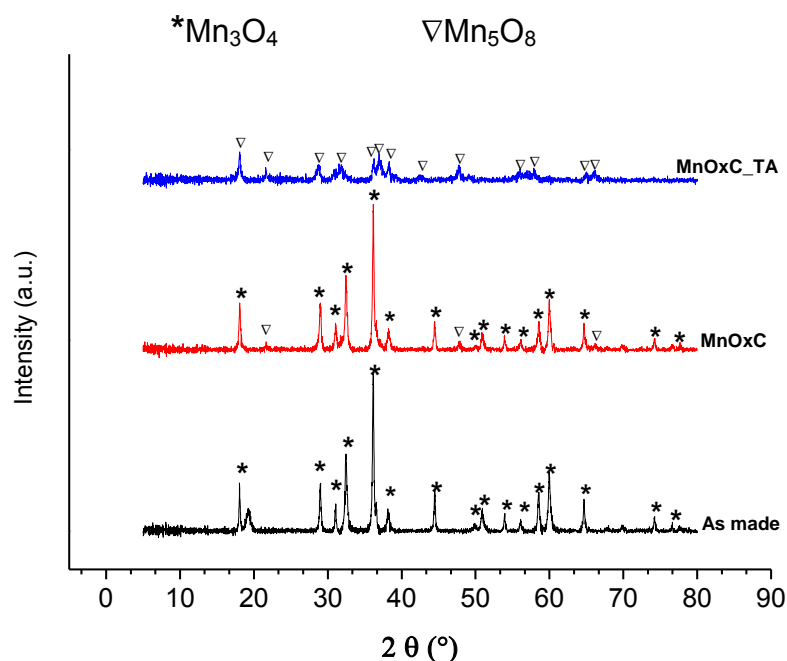


Figure 4.3. XRD patterns of the solid prepared without surfactant after each step of the synthesis.

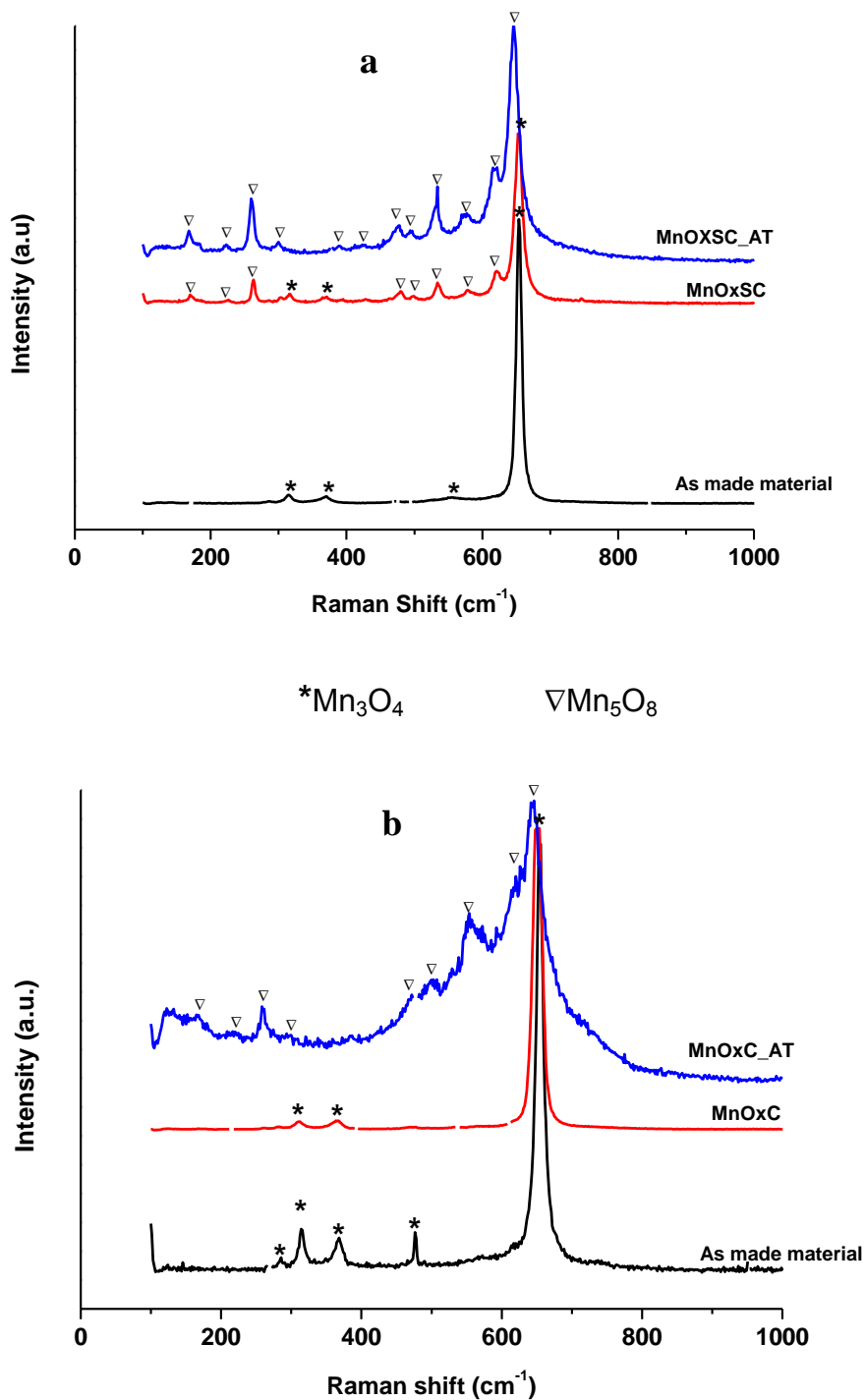


Figure 4.4. Raman scattering spectra of solids prepared a) with surfactant b) without surfactant after each step of the synthesis.

Figure 4.4 shows the Raman scattering spectrum of the materials after each step of the synthesis. Figure 4.4a shows the Raman spectrum of a representative sample prepared using

surfactant. For the as-made material three Raman modes are detected at 314 cm^{-1} , 370 cm^{-1} and 657 cm^{-1} , characteristic of Mn_3O_4 according with the literature data [14,15,]. These bands are still observed after calcination, for MnOxSC sample, together with Raman modes at 167, 260, 290, 430, 476, 533, 575 and 617 cm^{-1} which are characteristic of Mn_5O_8 [14,15]. After acidic treatment (MnOxSC_TA), the characteristic lines of Mn_3O_4 disappear and at least 10 Raman bands are identified within the spectral region of 200-1000 cm^{-1} , these bands are in good agreement with literature data for Mn_5O_8 powders (Table 4.1). These results are in accordance with those obtained by X-ray diffraction.

Table 4.1. Vibrational Frequencies of Raman Scattering Bands of Mn_5O_8 (cm^{-1}).

Raman bands	Mn_5O_8 powders ¹⁶	MnOxSC_TA
v1	171	167
v2	264	260
v3	302	290
v4	394	390
v5	431	430
v6	477	476
v7	533	533
v8	577	575
v9	617	617
v10	648	646

For the samples prepared without surfactant (Figure 4.4b) it can be observed for the as-made material three Raman modes at 655 cm^{-1} , 344 cm^{-1} and 322 cm^{-1} , which are characteristic of Mn_3O_4 . After calcination (MnOxC), we observed the same bands and, finally, after acid treatment (MnOxC_TA), the characteristic Mn_3O_4 bands disappear and only lines characteristic of Mn_5O_8 were detected. However, the Raman spectrum for the acid treated sample is much less clear when compared to the Raman spectrum of the acid treated sample using surfactant. It appears that much poorer organization of Mn_5O_8 phase is obtained when surfactant is not used. These results are consistent with those obtained by X-ray diffraction in which higher crystallinity was observed for the sample prepared using surfactant. It seems clearly that the use of surfactant affects not only the crystallographic structure and organization of the materials but also the evolution of the oxidation states during the synthesis.

The texture properties of the samples are listed in Table 4.2. For the calcined samples, the specific surface areas (SSA) are similar, 20 and 31 m^2/g for MnOxC and MnOxSC respectively. Indicating that the use of surfactant does not significantly modify their textural

properties. However, the acidic treatment produces considerable effect on the SSA of the samples (increase of 75%), this effect being equivalent for both samples. This increase in the SSA is probably related to the decrease of the particle size under the strong acidic conditions. This assumption is supported by wide angle XRD results, which showed weaker and broader peaks of Mn₅O₈ monoclinic phase and then smaller crystallite size after the acidic treatment (Figure 4.1 and 4.3). Sinha *et al.* [9] showed that the strong acidic condition breaks down larger particles into smaller ones, significantly increasing the SSA. After calcination, formation of manganese oxide agglomerates made of crystallized particles together with amorphous species probably took place. In agreement with reaction (1) the acidic treatment dissolves one part of the manganese species to generate Mn²⁺ in solution. This dissolution concerns most probably first the amorphous species located between the particles, promoting or showing SSA.

Table 4.2. Textural properties of manganese based samples calcined and acid treated.

Sample	BET Surface Area (m ² /g)	Pore Size diameter at maximum value (nm)	Pore Volume (cm ³ /g)
MnO _x C	31	30	0.15
MnO _x SC	20	30	0.13
MnO _x C_TA	121	10	0.30
MnO _x SC_TA	90	5	0.25

Figure 4.5 shows the pore size distribution of the different oxides before and after acidic treatment. For the calcined samples, the pore size distribution was broader and centred at a maximum pore diameter value of 30nm (Table 4.2). After acidic treatment and for MnO_xSC_TA, the development of a narrow mesoporous distribution with maximum value at around 5nm was observed (Figure 4.5), whereas for the sample MnO_xC_TA these narrow mesopores are not present. However, a broader mesoporous distribution centred at around 10nm was observed. It can also be noticed for the acid treated samples the broader distribution centred at 30nm, described above, in a minor proportion. Considering the explanation described previously for the increase in SSA, it seems reasonable to suppose that the dilution of the amorphous manganese species unveils the narrow mesoporous distribution present in the particles. This result is consistent with the pore volume of the samples being 0.134 cm³/g for the calcined and 0.255 cm³/g for the acid treated (Table 4.2).

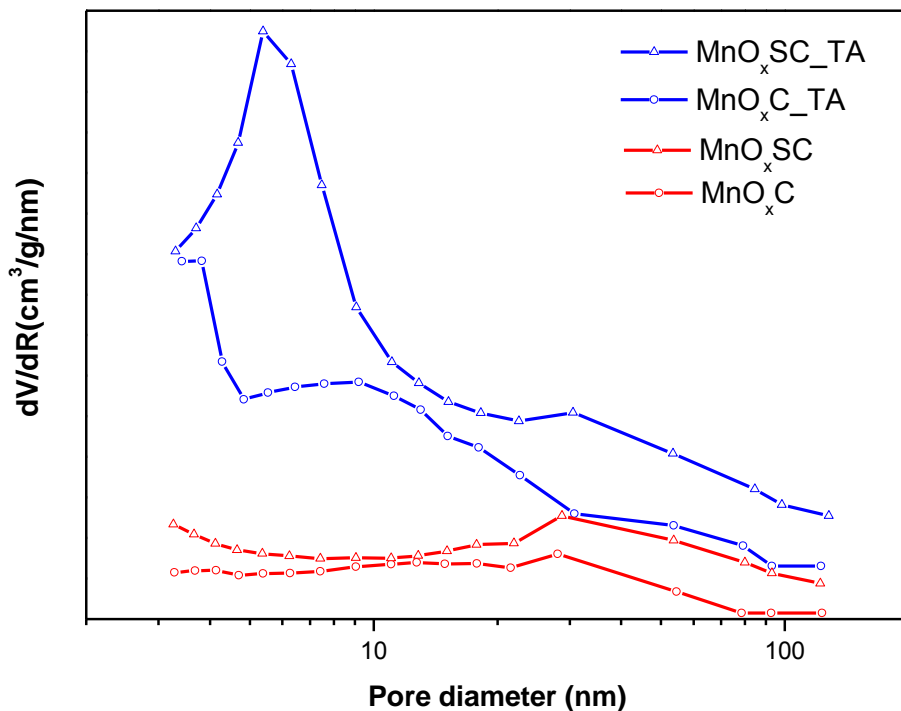


Figure 4.5. Pore size distribution of the calcined and acid treated MnO_x samples.

The adsorption-desorption isotherms of the samples prepared using surfactant at each step of the synthesis are presented in Figure 4.6. The isotherms for calcined and acid-treated samples showed hysteresis loop shapes that are indicative of poorly defined mesopores, suggesting that no ordered mesoporous structures were formed in the materials. Actually, the as-made and the calcined material exhibit a type II isotherm, which indicates an open surface or a macroporous structure. After acidic treatment, the hysteresis loop involves a higher range of relative pressure, indicating the evolution of the narrow mesoporous distribution described previously. It is well known that syntheses and structures of transition metal oxides and particularly manganese and cerium oxides could be complicated under the conditions described above due to the multitude of different coordination numbers and oxidation states [11,17]. Furthermore, if the synthesis is done in air, some Mn^{2+} ions can be readily oxidized to Mn^{3+} and Mn^{4+} , therefore the interaction between the inorganic precursor and the surfactant could be affected. Moreover, during calcination, reduction of Mn ions operated by the surfactant and reoxidation by oxygen can occur, preventing ordering of the structure or at least limiting it to only a few regions.

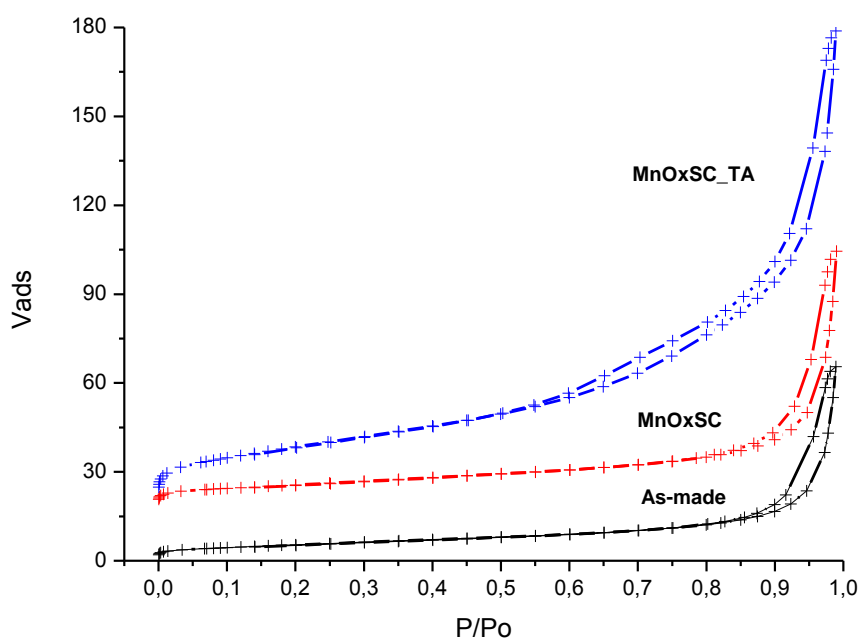


Figure 4.6. Adsorption desorption isotherms for the materials prepared using surfactant after each step of the synthesis.

In order to investigate the effect of the acidic treatment on the sample morphology, TEM analyses of the solid prepared using surfactant, calcined and acid treated, were carried out (Figure 4.7). The calcined samples consist of sphere like nanoparticles, as shown in Figure 4.7a. No regular images were obtained by high-resolution transmission electron microscopy (HRTEM) studies, indicating that the formation of ordered mesoporous structures was not achieved in the catalyst, as previously suggested by adsorption desorption isotherm. It can also be observed by HRTEM (Figure 4.7a inset) the orientation of the MnO_x diffraction plane; for the calcined sample the (2 0 0) orientation corresponding to Mn_5O_8 was detected. After the acidic treatment, the presence of smaller particles together with larger spheres like nanoparticles is detected (Figure 4.7b). This observation is in conformity with the obtained by XRD and BET analyses, in which weaker and broader peaks and higher specific surface area were observed, respectively. HRTEM images of the sample treated with sulfuric acid is shown in Figure 4.7c; it can be clearly seen that the acidic treatment strongly modified the size and the shape of the particles from sphere-like nanoparticles of 60nm to small plate-like particles of 10 nm.

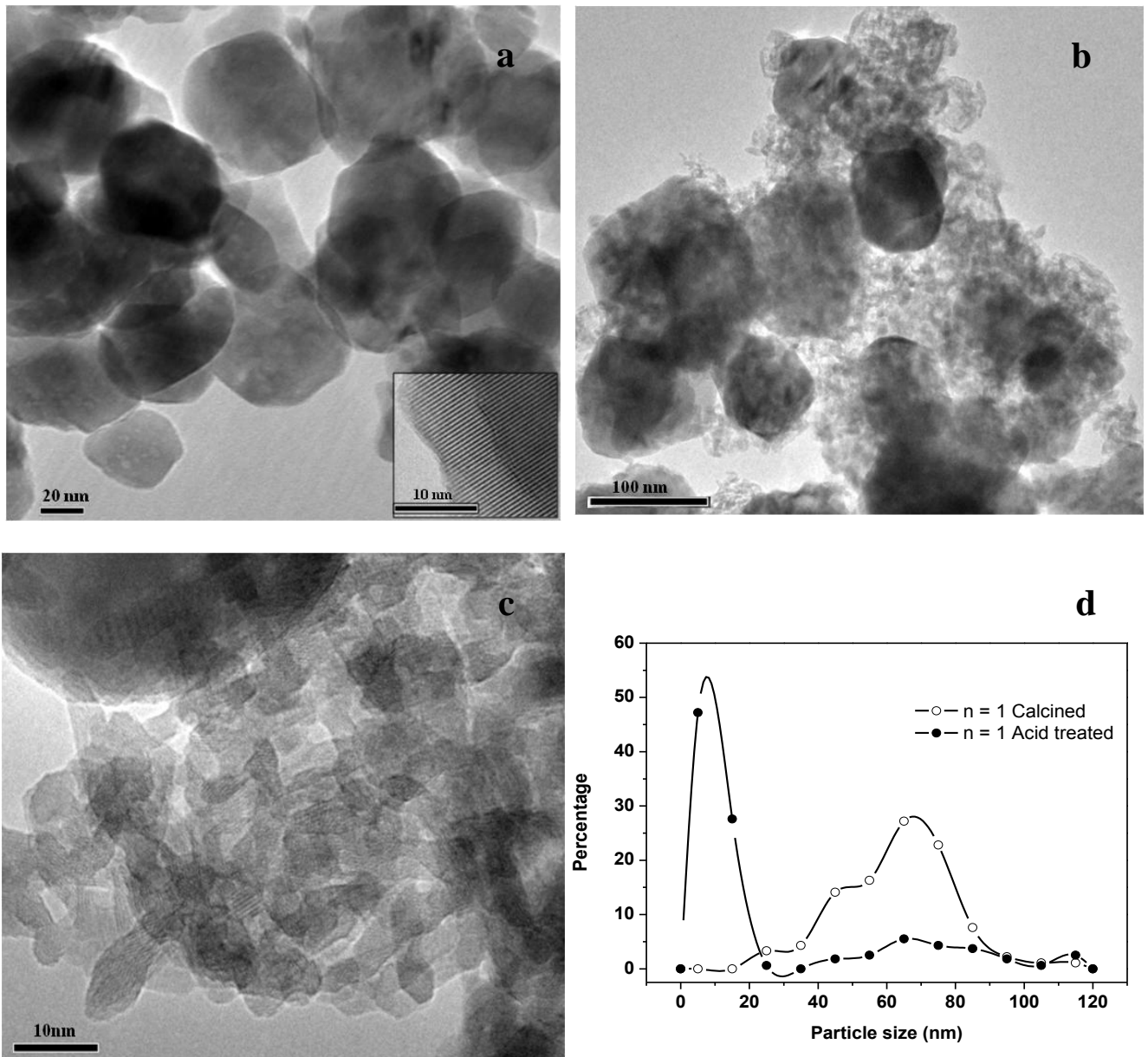


Figure 4.7. TEM images of MnS sample a) Calcined and b) Acid treated c) HRTEM of acid treated sample and d) Particle size distribution of the calcined and acid treated n=1 samples from TEM images.

The particle size distribution for the MnO_xS sample calcined and acid treated is presented in Figure 4.7d. It can be observed that for the calcined sample the particle size distribution is centered at around 70 nm. After the acidic treatment, the particle size was shifted towards smaller values and centered at around 10 nm. However, it can be detected that larger particles are also present in this sample, indicating that probably the time of the

treatment was not sufficient to modify all the manganese oxide phase. This result confirms the assumption described by Sinha *et al.* [9] according to which the strong acidic conditions break down larger particles into smaller ones. It can also be observed that smaller particles surround larger particles, supporting the explanation described above, where dissolution or breaking of amorphous species located between the particles unveil the porosity of higher particles.

4.1.3.1.2 Redox properties

Figure 4.8 shows the H₂-TPR profiles of the calcined and acid treated MnO_x materials. The reduction profiles are characterized by two regions of hydrogen consumption extended in the ranges 150°C - 400°C, low temperature region (LTR), and 400°C - 650°C, high temperature region (HTR). Several authors have obtained these profiles in MnO_x based materials and in general it has been established that the LTR could be assigned to the reduction of poorly crystalline MnO₂/Mn₂O₃ into Mn₃O₄, while the HTR would correspond to the reduction Mn₃O₄ to MnO [18, 19].

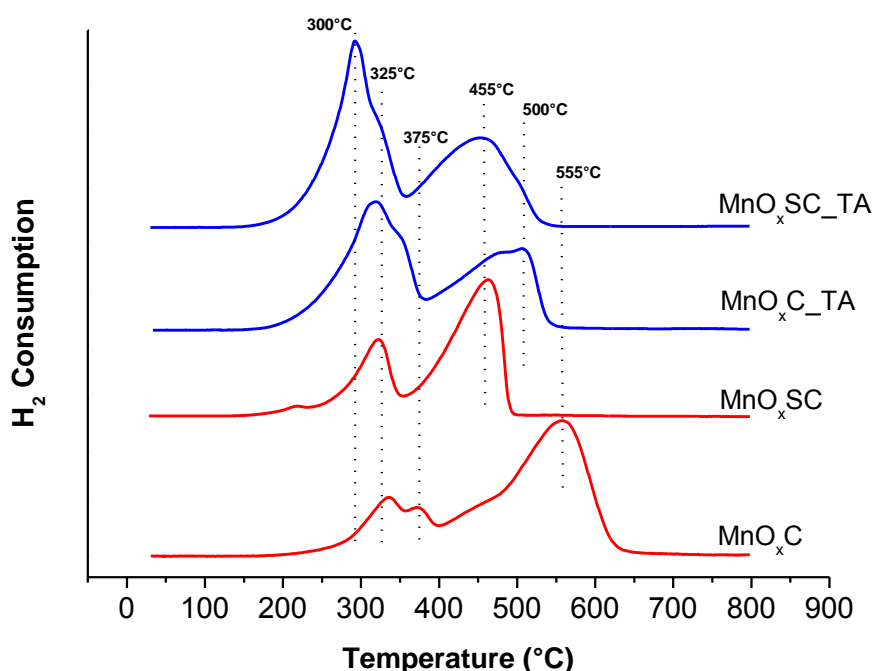


Figure 4.8. H₂-TPR profiles of the calcined and acid treated MnO_x samples.

The reduction profiles of the calcined samples prepared without surfactant (MnO_xC) showed two strong reduction peaks with maximum at 325°C and 555°C, together with a

shoulder at 375°C. This profile suggests that reducible manganese species could be formed by a mixture of different oxides. This is in agreement with the XRD and Raman results, which showed that at least two different manganese oxides are present in this sample. Therefore, the low temperature reduction peaks at 325°C and 375°C could be ascribed to the reduction of high-oxidation state manganese species Mn_5O_8 into Mn_3O_4 and Mn_2O_3 into Mn_3O_4 , whereas the high temperature peak at 555°C was assigned to further reduction of Mn_3O_4 into MnO . For the calcined sample prepared using surfactant (MnO_xSC), the same two strong reduction peaks with maximum at 325°C and 455°C were observed, corresponding to two step reduction process described above. Noticeably for this sample, the second reduction peak is shifted to lower temperature (-100°C); it seems that the use of surfactant enhanced the interaction with H_2 , which is probably due to the development of different morphology and stability of the material that can influence the reduction process. For instance, preferential exposure of more reactive surfaces. It can also be observed in this sample a slight shoulder at 220°C responsible for the reduction of MnO_2 traces or to small cluster of surface manganese oxides [18,19].

The H_2 -TPR profiles of the acid treated were also studied (Figure 4.8). For the sample $\text{MnO}_x\text{C_TA}$ prepared without surfactant, the TPR profile reveals the same two-step reduction process describe above for the calcined samples, with maxima at 325°C and 500°C, respectively. Remarkably, for this sample, the second reduction peak was shifted to lower temperature, indicating that the acidic treatment enhanced the reducibility of the material probably due to the decrease of the particle size or the creation of less organized species, as was shown by XRD and Raman characterization. It can also be observed that this sample presents a higher contribution for the first reduction peak towards the total reduction profile, indicating that manganese species are probably present in higher oxidation state. XRD and Raman analyses support this result revealing Mn_5O_8 monoclinic phase after acidic treatment, where manganese ions are found in higher oxidation states. For the sample prepared using surfactant ($\text{MnO}_x\text{SC_TA}$), the same trend was observed; two reduction peaks with maxima at 300°C and 455°C were registered. However, it can be remarked that the first reduction peak was shifted to lower temperature. Actually, this sample presents the highest reducibility; this behaviour indicates that not only the acid treatment but also the use of surfactant improves the redox properties of the material.

Table 4.3 presents the H₂ consumption for the samples together with the theoretical H₂ consumption for the various Mn-phases, Mn₂O₃, Mn₃O₄, Mn₅O₈ and MnO₂ in mmolH₂/g. For the acid treated samples, the H₂ total consumption is the most important. This is probably due to the presence of manganese species in higher oxidation states in these samples. Moreover, for the calcined and acid treated samples, the H₂ consumption increases when surfactant is employed; explanations of this behaviour have been described above. Deconvolution of the H₂-TPR profile allows us to obtain the partial H₂ consumption for LTR and HTR (Table 4.3). For the calcined sample, the H₂ consumption in LTR and HTR region is around 1.4 and 4.0 mmol/g, respectively, indicating a higher contribution for the HTR. This is probably due to the presence in higher proportion of the hausmannite phase for these samples. After acid treatment, higher contribution of the LTR was observed for both samples due to the presence of Mn⁴⁺ in higher proportion.

Table 4.3. Quantitative results from H₂-TPR.

Sample	Consumed H ₂ /mmol/g	LTR Consumed H ₂ /mmol/g	HTR Consumed H ₂ /mmol/g	Average Oxidation State ^a
MnO _x C	5.2	1.3	4.0	2.8
MnO _x SC	6.3	1.5	4.6	3.0
MnO _x C_TA	7.6	3.9	3.7	3.2
MnO _x SC_TA	8.6	4.4	4.1	3.4

^a $Mn_2O_3 + H_2 = 2MnO + H_2O$ (6.3 mmol/g)

$Mn_3O_4 + H_2 = 3MnO + H_2O$ (4.4 mmol/g)

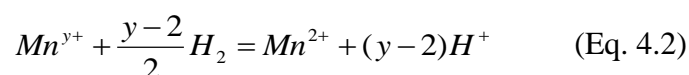
$Mn_5O_8 + 3H_2 = 5MnO + 3H_2O$ (7.5 mmol/g)

$MnO_2 + H_2 = MnO + H_2O$ (11.4 mmol/g)

Comparison between theoretical and experimental amounts of H₂ consumed during reduction allows additional evidence in order to identify each phase. For instance, the H₂ consumption for MnO_xSC is 6.2 mmol/g, which is very close to the theoretical value 6.3mmol/g corresponding to the reduction of Mn₂O₃ into MnO. However, for this sample, the reduction profile takes place in a two-step process (Figure 4.8), and the TPR profile for commercial Mn₃O₄ takes place in one step (Figure 4.9). Furthermore, XRD and Raman investigations indicated the presence of different manganese oxides. Thus, contributions of different oxides towards H₂ consumption are expected for this sample. For the acid treated sample (MnO_xSC_TA), the H₂ consumed is 8.6mmol/g, which lies between the theoretical values 7.5 and 11,4 mmol/g corresponding to reduction of Mn₅O₈ into MnO and MnO₂ into MnO, respectively. For this sample, XRD analyses showed the presence of monoclinic Mn₅O₈

phase. Nevertheless, the H₂ consumption was significantly higher than the theoretical value reported for this oxide. This implies that reduction of Mn₅O₈ takes place along with reduction of amorphous MnO₂ oxide.

The average oxidation states (AOS) from TPR analyses are also shown in Table 4.3. These values were estimated from the following equation



where $y+$ is the AOS of Mn ions. AOS values of 2.8 and 3 were obtained for the calcined MnO_xC and MnO_xSC samples, respectively (Table 4.3). This result can be correlated to the presence of Mn₅O₈ phase in higher proportion in the MnO_xSC sample, as described by XRD and Raman analyses. After acidic treatment, an increase in the AOS values was observed, according to the presence of Mn⁴⁺ in higher proportion.

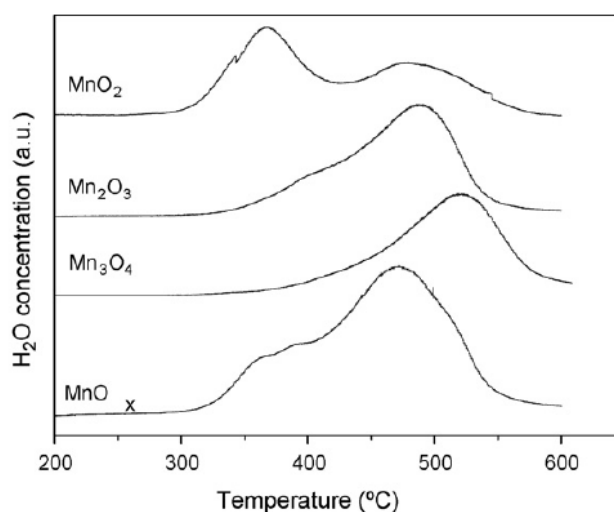


Figure 4.9. TPR profiles of MnO_x and commercial Mn₃O₄, Mn₂O₃ and MnO₂. From reference [18].

4.1.3.1.3 XPS analyses

The oxidation state of catalyst surface species was examined by XPS. The XPS spectra of the core levels of Mn (2p) and Mn (3s) were analysed to estimate the manganese oxidation states. As reported in Figure 4.10, the calcined and acid treated samples show predominantly two Mn 2p components. For the calcined samples the binding energies are 641.9 and 653.7

eV for Mn 2p_{3/2} and Mn 2p_{1/2} respectively. After acid treatment, the Mn 2p binding energies are slightly shifted to the higher binding energy side, with the Mn 2p_{3/2} and Mn 2p_{1/2} peaks being at 642.2 and 654eV, respectively. Higher binding energies denote typically a chemical state more oxidized, which seems in line with the presence of tetravalent Mn ions in Mn₅O₈ for the acid treated samples. Noticeably, an additional Mn 2p component apart from the main contributions can be seen in the spectrum. For instance, a distinctive shoulder appears at about 639.8 eV. It has been suggested [14] that this new contribution might correspond to the divalent Mn ions in Mn₅O₈ since Mn²⁺ ions have usually lower binding energies than Mn³⁺ and Mn⁴⁺. Further identification of the Mn oxidation state is difficult to achieve using only Mn 2p, since the binding energies are very close each other.

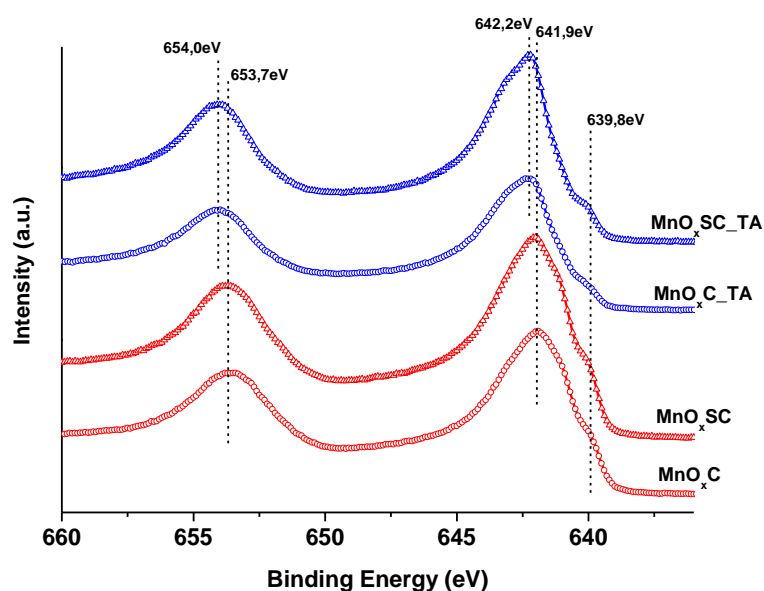


Figure 4.10. Mn 2p XPS spectrum of the samples calcined and acid treated.

The multiplet splitting of Mn (3s) peaks is useful for determining oxidation state of Mn. This splitting occurs when the 3s electron is photoejected from a paramagnetic atom, the remaining 3s electron couples with the valence 3d electron giving rise to parallel or antiparallel spin configuration. Therefore two photoelectron peaks appear. Such an exchange between electrons in the 3s-3d level of Mn is described in terms of exchange interaction energy in Eq. 4.3. [20,21]

$$\Delta E = (2S + 1) K[3s, 3d] \quad (\text{Eq. 4.3})$$

where S is the local spin of the 3d electrons in the ground state and $K[3s, 3d]$ is the exchange coupling between 3s hole and 3d electrons. Consequently, the lower valence of Mn gives rise to wider splitting of the 3s peaks. The expected splitting of the 3s level is about 6.5 for Mn^{2+} , 5.5 for Mn^{3+} , and 4.5 for Mn^{4+} [22].

Gao *et al.*[14] have obtained, by analysing the reported literature data, a linear relationship between the magnitude of the splitting energy of Mn 3s photoelectron peaks and the Mn oxidation states Eq. 4.4.

$$\Delta E \approx 7.88 - 0.85n \quad (\text{Eq. 4.4})$$

where ΔE is the Mn 3s multiplet splitting energies and n ($2 \leq n \leq 4$) is the average oxidation states (AOS) of the Mn atoms. Figure 4.11 shows the Mn 3s XPS spectra for the calcined and the acid treated samples prepared with and without surfactant. Table 4.4 summarizes the XPS data for the Mn 3s spectral region for all samples and compares them to some references taken from the literature in order to support the assignment of the main structure in the samples.

As reported in Figure 4.11 and Table 4.4, the Mn 3s splitting energy for the calcined samples (MnO_xC and MnO_xSC) is about 5.4 eV, suggesting that the use of surfactant does not affect the manganese species at the surface. The calculated average oxidation state of surface Mn atoms for these samples is about 2.9. This value corresponds to the AOS observed for Mn_3O_4 reference $n = 3.0$ (Table 4.4). This result is in agreement with Mn_3O_4 phase identified by XRD and Raman analyses for the calcined samples.

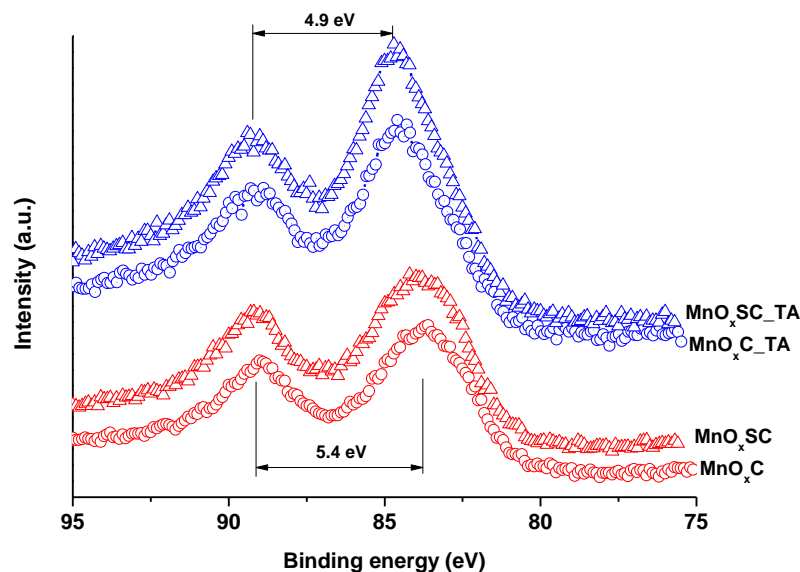


Figure 4.11. Mn 3s XPS spectrum of calcined and acid treated samples. Prepared with and without surfactant.

Table 4.4. Mn 3s Surface characterization results from XPS analysis.

Sample	Mn 3s			Mn oxidation State ^c
	Eb(1)/eV ^a	Eb(2)/eV ^a	ΔE /eV ^b	
MnO _x C	89.0	83.5	5.5	2.8 (2.8) ^d
MnO _x SC	89.2	83.8	5.4	2.9 (3.0)
MnO _x C_TA	89.2	84.3	4.9	3.5 (3.2)
MnO _x SC_TA	89.4	84.4	4.9	3.5 (3.4)
From literature ^d				
MnO	88.6	82.8	5.8	2.4
Mn ₃ O ₄	88.3	83.0	5.3	3.0
Mn ₂ O ₃	88.8	83.6	5.2	3.2
Mn ₅ O ₈	-	-	4.8	3.6
MnO ₂	89.4	84.7	4.7	3.7

^a Position of Mn 3s split peak at (1) higher and (2) lower binding energy

^b Splitting width of Mn 3s: Eb(1)-Eb(2)

^c Calculated from $\Delta E \approx 7.88 - 0.85n$

^d Calculated from H₂-TPR

After acidic treatment, differences were observed in the Mn 3s splitting energy. For both samples, the ΔE value was 4.9 eV. The calculated AOS of surface Mn atoms in these samples is about 3.5, corresponding to the expected value found in the literature for Mn₅O₈ (Table 4.4). However, according to the compositional formula of Mn₅O₈ (Mn₂²⁺Mn₃⁴⁺O₈), the expected AOS value is 3.2, which is lower than the value found in Table 4.4 and the literature.

This is probably due to a preferential exposure of Mn^{4+} on the surface. The XPS results are in agreement with the results obtained by H_2 -TPR (Table 4.4), validating the effect of the acid treatment in the structure and oxidation state of manganese oxide.

The XPS spectra of the core levels of O(1s) was analysed to obtain information related to the oxygen nature. According to the peak position, three types of oxygen species can be identified: the low binding energy peak ($\text{O}_I = 529.8\text{-}530.1\text{eV}$), which is ascribed to lattice oxygen (O^{2-}), the medium binding energy peak ($\text{O}_{II} = 531.0\text{-}531.7\text{eV}$), assigned to surface adsorbed oxygen (O_2^- or O^-), hydroxyl group (OH), oxygen vacancies and defect oxide, and, finally, the high binding energy peak ($\text{O}_{III} = 533.0\text{eV}$), associated with adsorbed molecular water and carbonate species. The relative surface oxygen composition plays a key role in the catalytic activity of oxidation catalysis. For instance, O_{II} species present higher mobility than lattice oxygen. Moreover, some authors correlate the higher activity of a particular catalyst with the amount of $^-$ OH groups and oxygen vacancies [18].

Figure 4.12 reports the O (1s) photoelectron peaks of the samples calcined and acid treated, prepared with and without surfactant. For all samples, the O (1s) spectrum has its maximum near 530 eV and a shoulder with a pronounced tail on the high energy side of the peaks. The separations, relative intensities and widths of the O (1s) peaks as deconvoluted by Gaussian fits are listed in Table 4.5. For the samples prepared using surfactant MnO_xSC and $\text{MnO}_x\text{SC_TA}$, three spectral contributions at around 530, 531 and 533 eV are present. These deconvoluted peaks were assigned to O^{2-} , OH^- and H_2O or CO_3^{2-} species, respectively. The sample MnO_xC reported similarly three overlapping O (1s) peaks in the XPS spectrum. However, for the sample MnO_xC_TA , in addition to the three peaks, a new contribution of oxygen species, present at 532.4 eV, was detected. This contribution could be related to the presence of sulphate ion on the surface, moreover the detection of sulphur S $2p_{3/2} = 168.5$ eV (Figure 4.12 inset) confirms this explanation. This signal was also detected for $\text{MnO}_x\text{SC_TA}$ sample with lower intensity (Figure 4.12 inset). Incomplete washing procedure after the acidic treatment could explain this discrepancy between these samples.

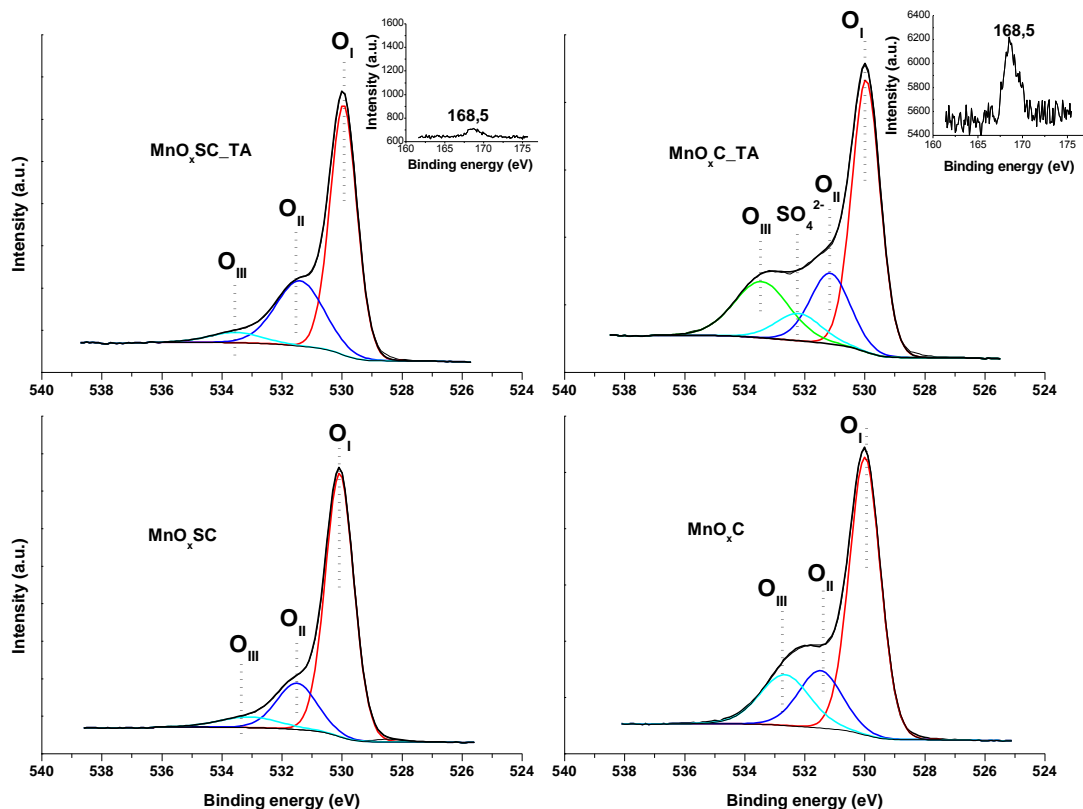


Figure 4.12. O 1s XPS spectrum of the calcined and acid treated samples. Prepared with and without surfactant.

Table 4.5 shows the binding energy, full width at half maximum (FWHM) values and percentage in surface of the different oxygen species. It can be seen for all the samples, that the oxide O^{2-} contribution is much higher than hydroxide OH^- peak. Remarkably, for the calcined sample, the abundance of lattice oxygen is higher when surfactant was used, being 74% and 63% MnO_xSC and MnO_xC , respectively. On the other hand, the contribution of O_{II} species ranges around 18% for both samples. Finally, for the high binding energy peak, higher contribution was detected for the sample prepared without surfactant, 18% and 6.3% for MnO_xC and MnO_xSC , respectively. The carbon contribution related to carbonate species was similar for both samples, indicating that this contribution is related to adsorbed molecular water. This result suggests that the MnO_xC sample presents higher water adsorption capacity (hydrophilic character) compared to the MnO_xSC sample. The O_{II}/O_I ratio was slightly higher for MnO_xC sample (Table 4.5), suggesting an increase of hydroxyl group (OH), oxygen vacancies and defect oxide, which is in accordance to a higher SSA obtained for this sample.

Table 4.5. O 1s Surface characterization results from XPS analysis.

Sample	O Species	Binding energy (eV)	FWHM (eV)	Percentage (%)	O _{II} /O _I
MnO _x C	O _I	529.9	1.2	63.3	0.29
	O _{II}	531.5	1.7	18.2	
	O _{III}	532.6	1.9	18.4	
MnO _x SC	O _I	530.0	1.1	74.5	0.25
	O _{II}	531.5	1.6	18.4	
	O _{III}	533.0	2.3	6.3	
MnO _x C_TA	O _I	529.9	1.1	52.0	0.36
	O _{II}	531.2	1.6	18.9	
	SO ₄ ²⁻	532.3	1.8	8.3	
	O _{III}	533.5	2.1	20.6	
MnO _x SC_TA	O _I	529.9	1.0	64.8	0.46
	O _{II}	531.4	1.8	30.1	
	O _{III}	533.5	2.0	5.1	

After acidic treatment, the contribution of lattice oxygen is still the highest. However, it can be observed a decrease of this contribution for both samples, when compared to the calcined ones (Table 4.5). Noticeably, for these samples the O_{II}/O_I ratio increases. Indicating that after acidic treatment more surface adsorbed oxygen species (O₂⁻ or O⁻), or hydroxyl group (OH), or oxygen vacancies and defect oxide have been created. This result is in accordance with the increase of SSA for these samples after the acidic treatment. It can also be observed that for MnO_xC_TA sample, higher contribution was detected for the high binding energy peak, associated with adsorbed molecular water. This result suggests that the adsorption capacity (hydrophilic character) of MnO_xC_TA sample is higher compared to MnO_xSC_TA. This is in accordance with higher SSA obtained for MnO_xC_TA sample.

4.1.3.2 Catalytic activity test

Figure 4.13a shows the variation in the concentration of HCOH and CO₂ during the catalytic test for the synthesized materials without surfactant calcined and acid treated. No CO was detected during the HCOH oxidation, indicating the suitable selectivity of the catalysts to produce only CO₂ and H₂O. At the beginning of the catalytic test, formaldehyde concentration ([HCOH]) was around 500ppm. It can be observed that [HCOH] increases from room temperature until 50°C, reaching the maximum value at around 750ppm and 1600ppm for the calcined and acid treated sample, respectively. The evolution of formaldehyde at low temperature could be explained by the presence of HCOH multilayer formation caused for surface coverage on the catalyst surface during the stabilization step. The higher HCOH

desorption for the acid treated sample is related to the increase in the specific surface area for this sample, and then to the increase of HCOH adsorption capacity at room temperature.

The formaldehyde concentration reaches the maximum value at 50°C. After this point, the concentration decreases progressively reaching the minimum value (0 ppm) at around 150 and 200°C for MnO_xC_TA and MnO_xC, respectively. Regarding the variation of carbon dioxide concentration [CO₂] as a function of the temperature, it can be observed that at the beginning of the reaction it was 0 ppm for both samples. As the temperature was increased, the CO₂ concentration gradually increases at low temperature and then reaches the maximum concentration at HCOH complete conversion at 190°C (2500 ppm) and 160°C (3500 ppm) for calcined and acid treated samples, respectively. The decomposition of formaldehyde has already been studied by many authors and the formation of surface formate intermediates was suggested. The oxidation of the formates species by the lattice oxygen produce CO₂ that is then desorbed as oxidation products. It seems that at lower temperature, some formaldehyde is already converted into formates species on the catalyst surface. These formates species are then desorbed as CO₂ when temperature is increased. This phenomenon could explain the significant increase in CO₂ concentration during the reaction for both samples. After this point, the concentration decreases until the stationary state [CO₂] = 500 ppm is reached, in agreement with the mass balance from equation 4, in which the stoichiometric relation between HCOH/CO₂ = 1.

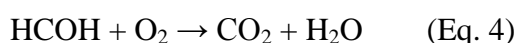


Figure 4.13b shows the variation in the concentration of HCOH and CO₂ during the catalytic test for the synthesized materials using surfactant. It can be observed that the variation in the [HCOH] and [CO₂] presents the same behaviour when compared to the sample prepared without surfactant. However, the different phenomena took place at lower temperature, suggesting that the use of surfactant during the preparation allowed to obtain MnO_x solids with higher catalytic activity.

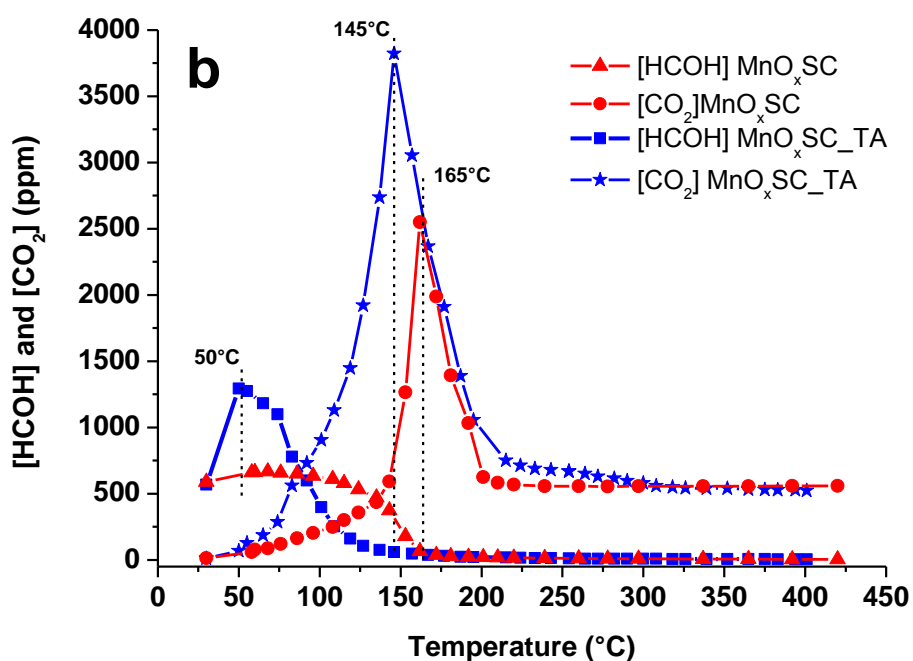
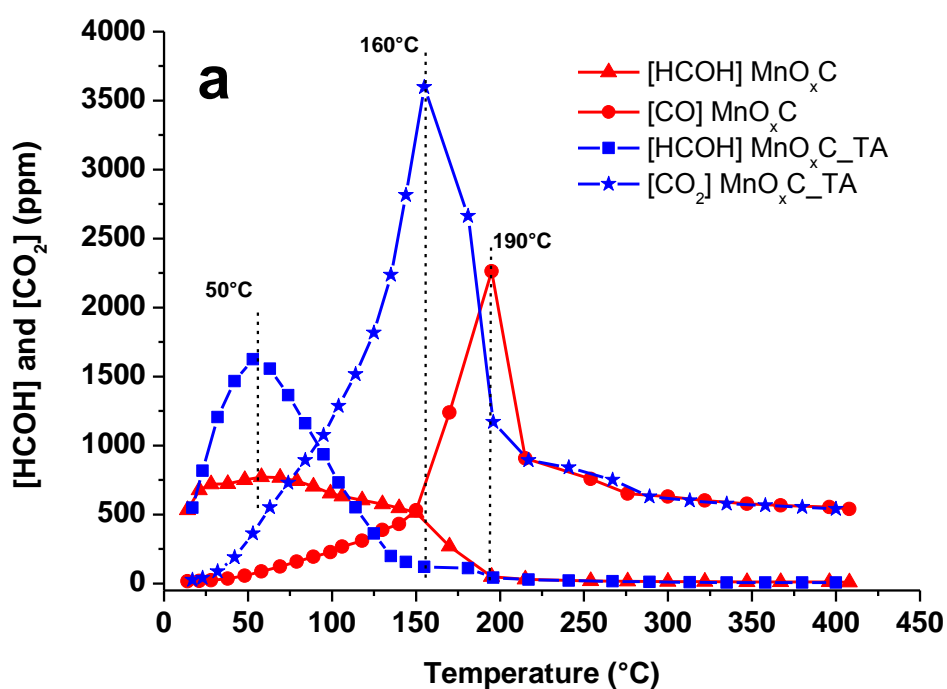


Figure 4.13. Variation of HCOH and CO₂ concentrations with the reaction temperature over the calcined and acid treated MnO_x catalysts a) synthesized without surfactant and b) synthesized with surfactant.

For a better comparison, Figure 4.14 shows the catalytic activities of the catalysts calcined and acid treated in terms of HCOH conversion into CO₂ as a function of temperature.

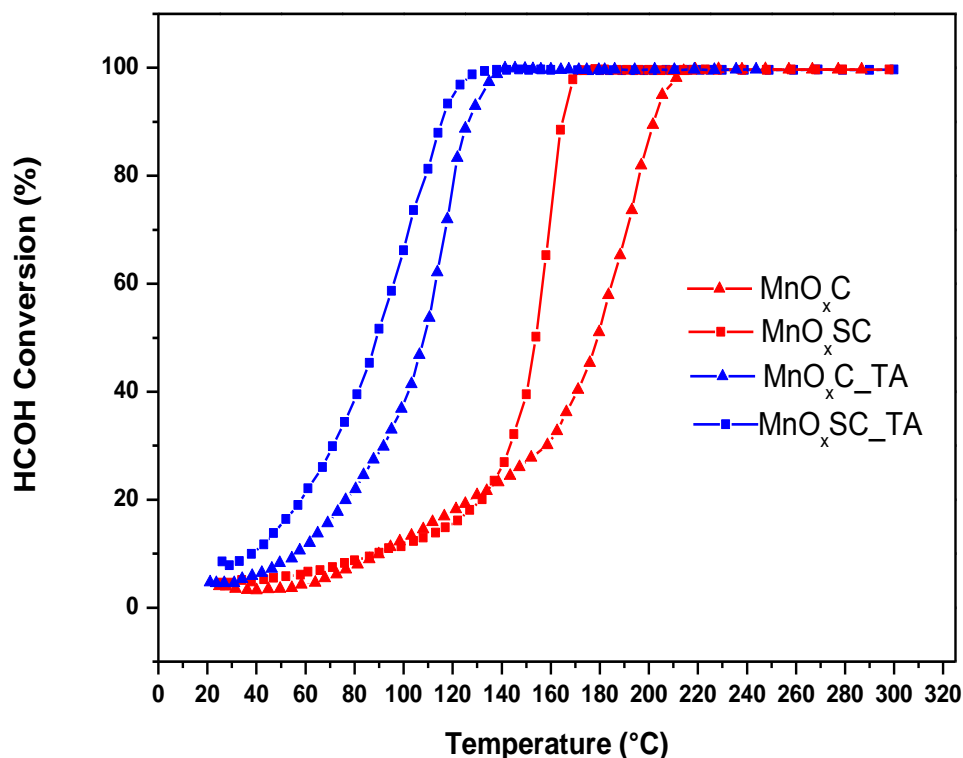


Figure 4.14. Comparison of HCOH conversion as a function of the temperature between the samples prepared with and without surfactant, calcined and acid treated.

Considering the T_{50} as a measure of the catalytic activity of the samples, the activity order can be established as $MnO_xSC_TA > MnO_xC_TA > MnO_xSC > MnO_xC$ (Table 4.6).

Table 4.6. Catalytic performance of the materials calcined, acid treated and principal characterization features

Sample	$T_{50\%}$ (°C)	$T_{100\%}$ (°C)	SSA (m ² /g)	AOS XPS	LTR ConsumedH ₂ /mmol/g	O _{II} /O _I
MnO _x C	180	170	31	2.8	1.3	0.29
MnO _x SC	150	210	20	2.9	1.5	0.25
MnO _x C_TA	110	150	121	3.2	3.9	0.36
MnO _x SC_TA	90	140	90	3.4	4.4	0.46

Regarding the calcined and acid treated samples, it can be observed that after acidic treatment a remarkable improvement in the catalytic activity occurs. This enhancement in the catalytic behaviour for samples treated with sulphuric acid could be explained by an increase of 75% in the specific surface area and the promotion of redox properties at lower temperatures due to the presence of manganese species in higher oxidation state, as evidence by H₂-TPR and XPS results (Table 4.6). Moreover, the ratio O_{II}/O_I was increased after the acidic treatment, suggesting the presence of more reactive sites by the creation of more defects.

Among calcined samples, the MnO_xSC sample prepared using surfactant presents better catalytic activity than the MnO_xC sample, with T₅₀ values of 150 and 180°C, respectively. This result is in accordance with the TPR results, in which the reduction profile was shifted to lower temperature and the total H₂ consumption was higher for the MnO_xSC sample. For these samples, total conversion is reached at 170°C and 210°C for the samples MnO_xSC and MnO_xC, respectively.

After the acidic treatment, the sample prepared using surfactant presents the best catalytic activity, T₅₀ = 90 and 110°C for the samples MnO_xSC_TA and MnO_xC_TA, respectively; even if higher SSA was found for MnO_xC_TA (Table 4.6). This result could be explained by the enhancement of redox properties at lower temperatures in higher proportion for the MnO_xSC_TA sample, due to the presence of manganese species in higher oxidation state, as was evidenced by H₂-TPR and XPS (Table 4.6). Furthermore, the increase of O_{II}/O_I ratio was also more significant for the MnO_xSC_TA sample. Finally, the presence of sulphate species in higher proportion on the surface of MnO_xC_TA sample, as was demonstrated by XPS analyses, can also affect the catalytic activity. Total formaldehyde conversion was reached at 150°C and 140°C for MnO_xSC_TA and MnO_xC_TA samples, respectively.

As was stated in the previous chapter, the HCOH oxidation is strongly influenced by the surface area and redox properties of the materials. From the results obtained in the present study, the catalytic behaviour observed in the formaldehyde oxidation is correlated to the easiest reduction observed by H₂-TPR and textural properties of the materials. Moreover, these results indicate that the MnO_x catalyst prepared by surfactant assisted synthesis followed by a chemical activation process possesses excellent HCOH oxidation performance.

4.2 Synthesis and characterization of chemically activated mesoporous MnO_x-CeO₂ catalysts

4.2.1 Introduction

As reviewed in Chapter 2, the addition of ceria was found to further enhance the catalytic activity of MnO_x through the formation of solid solution, in which the synergistic interaction between manganese and cerium oxides was explained by an oxygen transfer mechanism [1]. The synthesis and characterization of high surface area ceria in the presence of cationic surfactant were reported by Trovarelli *et al.* [17,23]. These ceria materials show enhanced textural and thermal resistance when compared to those prepared by conventional route, as well as improved oxygen storage and redox behaviour. More recently, Meng *et al.* [24] have synthesized MnO_x-CeO₂ by surfactant assisted precipitation using CTAB as template; the solids obtained showed high specific surface area but no regular TEM images were obtained, indicating that ordered mesoporous structures were not formed in the catalyst. Herein, the study is extended to account for the effect of chemical activation (acidic treatment) in the mixed MnO_x-CeO₂ catalysts with different Mn/Ce ratios prepared by surfactant assisted wet-chemistry route.

4.2.2 Experimental procedure

4.2.2.1 Materials preparation

Binary oxides (*n*)MnO_x-(1-*n*)CeO₂ (*n* = 0, 0.25, 0.5, 0.75 and 1) atomic ratios, were prepared by co-precipitation from aqueous solution of nitrates by sodium hydroxides in the presence of cetyltrimethyl-ammonium bromide as surfactant (CTAB). In a specific synthesis, appropriate quantities of Mn(NO₃)₂.6H₂O and Ce(NO₃)₃.6H₂O were dissolved in 150 ml of H₂O, followed by the addition of a solution of NaOH (4.8 g NaOH in 50 ml of H₂O). The resulting manganese-cerium hydroxide precipitated solution was added to an aqueous solution of cetyltrimethylammonium bromide (67 g in 150 ml of H₂O). The resulting mixture was heated to 75°C and then stirred for 1 h. The final gel obtained in a sealed beaker was transferred to an oven and heated at 75°C for 12 h. The solid residue was filtered, washed with water, dried in air, and finally calcined at 500°C for 6 h (1°C min⁻¹). The calcined samples were treated with an aqueous solution of H₂SO₄ (120 ml - 10 mol l⁻¹) by stirring in a beaker for 1 h. The final product was filtered and the residue was washed with water and

dried at 100°C. In order to evaluate the effect of ceria addition in the MnO_x-CTAB system, the results concerning pure manganese oxides, studied in the first part of this chapter and noted as MnO_xSC and MnO_xSC_TA, will be also presented in this part identified as $n = 1$.

4.2.3 Results and discussions

4.2.3.1 Materials characterization

4.2.3.1.1 Bulk structure and specific surface area

The wide angle powder XRD patterns of the calcined MnO_x-CeO₂ catalysts are presented in Figure 4.15.

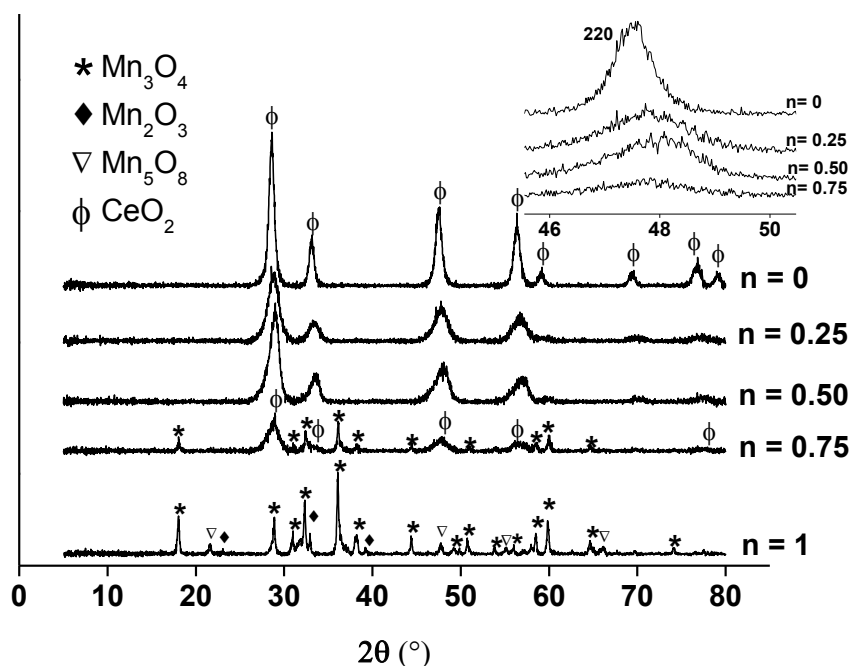


Figure 4.15. Powder X-Ray diffraction patterns of calcined $(n)\text{MnO}_x-(1-n)\text{CeO}_2$ samples.

Inset: expanded view of (220) diffraction peak of CeO₂.

For calcined samples with low Mn content (n values from 0 to 0.5), the main peaks in the patterns were those of a fluorite structure similar to that of pure ceria (JCPDS 34394). However, the diffraction lines were broader for samples with $n = 0.25$ and $n = 0.50$. No peak of manganese oxide phase was found, probably due to the formation of Mn-Ce solid solution or the existence of amorphous manganese oxide. Figure 4.15 inset shows the incremental shift to higher angles of the fluorite phase (220) diffraction peak related to the formation of solid

solution $\text{MnO}_x\text{-CeO}_2$. The incremental shift of each diffraction line to higher angles is associated with the smallest ionic radius of manganese ions (Mn^{4+} 0.054 nm, Mn^{3+} 0.066 nm, Mn^{2+} 0.080 nm) in comparison to that of Ce^{4+} (0.094 nm)[25]. Considering the 2θ maximal value of the (220) diffraction peak (Figure 4.15 inset), it seems that the solubility limit of manganese ions into the ceria structure is reached for $n = 0.5$. The diffraction profiles of samples with high Mn content ($n = 0.75$) showed the crystallization of Mn_3O_4 hausmannite together with fluorite structure. For $n = 1$, Mn_3O_4 , as well as Mn_2O_3 and Mn_5O_8 phases were detected.

After acidic treatment (Figure 4.16), differences were found only for samples with high Mn content ($n \geq 0.75$): peaks due to the hausmannite phase disappeared and only peaks due to the monoclinic phase Mn_5O_8 were observed. Noticeably, for $n = 0.75$ sample the peaks ascribed to the Mn_5O_8 phase were present with lower intensity. Figure 4.21 inset shows that the incremental shift of the (220) peak towards higher angles took place in a minor extension in comparison with the untreated samples. It seems that the strong acidic conditions could affect the formation of the solid solution.

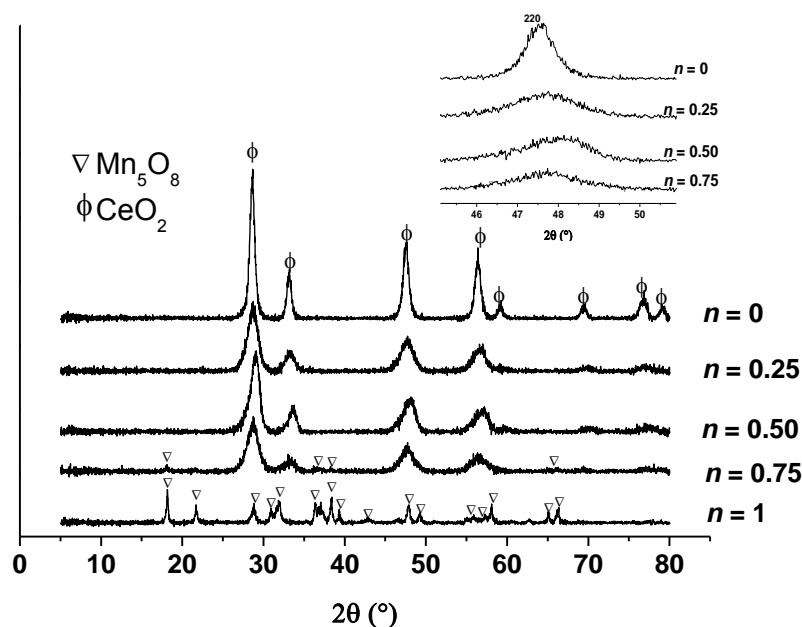


Figure 4.16. Powder X-Ray diffraction patterns of acid treated $(n)\text{MnO}_x\text{-(1-n)}\text{CeO}_2$ samples.
Inset: expanded view of (220) diffraction peak of CeO_2 .

Table 4.7 shows the crystallites size of the samples estimated from the Scherrer equation applied to the two diffraction peaks (111) and (220) of CeO₂ for the Ce containing samples and to the diffraction peak of Mn₅O₈ ($2\theta = 22^\circ$) for the free Ce samples. For the calcined samples the crystallite size was found to be 10 nm for pure ceria, between 4 nm - 6 nm for the mixed oxides, and around 30 nm for pure manganese oxide. After acidic treatment, the crystallites sizes remained unchanged.

Table 4.7. BET surface area, BJH desorption average pore diameter and size of the materials.

Sample	Crystallite size (nm)		BET surface area (m ² /g)		Pore Size diameter at maximum value (nm)	
	Calcined	Acid treated	Calcined	Acid treated	Calcined	Acid treated
1	31.0	29.0	20	82	30	5
0.75	5.2	4.5	91	160	30	3
0.5	5.3	5.1	100	112	30	30
0.25	4.8	4.8	130	137	15	15
0	10	10	73	75	15	15

The textural properties of the samples are also listed in Table 4.7. The SSA of the single oxides MnO_x and CeO₂ (20 and 73 m²/g, respectively) were lower than those of the binary oxides. Among mixed oxides calcined samples, the largest SSA was found for the sample $n = 0.25$ with 130 m²/g, while the $n = 0.75$ sample presented the lowest SSA (91 m²/g) and $n = 0.5$ an intermediate SSA value (100 m²/g). These results suggest that cerium addition to pure manganese oxide increases the SSA. The interaction between Ce and Mn oxides may produce more opened and distorted structures when the two oxides are mixed, considering the difference of the ionic ratio of each component, resulting in a higher SSA for the binary oxides. These results are in agreement with the XRD results for the calcined mixed oxides, in which broader peaks and, as a consequence, smaller crystallite sizes were observed. The acidic treatment had important effects on the SSA of rich manganese samples (Table 4.7). This result was discussed in the first part of this chapter for the $n = 1$ sample, in which a 75% increase in SSA was obtained. For $n = 0.75$, a significant increase in SSA was also observed (70%). This result supports the consideration stated before, in which the dissolution of amorphous manganese species located between the particles promotes the SSA. This effect was strongly attenuated with the increase in cerium concentration in the sample. Actually, for $n = 0.5$ and $n = 0.25$, almost the same SSA was obtained after the acidic treatment,

corresponding to 112 and 137 m²/g, respectively. This result can be explained by the low solubility of ceria in acid [26].

Figure 4.17 shows the BJH pore size distribution of the $(n)\text{MnO}_x-(1-n)\text{CeO}_2$ samples calcined and acid treated. Table 4.7 presents the pore size at maximum value of the different oxides before and after acidic treatment.

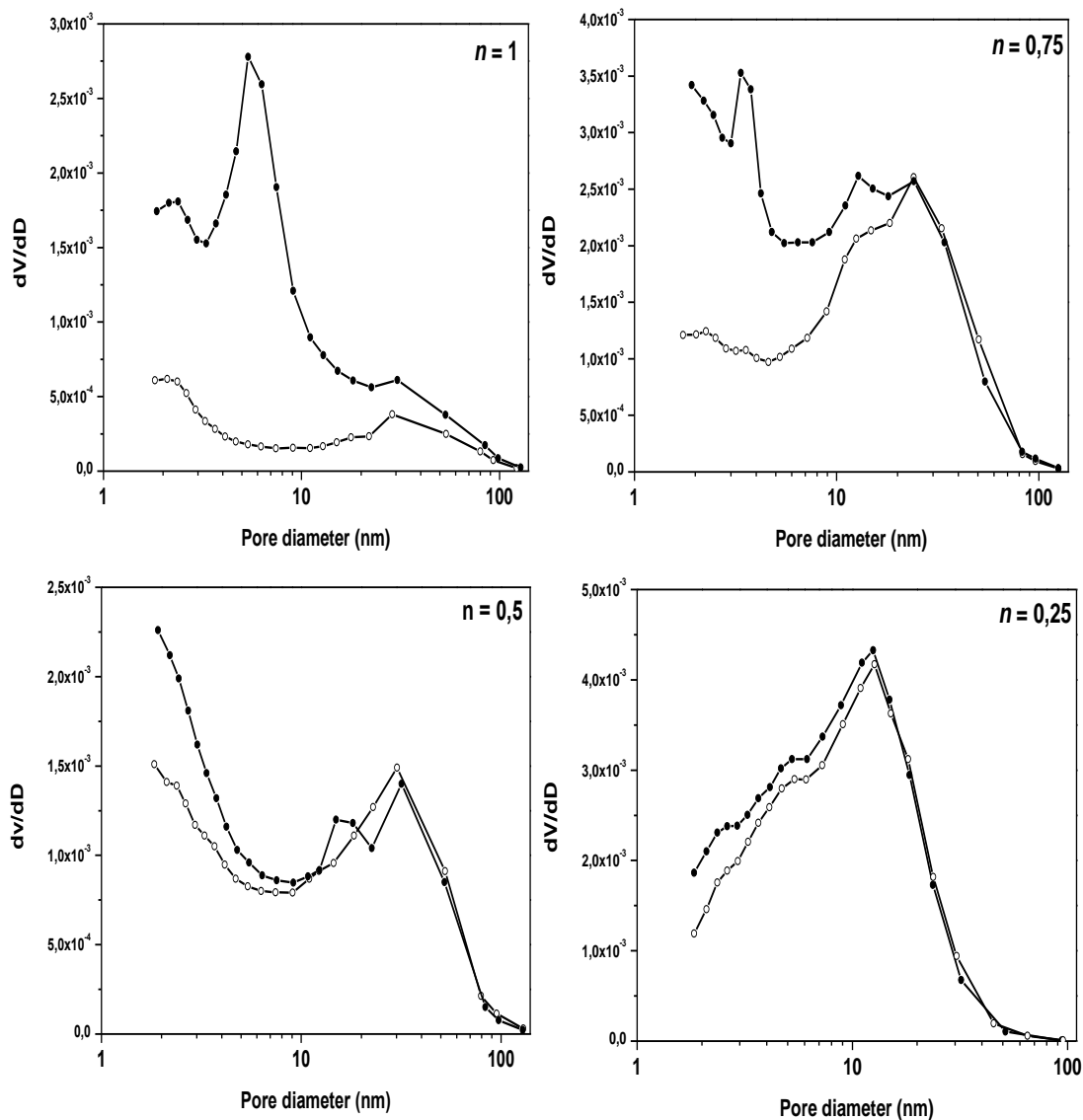


Figure 4.17. BJH pore size distribution obtained on the $(n)\text{MnO}_x-(1-n)\text{CeO}_2$ samples: a) calcined (open symbols) and b) acid treated (full symbols).

For the calcined samples, the pore size distribution was broader and centered at a maximum pore diameter value of 30 nm for samples $n = 1$, $n = 0.75$ and $n = 0.5$. For samples with high cerium content ($n = 0.25$ and $n = 0$) the maximum pore diameter was 15 nm. After

acidic treatment the development of porous distribution at lower values was observed for the sample with high manganese content. For the sample $n = 0.75$, the formation of a narrow mesoporous distribution was also observed and centered at around 3.5 nm. However, in this case, the formation took place in a minor proportion, when compared to $n = 1$. Finally, for $n \leq 0.5$, no significant effect of the H_2SO_4 treatment was observed and similar pore size distributions before and after the acidic treatment were perceived. These results suggest that the addition of ceria in the system attenuated the effect of the acid treatment to unveil the porous present in the particles. As it was mentioned previously, this could be explained by the low solubility of ceria in acid.

4.2.3.1.2 Redox properties

Figure 4.18 shows the H_2 -TPR profile of the calcined $\text{MnO}_x\text{-CeO}_2$ solids. The H_2 -TPR profile of pure ceria reveals small peaks between 200°C and 400°C and a wide peak centred at 640°C , which could be assigned to the reduction of easily reducible surface cerium and the partial reduction of the innermost layer of CeO_2 to Ce_2O_3 , respectively [27].

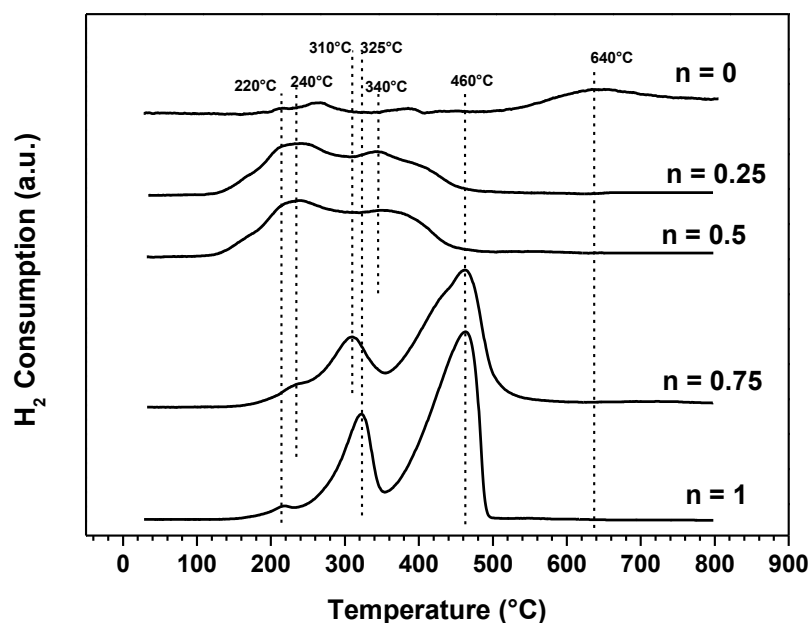


Figure 4.18. H_2 -TPR profiles of calcined $(n)\text{MnO}_x\text{-(1-n)}\text{CeO}_2$ samples.

For the $n = 0.25$ and $n = 0.5$ samples, the reduction peaks took place over a rather broad temperature range ($100\text{-}500^\circ\text{C}$) with overlapping peaks characterized by two apparent

maxima at 240°C and 340°C, respectively. Several authors have reported this similar reduction behaviour in $\text{MnO}_x\text{-CeO}_2$ [28,29,30]. Generally, it was suggested in these works that these reduction profile could be assigned to the combined reduction of MnO_x into MnO and CeO_2 into Ce_2O_3 . Noticeably, for the $n = 0.25$ and $n = 0.5$ samples, the reduction process is shifted to lower temperatures region. It seems that the reduction of the manganese and cerium oxides results from their mutual interaction, probably through the formation of solid solution in which the mobility of oxygen species was greatly enhanced. This result is in agreement with that obtained by XRD, where the formation of solid solution was observed for these samples.

The reduction profiles of samples with high Mn content ($n \geq 0.75$) showed the same profile. For $n = 0.75$, two strong reduction peaks with maximum at 310°C and 460°C were observed, corresponding to the two-step reduction process described previously. Noticeably, for this sample, the first reduction peak is shifted to lower temperature; this is probably due to the formation of Mn-Ce-O species reduced at lower temperature, as described earlier. The weak shoulder observed at 240°C presents a maximum value similar to that found for the first reduction peak of combined reduction Mn-Ce-O solid solution in samples $n = 0.5$ and $n = 0.25$. This means that probably for this sample one part of manganese forms solid solution and the other crystallizes as MnO_x .

The redox properties of the acid treated samples were also studied (Figure 4.19). For the samples with $n \leq 0.5$, the reduction profile reveals two remarkable features: (i) the decrease of the reduction peak related to the reduction of manganese oxide species and Mn-Ce-O solid solution, and (ii) the development of a broad peak at 520°C, probably due to the partial reduction of CeO_2 to Ce_2O_3 . It seems that the acidic condition breaks the solid solution to produce separately amorphous MnO_x and CeO_2 for these samples.

For $n = 0.75$, the reduction profile is different from that observed on the non-acid treated sample, showing a three-step reduction process with maxima at 320, 450 and 520°C, respectively. It seems that the acidic condition breaks the solid solution, presenting lower reducibility. Thus, the peaks at 320°C and 450°C could be attributed to the reduction of high-oxidation state manganese species and to further reduction of Mn_3O_4 into MnO , respectively. The peak at higher temperature is due to the partial reduction of CeO_2 to Ce_2O_3 . For the sample with $n = 1$, the TPR profile was discussed in the first part of the chapter.

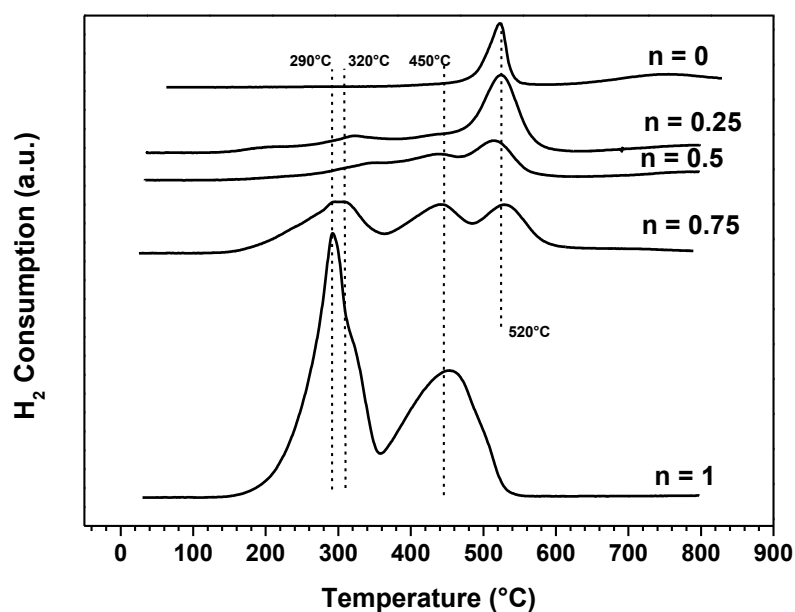


Figure 4.19. H₂-TPR profiles of acid treated (*n*)MnO_x-(1-*n*)CeO₂ samples.

Table 4.8 presents the H₂ consumption values obtained from the H₂-TPR profiles. For the calcined and acid treated samples, the H₂ consumption decreased when the Mn content in the samples was reduced. This means that the contribution of manganese species towards H₂ consumption is more important. For the acid treated samples, the H₂ consumption was the most important, with *n*= 1 and *n* = 0.75 samples having the main increase. This is probably due to the presence of manganese species in higher oxidation states in these samples.

Table 4.8. Quantitative results from H₂-TPR for the (*n*)MnO_x-(1-*n*)CeO₂ samples.

Sample	Consumed H ₂ (mmol/g)	
	Calcined	Acid treated
1	6.2	8.6
0,75	3.4	3.9
0,5	2.4	2.8
0,25	2.1	2.0
0	0.5	0.9

4.2.3.1.3 XPS

analyses

XPS measurements were carried out to evaluate the effects of the ceria loading on the surface composition and dispersion for the (*n*)MnO_x-(1-*n*)CeO₂ samples, calcined and acid treated.

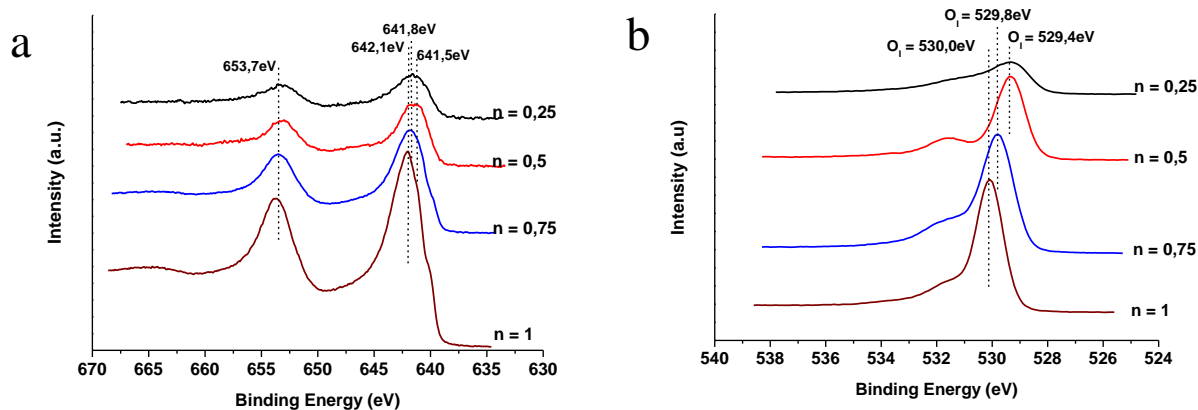


Figure 4.20. X-Ray photoelectron spectra of the calcined $(n)\text{MnO}_x-(1-n)\text{CeO}_2$ samples a) Mn(2p) and b) O(1s).

Figure 4.20 shows the Mn 2p and O 1s XPS spectra of the calcined samples. It can be seen that the Mn $2p_{3/2}$ peak shifted to lower binding energy with the increase of ceria content in the $\text{MnO}_x\text{-CeO}_2$ mixed oxides catalyst, varying from 642.1 eV to 641.6 eV for $n = 1$ to $n = 0.25$ (Figure 4.20a). It seems that the Ce addition prevents the formation of Mn species with higher oxidation state. This could be explained by a preferential substitution of manganese species in the fluorite structure. Machida *et al.* [25] stated that the substitution of Ce^{4+} by Mn^{3+} is suitable. The O 1s XPS spectra of the calcined samples (Figure 4.20b) confirmed the interaction between Mn and Ce. It can be observed that the position of the lattice oxygen (O_1) shifted towards lower binding energy with the increase of ceria content, changing from 530 eV to 529.4 eV for $n=1$ and $n= 0.25$, respectively. Comparing with the binding energies of two single oxides (530 eV for MnO_x and 528.5 eV for CeO_2), the intermediate binding energy obtained suggests the formation of the solid solution between CeO_2 and MnO_x . These results are in agreement with those obtained by XRD and H_2 -TPR, in which the formation of the solids solution was proposed for these samples.

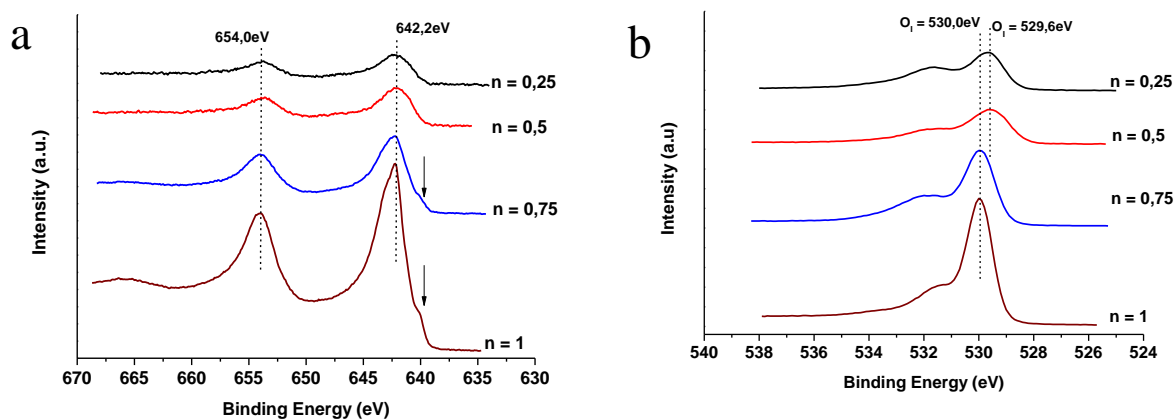


Figure 4.21. X-Ray photoelectron spectra of $(n)\text{MnO}_x-(1-n)\text{CeO}_2$ samples acid treated a) Mn(2p) and b) O(1s).

Figure 4.21 presents the Mn 2p and O 1s XPS spectra for the samples after acidic treatment. As can be seen in figure 4.21a, no significant change was found for different oxide compositions in the position of the Mn 2p_{3/2} signal, indicating probably less or no Mn-Ce interaction. Noticeably, for $n = 0.75$ sample the additional Mn 2p component, identified previously for $n = 1$ sample, was observed at about 639.8 eV. It has been suggested that this contribution might correspond to the divalent Mn ions in Mn₅O₈. This result suggests the presence of Mn₅O₈ in this sample, as was previously observed by XRD. The O 1s spectra (Figure 4.21b) revealed a shift towards lower binding energies for the samples with high cerium content ($n = 0.5$ and $n = 0.25$), it can also be observed an important broadening of the O1s peak, for these samples. This result suggests that probably after acidic treatment, rupture of the solid solution causes the overlapping of the two different O components from MnO_x and CeO₂ 530 eV and 528.5 eV, respectively: large peak instead of a relatively narrow peak in the case of solid solution is then observed. These results support the rupture of the solids solution after acidic treatment for these samples, as have been confirmed previously by XRD and H₂-TPR analyses.

The variation of manganese average oxidation state (AOS) as a function of cerium content in the samples was evaluated by the multiplet splitting of Mn (3s) peaks (Figure 4.22). It can be seen that for calcined samples the average oxidation state of manganese species remained almost constant with the increase of cerium content in the sample, varying from 2.9 for $n = 1$ and 0.75 to 2.8 for $n = 0.5$ and 0.25, respectively. This slight variation is in

accordance with the trend observed with Mn 2p_{3/2}, in which Ce addition prevents the formation of Mn species with higher oxidation state. After the acidic treatment the oxidation state was only modified for samples with higher Mn content, changing from 3.4 for n= 1 to 3.2 for n = 0.75 sample, respectively. This result suggests that acidic treatment only modifies the oxidation states of pure manganese oxides species; the addition of cerium to the system causes the formation of solid solutions and dispersion of manganese species in the lattice. This interaction avoids the oxidation of manganese species once that the acidic treatment was carried out.

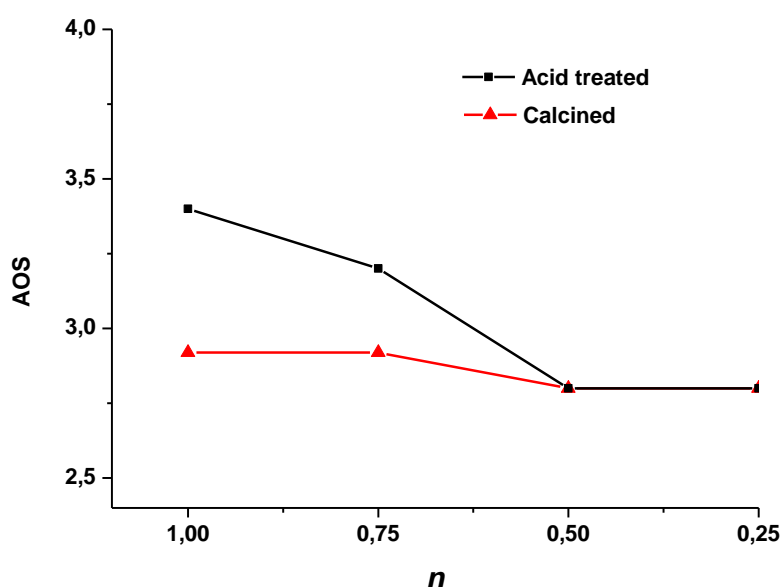


Figure 4.22. Variation of manganese average oxidation state as a function of cerium addition in the samples.

The surface atomic percentages are listed in Table 4.9. It can be observed that for calcined samples the oxygen concentration remained unchanged at around 65%. Additionally, it is expected that the Mn content increases with the increase of the *n* value, as well as the cerium content decreases with diminution of *n* value. Noticeably, for samples with high Ce content, *n* = 0.5 and 0.25, the percentage of manganese and ceria are similar, 8% and 6% for Mn and, 25 and 26% for Ce, respectively. This result suggests a surface enrichment of ceria for *n* = 0.25. After the acidic treatment the concentration of the different species on surface remained almost unchanged.

Table 4.9. Surface characterization results from XPS analyses

Sample code (<i>n</i>)	Surface atom percentage (%)			Surface atom percentage (%)		
	Calcined			Acid treated		
	O	Mn	Ce	O	Mn	Ce
1	62	38	-	63	37	
0.75	65	21	14	67	19	13
0.5	68	8	25	69	6	25
0.25	67	6	26	72	5	23

4.2.3.2 Catalytic activity tests

Figure 4.24 shows the catalytic activities of the catalysts calcined and acid treated in terms of HCOH conversion (into CO₂) as a function of temperature. It is important to state that for all samples containing manganese ($n \geq 0.25$) H₂O and CO₂ are the only products observed, while for pure ceria the formation of small quantities of by-products have been detected. The light-off curves obtained for the Mn containing calcined samples presented the same evolution. Pure ceria presented a different shape with a plateau at around 165°C in HCHO conversion. It can be also observed that the catalytic activity of the mixed oxides is better than those of single oxides. The catalytic activity order, based on T₅₀ value (Table 4.10), can be established as $n = 0.25 > n = 0.75 > n = 0.50 > n = 1$. Tang *et al.* [31,32] already evidenced the enhancement in the catalytic activity in formaldehyde oxidation for the Mn/Ce mixed oxides compared to pure MnO_x, related to the formation of solid solution between MnO_x and CeO₂, in which the interaction between manganese and cerium oxides improves the oxygen transfer mechanism. This could be explained by considering the effective activation of molecular oxygen in the feed stream over the MnO_x-CeO₂ solid solution. Initially, the released oxygen species (O*) from MnO_x participated in the oxidation of formaldehyde. Then, the oxidation of Mn₂O₃ to MnO₂ would be realized via the oxygen species generated from the oxygen reservoir of CeO₂. Finally, the Ce₂O₃ produced would be reoxidized into CeO₂ by oxygen molecule in the feed stream. This process is schematically presented in Figure 4.23 and has been proposed Tang *et al.* [31]

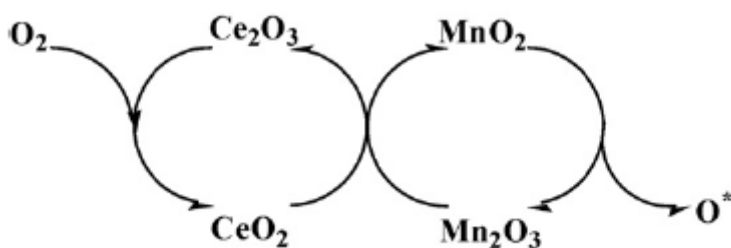


Figure 4.23. Oxygen activation and the oxygen transfer through the redox recycles of $\text{Mn}^{4+}/\text{Mn}^{3+}$ and $\text{Ce}^{4+}/\text{Ce}^{3+}$. [31]

Comparison between the mixed oxides shows that the sample with $n = 0.25$ shows the higher catalytic activity, $T_{50} = 125^\circ\text{C}$. This result is probably correlated to the highest specific surface area value obtained for this sample $130 \text{ m}^2/\text{g}$, which can provide more active sites, better dispersion and interaction between Mn and Ce oxides. Moreover, for this sample the H_2 TPR results indicated a combined reduction at lower temperatures region, and, when compared with samples with higher Mn content, the consumed H_2 values are in the same order. For the samples $n = 0.75$ and $n = 0.5$ the conversion took place at slightly higher temperature $T_{50} = 130$ and 135°C , respectively. Similar specific surface area are obtained for these samples, but higher reducibility was found for the sample with $n = 0.75$, which could explain the higher activity. Total conversion for these samples was reached at 160°C .

Table 4.10. Catalytic performances of the $(n)\text{MnO}_x-(1-n)\text{CeO}_2$ samples calcined and acid treated

Sample code (n)	Calcined		Acid treated	
	T_{50} ($^\circ\text{C}$)	T_{100} ($^\circ\text{C}$)	T_{50} ($^\circ\text{C}$)	T_{100} ($^\circ\text{C}$)
1	155	175	90	130
0.75	130	160	105	160
0.5	135	160	155	180
0.25	125	160	185	220
0	165	250	200	250

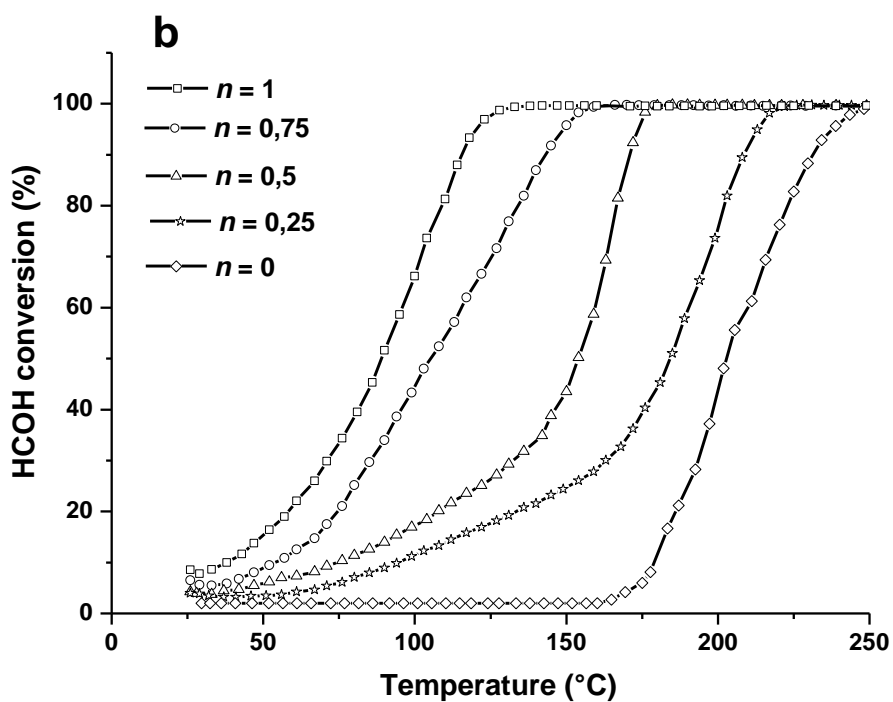
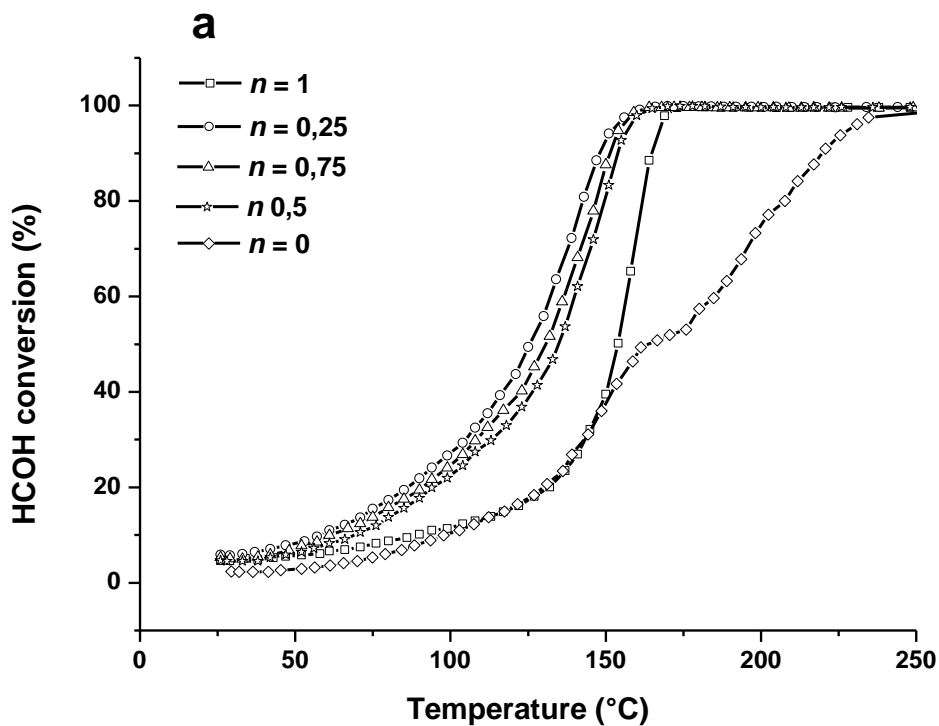


Figure 4.24. HCOH conversion as a function of the temperature for the $(n)\text{MnO}_x-(1-n)\text{CeO}_2$ samples. a) calcined and b) acid treated.

After acidic treatment, the catalytic activity follows the order $n = 1 > n = 0.75 > n = 0.5 > n = 0.25 > n = 0$. This improvement in the catalytic behaviour for pure manganese oxide was already explained in our previous sections of this chapter. For acid treated mixed oxides, the higher catalytic activity of the sample with $n = 0.75$ ($T_{50} = 105^\circ\text{C}$) should result from the following facts. First, compared with the samples with lower manganese content, the sample $n = 0.75$ presents the higher specific surface area, $160\text{m}^2/\text{g}$. Second, the H_2 -TPR results indicate that this sample possess higher reducibility. Third, the XPS results showed the presence of Mn species in higher oxidation states. The lower activity shown for samples with low Mn content $n \leq 0.5$ could be explained by the following remarks. From the H_2 -TPR profiles it seems that after the acidic treatment the solid solution $\text{MnO}_x\text{-CeO}_2$ disappears, having an adverse effect toward the oxygen transfer mechanism. Finally, XPS analyses detected lower concentration of Mn species. It could be the major reason causing the important decrease of activity for HCOH oxidation for these samples.

Regarding the pure ceria ($n = 0$) it can be observed that after acidic treatment the catalytic activity is lower compared to the calcined sample, $T_{50} = 165$ and 200°C calcined and acid treated, respectively. It can be probably due to the formation of cerium hydrogen sulphate on the surface of the catalyst as was reported by Wyruboff [26].

4.2.3.3 Formaldehyde adsorption and surface reaction experiments

In order to study the adsorption and transformation of formaldehyde on the MnO_x based catalyst, complementary experiments were carried out: (1) Temperature programmed desorption HCOH-TPD; (2) *In situ* XPS, and (3) FTIR studies of previous formaldehyde dosed sample. The sample $\text{MnO}_x\text{SC_TA}$, presenting the best catalytic activity towards HCOH oxidation, was selected to perform these studies.

4.1.3.3.1 Formaldehyde Temperature Programmed Desorption

The adsorption and surface reaction of HCOH were performed in the same facilities used for the catalytic test. The solid was first pre-treated with argon at 150°C to remove water and surface impurities. A HCOH adsorption curve was obtained at RT to ensure the saturation of the catalyst surface by using mass spectrometry (Omnistar, GSD 301-Pfeiffer). The catalyst was purged with argon for 2 h to remove physically adsorbed HCOH, and then the temperature was increased from RT to 500°C at a rate of $10^\circ\text{C}/\text{min}$ in a continuous flow of argon. The effluents from the reactor were analyzed by mass spectrometry, indicating HCOH ($m/z = 30$), CO_2 ($m/z = 44$), CO ($m/z = 28$) and H_2O ($m/z = 18$).

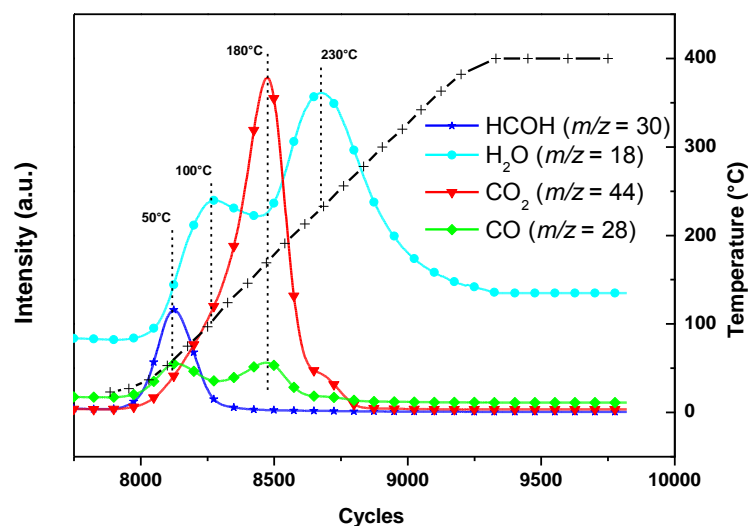


Figure 4.25. Temperature programmed desorption experiment after HCOH adsorption on the MnO_x acid treated surface at room temperature.

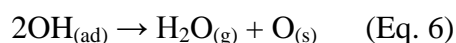
Figure 4.25 shows desorption profiles of different products from the sample $\text{MnO}_x\text{SC_TA}$ after HCOH adsorption. It can be seen the HCOH non dissociative desorption

between 50°C and 100°C, with a maximum value around 75°C. Carbon dioxide desorption also took place in a single broad peak, between 50°C and 200°C, with maximum at 150°C. Carbon monoxide was found to desorb in two stages between 50°C and 170°C: the first one in the temperature range of HCOH desorption, and the second one took place together with CO₂ desorption. Water was also found to desorb from the surface in a two broad peaks with maxima at 100°C and 200°C, even if the material was pre-treated with argon at 150°C to remove water and surface impurities. It means that desorbed water is probably a product of the surface reaction.

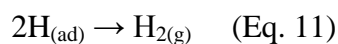
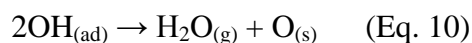
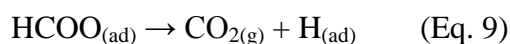
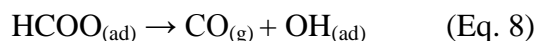
The evolution of formaldehyde at low temperature (50°C) can be expressed by the equilibrium that follows:



The water production can be related to the production of OH species on the surface, as a result of the formation of formate species with the participation of lattice oxygen from the manganese oxide (O_s). Indeed, the formation of formate species is often proposed in the formaldehyde oxidation as intermediate.



The formation of oxidation products like CO or CO₂ and the desorption of water at 200°C during the HCOH TPD could be explained by decomposition of formate species. The oxidation of the formate species by oxygen from MnO_x produces CO and CO₂, which are then desorbed as oxidation products as follows:



From the TPD results, it was shown the participation of oxygen from manganese oxide since oxidation products were observed.

4.1.3.3.2 FTIR studies of the formaldehyde dosed MnOx

In order to identify the surface species formed from adsorption of HCOH over the MnOxSC_TA sample, *in situ* Fourier transform infrared spectroscopy at temperatures between RT and 200°C were carried out. Vannice *et al.*[33] studied the adsorption of formaldehyde on Ag/Al₂O₃ catalyst. The authors proposed the formation of different species on the surface of these catalysts, as shown in Figure 4.26.

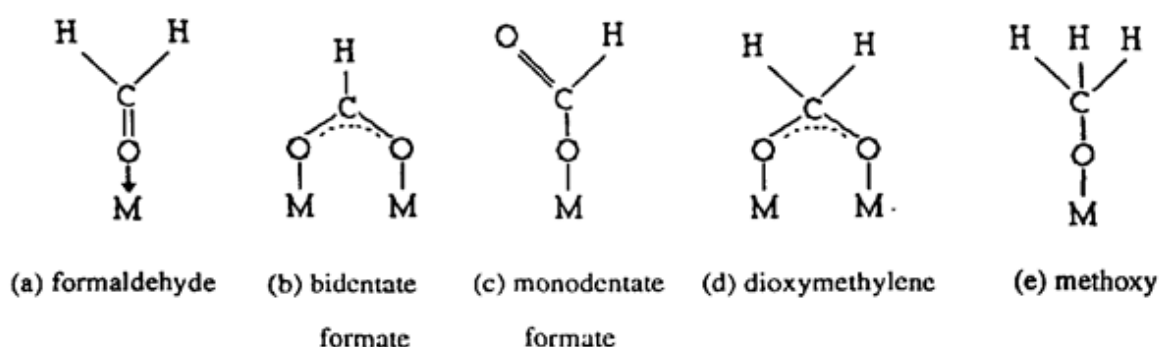


Figure 4.26. Possible surface species formed from the HCOH adsorption [33].

Figure 4.27 shows the IR spectra of adsorbed HCOH on the MnOxSC_TA sample surface at different temperatures, where four intense bands at 2864, 1573 1371 and 1355cm⁻¹ were observed. These bands can be ascribed to formate species adsorbed on the catalyst surface [34]. It can also be detected in Figure 4.27 that the formate species were stable upon heating the sample to 200°C. The formation of dioxymethylene, methoxy species and/or adsorbed formaldehyde was not evidenced under our experimental conditions.

In order to appreciate the evolution of species upon the heating, Figure 4.28 presents the difference of spectra registered at different times. It can be clearly seen from 0 to 25 min the bands corresponding to formate species. Moreover, the principal bands related to $\nu(\text{OCO})$ as are shifted towards lower wave numbers from 1621 cm⁻¹ to 1576 cm⁻¹. It can also be observed that the relative intensity of the bands present between 1300 and 1400 cm⁻¹ also evolved. This result probably indicates that after heating the interaction between the formate species and the material was modified. Formate can be adsorbed in two forms on the surface, i.e. monodentate and bidentate (Figure 4.26). The frequency separation between $\nu(\text{OCO})$ as and

(OCO)s was employed to distinguish these two forms. The frequency separation after 10 min of heating was around 264cm^{-1} , while after 25 min the frequency separation was 220 cm^{-1} . It has been stated that, when the frequency separation is higher than 250 cm^{-1} , the monodentate species prevail over the bidentate formate species [34]. This result suggests that the formate species on the surface of the materials change from monodentate to bidentate species with an increase in the temperature.

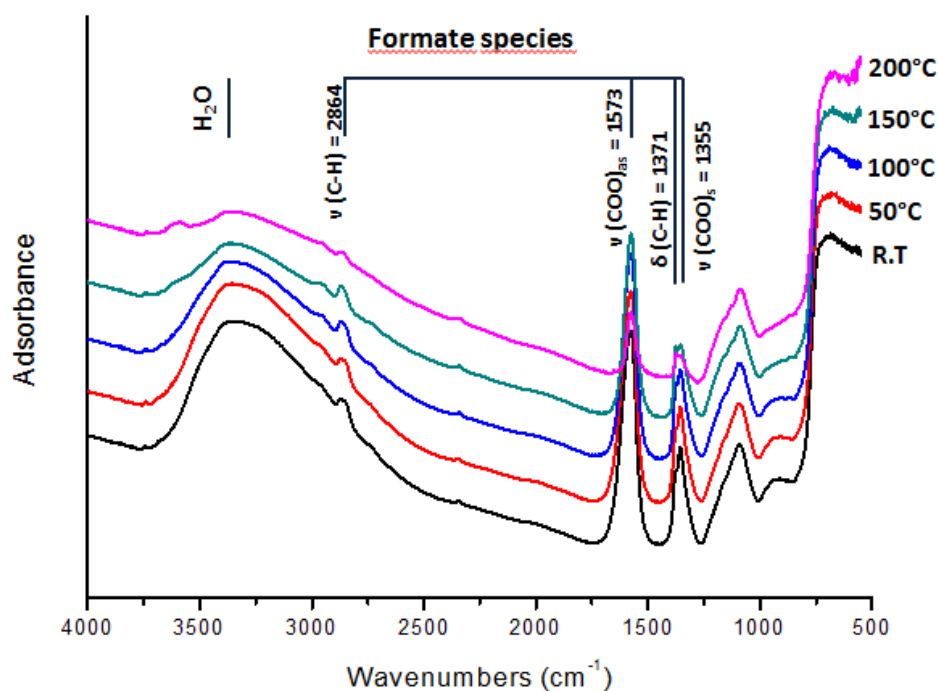


Figure 4.27. IR spectra of adsorbed HCOH on MnO_xSC_TA.

The FTIR results clearly showed the formation of formate species on the surface of the catalyst. Moreover, when the sample was heated, the principal band at 1573 cm^{-1} was slightly shifted towards lower frequency, suggesting the conversion of bidentate species in monodentate.

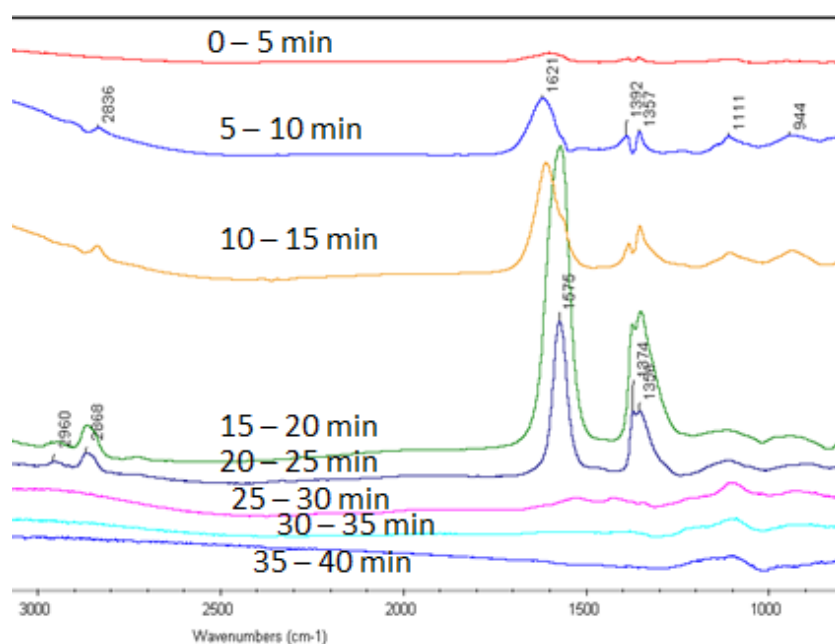


Figure 4.28. Evolution of species after the heating.

4.1.3.3.2 XPS studies of the formaldehyde dosed MnOx

X-ray photoelectron spectroscopy *in situ* analysis was performed on a previously saturated HCOH catalyst using the process described before for the TPD analysis. A small part of this solid was placed in the special catalytic cell, and set up near the analysis chamber, where it was heated up to 200°C (2°C/min) by steps of 25°C under a flow of argon. The XPS analyses were carried out each 25°C.

The C(1s) spectra for the samples at RT and 175°C, shows two maxima at 284.5 eV and 288.5 eV, respectively. The deconvolution of these peaks confirms the presence of three different carbon species on the surface, with maxima at 284.5eV, 286.1 eV and 288.5eV. Previous studies show that methoxide and formate species were formed from formaldehyde on a variety of oxides. Moreover, on TiO₂ methanol was dissociated to methoxy species at room temperature, giving a C(1s) peak centred at 286.3eV, while formic acid dissociated to formates, also at room temperature, to give a C(1s) peak at 289eV.

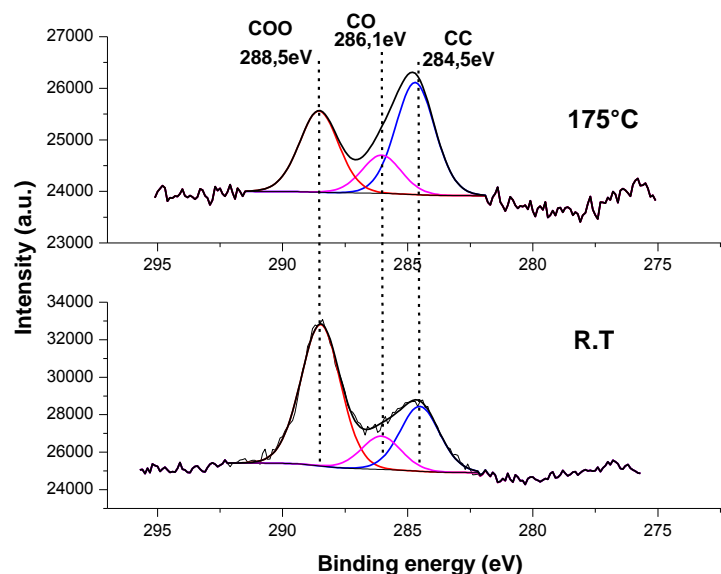


Figure 4.29.C(1s) spectra at R.T and 175°C.

The three peaks, at 284.5eV, 286.1 eV and 288.5eV, detected after formaldehyde adsorption in the MnOxSC_TA sample (Figure 4.29), were then assigned to the presence of surface carbon (C-C), methoxides (C-O) and formate (COO) species, respectively.

In order to evaluate the evolution of methoxy and formate species as a function of the temperature, the ratio (COO/C-C C-O/CC) was estimated taking into account that the contribution of the C-C peak remained constant during all experiment. Figure 4.30 shows the evolution of these ratios as a function of temperature.

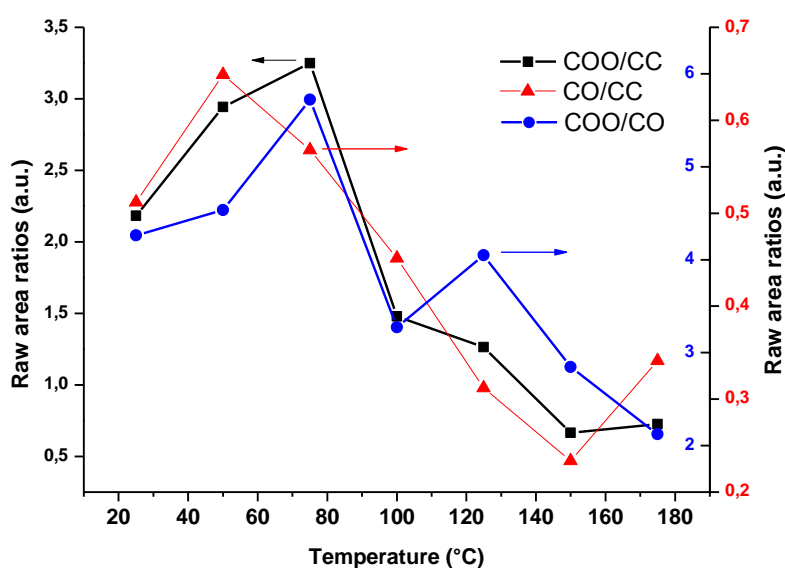


Figure 4.30.Evolution of carbon species (raw area ratio) as a function of temperature.

It can be observed in Figure 4.30 that the evolution of formate (COO) and methoxy species (C-O) follows the same trend. The evolution of these species starts with the increase of the temperature, reaching the maximum value at 50 and 75°C for methoxy and formate species, respectively. Subsequently, the COO and CO signals decrease with the increase of the temperature. This result suggests that, after HCOH adsorption at room temperature on the surface of the catalyst, the formation of formate and methoxy species occurs with participation of lattice oxygen. Moreover, it can be observed in Figure 4.30 that formation of formate species takes place in higher proportion when compared to methoxy species (ratio COO/CO >> 1 in Figure 4.30). Busca *et al.*[35] proposed a reaction scheme in which both methoxy and formate species were detected by IR spectroscopy, in formaldehyde dosed TiO₂, ThO and V-Ti oxide surface. It was explained by a Cannizzaro type reaction with addition of lattice oxygen from the surface as follows:



These results suggest that the reactions of formaldehyde include both oxidation and Cannizzaro type disproportionation. The formation of formate species in higher proportion could be explained by the conventional HCOH decomposition process.



In order to investigate the evolution of the manganese oxidation state during the study, the evaluation of the Mn(3s) spectra was carried out. Figure 4.31 shows the variation of the average oxidation state of manganese as a function of the temperature. It can be seen in Figure 4.31 that the oxidation state of manganese species was not modified after HCOH adsorption at room temperature. It can be clearly observed in Figure 4.31 that the average oxidation state of manganese decreases with the increase of the temperature. Noticeably, from RT to 75°C the AOS changes from 3.8 to 3.4. In this same temperature range, the formation of formate and methoxy species reaches the maximum value, confirming the participation of oxygen from MnO_x in the formation of these species. Subsequently, at higher temperatures the decrease of the AOS took place in minor extension. Figure 4.31 also shows the variation of the ratio O_{II}/O_I as a function of the temperature. Noticeably, it can be observed that the O_{II}/O_I ratio follows the same trend than that observed for manganese AOS. This result suggests the participation of O_{II} species assigned to surface adsorbed oxygen (O₂⁻ or O⁻), hydroxyl group

(OH), oxygen vacancies and defect oxide, indicating that these oxygen species are very reactive for the formation of formate and methoxy species.

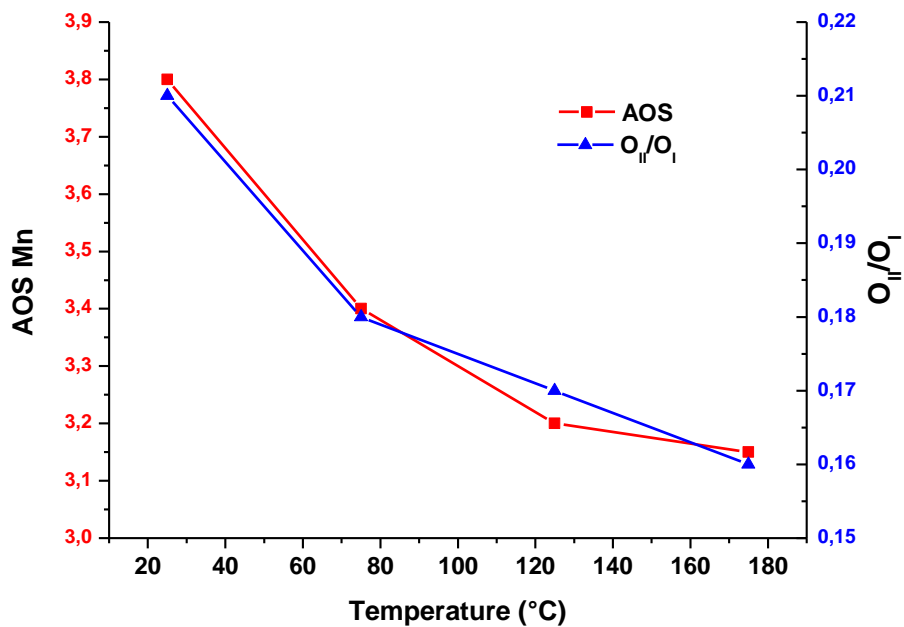


Figure 4.31. Variation of the average oxidation state as a function of the temperature.

4.3 Conclusions

In the first part of this chapter it has been proposed the synthesis of mesoporous manganese oxide materials by the surfactant assisted wet-chemistry route followed by chemical activation under acidic treatment. The acidic treatment has important effects in the SSA (increase of 75%), redox properties and manganese oxidation state (bulk and surface). High formaldehyde removal ability and capacity adsorption at low temperatures are observed in the presence of acid treated MnO_x samples. The catalytic performance in HCOH oxidation is emphasized when the cetyltrimethylammonium bromide surfactant is used in the preparation of MnO_x samples before acidic treatment. The formation of narrow mesopores and manganese species in high oxidation state in MnO_x sample seems to be responsible for this catalytic property enhancement.

The effect of chemical activation (acidic treatment) in the mixed MnO_x-CeO₂ catalysts with different Mn/Ce ratios prepared by surfactant assisted wet-chemistry route was studied in the second part of this chapter. The substitution of Ce⁴⁺ by Mn species in the fluorite structure to form the solid solution is demonstrated by XRD and XPS measurements in calcined samples, with a solubility limit of 50% Mn. After acidic treatment, the formation of solid solutions was strongly affected. Moreover, the acidic treatment has important effects in the BET surface area, redox properties and manganese oxidation state for binary oxides having high Mn content. The catalytic activity in formaldehyde oxidation for calcined Mn/Ce mixed oxides presents higher performance when compared to pure MnO_x. This result shows that the formation of MnO_x-CeO₂ solid solution is crucial for the complete oxidation of formaldehyde at lower temperatures due to the effective activation of molecular oxygen through the oxygen transfer mechanism. After the acidic treatment the beneficial effect of the solid solution disappears, having an adverse effect toward the oxygen transfer mechanism, resulting in lower catalytic activity for the mixed oxides. Actually, among acid treated samples, the pure manganese oxide presents the highest catalytic activity.

In the last part of this chapter, a mechanistic approach of formaldehyde adsorption and transformation on the MnO_x based catalyst was investigated by surface reaction experiments using (1) Temperature programmed desorption HCOH-TPD; (2) *In situ* XPS, and (3) FTIR studies of previous formaldehyde dosed sample. The TPD results clearly show the participation of oxygen from manganese oxide since oxidation products are observed. The FTIR results clearly show the formation of formate species on the catalyst surface, suggesting

a classical HCOH oxidation mechanism, in which the formation of formate intermediate species has been often proposed. However, the XPS analysis reveals the presence of formate and methoxy species, indicating that the reactions of formaldehyde on the MnO_x based catalyst include both oxidation and Cannizzaro type reaction. Finally, changes in the manganese oxidation state together with a reduction of the O_{II}/O_I ratio confirm the participation of oxygen from MnO_x in the formation of formate and methoxy species on the catalyst surface.

4.4References

- ¹ X. F. Tang, Y.G. Li, X.M. Huang, Y.D. Xu, H.Q. Zhu, J.G. Wang, W.J. Shen, *Appl. Catal. B*, **2006**, 62, 265.
- ² S.Imamura, D. Uchihori, K.Utani, T.Ito. *Catal. Lett.*, **1994**, 24, 377.
- ³ M. Peluso, J. Sambeth, H. Thomas, *Catal. Lett.* **2003**, 80, 241.
- ⁴ M. Alvarez-Galvan, V. de la Pena O'Shea, J. Fierro, P. Arias, *Catal. Commun.* **2003**, 4, 223.
- ⁵ L. Gandia, M. Vicente, A. Gil, *Appl. Catal. B*, **2002**, 38, 295.
- ⁶ F. Kapteijn, L. Singoredjo, A. Andreini, *Appl. Catal. B*, **1994**, 3, 173.
- ⁷ J. Brenet, M. Beley, *Electrochim. Acta*, **1973**, 18, 1003.
- ⁸ M. Askar, H. Abbas, *J. Power Sources*, **1994**, 51, 319.
- ⁹ A. Sinha, K. Suzuki, M. Takahara, H. Azuma, T. Nonaka, N. Suzuki, N. Takahashi, *J.Phys.Chem.C* , **2008**, 112, 16028.
- ¹⁰ A. Sinha, K. Susuki, M. Takahara, H. Azuma, T. Nonaka, K. Fukumoto, *Angew. Chem. Int. Ed.* **2007**, 46, 891.
- ¹¹ Z. Tian, W. Tong, J. Wang, N. Duan, V. Krishnan, S. Suib, *Science*,**1997**, 276, 926.
- ¹² B. Gillot, M. El Guendouzi, M. Laarj, *Mater. Chem. Phys.* **2001**, 70, 54.
- ¹³ H. R. Oswald, M. J. Wampetich, *Chim. Acta*, **1967**, 50, 2023.
- ¹⁴ T. Gao, P. Norby, F. Krumeich, H. Okamoto, R. Nesper, H. Fjellvåg. *J. Phys. Chem. C* **2010**, 114, 922.
- ¹⁵ F. Buciuman, F. Patcas, R. Craciun, D. Zahn. *Phys. Chem. Chem. Phys.* **1999**, 1, 185.
- ¹⁶ C. B. Azzoni, M.C. Mozzati, P. Galinetto, A. Paleari, Massaroti. *Solid State Commun.* **1999**, 112, 375.
- ¹⁷ D. Terribile, A. Trovarelli, C. De Leitenburg, G. Dolcetti, *Chem. Mater.* **1997**, 9, 2676.
- ¹⁸ D.Delimaris, T. Loannides, *Appl. Catal. B* **2008**, 84, 303.
- ¹⁹ F. Arena, G. Trunfio, J. Negro, B. Fazio, L. Spadaro. *Chem. Mater.* **2007**,19, 2269.
- ²⁰ J. C. Carver, G. K. Schweitzer, T. A. Carlson, *J. Chem. Phys.* **1972**, 57, 973.
- ²¹ M. Oku, K. Hirokawa, S. Ikeda, *J. Electron Spectrosc. Relat. Phenom.* **1975**, 7, 465.

-
- ²² V.A.M. Brabers, F.M. van Setten, P.S.A. Knapen, *J. Solid State Chem.* **1983**, 49, 93.
- ²³ D. Terribile, A. Trovarelli, J. Llorca, C. de Leitenburg, G. Dolcetti, *J. Catal.* **1998**, 178, 299.
- ²⁴ Z-Q Zou, M. Meng, Y-Q Zha, *J. Phys. Chem. C.* **2010**, 114, 468.
- ²⁵ M. Machida, M. Uto, D. Kurogi, T. Kijima. *Chem. Mater.* **2000**, 12, 3158.
- ²⁶ Wyruboff, G. *Bulletin de la Societe Chimique de France* **2**, 3, 745.
- ²⁷ V. Perrichon *et al.* *J. Chem. Soc. Faraday Trans.* **1991**, 87, 1601.
- ²⁸ Z. Zou, M. Meng, Y. Zha, *J. Phys. Chem. C*, 114, (2010), 468.
- ²⁹ W. Xingyi, K. Qian, L. Dao, *Appl. Catal. B*, **2009**, 86, 166.
- ³⁰ H. Chen, A. Sayari, A. Adnot, F. Larachi, *Appl. Catal. B*, **2009**, 86, 166.
- ³¹ X. Tang, J. Chen, X. Huang ; Y. Xu, W. Shen, *Appl. Catal. B* **2008**, 81, 115
- ³² X. Tang, J. Chen, Y. Li; Y. Xu, W. Shen, *Chem. Eng. J.* **2006**, 118, 119
- ³³ C. Mao, A. Vannice, *J. Catal.* **1995**, 154, 230.
- ³⁴ C. Li, K. Domen, K. Maruya, T. Onishi. *J. Catal.* **1990**, 125, 445.
- ³⁵ G. Busca, J. Lamotte, J. Lavalley, V. Lorenzelli. *J. Am. Chem. Soc.* **1987**, 109, 5197.

CHAPTER 5

Chapter 5 Optimized synthesis of mesostructure manganese oxides and their impact on formaldehyde removal performances

5.1 Introduction

In Chapter 4 it was shown that the synthesis of mesostructured of transition metal oxides and particularly manganese oxides could be hindered due to the multitude of different coordination numbers and oxidation states of manganese [1,2]. In this previous chapter, manganese oxides were chemically synthesized under high surfactant concentration, using CTAB as organic template and $\text{Mn}(\text{NO}_3)_2$ and NaOH as inorganic precursors. The mixture of the two systems leads to the formation of a mesoporous phase, as schematically shown in Figure 5.1.

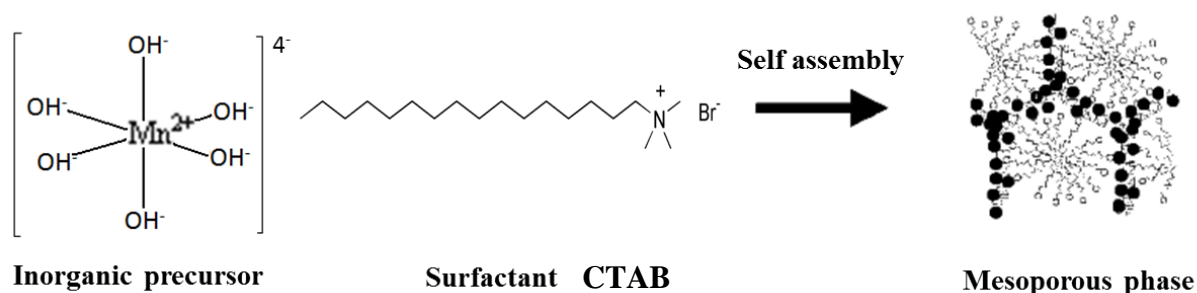


Figure 5.1. Formation of manganese oxide mesoporous phase.

Manganese hydroxide $\text{Mn}(\text{OH})_2$ is a white layered material built from edge sharing of $[\text{Mn}(\text{OH})_6]^{4-}$ octahedral clusters. These negatively charged octahedral clusters have higher probability of binding to positively charged surfactant head than to another one [1]. If the mixture step occurs in air, some Mn^{2+} ions present in $[\text{Mn}(\text{OH})_6]^{4-}$ can be oxidized to Mn^{3+} and Mn^{4+} , thus the overall charge of such clusters become less negative, disturbing the interaction between inorganic precursor and surfactant.

Herein, we present a novel synthetic route under controlled atmosphere adapted from Suib *et al.* [1] that permits $[\text{Mn}(\text{OH})_6]^{4-}$ octahedral clusters to be stabilized. The interaction of these inorganic precursors with surfactant molecules will be discussed. Additionally, several important factors that influence the obtention of mesostructure phase will be considered, comprising, for instance, the surfactant concentration, the OH/Mn ratio, and the addition sequence.

5.2 Experimental

5.2.1 Description of the experimental setup used for the preparation under controlled atmosphere

Figure 5.2 presents the experimental setup used for the preparation under controlled atmosphere. Argon was chosen as the carrier gas for all syntheses. Mechanical stirring was chosen considering the density of the concentrated CTAB solution. The water cooled condenser system allows the maintenance of a constant concentration of precursors during the synthesis.

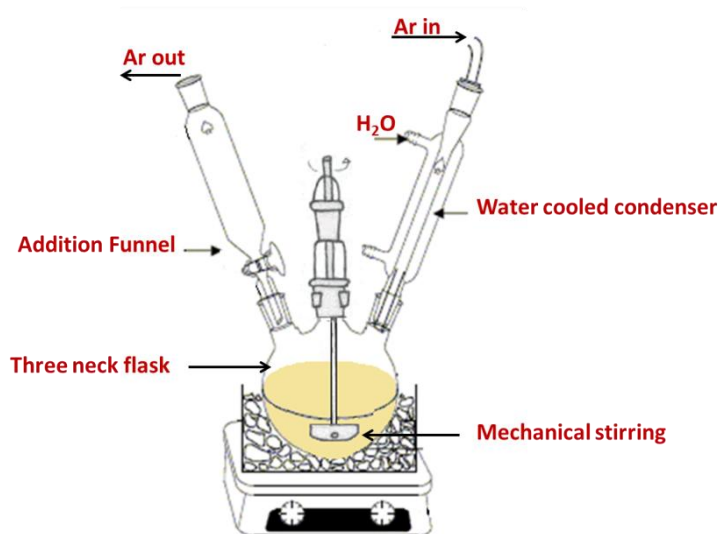


Figure 5.2. Experimental setup for controlled atmosphere preparation.

5.2.2 Synthesis procedure of mesostructured manganese oxides

The solids were first prepared in two steps i) dilution of the manganese nitrate precursors and surfactant in aqueous solution, and ii) addition of NaOH to form $\text{Mn}(\text{OH})_2$ *in situ*, which then reacts with the surfactant to produce the mesophase. The typical synthetic process can be described by the following steps:

- 1) Dilution of 6.67g of CTAB and 0.75g of MnCl_2 in 30ml of water under stirring until a homogeneous solution was obtained
↓
- 2) Slow addition of NaOH solution contained in the addition funnel, producing white slurry
↓
- 3) The resulting slurry was heated to 75°C under stirring, and then further stirred for 30min
↓

- 4) The final mixture was aged at 75°C for 12h
 ↓
 5) The sample was then decanted, washed, dried at RT and calcined at 550°C for 3h

5.3 Results and discussions

5.3.1 Parameters evaluated during the preparation of hybrid manganese oxide inorganic-organic materials

5.3.1.1 Washing procedure

During the synthesis of manganese oxide mesophase, the control of the Mn(OH)₂ oxidation to improve the interaction with the surfactant is the main parameter to study. The washing procedure permits to remove the surfactant excess that not interacts with the inorganic precursors. After several attempts, it was possible to maintain the white slurry until the washing procedure (step 5 in the synthesis process). However, the solids become brown after washing (6x100ml), indicating that the oxidation of Mn(OH)₂ is taking place. In order to control this parameter, different water volumes were employed to remove the excess of surfactant, as shown in Table 5.1. Especially less quantity of water has been used for the washing procedure.

Table 5.1. Synthesis compositions for controlling washing process.

Synthesis	CTAB/Mn ²⁺	OH ⁻ /Mn ²⁺	[CTAB] %wt	Washing process
MnOx 1	3	2	18	6x100ml ^a
MnOx 2	3	2	18	4x100ml
MnOx 3	3	2	18	2x100ml

^a Same washing procedure used in Chapter 4

The formation of ordered structures in the samples was investigated by low angle XRD analyses. The low angle patterns of the samples listed in Table 5.1 are presented in Figure 5.3. It can be seen that for the samples MnOx 1 and MnOx 2, in which higher volumes of water were employed for the surfactant removal, no peaks at low angle were detected. However, for the MnOx 3 sample washed with low volume of water, two low angle diffraction peaks at 2θ=3.4 and 6.9° were observed. These low angles could be characteristic of a mesostructured material. This result suggests that the washing procedure could affect the oxidation of Mn(OH)₂ inorganic precursor. It seems that, when low water volumes were employed, Mn(OH)₂ binding to surfactant molecule may not be oxidized due to diffusion limitations of O₂ through the dense phase of the surfactant. However, when higher volumes

were employed, the surfactant was removed, the dense phase was probably broken and oxidation of $\text{Mn}(\text{OH})_2$ could take place and produce brown to dark grey phases of manganese oxide.

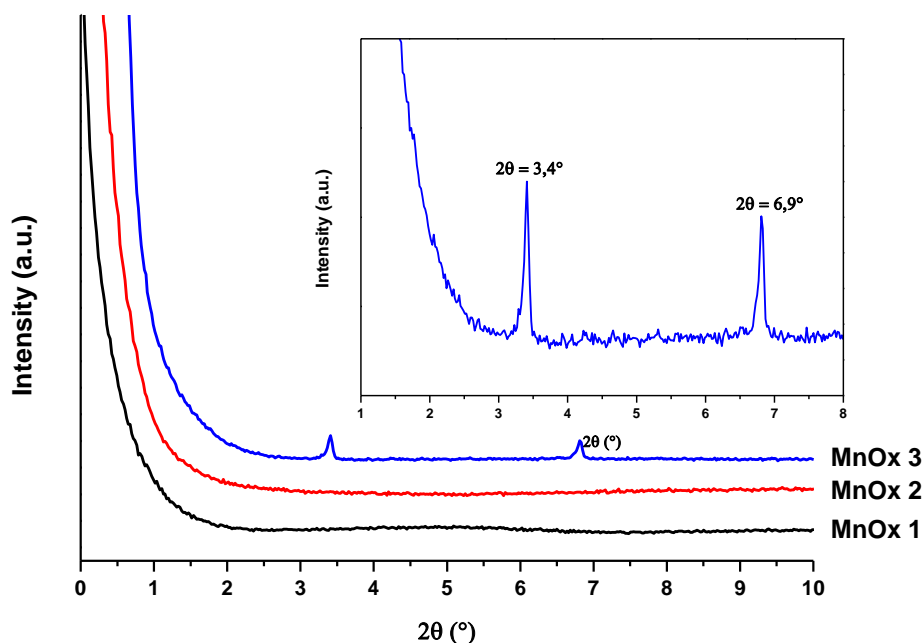


Figure 5.3. Low angle XRD patterns of dried samples listed in Table 5.1. Inset: zoom of XRD pattern of MnOx 3.

In order to confirm the presence of surfactant molecule after the washing step, FTIR studies have been carried out. The FTIR spectrum of dried MnOx 3 sample is presented in Figure 5.4. The IR absorption bands in the region of $2800\text{-}2900\text{ cm}^{-1}$ are typical of the C-H stretching mode of hydrocarbons; these bands are assigned to the presence of the surfactant hydrocarbon chain. Residual water and hydroxyl groups were detected with a large band around 3400 cm^{-1} , corresponding to O-H stretching frequency. Broad bands at 1900 and 2100 cm^{-1} were probably due to the bending vibration of associated water. Additional bands at 1450 cm^{-1} are assigned to the bending vibration of the C-H bond of methylene groups, attributed also to the presence of surfactant hydrocarbon chain. Similar spectra have been obtained with dried MnOx 1 and 2 samples.

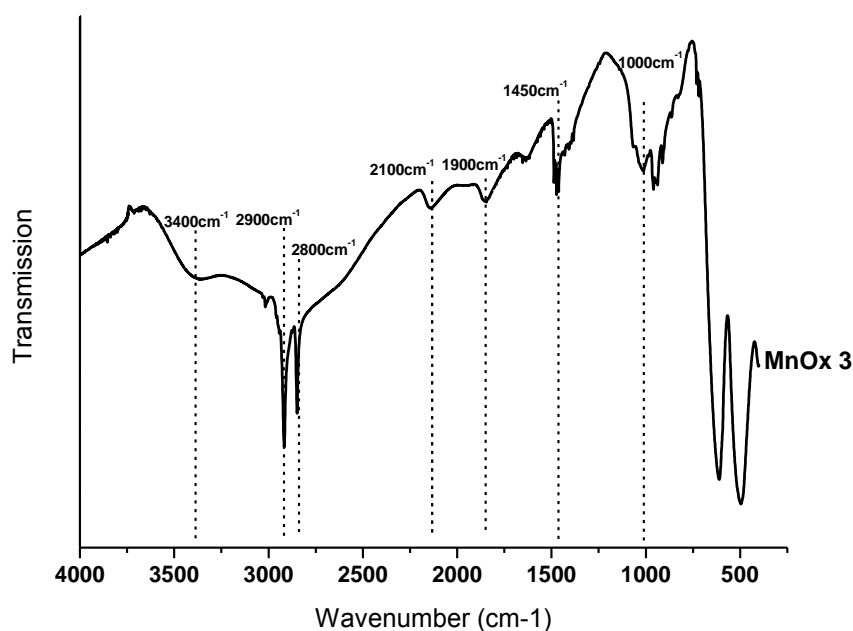


Figure 5.4. FTIR spectrum of dried MnOx 3 sample dried in air.

In order to evidence a possible interaction between the inorganic precursor and surfactant molecule, TG-DTA studies were carried out on MnOx 2 and MnOx 3 samples. Figure 5.5 shows the TG-DTA curves obtained for these samples. For the MnOx 2 sample (Figure 5.5a), a weight loss of 6.2% was registered from TG measurements in the temperature range from 100°C to 300°C. At the same temperature range, a single exothermic peak was observed in the DTA profile with maxima at 180°C (Figure 5.5a inset). This result suggests that weight loss is related to the oxidation of carbon from the surfactant molecules to CO₂, generating an exothermic reaction. After this, a weight increase of 1% at around 400°C together with a weight loss of 3.2% between 600°C and 800°C were observed, which is probably due to changes of manganese phase as reported previously by Azzoni *et al.* [3,4]. For the MnOx 3 sample (Figure 5.5b), an important weight loss of 24.9% was registered in the temperature range from 200°C to 400°C. This higher value is in agreement with the lower water volume employed and, consequently, with the higher surfactant content in this sample. In this temperature range, three exothermic peaks with maxima at 230, 275 and 325°C were clearly observed (Figure 5.5b inset). The second weight loss of 1.8% at around 700°C is probably due to changes of manganese phase.

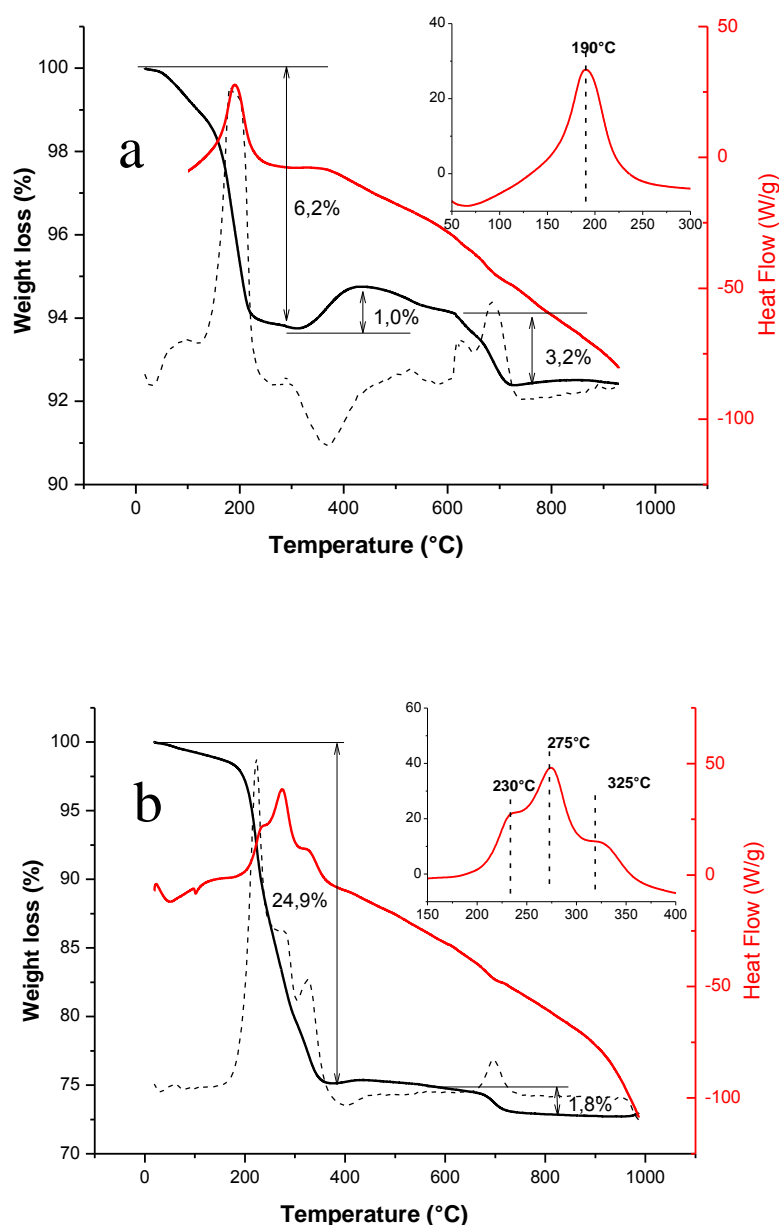


Figure 5.5. TG-DTA curves obtained for dried a) MnOx 2 and b) MnOx 3 samples. Inset: Zoom of DTA profile.

These results suggest that for the MnOx 3 sample, surfactant decomposition takes place in three steps and at a higher temperature compared to the MnOx 2 sample, indicating not only the presence of surfactant in the solid but also a more pronounced interaction between inorganic precursors and surfactant molecules. It means that probably for the MnOx 2 sample, the oxidation of the inorganic precursor during the washing procedure decreases the interaction with the surfactant molecule and/or no interaction occurs. Therefore, the weight loss observed for this sample could be related to weakly bonded or free surfactant molecule.

Further structural investigations were carried out using wide angle XRD analyses. Figure 5.6 shows the XRD patterns obtained for MnOx 3 sample dried in air. The XRD pattern presents oxidation products due to XRD peaks related to hausmannite (Mn_3O_4) phase (JCPDS 71841) and a broad XRD peak at $2\theta = 19^\circ$ which was ascribed to hydrohausmannite (MnOOH) phase (JCPDS 120252). It can also be observed an intense set of peaks at $2\theta = 6.9^\circ, 10.3^\circ, 13.8^\circ$ and 16.4° , corresponding to d spacing of 12.7, 8.6, 6.4 and 5.1 Å, respectively. These peaks can be related to the presence of a mesostructured material, (see the low angle XRD analysis). No match was found when these peaks were compared with those listed in the Power Diffraction File.

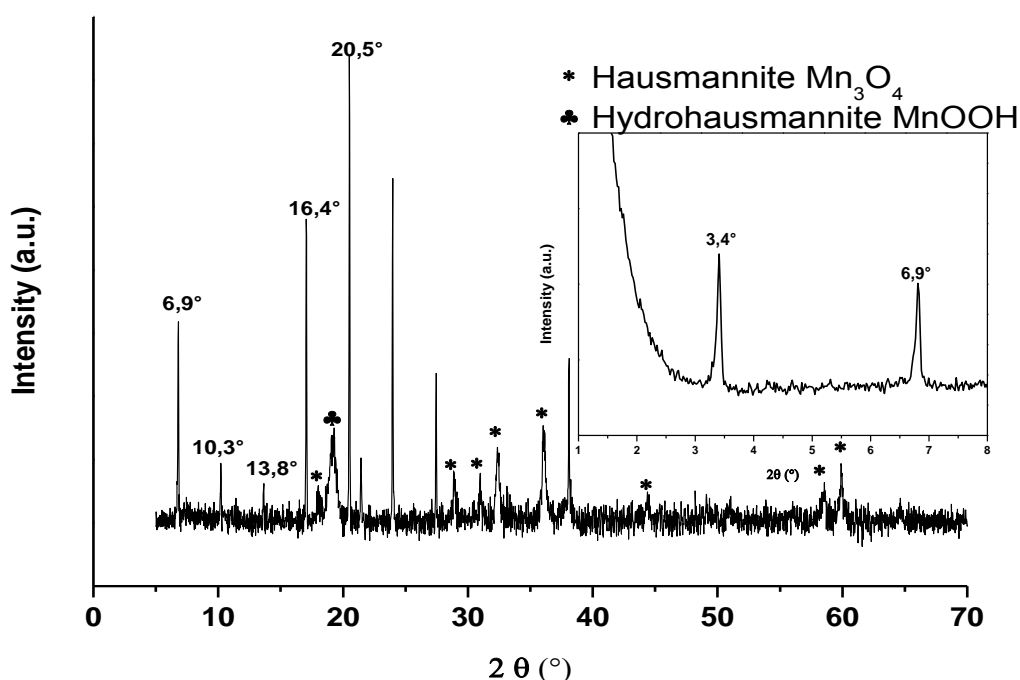


Figure 5.6. Wide angle X-ray diffraction profile for dried MnOx 3.

Suib *et al.* [5] have identified similar diffraction patterns corresponding to expanded layered structures in birnessite. The authors stated that when an organic ammonium species is introduced between the layers, the interlayer spacing is increased to an extent related to the dimension of the organic ammonium ion. For instance, for a $(\text{C}_{12}\text{H}_{25})\text{NME}_3$ -Birnessite the preferential oriented XRD occurs at $d = 24.1$ (001), 12.0 (002), 8.0 (003), 6.0 (004) and 4.8 Å (005), where the numbers in parentheses are the reflection indices. These reflections are similar to that obtained for the sample MnOx 3. Indeed, the (001) reflection for MnOx 3

sample presents a higher value, $d = 25.5 \text{ \AA}$, which was expected considering that CTAB, $(\text{C}_{16}\text{H}_{33})\text{NMe}_3$, dimension is higher. It seems that during the self-assembly process the surfactant molecules diffuse into the layers of $\text{Mn}(\text{OH})_2$ to produce an expanded layered material. Nevertheless, the existence of oxidation products like hausmannite and hydrohausmannite suggests that probably, one part of the inorganic ions are involved in the self-assembling process and the other part is oxidized. Furthermore, hydrohausmannite have been identified as an intermediate oxidation product of $\text{Mn}(\text{OH})_2$ in the synthesis of birnessite [6]. This observation suggests that the interaction between $\text{Mn}(\text{OH})_2$ with surfactant molecules avoids its oxidation.

These results suggest that the best washing procedure to remove the excess of surfactant and to control the oxidation of inorganic precursor is 2x100 ml. Further syntheses were carried out according to this washing procedure condition.

5.3.1.2 Influence of the OH/Mn ratio

Table 5.2 presents the initial composition of the samples prepared for the study of the influence of the OH/Mn ratio. This ratio was modified by increasing the quantity of NaOH while maintaining the manganese content fixed.

Table 5.2. Initial composition of the samples for investigating the influence of OH/Mn⁺².

Synthesis	CTAB/Mn ²⁺	OH ⁻ /Mn ²⁺	[CTAB] % wt
MnOx 3	3	2	18
MnOx 4	3	4	18
MnOx 5	3	6	18
MnOx-6	3	8	18
MnOx-8	3	>10	18

The wide angle powder XRD profile of the samples listed in Table 5.2 are shown in Figure 5.7. It can be seen that for samples with OH/Mn ratio in the range 2-6, the layered structure together with hydrohausmannite and hausmannite phases were obtained. For the sample with OH/Mn = 8, only the hausmannite phase was identified. Finally, the sample with ratio OH/Mn >10 presents a mixture of birnessite and hausmannite phases. Noticeably, for samples with OH/Mn ratio in the range 2-6, the intensity of diffraction peaks, ascribed to the layered structure, enhanced with the increase of the OH/Mn ratio (Figure 5.7). The regularity of the layered mesostructure could be qualitatively evaluated from the intensity and width of diffraction peaks. It means that the highest and narrowest diffraction peaks are ascribed to the

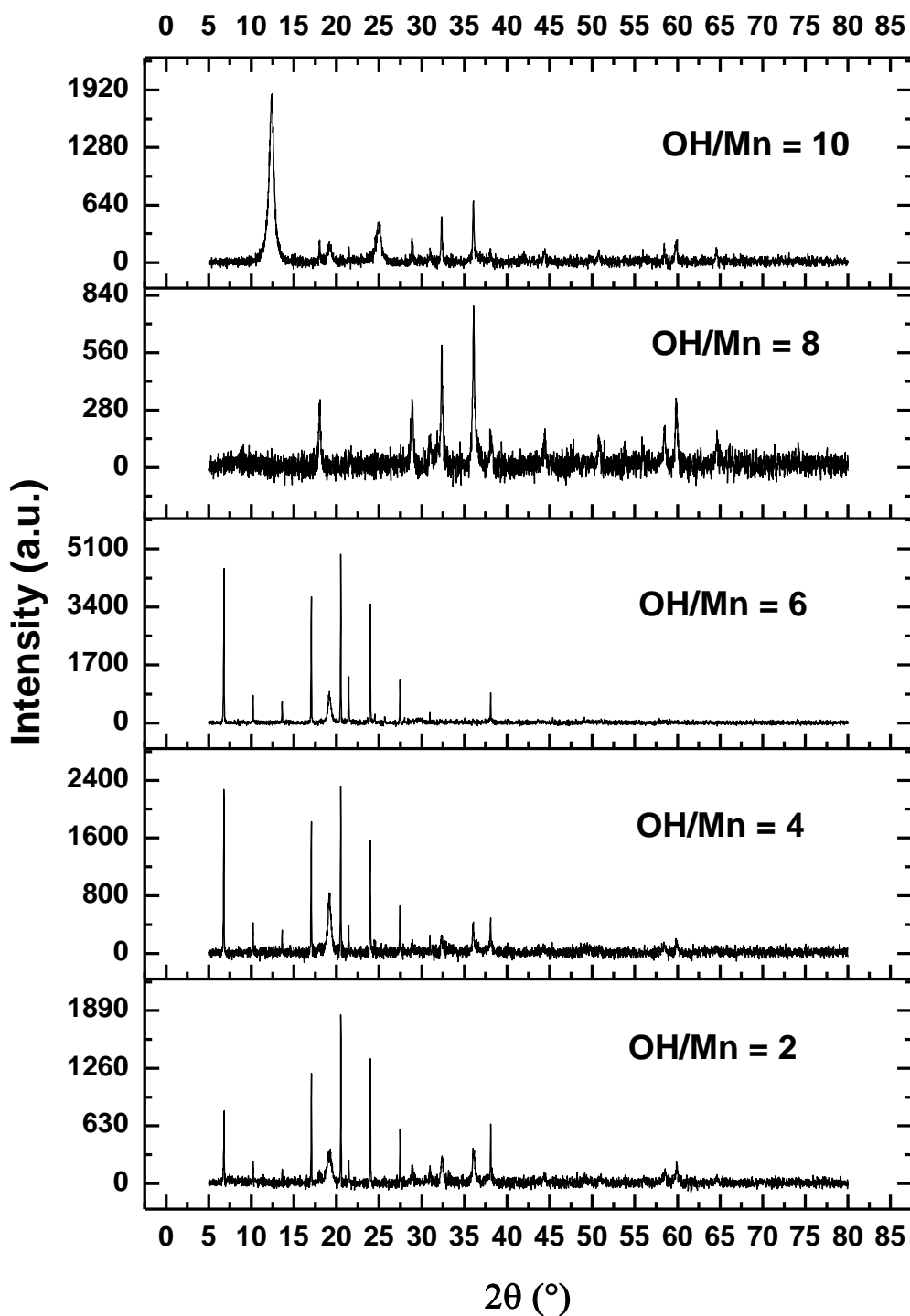


Figure 5.7. XRD pattern of the dried samples prepared with different OH/Mn ratios.

longest range ordered material. The sample with OH/Mn= 6 presents the highest peaks and consequently the most ordered structure. When the OH/Mn ratio increase, probably a higher proportion of $[\text{Mn}(\text{OH})_6]^{4+}$ ions self-assemblies around the positively charged surfactant head, increasing the ordering in the resulting material. This is confirmed by a decrease in the

intensity of diffraction peaks attributed to oxidation products like hausmannite and hydrohausmannite for these samples (Figure 5.7). The obtention of oxidation phases for the samples prepared with $\text{OH}/\text{Mn} \geq 8$ is probably due to the presence of many OH^- species around the positively charged surfactant head. The probability of binding between inorganic precursor and surfactant decreases and the oxidation of $\text{Mn}(\text{OH})_2$ produces crystalline Mn_3O_4 . The obtention of birnessite phase at $\text{OH}/\text{Mn} > 10$ was expected considering the conditions typically employed to obtain this phase, in which higher OH/Mn are used [8]. These results suggest that the best condition to enhance the inorganic/organic interaction and control the oxidation of inorganic precursor is the $\text{OH}/\text{Mn} = 6$.

5.3.1.3 Influence of surfactant concentration

Until now, the oxidation control of inorganic precursors has been achieved. However, a layered mesostructured material is obtained rather than a hexagonal mesostructured one, which was observed in literature [1]. For this reason, it was decided to study the effect of surfactant concentration in the organization of the final structure.

Surfactants are molecules with hydrophilic (polar) and lipophilic (apolar) parts. This nature of surfactant molecules leads to self-aggregation in solution so that hydrophobic and hydrophilic parts are separated. The type of self-aggregated structure depends on the concentration and temperature. The phase diagrams of surfactant in different solvents have been studied [8]. For water/CTAB system the phase diagram is presented in Figure 5.8.

As can be seen in Figure 5.8, CTAB forms an isotropic phase L at low surfactant concentration. At higher surfactant concentration, a hexagonal phase E is formed and a further increase of the surfactant concentration leads to the formation of a cubic (I) and lamellar (D) phases. The surfactant concentration used in previous syntheses was around 18 wt.% (blue point in Figure 5.8). It can be roughly evaluated that at 30°C the surfactant structure lays in the limit between the isotropic and the hexagonal phases. After heating at 75°C , only the isotropic phase is present. Based on this phase diagram, an increase of surfactant concentration at around 30 wt.% could be enough to obtain an hexagonal phase (red points in Figure 5.8).

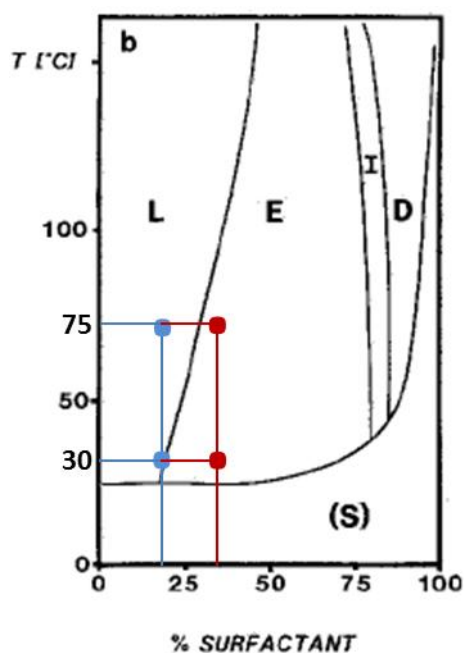


Figure 5.8. Phase diagram of the system water/hexadecyltrimethylammonium bromide (CTAB) at different temperatures. (S) is solid surfactant, L is solution phase, E, I and D are hexagonal, cubic, and lamellar liquid crystalline phase, respectively. From reference [9].

In order to accomplish this, experimental modifications in the synthesis procedure were adopted. Instead of producing the $\text{Mn}(\text{OH})_2$ precursor *in situ*, it was generated in a different flask (*ex-situ*) and then added slowly to the solution containing highly concentrated surfactant solution, under argon atmosphere. The experimental setup is shown in Figure 5.9.

The dilution of inorganic precursor in the minimum volume and its slow addition allowed the maintenance of a constant surfactant concentration during the preparation. Table 5.3 presents the initial composition of the sample prepared under the surfactant concentration adopted.

Table 5.3. Initial composition of the samples for investigating the influence of CTAB concentration.

Synthesis	CTAB/ Mn^{2+}	$\text{OH}^-/\text{Mn}^{2+}$	[CTAB] % wt
MnOx 9	3	6	30

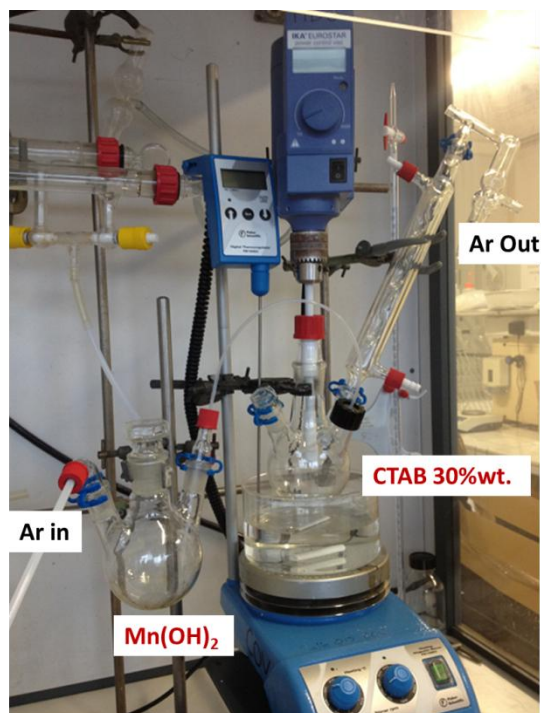


Figure 5.9. Experimental setup used for *ex-situ* preparation.

The XRD pattern of MnOx 9 sample prepared under the conditions listed in Table 5.3 is presented in Figure 5.10. It can be observed the formation of layered mesophase, together with small diffraction peaks related to hausmannite and hydrohausmannite phases. Remarkably, for this sample the intensities of the diffractions lines are the highest obtained until now. It seems that for *ex-situ* preparation the interaction between the inorganic precursor and surfactant is enhanced, increasing the ordering in the material. This is probably due to a better diffusion of inorganic precursor in the surfactant solution, caused by the slow addition of Mn(OH)_2 . This result is supported by the TG-DTA analysis (Figure 5.11), in which a higher weight loss in the temperature range from 200°C to 400°C was obtained (around 45%), suggesting higher incorporation of surfactants molecules in the inorganic framework. Moreover, for this sample, the DTA profile (Figure 5.11 inset) reveals four exothermic peaks at 190, 240, 290 and 350°C, respectively. The peak at 190°C could be related to weakly bonded or free surfactant molecule, as observed previously for the MnOx 2 sample. The set of peaks at higher temperatures concerning the surfactant to inorganic precursor interaction are slightly shifted to higher temperatures, compared with the MnOx 3 sample. It means that not only higher surfactant incorporation in the inorganic framework was obtained for *ex situ* preparation, but also a stronger interaction between them was confirmed. Considering that higher ordering and better interaction were obtained for *ex situ* preparation, further synthesis was carried out based on this experimental condition.

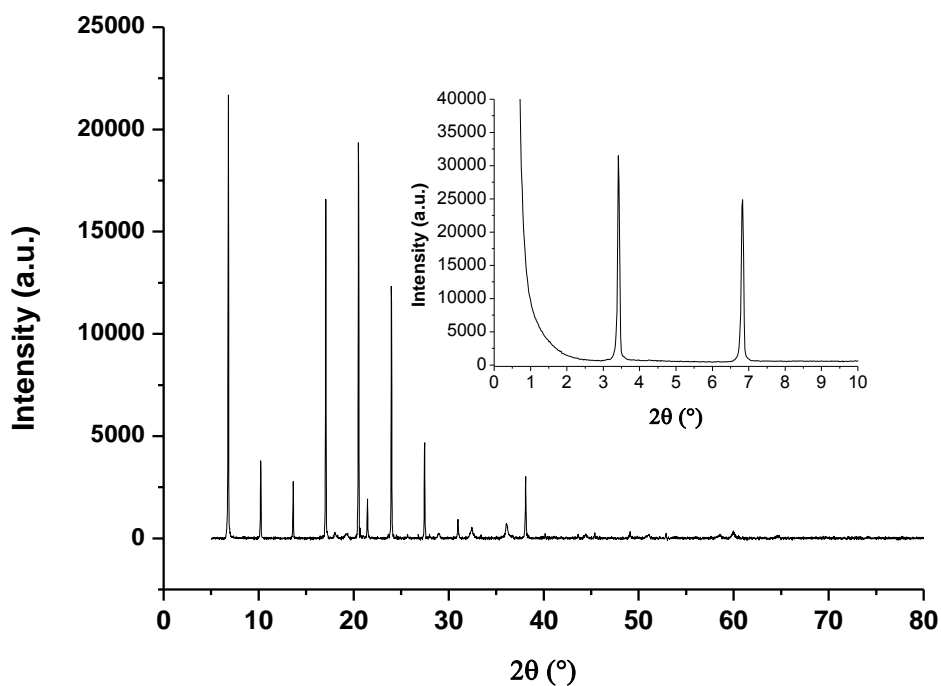


Figure 5.10. Wide XRD pattern of MnO_x 9 dried sample prepared at higher CTAB concentration (Table 5.3). Inset: low angle pattern.

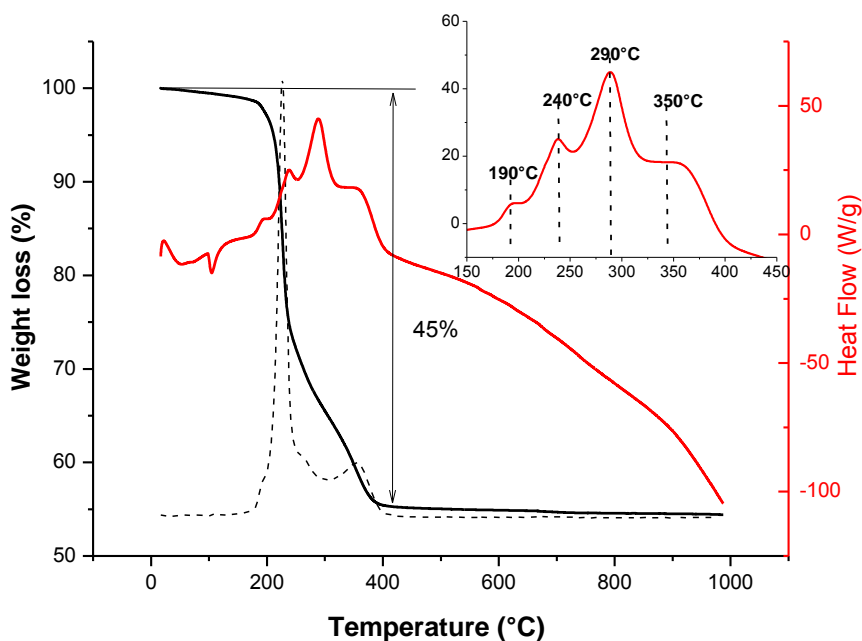


Figure 5.11. ATG-DTA curves obtained for dried MnO_x 9 sample. Inset: Zoom of DTA profile.

Since layered mesostructure material is also obtained under high surfactant concentration, it seems that the self-assembling process is governed by the layered $\text{Mn}(\text{OH})_2$ crystalline structure, rather than surfactant self-aggregated phase. The intercalation of tetraalkylammonium ions in birnessite type manganese oxide has been studied [10]. Birnessite is generally prepared by oxidation of $\text{Mn}(\text{OH})_2$ in concentrated aqueous NaOH . The authors suggest that the intercalation of the organic ion occurs by an ion-exchange process, in which the sodium located between the layers is replaced by the alkylammonium ions. Considering these observations, the formation of highly ordered layered mesostructure manganese oxide in the present work could be related to an ion-exchange process rather than a self-assemble one, as schematically presented in Figure 5.12.

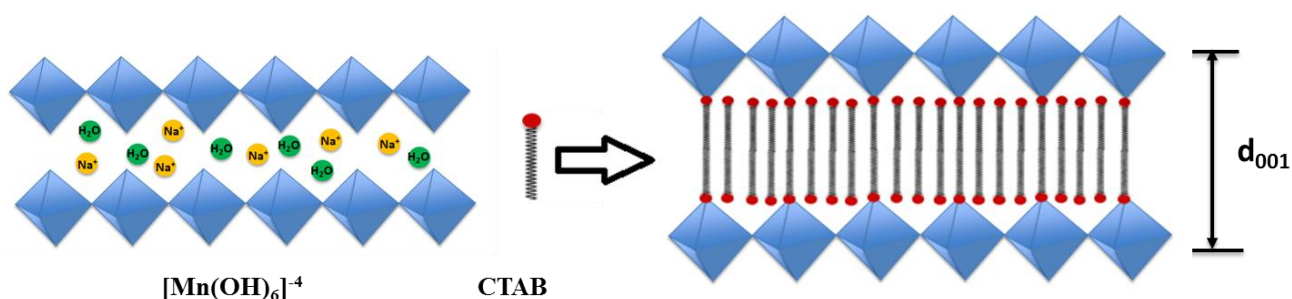


Figure 5.12. Schematic illustration of the formation of layered manganese mesostructure oxide.

Synthesis, structures, and physicochemical properties for layered manganese oxides (birnessite, busenite, etc.) have been studied and their ion exchange properties have been also reported [11,12,13,14,15]. The intercalation of alkylammonium ions into the layered manganese oxide causes the expansion of the interlayer distance [5,16]. The intercalation of $(\text{C}_{12}\text{H}_{25})\text{NMe}_3$ or TBA^+ ions into sodium birnessite gives layered manganese oxides with a basal spacing of 24.1 or 12.8 Å, respectively. However, in these studies amorphous layered materials are generally obtained and the oxidation control of manganese precursors has not been reported. In the present work, the intercalation of large organic ions into layered manganese oxide under controlled atmosphere was carried out. This method allows the achievement of highly ordered layered materials. These solids are expected to act as precursors for preparing mesoporous manganese oxides.

In order to validate the effect of surfactant to control the precursor oxidation and obtention of the layered material, a synthesis without surfactant was carried out. Table 5.4 presents the initial composition employed for this preparation.

Table 5.4. Initial composition of the samples prepared without surfactant (*ex situ*).

Synthesis	CTAB/Mn ²⁺	OH ⁻ /Mn ²⁺	[CTAB] %wt
MnOx 10	0	6	0

The XRD pattern of the resulting solid prepared without surfactant is showed in Figure 5.13. The profile was ascribed to hausmannite phase (Mn₃O₄). No peaks at low angle were detected (Figure 5.13 inset). This result confirms the fact that without surfactant the oxidation of Mn(OH)₂ layered precursor can readily produce manganese oxides in our experimental conditions.

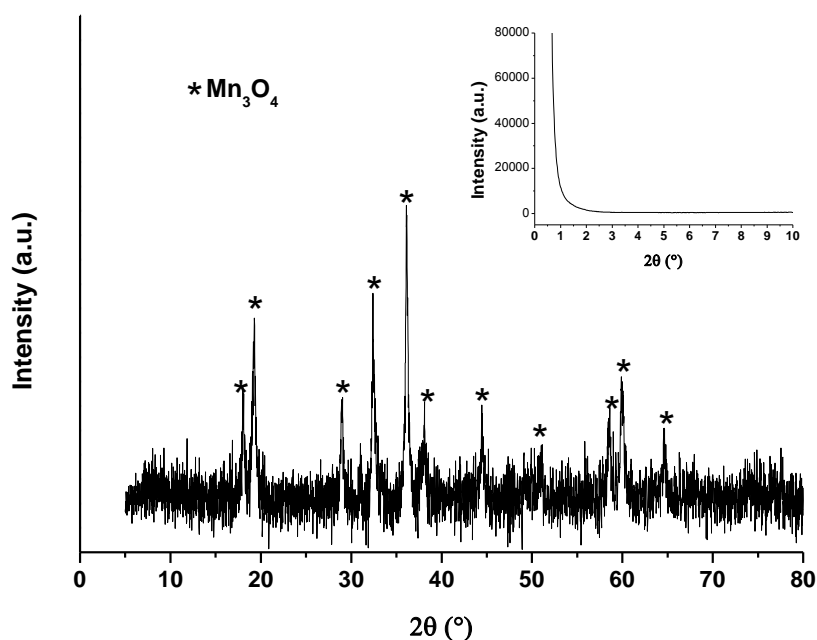


Figure 5.13. Wide XRD profile of dried sample prepared without CTAB. Inset: low angle pattern.

5.3.1.4 Influence of Cerium incorporation

In Chapter 4 it was shown that the combination of manganese and cerium can improve the catalytic properties of the resulting material by formation of solid solution. In this section, the influence of cerium incorporation in layered mesostructure manganese oxide material will be described. Table 5.5 presents the initial composition of the samples used for this study and the final structure obtained.

Table 5.5. Initial composition of the samples prepared with cerium and the obtained structure.

Synthesis	Ce/Mn	CTAB/Ce ³⁺ Mn ²⁺	OH ⁻ /Ce ³⁺ Mn ²⁺	[CTAB] %wt
CeMnOx 1	5	3	6	30
CeMnOx 2	10	3	6	30
CeMnOx 3	20	3	6	30

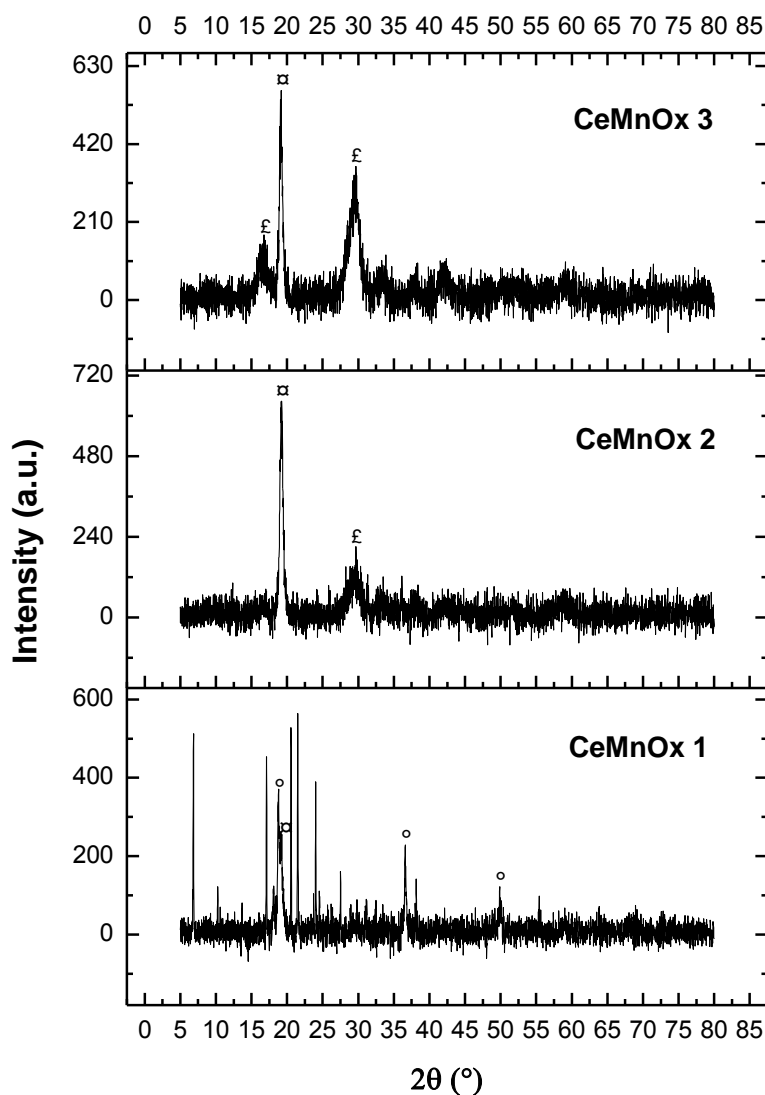


Figure 5.14. Wide XRD profile of dried sample prepared at different Cerium loading (Table 5.5). ° Pyrochroite Mn(OH)₂, □ Hydrohausmannite (MnOOH) and ° CeOx.

As show in Figure 5.14, the layered structure is only produced by the sample with low ceria content (CeMnOx 1). For this sample, the reflection peaks were located at the same position

and the basal spacing was $d_{001} = 25.4 \text{ \AA}$. However, the intensity of diffraction peaks is the lowest obtained, indicating a poor ordering structure. Cerium inorganic precursor is probably well dispersed in manganese layers without modification of basal spacing, or leads to an amorphous phase not detected by XRD. Pyrochroite $\text{Mn}(\text{OH})_2$ and hydrohausmannite MnOOH phases were also identified in the CeMnO_x 1, indicating that, probably due to ceria loading, one part of manganese ions will escape from the layered structure without further oxidation.

Cerium nitrate $[\text{Ce}(\text{NO}_3)_3]$ under basic conditions leads to the precipitation of gelatinous cerium hydroxide $\text{Ce}(\text{OH})_3$. It has been reported that Ce^{3+} could be oxidized in basic medium to Ce^{4+} to form hydrous cerium oxide. The occurrence of this process is confirmed by a colour change from white to violet during the synthesis, which is consistent with a variation of the cerium oxidation state. Terribile *et al.* [17] have proposed a reaction path to describe the interaction between hydrous cerium oxide and surfactant.

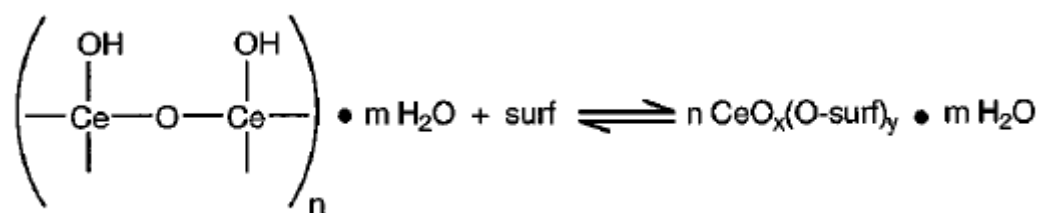


Figure 5.15. Interaction between cerium inorganic precursor and surfactant molecule.

From reference [17].

Hydrous cerium hydroxide can be deprotonated at higher pH values. In this case, an exchange between the deprotonated hydroxyl group and the positively charge surfactant head takes place, with the formation of an inorganic/organic composite. Under the conditions presented in Table 5.5, the pH value is well above that of isoelectric point of hydrous cerium oxide ($\text{pH} = 7\text{-}8$), indicating that the interaction presented in Figure 5.15 is possible. However, at higher Ce loading the layered mesostructure material was not obtained. It is probably due to a different self-assembly process for ceria oxides, perturbing the interaction between manganese inorganic precursor and surfactant. Competitive effect and manganese-cerine condensation also play a role in this result.

In order to investigate the inorganic to organic interaction, TG-DTA studies were carried out for the samples listed in Table 5.5. For all samples, the TG profiles (not showed) present an important weight loss of 42%, 22% and 23%, in the temperature range from 200°C

to 400°C for the samples CeMnOx 1, CeMnOx 2 and CeMnOx 3, respectively. As previously discussed, this weight loss corresponds to surfactant oxidation, suggesting the presence of surfactant in all samples. Higher weight loss was found to the sample CeMnOx 1, which presents a layered structure.

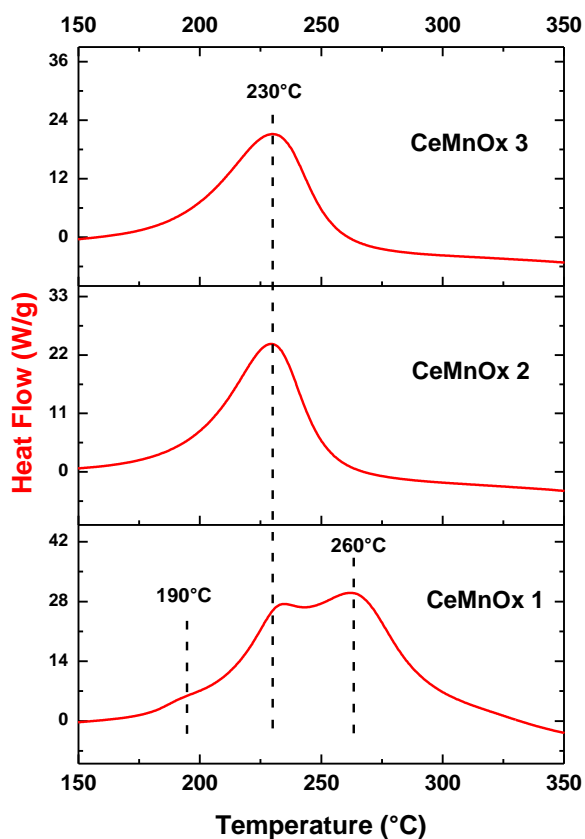


Figure 5.16. DTA profiles for CeMnOx 1, CeMnOx 2 and CeMnOx 3 samples.

Regarding the DTA profiles (Figure 5.16), three exothermic peaks can be observed for the sample CeMnOx 1 with maxima at 190, 230 and 260°C, respectively. As stated before, the peak at 190°C could be assigned to weakly bonded or free surfactant, while the peaks at higher temperatures are assigned to inorganic precursor to surfactant interaction. Noticeably, for the CeMnOx 1 sample, these peaks are shifted to lower temperatures with respect to the pure manganese oxide samples. At higher cerium loading, the DTA profile reveals a single exothermic peak at 230°C, indicating a single inorganic precursor to surfactant interaction rather than a multiple interaction, as it was observed previously for CeMnOx 1 and pure MnOx. These results confirm that Ce addition strongly modifies the interaction between

inorganic precursors and surfactant molecules, affecting the obtention of layered mesostructure precursors.

In the next section, calcination of these precursors, their characterization and application in formaldehyde oxidation will be discussed.

5.3.2 Calcined Precursor: Characterization and their Application to Formaldehyde Oxidation.

5.3.2.1 Structural stability of layered mesostructure manganese phase

Before the calcination of the solids, the study the structural stability of layered mesostructure material, as a function of temperature has been carried out by *in situ* XRD analysis. The results obtained for MnOx 9 sample are presented in Figure 5.17. It can be seen that the peaks ascribed to the layered mesostructure are present until 150°C. The intensity of these peaks decreases as temperature is increasing, indicating that the material ordering is lowered. Total delamination of the sample occurs at 200°C; this temperature corresponds to the beginning of surfactant decomposition observed by TGA analysis (Figure 5.11). These results clearly suggest that stability of the layered phase is related with the organic/inorganic interaction. Moreover, when the surfactant is decomposed, oxidation of inorganic phase occurs immediately. Figure 5.17 (inset) presents the XRD pattern registered at higher temperatures (> 250°C). The formation of different manganese oxides can be observed, with the presence of Mn₃O₄ in almost all temperature range. Small peaks ascribed to amorphous phase MnO₂ were observed between 200 and 400°C. The Mn₅O₈ phase was observed as an intermediate phase between 400°C and 600°C, while the Mn₂O₃ phase was detected at higher temperatures.

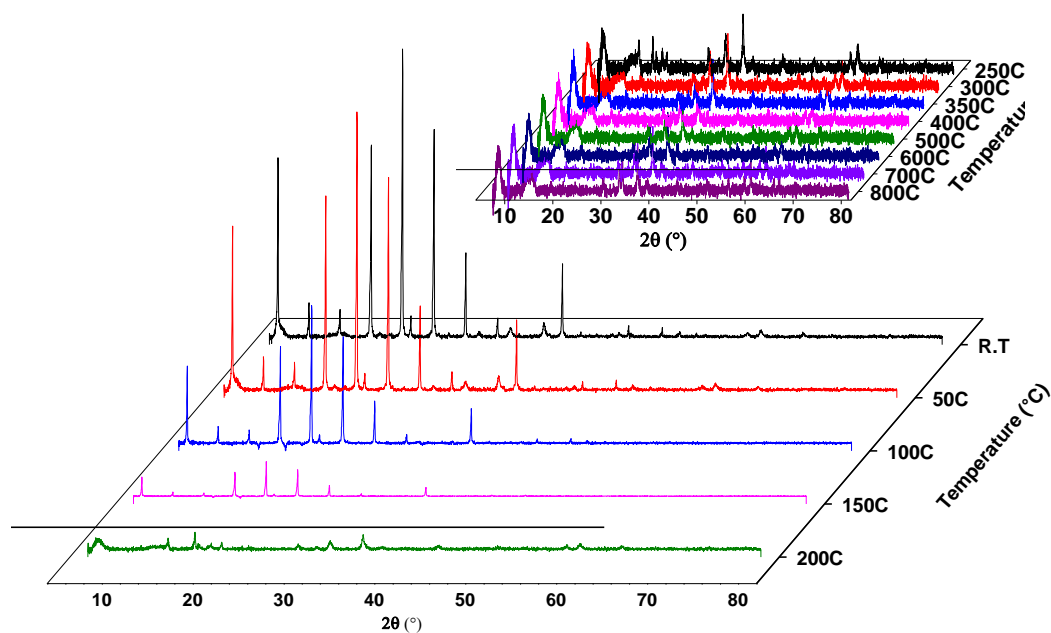


Figure 5.17. *In situ* XRD patterns for MnOx 9 sample obtained under air atmosphere as a function of temperature. Inset: From 250°C to 800°C.

Table 5.6 presents the samples selected for calcination, characterization and formaldehyde total oxidation studies. The temperature of 550°C has been chosen as calcination temperature for all the samples. The calcination protocol briefly described in section 5.2.2 is depicted in Figure 5.18.

Table 5.6. Selected samples for thermic treatment and HCOH total oxidation.

Synthesis	CTAB/Mn ²⁺	OH ⁻ /Mn ²⁺	[CTAB] % wt
MnOx 3	3	2	18
MnOx 5	3	6	18
MnOx-9	3	6	30
MnOx-10	3	6	0
CeMnOx 1	3	6	30

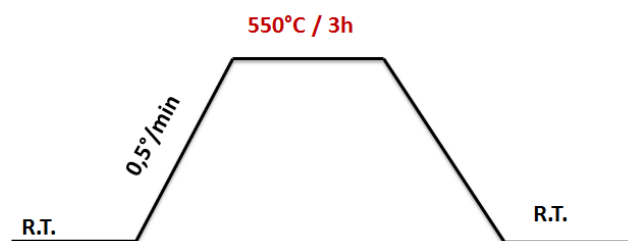


Figure 5.18. Calcination (air atmosphere) protocol.

5.3.2.2 Wide angle XRD

After calcination, the brownish samples listed in Table 5.6 become black. The wide angle powder XRD profiles for these samples are presented in Figure 5.19. It can be seen for all samples that the diffraction peaks become weaker and broader. The identification of these patterns reveals the presence of different manganese oxides. The hausmannite phase (Mn_3O_4) seems to be the most stable phase after calcination. Diverse proportion of Mn_5O_8 phase was observed but without a clear trend. No peaks of fluorite structure phase (CeO_2) in $CeMnO_x$ 1 were observed (see Table 5.5). No peaks at low diffraction angles were detected, indicating that after calcination the layered mesostructure was well destroyed. The delamination (exfoliation) of layered oxides into their elementary host is typically observed for some of the mineral clays, such as smectite and montmorillonite [10]. The delamination process was carried out by decomposing the surfactant molecules between the layers under oxidative atmosphere. As was previously evidenced by TG-DTA analyses, complete surfactant decomposition takes place at around 400°C.

Further oxidation of $Mn(OH)_2$ precursors at 550°C produces dark-black manganese mixed oxides, Mn_3O_4 being the more stable phase (Table 5.7). Mn_5O_8 was a common phase present in the samples prepared using surfactant, in which layered mesostructure precursors were obtained (Table 5.7).

Table 5.7. Tentative XRD identification of oxides present in calcined samples.

Samples	Identified phases		
	Mn_3O_4	Mn_5O_8	Mn_2O_3
MnOx 3	●	●	
MnOx 5	●	●	
MnOx-9	●	●	●
MnOx-10	●		
CeMnOx 1	●	●	

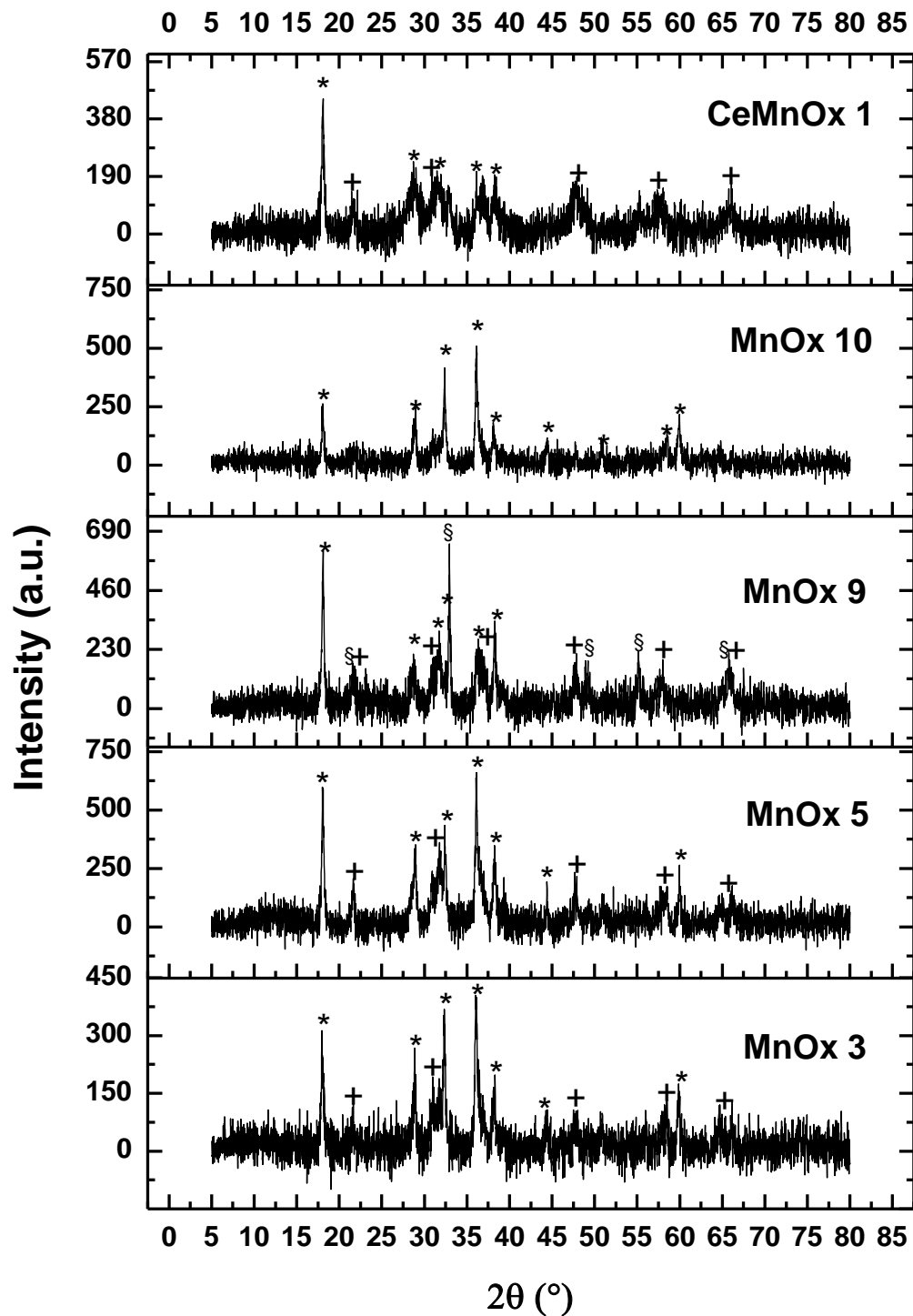


Figure 5.19. Wide angle XRD of calcined samples listed in Table 5.6.

*Hausmannite (Mn_3O_4), + Mn_5O_8 , § Bixbyite Mn_2O_3 .

5.3.2.3 Textural properties

The delaminated oxides obtained are expected to have exceptional chemical and physical properties, distinctive from those in the stacked state. It has been shown in previous chapters that textural and redox properties play an important role in the catalytic activity of formaldehyde oxidation. Table 5.8 lists the textural properties obtained for the calcined samples.

Table 5.8. Physical properties of calcined materials.

Sample Name	S_{BET} (m^2/g)	Pore Size at maximum value (nm)	Pore volume (cm^3/g)
MnOx 3	62	74	0.28
MnOx 5	63	75	0.30
MnOx-9	70	60	0.53
MnOx-10	24	60	0.15
CeMnOx 1	56	50	0.26

The MnOx 10 sample, prepared without surfactant, presents the lowest specific surface area SSA ($24 \text{ m}^2/\text{g}$). Among the pure manganese oxides, the largest SSA of $70 \text{ m}^2/\text{g}$ was obtained for the MnOx 9 sample, in which a better surfactant-inorganic phase interaction was evidenced. Finally, for the sample CeMnOx 1 the SSA decreases ($56 \text{ m}^2/\text{g}$); this result can be related to the poorly ordered precursor obtained. The N_2 adsorption-desorption isotherm exhibits for all samples a type II isotherm, which indicates an open surface or a macroporous structure (Figure 5.20).

Mean pore size diameter are also reported in Table 5.8. For all samples a broad pore size distribution was observed, all distributions are roughly monomodal with small shoulders at lower and higher pore diameters (Figure 5.20 inset). The mean diameter at maximum value was around 60nm, indicating the presence of macroporous. In addition, the MnOx 9 sample presents the larger pore volume ($0.53 \text{ cm}^3/\text{g}$). These results suggest that the delamination of this layered mesostructure materials results in a macroporous opened structure with interesting physical properties. Moreover, it was evidenced that an effective interaction between surfactant and inorganic precursor strongly affect the physical properties. For the MnOx 9 sample, the highest ordering was observed, and the most interesting textural properties were also found for this sample.

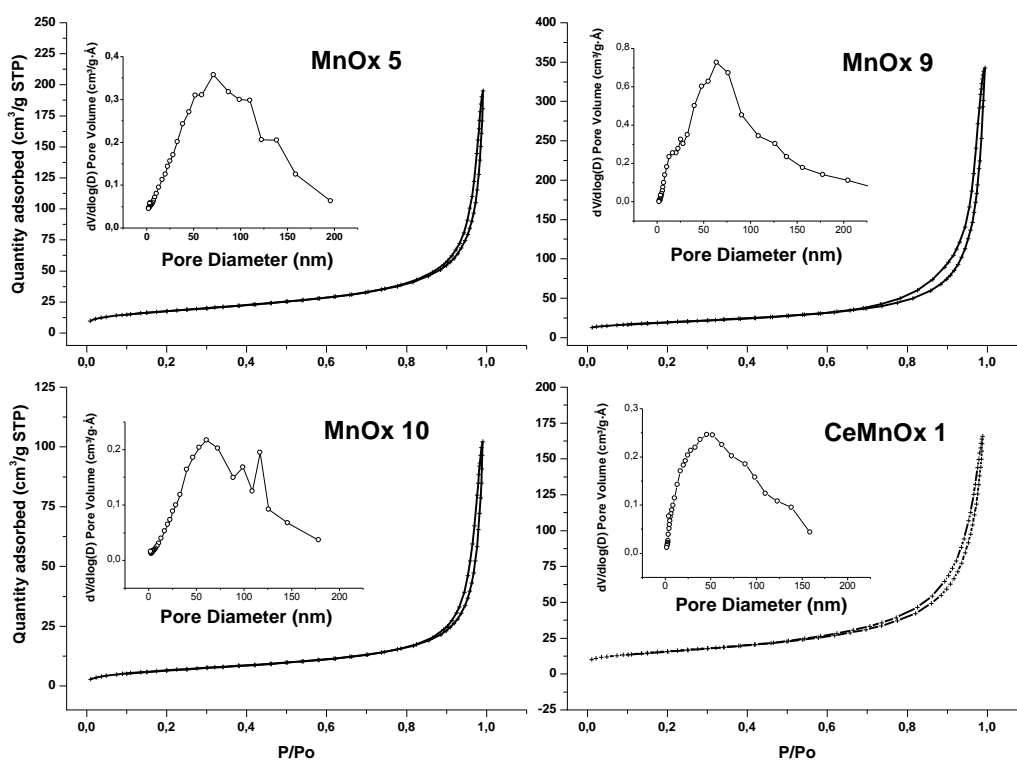


Figure 5.20. Isotherms and pores size distribution (inset) obtained for calcined samples.

5.3.2.4 Redox properties

As it was stated in the previous chapter, the redox properties are important features to evaluate since the catalytic activity in VOC oxidation is related to these properties (redox mechanism). The selected samples allow the comparison between the two synthetic route *in situ* (MnOx 5), *ex situ* (MnOx 9), the sample prepared without surfactant (MnOx 10) and the addition of Cerium (CeMnOx 1). The MnOx 3 sample, also listed in Table 5.6, was not considered in further studies since it presents the same properties as the MnOx 5 sample.

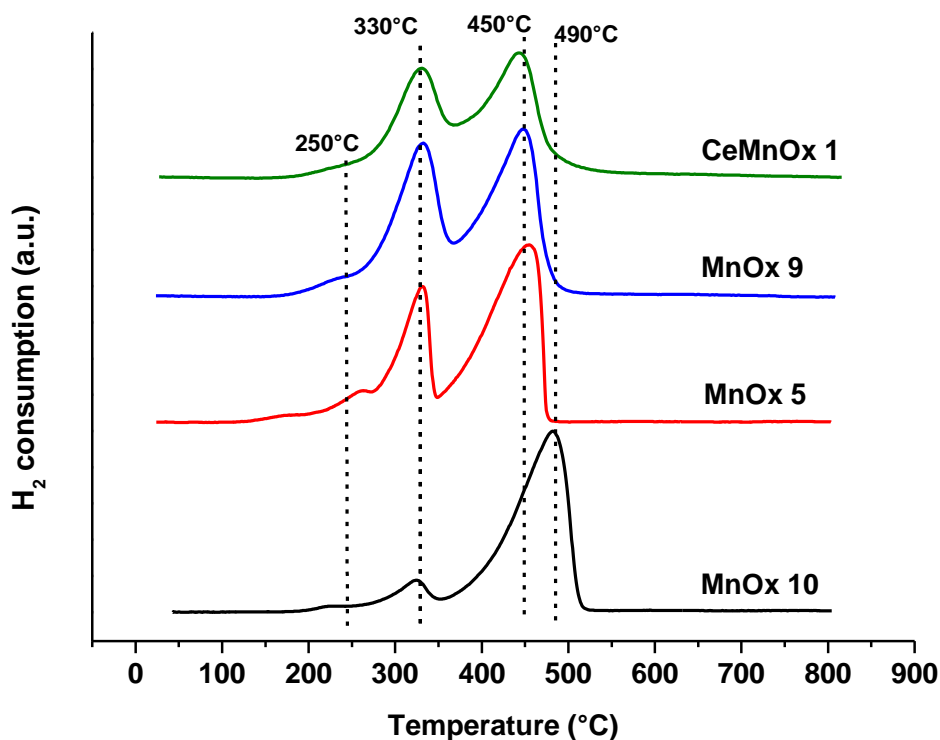


Figure 5.21. Representative H₂-TPR profile of selected calcined samples.

As can be seen in Figure 5.21, the TPR profiles correspond to typical two step reduction of MnOx, in which higher oxidation state species are reduced in the first step, with maxima at 330°C for all samples, and this reduction is completed in second step until MnO, as was discussed in the previous chapter. It can also be observed that after cerium addition (CeMnOx 1 sample) the TPR profile was not changed, indicating that ceria is probably well dispersed in the resulting mixed oxide. For the samples prepared using surfactant (MnOx 5, MnOx 9 and CeMnOx), the second reduction peak took place at 450°C, while for MnOx 10 sample the maximum of the second peak was shifted to higher temperature at 490°C. This suggests that the use of surfactant enhanced the reduction of the material by the formation of smaller crystallites of mixed oxides. Noticeably, for the MnOx 5, MnOx 9 and CeMnOx 1 samples, higher contribution of the first reductions peak was observed, indicating the presence of manganese in higher oxidation states. This result is in good agreement with XRD measurements which reveals the presence of Mn₅O₈ for these samples (Table 5.7). It means that, probably during calcination, the Mn(OH)₂ crystallites binding to surfactant molecule oxidized in air much more quickly, since the smaller Mn(OH)₂ particles react with O₂ more faster and completely [1]. It was further evidenced, by the fact that the MnOx 9 sample

presents higher H₂ consumption to the first reduction peak, that the precursor presented the highest ordering and consequently an enhanced inorganic/organic interaction.

Table 5.9. H₂ consumption and average oxidation state (AOS).

Sample	Consumed H ₂ mmol/g	Average Oxidation State
MnOx 5	6.3	2.9
MnOx 9	6.8	3.1
MnOx 10	4.8	2.7
CeMnOx 1	5.2	2.8

Table 5.9 confirms the observations described previously. The highest H₂ consumption was obtained for the sample MnOx 9 (6.8 mmol/g), which is consistent with a mixture of different manganese oxides, as reported by XRD analysis (Table 5.7). For the MnOx 5 sample, the H₂ consumption of 6.3mmol/g agrees with the corresponding theoretical value reported for the reduction of Mn₂O₃ into MnO. However, the XRD measurements show the presence of Mn₃O₄ and Mn₅O₈, indicating that contributions of different oxides towards H₂ consumption are expected for this sample. A significant difference was observed between the samples prepared with and without surfactant, respectively. For the MnOx 10 sample the H₂ consumption was 4.8mmol/g, which is very close to the theoretical value of 4.4mmol/g related to the reduction of Mn₃O₄ into MnO. This result is in accordance with the XRD measurement in which the Mn₃O₄ phase was identified in the MnOx 10 sample. After the cerium addition, the H₂ consumption decreases (Table 5.9), since the Mn content is reduced. This indicates that the contribution of manganese species towards H₂ consumption is more important with respect to that of ceria species, as it was shown in the previous chapter. The AOS of the samples changes between 2.7 and 3.1 for MnOx 10 and 9, respectively. These results support the ability of layered mesostructure precursors to form mixed valent macroporous systems.

5.3.2.5 Catalytic activity test

To further investigate the influence of the preparation and formation of layered mesostructure precursor, the catalytic activities of selected calcined samples were evaluated in HCHO oxidation. In all cases studied, only CO₂ was detected as the oxidation product of HCHO. The light-off curves are shown in Figure 5.22.

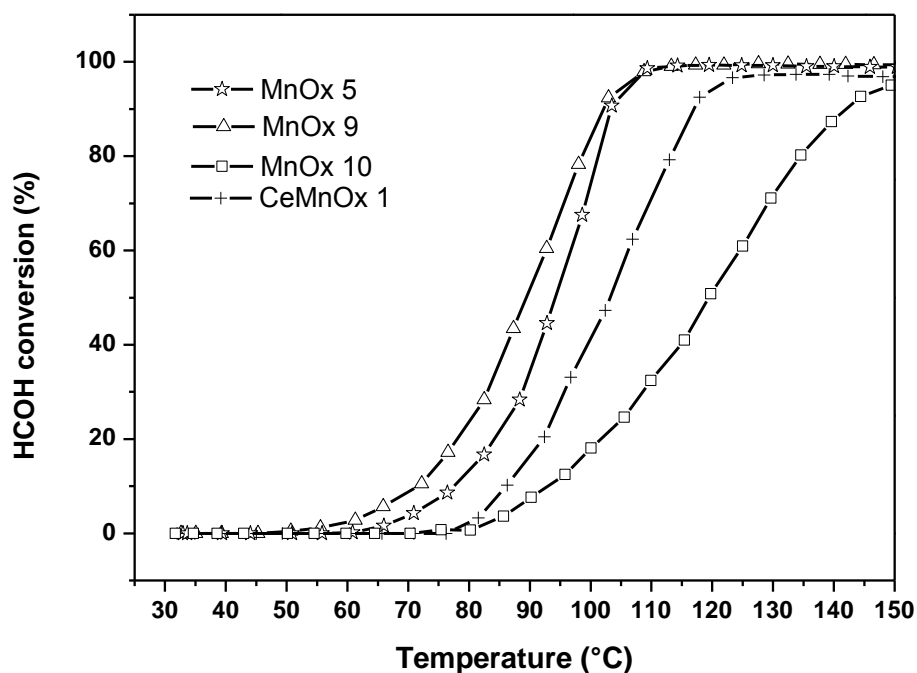


Figure 5.22. Catalytic performance of calcined solid listed in table 5.6.

It can be seen in Figure 5.22 that catalytic activity is clearly related to SSA and redox properties. The catalytic activity follows the order MnOx 9 > MnOx 5 > CeMnOx 1 > MnOx 10. These results suggest that synthesis of manganese oxide using mesostructure layered material as precursor enhanced the catalytic properties of the resulting material by increasing the textural properties and improving the redox properties. It can also be observed that addition of cerium into the system resulted in diminution of the catalytic activity, low surface area and lower inorganic/surfactant interaction.

Table 5.10. Catalytic performance of calcined materials.

Sample Name	T _{50%} (°C)	T _{100%} (°C)
MnOx 5	95	110
MnOx-9	90	110
MnOx-10	120	160
CeMnOx 1	110	140

The temperatures of 50% HCOH conversion (T₅₀) and 100% HCOH conversion (T₁₀₀) over different catalysts are presented in Table 5.10. The sample MnOx 9 oxidized 50% of HCOH at 90°C. In this case, total conversion is reached at 110 °C, which is comparable to other manganese oxides tested under similar conditions, indicating that manganese oxides

obtained from layered mesostructure precursor is an excellent catalyst for HCOH total oxidation. The sample MnOx 10 prepared without surfactant shows the lowest activity with $T_{50} = 120^{\circ}\text{C}$ and $T_{100} = 160^{\circ}\text{C}$. As discussed in Chapter 3, the SSA, redox properties and morphology are the major factors controlling the HCOH oxidation. Probably in the samples prepared from layered precursors, the more opened porous structure of the catalyst may facilitate the diffusion of the HCHO molecules. Furthermore, for these samples higher relative amounts of reducible species at low temperature were observed, as a consequence of more complete oxidation during the calcination step. From the results obtained in the present study, it is clear that the catalytic activity of manganese oxides for HCHO oxidation is influenced by a combination of factors including surface area and surface reducibility.

5.4 Conclusions

It has been proposed in this chapter a novel synthetic route to obtain highly ordered manganese based layered mesostructure material with a basal spacing up to 25 Å. The control of manganese oxidation states in the inorganic precursor $[\text{Mn}(\text{OH})_2]$, as a result of their interaction with surfactant molecule, is the basis for developing this synthesis.

Several factors that are important to the formation of mesostructured materials have been investigated, including the washing procedure, OH/Mn ratio, surfactant concentration (addition sequence) and cerium incorporation. Noticeably, when OH/Mn ratio was equal to 6 the most ordered layered mesostructure was obtained, indicating at optimal value for inorganic precursor/surfactant interaction. Changes in the surfactant concentration confirm that the formation of highly ordered layered mesostructure could be related to an ion-exchange process rather than a self-assemble one. Cerium incorporation in the system produces less ordered mesostructure at low loading (5%Ce), while at higher loading ($\geq 10\%$ Ce) the layered mesostructure was not formed, indicating perturbation of the inorganic/organic interaction. Finally, when surfactant is not employed, the mesostructure is not formed and oxidation of the inorganic precursor was observed. Thermal stability studies reveal that this layered structure is stable until 150°C.

After calcination, delamination of the layered mesostructure to produce a mixture of manganese oxides was demonstrated. The textural properties of the resulted manganese oxides reveal a type II isotherm characteristic of macroporous material. The redox properties of the material were improved by a more complete oxidation in the presence of surfactant molecule. Moreover, better inorganic/surfactant interaction results in a better oxidation, and the presence of Mn in higher oxidation states.

The catalytic activity of obtained manganese oxides by HCHO oxidation is excellent, and is highly dependent on their surface area and surface reducibility. The most active catalyst (MnOx 9) could completely oxidize HCHO into CO_2 and H_2O at 110 °C.

5.5 References

- ¹ Z. Tian, W. Tong, J. Wang, N. Duan, V. Krishnan, S. Suib, *Science*. **1997**, 276, 926.
- ² D. Terribile, A. Trovarelli, C. De Leitenburg, G. Dolcetti, *Chem. Mater.* **1997**, 9, 2676.
- ³ C. B. Azzoni, M. C. Mozzati, P. Galinetto, A. Paleari, V. Massarotti, D. Capsoni, M. Bini, *Solid State Commun.* **1999**, 112, 375.
- ⁴ B. Gillot, M. El Guendouzi, M. Laarj, *Mater. Chem. Phys.* **2001**, 70, 54.
- ⁵ J.Luo, S. Suib, *Chem. Commun.* **1997**, 11, 1031
- ⁶ J. Cai, S. Suib, *Inorg. Chem. Commun.* **2001**, 4, 493.
- ⁸ X.H. Feng, F. Liu, W.F Tan, X. W. Liu. *Clays Clay Miner.* **2004**, 52, 240.
- ⁹ T. Waernheim, A. Joensson, *J. Colloid Interface Sci.* **1988**, 125, 627.
- ¹⁰ Z. Liu, K. Ooi, H. Kanoh, W. Tang, T. Tomida, *Langmuir.* **2000**, 16, 4154.
- ¹¹ S.L. Brock, N. Duan, Z.R. Tian, O. Giraldo, H. Zhou, S. Suib, *Chem Mater.* **1998**, 10, 2619.
- ¹² Q. Feng, H. Kanoh, Y. Miyai, K. Ooi, *Chem Mater.* **1995**, 7, 1226.
- ¹³ H. Kanoh, W. Tang, Y. Makita, K. Ooi, *Langmuir.* **1997**, 13, 6845.
- ¹⁴ Y. Shen, S. Suib, C. O'Young, *J. Am. Chem. Soc.* **1994**, 116, 11020.
- ¹⁵ B. Aronson, A. Kinsler, S Passerini, W. Smyrl, A. Stein, *Chem. Mater.* **1999**, 11, 949.
- ¹⁶ S.-T.Wong, S.-F Cheng, *Inorg. Chem.* **1992**, 31, 1165.
- ¹⁷ D. Terribile, A. Trovarelli, J. Llorca, C. De Leitenburg, G. Dolcetti, *J. Catal.* **1998**, 178, 299.

CHAPTER 6

Chapter 6 : Sono-assisted preparation of Mg-Mn-Al Hydrotalcite like compounds and their application to formaldehyde removal

6.1 Introduction

Hydrotalcites (HT) are naturally occurring minerals with chemical composition $Mg_6Al_2(OH)_{16}CO_3 \cdot 4H_2O$ exhibiting layered crystal structures, comprised of positively charged hydroxide layers and interlayers composed of bicarbonate anions and water molecules. Their most general formula can be written as $[M^{2+}_{1-x}M^{3+}_x(OH)_2]^{x+}(A^{n-})_{x/n} \cdot mH_2O$. Figure 6.1 gives a schematic view of its structure.

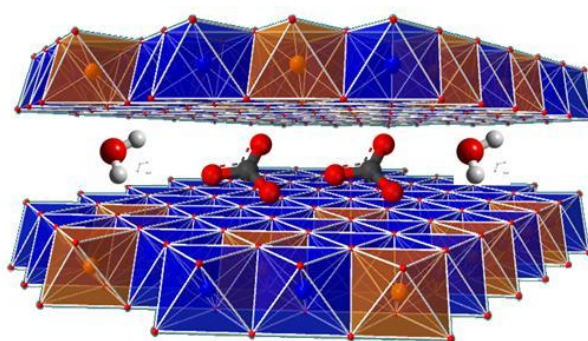


Figure 6.1. Schematic view of the structure of hydrotalcite. Bivalent and trivalent cations (e.g. Mg^{2+} and Al^{3+}) are six fold coordinated to form octahedra that share edges to constitute infinite layers. H_2O and CO_3^{2-} in the interlayer region represent the compensating anions.

As previously mentioned in the bibliographic chapter the application of US irradiation for the hydrotalcite synthesis was not extensively studied despite interesting features such as reducing time of preparation and small crystallites of HT that can be obtained using the US procedure. As discussed in the previous chapters, manganese oxides are one of the most active phases for HCOH complete catalytic oxidation, but usually these oxides present low specific surface area. The use of hydrotalcites (HTs) as precursor is an interesting way to obtain high surface area mixed manganese oxides. In this chapter we have attempted the preparation of Mn/Al HT using ultrasound. The effects of US on the structural, textural and acid-base properties of the solids and their performance in formaldehyde catalytic oxidation are studied.

This chapter concerns the results obtained within a collaboration project, ECOS-Nord France-Colombia, in conjunction with the National University of Colombia, including an

internship in the Solid State and Environmental Chemistry Laboratory during one month. At the same time, additional results were obtained in the context of the PHC-Galilée France-Italy collaboration project, including an internship at the University of Milan, Physic Chemistry and Electrochemistry Department for the period of half a month.

6.2 Experimental Section

6.2.1 Description of the experimental setup used for the preparation of hydrotalcites precursor using ultrasound (US)

Figure 6.2 presents the experimental setup employed for the hydrotalcite preparation using ultrasound. Sonic energy was provided by an ultrasonicator VWR International USC 200-2600, which generates 45 kHz ultrasound waves. Different parameters, like pH, *in-situ* temperature, US bath temperature and US power, were controlled during the synthesis of hydrotalcites, as shown in Figure 6.2.

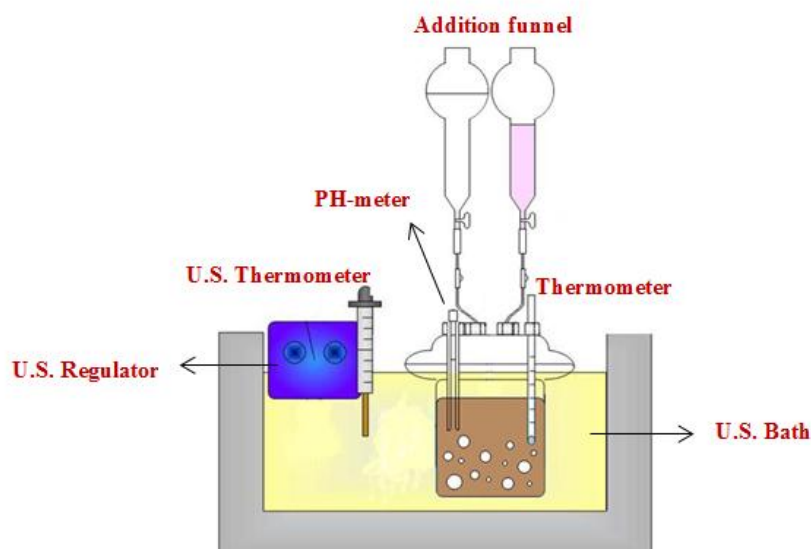


Figure 6.2. Experimental setup used for hydrotalcites preparation using Ultrasound

6.2.2 Synthesis of hydrotalcites precursors

The preparations of hydrotalcites precursors were made using the simultaneous co-precipitation technique at a constant pH. Sonication was applied during the co-precipitation. A solution containing adequate quantities of nitrates $\text{Mg}(\text{NO}_3)_2 \cdot 6\text{H}_2\text{O}$, $\text{Mn}(\text{NO}_3)_2 \cdot 4\text{H}_2\text{O}$ and $\text{Al}(\text{NO}_3)_3 \cdot 9\text{H}_2\text{O}$ [$\text{M}^{2+}(\text{Mg}^{2+}$ and/or $\text{Mn}^{2+})/\text{Al}^{3+} = 3$] was added slowly and mixed with a basic

solution containing NaOH and Na₂CO₃. The final pH was controlled between 9 and 10. The resulting slurry was filtered, washed several times with deionized water (6x200ml), dried in air at 60°C for 12h and calcined at 500°C for three hours. Four samples were synthesized with different Mg and Mn contents: Mg_{6-x}Mn_xAl₂HT with x = 0, 2, 4 and 6. These samples were denoted as Mg_{6-x}Mn_xAl₂HT_US. With the purpose of comparison, conventional syntheses of Mg_{6-x}Mn_xAl₂HT with x = 6 were also carried out according to reference [1]. This solid was denoted as Mn₆Al₂HT_Conv.

6.3 Results and discussion

6.3.1 Characterization of the as made hydrotalcites (HT)

6.3.1.1 Wide angle XRD and specific surface area

The wide angle XRD patterns of dried HT precursors are presented in Figure 6.3. The XRD pattern for Mg₆Al₂HT_US sample presents symmetric peaks for (003), (006), (110) and (113) planes, as well as broader peaks for the (009), (015) and (016) planes. These peaks are characteristics of clay minerals having layered hydrotalcite structures. Partial and total substitutions of Mn²⁺ into Mg²⁺ in the hydrotalcite structure resulted in the coexistence of hydrotalcite phase Mn₄Al₂(OH)₁₂CO₃·3H₂O (JCPDS 511526) and MnCO₃ (JCPDS 441472). For the Mn₆Al₂HT_Conv sample, the same hydrotalcite phase together with manganese carbonate was also obtained.

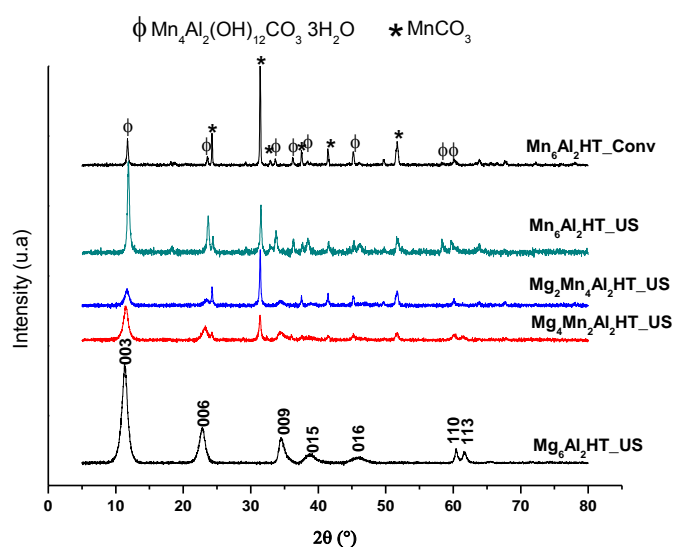


Figure 6.3. XRD patterns of Mg_{6-x}Mn_xAl₂HT_US and Mn₆Al₂HT_Conv samples

Taking into account that the crystallization process starts at the beginning of the coprecipitation step, these results suggest that the use of ultrasound during the coprecipitation step accelerates the crystal formation and, consequently, the hydrotalcite phase is obtained only after 2h. These results put forward that the use of ultrasound reduces the hydrotalcite preparation time from 24h (conventional synthesis) to 2h (US synthesis).

The formation of manganese carbonate during the synthesis of Mn based hydrotalcites has already been studied by Lamonier *et al.* [2]. The authors stated that, despite using a M^{2+}/M^{3+} ratio of 3, the $Mn_4Al_2(OH)_{12} \cdot 3H_2O$ hydrotalcite is preferably formed and the remaining Mn^{2+} species are available to react with carbonate to produce $MnCO_3$. Remarkably, for all samples a difference in the intensity of diffraction peaks of hydrotalcite and manganese carbonate phases was detected. For Mn_6Al_2 samples, the use of US procedure leads to lower proportion of $MnCO_3$ phase in comparison with conventional preparation. Then it seems that the US procedure favour the formation of $Mn_4Al_2(OH)_{12} \cdot 3H_2O$ phase to $MnCO_3$ phase.

It can also be observed for these samples that the diffraction peak (003) is shifted to higher 2θ values as the Mn content is increased in the sample (Table 6.1), varying from 11.3° for the $Mg_6Al_2HT_US$ sample to 11.9° for the $Mn_6Al_2HT_US$ sample. The substitution of Mn^{2+} confirms the slight change in 2θ values towards higher angles, since the ionic radius of Mn^{2+} (0.80Å) is slightly smaller than that of Mg^{2+} (0.86 Å).

Table 6.1. XRD parameters and surface areas for HT precursors

Sample code	Position of (003) XRD peak (2θ in $^\circ$)	Half width of (003) XRD Peak (2θ in $^\circ$)	Crystallite size Plane (003) in Å	BET surface area (m^2/g)
$Mg_6Al_2HT_US$	11.3	0.95	93	76
$Mg_4Mn_2Al_2HT_US$	11.5	0.90	100	66
$Mg_2Mn_4Al_2HT_US$	11.7	0.85	105	50
$Mn_6Al_2HT_US$	11.9	0.35	250	45
$Mn_6Al_2HT_Conv$	11.8	0.22	400	20

Table 6.1 also presents the crystallite size and BET surface area of dried HT precursors. It can be observed that the specific surface area is reduced with the increase of the crystallite size, indicating a lower crystallinity of the hydrotalcite structure when Mn is

present. This decrease can also be related to the presence of the MnCO_3 phase (Figure 6.1), which can contribute also to the decrease of the BET surface area. Noticeably, the $\text{Mn}_6\text{Al}_2\text{HT}$ sample prepared by ultrasound presents a higher BET surface area when compared to that prepared by the conventional method, corresponding to $45\text{m}^2/\text{g}$ and $20\text{m}^2/\text{g}$, respectively. This result can be directly related to the lower crystallite size in the $\text{Mn}_6\text{Al}_2\text{HT_US}$ sample (250\AA) in comparison with $\text{Mn}_6\text{Al}_2\text{HT_Conv}$ sample (400\AA). These results suggest that the use of ultrasound modifies the textural properties and crystallinity of dried HT precursor. In order to confirm this observation, $\text{Mn}_6\text{Al}_2\text{HT_Conv}$ and $\text{Mn}_6\text{Al}_2\text{HT_US}$ samples were studied by scanning electron microscopy (SEM). The SEM images are presented in Figure 6.4.

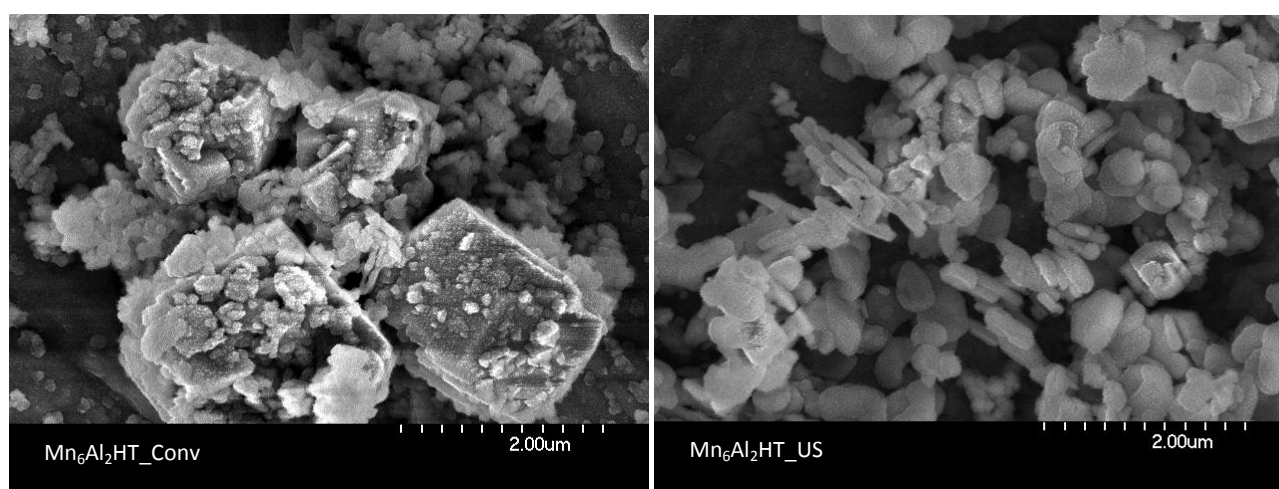


Figure 6.4. SEM images of the $\text{Mn}_6\text{Al}_2\text{HT_Conv}$ and $\text{Mn}_6\text{Al}_2\text{HT_US}$ samples.

The sample synthesized using the conventional procedure presents heterogeneous morphology, with large cubic particles surrounded by small plate-like particles (Figure 6.4). However, the sample prepared under sonication presents homogeneous plate-like particles morphology. These results are in agreement with the results obtained by XRD (Figure 6.3 and Table 6.1), in which a lower crystallite size was obtained for the $\text{Mn}_6\text{Al}_2\text{HT_US}$ sample. It is known that, when a liquid solid is submitted to ultrasound acoustics cavitations near the surface, the asymmetric bubble collapse is clearly induced, which generates a high speed jet of liquid to the surface. The collision of this jet can cause particle fragmentation as well as the reduction of agglomeration during the nucleation and crystal growing process, giving rise to particles with small crystal sizes, which can increase the surface area as was observed in Table 6.1. The sample prepared by conventional procedure was submitted to an ageing time of 24h at 60°C after coprecipitation, which favours the crystallization process, producing larger crystals and decreasing the surface area (Table 6.1).

6.3.1.2 Thermogravimetric and differential thermal analyses

The TG-DTA curves of the $\text{Mn}_6\text{Al}_2\text{HT_Conv}$ and $\text{Mn}_6\text{Al}_2\text{HT_US}$ samples are presented in Figure 6.5. The total weight loss for both samples was around 30 wt%. For the $\text{Mn}_6\text{Al}_2\text{HT_Conv}$ sample (Figure 6.5a), multiple weight losses were observed, the first weight loss of 5.7% was registered in the temperature range from 50 to 150°C. At the same temperature range, a single endothermic peak was observed in the DTA profile with a maximum at 140°C. The second weight loss of 3% was detected in the temperature range from 150 to 250°C. At the same temperature range, an endothermic peak with higher intensity was observed in the DTA profile with a maximum at 230°C. Subsequently, two weight losses of 5.7 and 12.7% between 300°C and 600°C were observed. The first weight loss should be ascribed to the removal of the interlayer water without collapse of the structure. The second weight loss corresponds to the elimination of water, from layer OH groups (dehydroxylation), and the remaining weight losses are attributed to decarbonation from interlayer carbonate.

Multiple weight losses were also observed for the $\text{Mn}_6\text{Al}_2\text{HT_US}$ sample (Figure 6.5b). Noticeably, the first weight loss, registered in the temperature range from 100 to 200°C, is higher for the $\text{Mn}_6\text{Al}_2\text{HT_US}$ sample (15.2%). It seems that the removal of interlayer water and water from layer hydroxyl groups (dehydroxylation) takes place at the same time for this sample. This weight loss coincided to an intense endothermic peak recorded at 150°C. The remaining weight losses are ascribed to decarbonation. It can be observed that the decarbonation occurred in three steps for this sample, with a total weight loss of 13.7% in this process, whereas for the sample prepared by the conventional method, a higher weight loss was observed in the decarbonation process (18.4%). This result can be explained by the higher proportion of carbonate species in the $\text{Mn}_6\text{Al}_2\text{HT_Conv}$ sample, as suggested previously by XRD analyses.

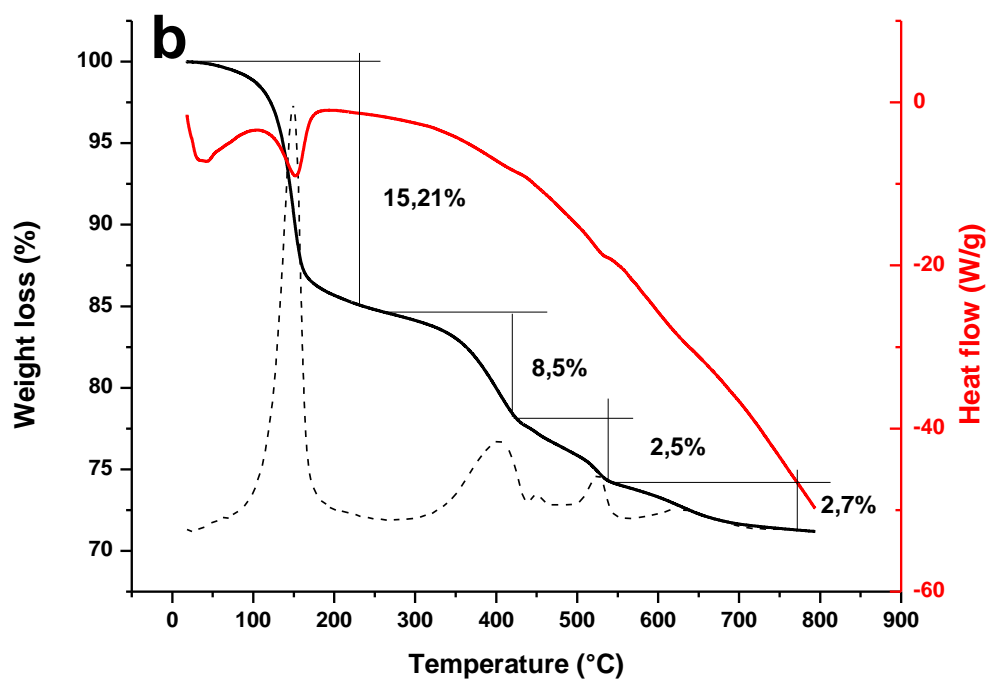
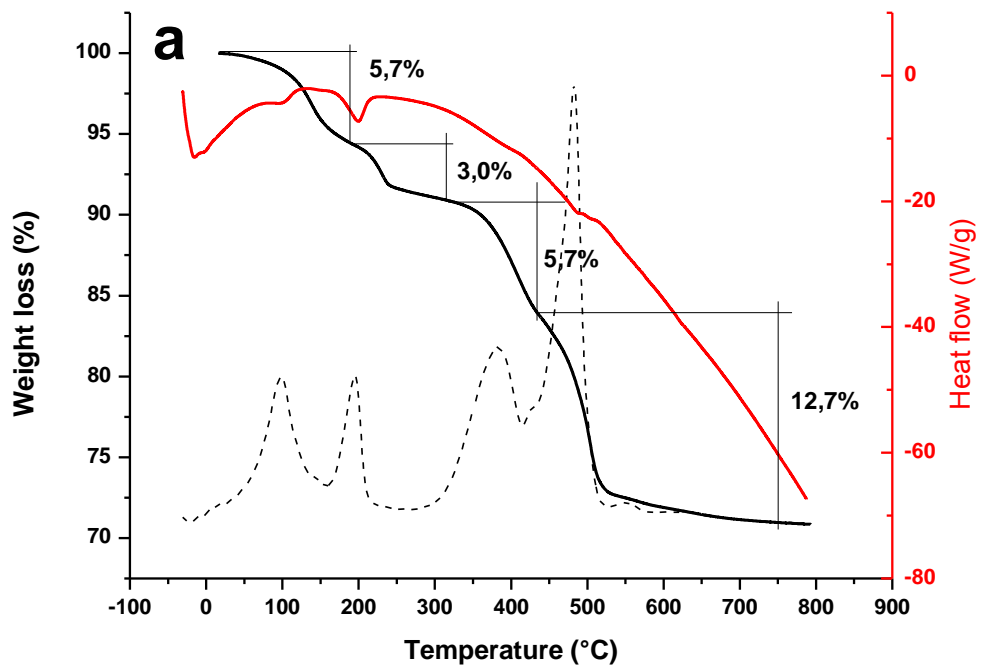


Figure 6.5. TG curves of Mg-Mn-HT for the samples a) $\text{Mn}_6\text{Al}_2\text{HT_Conv}$ and b) $\text{Mn}_6\text{Al}_2\text{HT_US}$.

6.3.2 Characterization of calcined hydrotalcites precursors

The HT precursors were calcined at 500°C in order to obtain the corresponding mixed oxides, following the protocol depicted in Figure 6.6.

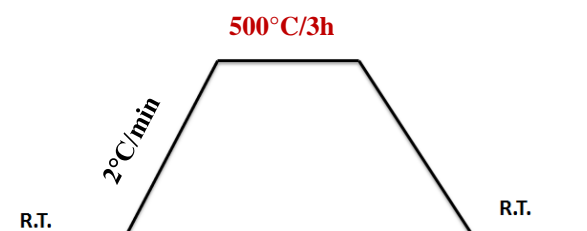


Figure 6.6. Calcination protocol. Air was used as atmosphere during calcination.

6.3.2.1. Wide angle XRD

The XRD patterns of resulting mixed oxides material are presented in Figure 6.7. The destruction of the HT phase and the formation of mixed oxides amorphous phase can be observed for all samples. Table 6.2 presents XRD identification of oxides present in calcined samples.

Table 6.2. Tentative XRD identification of oxides present in calcined samples.

Samples	Identified phases				
	Mn ₃ O ₄	Mn ₅ O ₈	Mn ₂ O ₃	MgMnO _x Spinel	MgO _x
Mg ₆ Al ₂ HT_US					•
Mg ₄ Mn ₂ Al ₂ HT_US	•			•	•
Mg ₂ Mn ₄ Al ₂ HT_US	•	•		•	
Mn ₆ Al ₂ HT_US	•	•	•		
Mn ₆ Al ₂ HT_Conv		•	•		

For the sample Mg₆Al₂HT_US, the magnesium oxide phase MgO (JCPDS 140286) was identified; no peak related to MgAl₂O₄ spinel phase was observed. The sample Mg₄Mn₂Al₂HT_US also presents peaks related with the MgO phase. It can also be observed a series of broader peaks related to the formation of Mg/Mn spinel phase, which are very difficult to identify and distinguish among those possibly formed upon decomposition of the starting material (MgMn₂O₄, Mg₂MnO₄, MgMnO₃), together with some peaks of hausmannite

phase Mn_3O_4 (JCPDS 751560) (Table 6.2). No peak related to aluminate phases was identified. For the sample $\text{Mg}_2\text{Mn}_4\text{Al}_2\text{HT_US}$, the peaks related to MgO disappear and the Mg/Mn spinel phase together with the Mn_3O_4 phase and Mn_5O_8 (JCPDS 391218) were observed (Table 6.2).

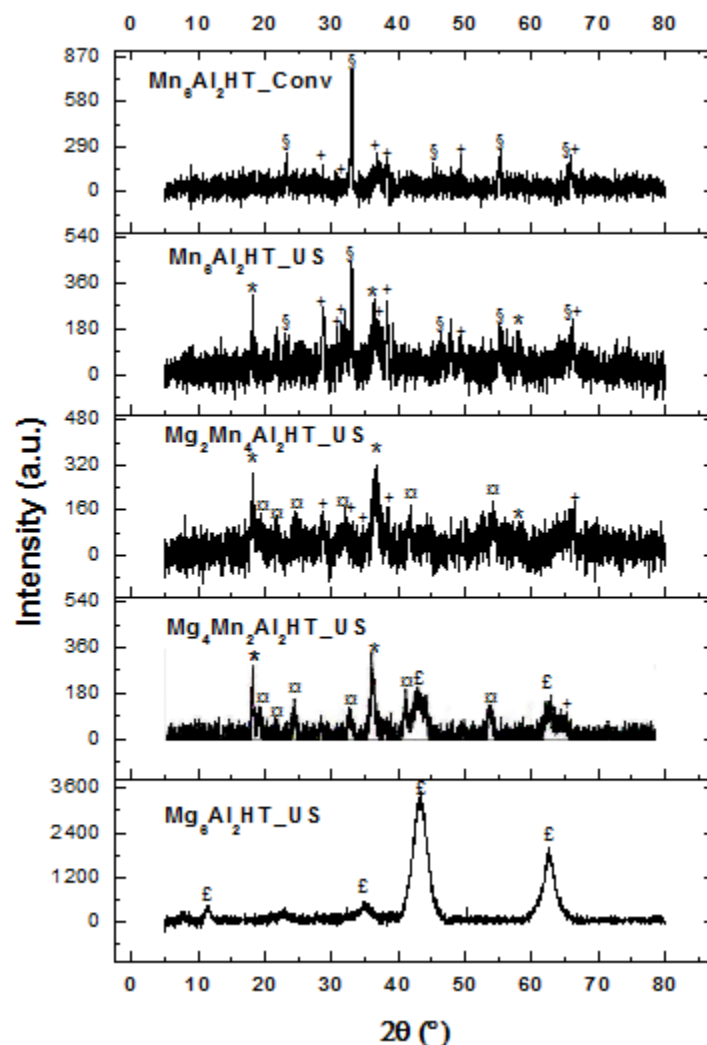


Figure 6.7. XRD patterns of calcined HT precursors £ MgO , ¤ Spinel MgMnO , * Mn_3O_4 , + Mn_5O_8 , § Mn_2O_3 .

Finally, the calcination of the sample containing only Mn and Al leads to the presence of amorphous manganese oxide phases; no peak of aluminate phases was detected for these samples. The Mn_3O_4 , Mn_5O_8 and Mn_2O_3 phases (JCPDS 894836) were roughly identified for the sample prepared under US (Table 6.2). Noticeably, for the sample prepared by the conventional method, diffraction peaks of higher intensity were obtained and only the Mn_2O_3 and Mn_5O_8 phases were identified as seen in Table 6.2. This result suggests that the oxidation

process of manganese species is different in Mg-free samples and depends on the composition of the starting precursor. The Mn_2O_3 and Mn_5O_8 phases are detected when starting from higher MnCO_3 proportion in the precursor ($\text{Mn}_6\text{Al}_2\text{HT_Conv}$), while starting from higher proportion of hydrotalcites phase in the precursor ($\text{Mn}_6\text{Al}_2\text{HT_US}$) results in the additional production of the Mn_3O_4 structure.

Hao *et al.* [3] studied the thermodynamic model of manganese carbonate oxidation. The authors stated that Mn_3O_4 and $\gamma\text{-MnOOH}$ are produced under air oxidation of MnCO_3 phase. Further oxidation of Mn_3O_4 was studied by Fritsch *et al.* [4], resulting in the proposal of two oxidation processes:



The same authors concluded that the reaction 1 is favoured at higher temperatures $> 450^\circ\text{C}$, while the reaction 2 occurs in the temperature range of $300\text{-}425^\circ\text{C}$. Supporting on this information it can be concluded that under the calcination conditions described above (Figure 6.6) the formation of the Mn_2O_3 phase is preferential, *via* formation of Mn_3O_4 as an intermediate product, when MnCO_3 was formed in the precursor. Apparently, the stabilization of Mn^{2+} cations into hydrotalcite structure does not facilitate the total oxidation of Mn_3O_4 into Mn_2O_3 and Mn_5O_8 at 500°C .

6.3.2.2 Textural properties

The delamination of HT precursors by calcination leads to an increase of specific surface area values. Table 6.3 shows the surface properties of calcined HT precursors.

Table 6.3. Textural properties of calcined HT precursors at 500°C

Sample code	BET surface area (m^2/g)	Pore diameter (nm)	Pore Volume (cm^3/g)
$\text{Mg}_6\text{Al}_2\text{HT_US}$	220	15.0	0.99
$\text{Mg}_4\text{Mn}_2\text{Al}_2\text{HT_US}$	177	13.5	0.63
$\text{Mg}_2\text{Mn}_4\text{Al}_2\text{HT_US}$	170	10.0	0.44
$\text{Mn}_6\text{Al}_2\text{HT_US}$	140	11.0	0.23
$\text{Mn}_6\text{Al}_2\text{HT_Conv}$	120	12.0	0.21

It can be seen in Table 6.3 that, for all calcined samples, the specific surface area (SSA) increases when compared to the dried precursors (Table 6.1). This result confirms previous observations, in which the delamination of hydrotalcite precursors through the calcination process leads to the formation of amorphous compounds that can significantly contribute to the increase of specific surface area [5]. It can also be observed that the SSA decreases with the increase of manganese content in the sample, with the samples $\text{Mg}_6\text{Al}_2\text{HT_US}$ and $\text{Mn}_6\text{Al}_2\text{HT_Conv}$ having the highest and lowest specific surface areas, $220\text{m}^2/\text{g}$ and $120\text{m}^2/\text{g}$, respectively. This result arises from the formation of manganese oxides having lower specific surface areas. Noticeably, the sample prepared under sonication presents a surface area ($140\text{m}^2/\text{g}$) higher than that of the conventionally synthesized sample ($120\text{m}^2/\text{g}$). This could be due to the production of smaller crystals in the HT precursor when sonication is applied, giving rise to an increase in the specific surface area of the mixed oxides obtained after calcination. The pore diameter of the sample is also presented in Table 6.3. It can be observed that all samples exhibited similar pore diameter, between 10nm and 15nm, indicating that the variation of the manganese content has no influence in the pore diameter of the resulting mixed oxides. However, decrease in the pore volume was observed when the Mn content was increased according to the diminution of the specific surface area.

6.3.2.3 Redox properties

The TPR profiles of the calcined samples are shown in Figure 6.8. It can be observed that, for the sample containing only Mg and Al ($\text{Mg}_6\text{Al}_2\text{HT_US}$), no reduction peak was detected in the temperature range considered. This indicates that the reduction of Mg^{2+} does not take place under these experimental conditions. Thus, any hydrogen consumption recorded during TPR analysis of the Mg-Mn-HT sample should be due to reduction of manganese.

The addition of manganese species in the HT structure results in an enhancement in the redox properties for all the samples. For the $\text{Mg}_4\text{Mn}_2\text{Al}_2\text{HT_US}$ sample, two reduction peaks with maxima at 350 and 450°C were detected, respectively, together with a shoulder at 520°C. This two-step reduction process was already described in the previous chapter and is related to the reduction of higher oxidation states manganese species Mn^{4+} into Mn^{3+} at low temperature (first reduction step) and the complete reduction of Mn^{3+} into Mn^{2+} is achieved in the second reduction step. The shoulder observed at 520°C could be ascribed to amorphous

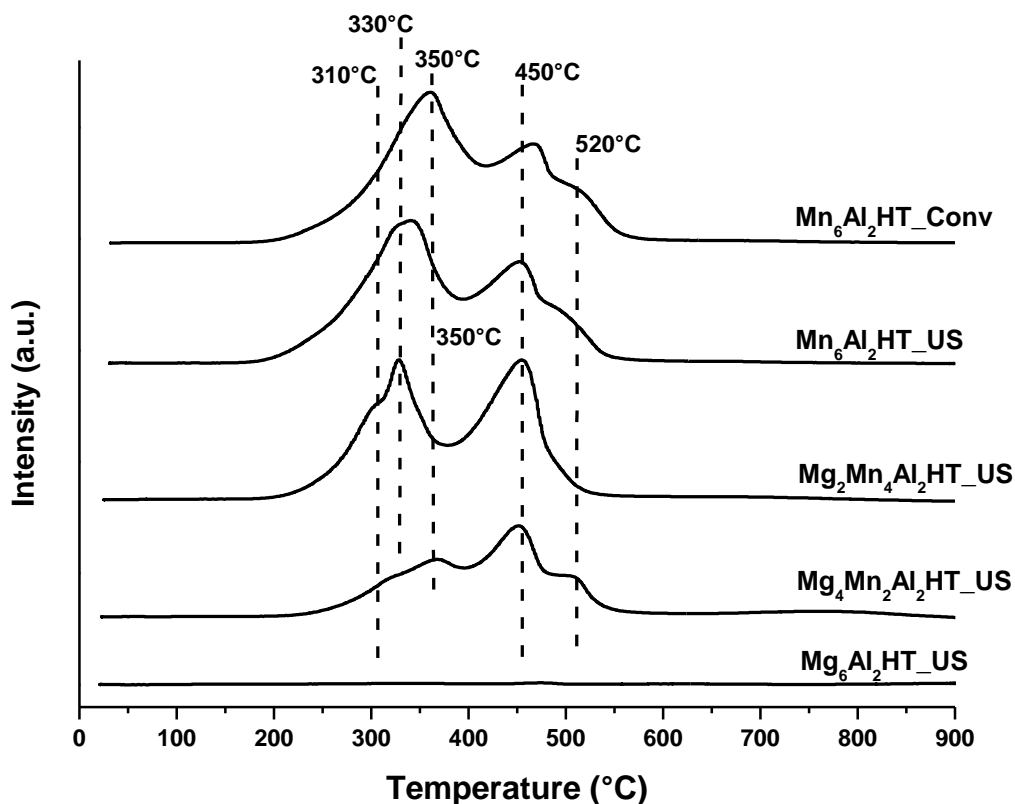


Figure 6.8. H₂-TPR profiles of calcined samples.

manganese aluminates not detected by XRD. An increase of Mn content leads to the same reduction profile. For the sample Mg₂Mn₄Al₂HT_US, the first reduction process takes place at lower temperatures with a maximum at 330°C, together with a small shoulder at 310°C. It can also be observed an increase in the relative intensities of the first reduction peak and the absence of the shoulder present at higher temperatures. These results are in agreement with the obtained by XRD analysis, in which the detection of the Mn₅O₈ phase, among others, confirms the presence of manganese in higher oxidation states. Moreover, the decrease in the intensity of diffraction peaks ascribed to the Mg/Mn spinel phase could explain that the reduction occurs at lower temperatures.

For the sample containing only Mn and Al, prepared under sonication and by conventional method, the same reduction profile was observed. Noticeably, for these samples, the relative intensity of the first reduction step increases, indicating the presence of

manganese species with higher oxidation states. It can also be detected that, for the sample prepared by the conventional process, the reduction process is shifted to higher temperatures with maxima at 350°C and 460°C, while for the sample prepared under sonication, maxima at 330°C and 450°C were observed. This is probably related to the presence of higher crystallite sizes of the mixed oxide obtained after calcination, as was demonstrated by high intensity peaks in XRD analysis for the Mn₆Al₂HT_Conv sample. These results suggest that the use of ultrasound not only modifies the structure of the resulting mixed oxides but also increases the reducibility of the resulting material by the creation of smaller particle sizes. Table 6.4 shows the H₂ TPR quantitative results of calcined samples.

Table 6.4. H₂-TPR quantitative results and Mn 3s surface characterization results from XPS

Samples	Consumed H ₂ mmol/g	AOS TPR	Mn 3s			AOS XPS
			BE(1)/eV ^a	BE(2)/eV ^a	ΔE/eV ^b	
Mn ₆ Al ₂ HT_US	6.5	3.1	89.2	84.2	5.0	3.4
Mn ₆ Al ₂ HT_Conv	6.3	3.0	89.2	84.1	5.1	3.3

^aPosition of Mn 3s split peak at (1) higher and (2) lower binding energy (BE)

^bSplitting width of Mn 3s: BE(1)-BE(2)

^c Calculated from $\Delta E \approx 7.88 - 0.85n$

It can be seen in Table 6.4 that the total H₂ consumption during reduction for the samples containing only Mn-Al. The highest H₂ consumption (6.5mmol/g) was obtained for the sample Mn₆Al₂HT_US, confirming the observation described previously, in which the reduction of mixed oxides synthesized via hydrotalcite using US is enhanced with respect to those obtained by the conventional method. The average oxidation states (AOS) from TPR analyses are also shown in Table 6.4, a higher oxidation state was observed for the sample prepared using US. This result is in accordance with the higher reducibility obtained for the Mn₆Al₂HT_US sample, in which the reduction took place at lower temperatures.

Table 6.4 also summarizes the XPS data obtained from the Mn 3s spectral region for the Mn₆Al₂ samples prepared by conventional and US methods. As reported in Table 6.4, the Mn 3s splitting energy is 5.0 and 5.1 eV for the samples Mn₆Al₂HT_US and Mn₆Al₂HT_Conv, respectively. This result suggests that the preparation method does not strongly affect the manganese species on the surface. The calculated average oxidation states of surface Mn atoms for these samples are 3.4 and 3.3, respectively. These values lie between

the AOS values 3.2 and 3.6 corresponding to Mn_2O_3 and Mn_5O_8 , respectively. This result is in agreement with the Mn_2O_3 and Mn_5O_8 phases identified by XRD analyses for the both calcined samples. This result agrees also with the AOS obtained from H_2 -TPR analyses (Table 6.4).

6.3.3 Catalytic activity of calcined hydrotalcites precursors

The samples calcined at 500°C were tested in the total oxidation of formaldehyde; the light-off curves are depicted in Figure 6.9. When formaldehyde conversion is complete, H_2O and CO_2 are the only products observed. It can be observed in Figure 6.9 that the catalytic activity follows the sequence $\text{Mn}_6\text{Al}_2\text{HT_US} > \text{Mn}_6\text{Al}_2\text{HT_Conv} > \text{Mg}_2\text{Mn}_4\text{Al}_2\text{HT_US} > \text{Mg}_4\text{Mn}_2\text{Al}_2\text{HT_US} > \text{Mg}_6\text{Al}_2\text{HT_US}$. The mixed oxide obtained from the simple hydrotalcite, containing only Mg-Al, presents the lowest catalytic activity. Moreover, for this sample, the light-off curve presents a different shape, suggesting a two-step oxidation process. The catalytic result also shows the effect of Mn addition in the hydrotalcite precursors, indicating a beneficial effect in the catalytic performance of the resulting mixed oxide by the incorporation of this metal. It can also be observed that the catalytic activity of the $\text{Mn}_6\text{Al}_2\text{HT_US}$ is slightly better compared to the sample prepared by conventional method. This result is in accordance with that obtained by H_2 -TPR and XPS, which suggests a higher proportion of manganese species with higher oxidation states for the $\text{Mn}_6\text{Al}_2\text{HT_USConv}$ sample. With the purpose of comparison to other manganese oxide tested under similar conditions, the temperature of 50% HCOH conversion (T_{50}) and 100% HCOH conversion (T_{100}) are presented in Table 6.5.

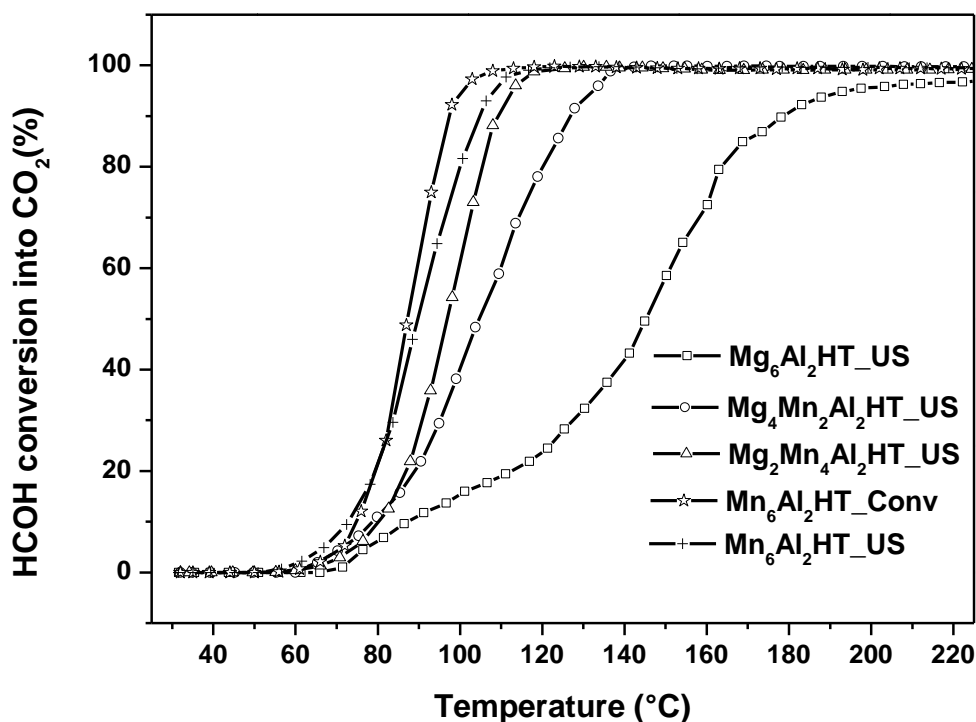


Figure 6.9. Catalytic performance of calcined hydrotalcite precursor.

Table 6.5. Catalytic performance of calcined materials

Sample code	T ₅₀ (°C)	T ₁₀₀ (°C)
Mg ₆ Al ₂ HT_US	145	210
Mg ₄ Mn ₂ Al ₂ HT_US	105	145
Mg ₂ Mn ₄ Al ₂ HT_US	98	130
Mn ₆ Al ₂ HT_US	85	120
Mn ₆ Al ₂ HT_Conv	90	115

It can be observed in Table 6.5 that the sample Mn₆Al₂HT_US, oxidized 50% formaldehyde selectively to H₂O and CO₂ at 85°C, total HCOH conversion is reached at 115°C. The sample obtained by the conventional method also presents an excellent catalytic activity (T₅₀ = 90°C). This small difference could be related to a better dispersion of manganese species for the sample prepared under sonication, as demonstrated by the specific surface area and TPR results. The addition of Mg in the system not only caused a decrease in the catalytic activity, but also a modification in the selectivity was observed. Actually, for

these samples, when conversion is incomplete by-products are produced in high proportion. In order to estimate the selectivity of the samples, the evolution of reaction products as a function of time during the catalytic test was studied.

Figure 6.10 shows the evolution of reaction products for the $\text{Mn}_6\text{Al}_2\text{HT_US}$ and $\text{Mn}_6\text{Al}_2\text{HT_Conv}$ samples. It can be seen in Figure 6.10 that, for the $\text{Mn}_6\text{Al}_2\text{HT_US}$ and $\text{Mn}_6\text{Al}_2\text{HT_Conv}$ sample, the evolution profile is similar and the formation of by-products was not detected during the HCOH oxidation, indicating the suitable selectivity of the catalysts to produce only CO_2 and H_2O . At the beginning of the catalytic test, during the stabilization, the formaldehyde signal slowly increases as a result of catalyst adsorption and saturation. Noticeably, for the sample prepared by conventional method the stabilization time is higher, suggesting a higher adsorption capacity for $\text{Mn}_6\text{Al}_2\text{HT_Conv}$ sample. Nevertheless, the SSA for this sample is lower. When the reaction starts, the HCOH signal increases reaching the maximum value around 55 and 65°C for $\text{Mn}_6\text{Al}_2\text{HT_US}$ and $\text{Mn}_6\text{Al}_2\text{HT_Conv}$, respectively. The evolution of formaldehyde at low temperatures was discussed in the previous chapter and is related to the HCOH multilayer formation due to surface coverage on the catalyst surface during the stabilization step. Subsequently, the HCOH signal decreases progressively reaching the minimum value around 100°C for both samples, while the CO_2 signal gradually increases and then reaches the maximum value at 125°C and 135°C for $\text{Mn}_6\text{Al}_2\text{HT_US}$ and $\text{Mn}_6\text{Al}_2\text{HT_Conv}$, respectively. Suggesting that the sample prepared under US presents a higher catalytic activity. After this point, the CO_2 signal decreases until the stationary state. This oxidation process was already discussed in the previous chapter, when the formation of surface formate intermediates was suggested. The oxidation of the formate species by the lattice oxygen produces CO_2 that is then desorbed as oxidation products. The addition of Mg modifies the evolution of products during the reaction. Figure 6.11 shows the evolution of reaction products for the sample $\text{Mg}_2\text{Mn}_4\text{Al}_2\text{HT_US}$ and $\text{Mg}_4\text{Mn}_2\text{Al}_2\text{HT_US}$.

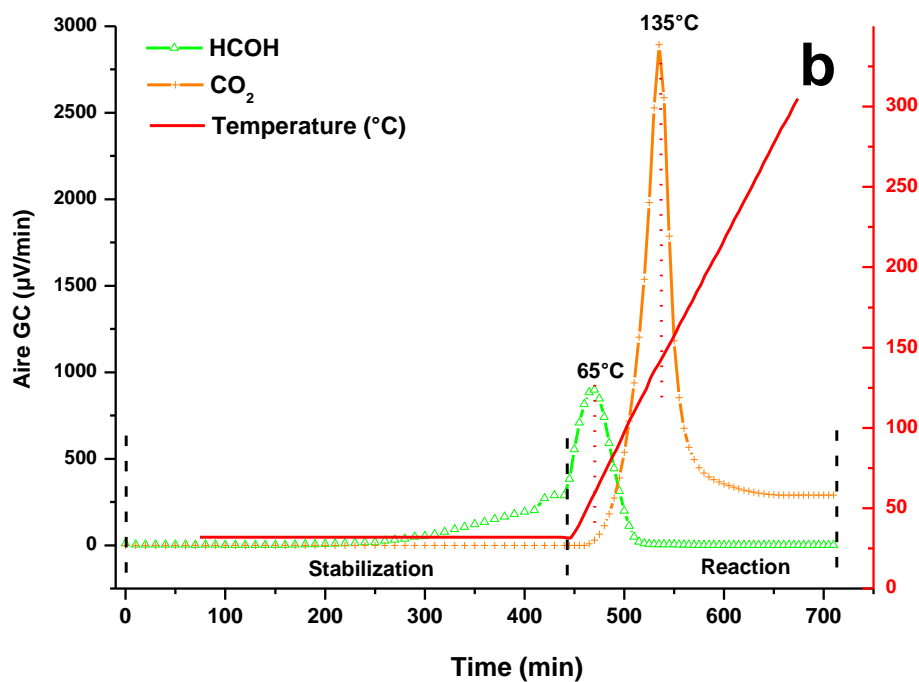
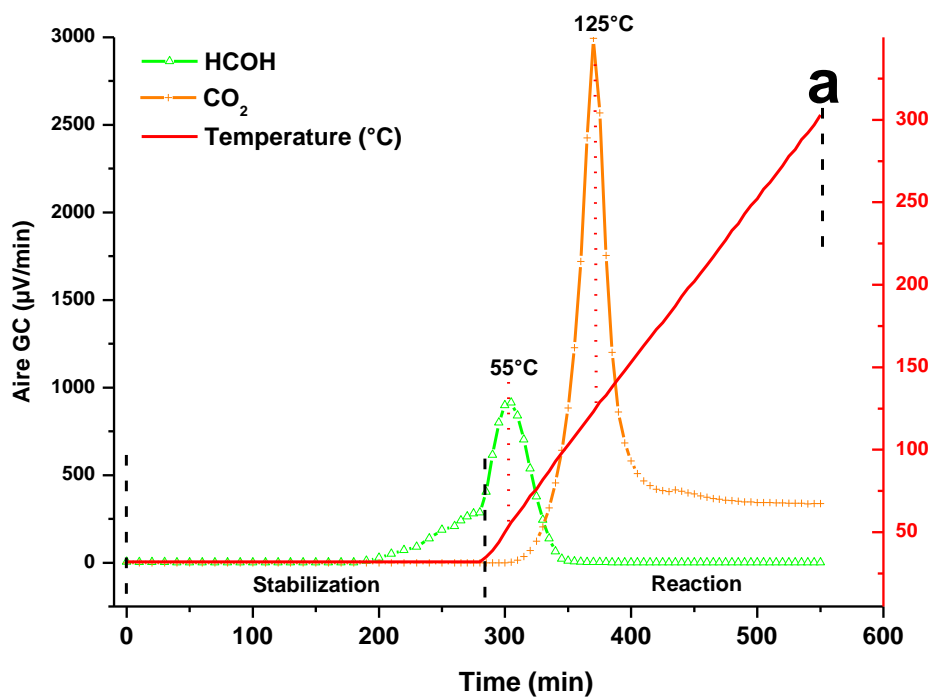


Figure 6.10. Evolution of reaction products during the catalytic test for the sample a) $\text{Mn}_6\text{Al}_2\text{HT_US}$ and b) $\text{Mn}_6\text{Al}_2\text{HT_Conv}$.

For the $\text{Mg}_2\text{Mn}_4\text{Al}_2\text{HT_US}$ sample (Figure 6.11a) the evolution of HCOH and CO_2 follows the same trend when compared to the previous sample, but the desorption phenomena are shifted to higher temperatures, suggesting a lower catalytic activity. Noticeably, for this sample, the formation of by-products was observed at an intermediate reaction level. The evolution of by-product 1 (B.P. 1) starts with a temperature increase, reaching the maximum value around 65°C . The evolution of methanol starts few minutes after, reaching the maximum value at 90°C . This result suggests that the formations of these by-products occurs at room temperature during the stabilization step and are then desorbed after heating. The formation of by-products during the catalytic test indicates a different HCOH oxidation mechanism. This could be related to the basic properties of Mg species present in the material.

Further addition of Mg in the material results in an increase of the by-products signal. Figure 6.11b shows the evolution of reaction products during the catalytic test for $\text{Mg}_4\text{Mn}_2\text{Al}_2\text{HT_US}$ sample. Remarkably, for this sample, the evolution of B.P. 1 starts at room temperature during stabilization and its signal increases slowly together with the HCOH signal until stabilization. This result suggests that one part of formaldehyde was already converted at room temperature during the stabilization to form B.P.1 on the catalyst surface. When the reaction starts, the B.P.1 and HCOH signals increase until the maxima values are reached at 47°C and 71°C , respectively. After this point, the B.P. 1 signal decreases progressively reaching the minimum value at around 125°C , while the methanol signal increases and then reaches the maximum value at 92°C . The progressively decrease of the methanol signal until the minimum value at 145°C was accomplished together with the increase of CO_2 signal, which reaches the maximum value at 145°C . After this point, the CO_2 signal decreases until the stationary state.

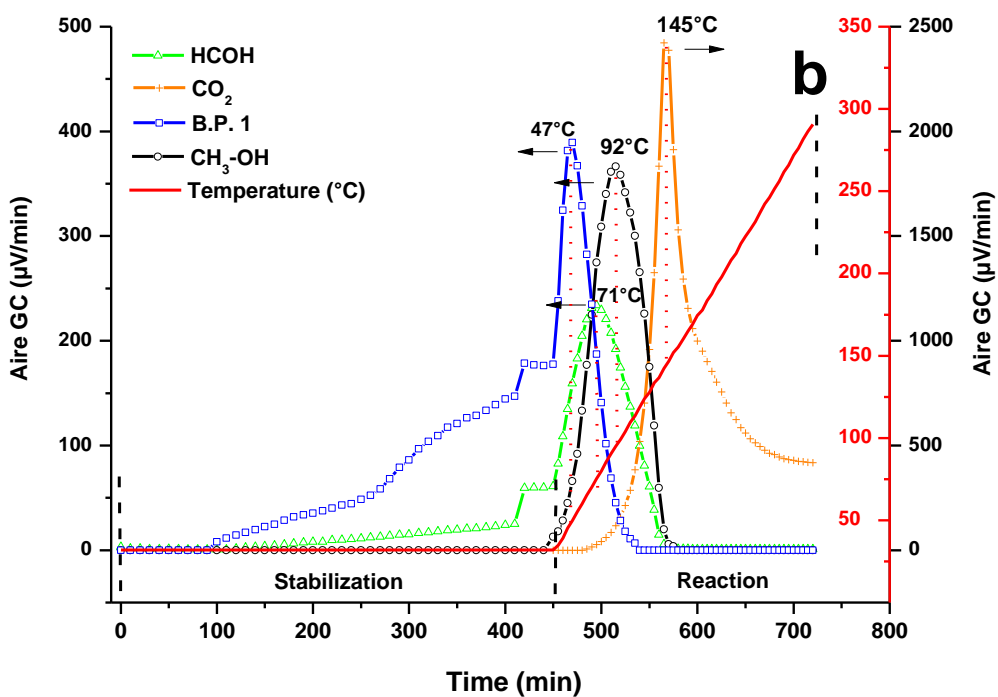
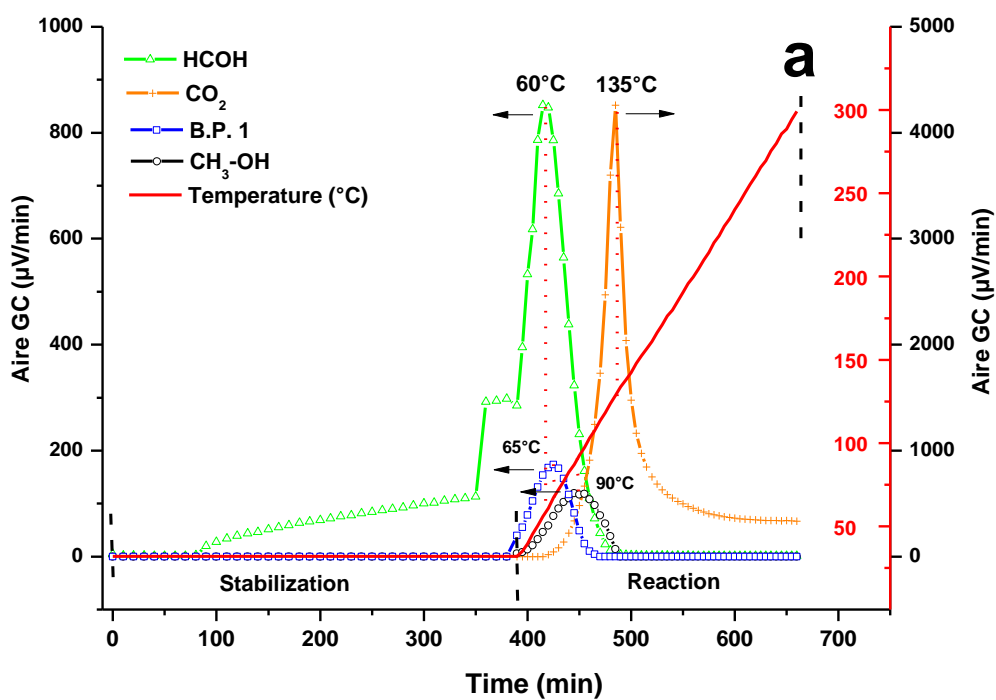


Figure 6.11. Evolution of reaction products during the catalytic test for the sample a) $Mg_2Mn_4Al_2HT_US$ and b) $Mg_4Mn_2Al_2HT_US$.

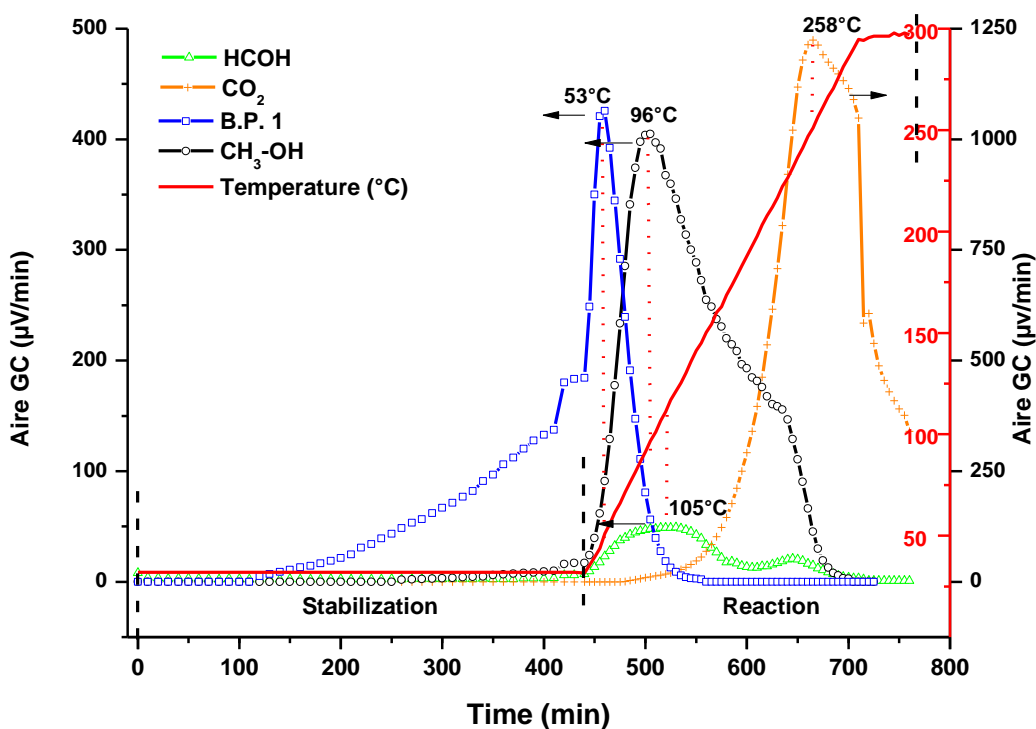


Figure 6.12. Evolution of reaction products during the catalytic test for the sample $Mg_6Al_2HT_US$

Figure 6.12 shows the evolution of reaction products for the sample containing only Mg/Al. It can be observed that the evolution of reaction products present the same behaviour when compared to the sample $Mg_4Mn_2Al_2HT_US$. However, for $Mg_6Al_2HT_US$ further increase of the by-products signal was detected. This result confirms that the presence of by-products is related to the basic properties of Mg species present in the material. It can also be observed in Figure 6.12 that when the reaction starts, the B.P.1, methanol and HCOH signals increase until the maxima values are reached at 53°C, 96 and 105°C, respectively. Noticeably, for this sample, the progressively decrease of the methanol signal until the minimum value was shifted to higher temperatures, at around 258°C. It was accomplished together with the increase of CO_2 signal, which reaches the maximum value at the same temperature. After this point, the CO_2 signal decreases until the stationary state.

Based on these results some trends can be established: samples containing only Mn/Al are capable to oxidized formaldehyde selectively towards CO_2 and H_2O . Mg addition strongly modifies the HCOH oxidation mechanism by the formation of two by-products. The B.P. 1,

produced and desorbed at room temperature for the samples containing high Mg content, was not possible to identify. However, the higher retention time of this product in the chromatogram suggest that could be related to heavy products such as condensation products, i.e methyl formate or dimethyl ether. It seems that during during the stabilization step at room temperature the probability to form and desorb these products is higher since the catalyst surface is saturated. Therefore, adsorbed formaldehyde molecules in the vicinity with other formaldehyde molecule could react at room temperature to produce methyl formate or dimethyl ether catalysed over MgO surface.

Methanol was the other by-product formed during the reaction. The production of methanol over MgO surfaces by formaldehyde adsorption have been studied by Peng and Barteau [6]. The authors proposed the formation of methoxy and formate species by a Cannizaro type reaction with addition of lattice oxygen from the surface as follows:

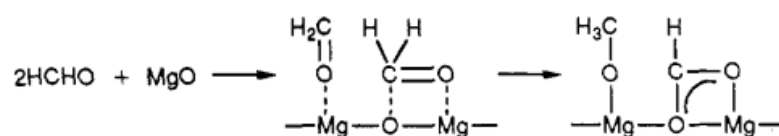


Figure 6.13. Schematic representation of Cannizaro reaction on the surface of MgO.

This reaction is similar to the Cannizaro reaction taking place in basic aqueous solution, in which a hydroxyl anion first adds to the carbonyl carbon of a formaldehyde molecule. The strong electron donating character of O^- in this intermediate facilitates the departure of the aldehydic hydrogen with its electron pair. This hydride attacks another formaldehyde molecule to form a methoxide ion and formic acid. Similar to this solution reaction, an adsorbed formaldehyde molecule attached to a surface base site (O^{2-}) on MgO could form a surface dioxymethylene intermediate. The transfer of electrons from the surface oxygen to the carbonyl carbon would weaken the bond between the hydrogen and the carbonyl carbon. An adsorbed HCOH molecule in the vicinity could accommodate this hydride, forming a surface methoxide group bonded on a weak acidic site (Mg^{2+} ion).

In order to evaluate the influence of Mg addition of the hydrotalcites precursors on the basic properties of the resulting mixed oxides, the determination of surface basicity by pulse

technique using benzoic acid as a probe molecule was carried out. Table 6.6 presents the results obtained.

Table 6.6. Summary of the results obtained from surface basicity by pulse technique using benzoic acid.

Sample code	Basicity by benzoic acid , C ₇ H ₆ O ₂ (mequiv/ g ⁻¹)			Basicity by benzoic acid , C ₇ H ₆ O ₂ (mequiv/ m ²)		
	Total sites	Weak sites	Strong sites	Total sites	Weak sites	Strong sites
Mg ₆ Al ₂ HT_US	665	35,60 (5.4%)	629.4 (94.6%)	3.60	0.19 (5,3%)	3.41 (94.7%)
Mg ₄ Mn ₂ Al ₂ HT_US	427,56	25,36 (5,9%)	402,20 (94.1%)	2,52	0,15 (5,9%)	2,37 (94,1%)
Mg ₂ Mn ₄ Al ₂ HT_US	525,08	32,49 (6.2%)	492,59 (93,8%)	2,48	0,15 (6,1%)	2,33 (93,9%)
Mn ₆ Al ₂ HT_US	341,23	64,21 (18.8%)	277,02 (81,2%)	2,3	0,43 (18,7%)	1,87 (81,3%)
Mn ₆ Al ₂ HT_Conv	273.29	36.20 (13.2%)	237.1 (86.7%)	1.45	0.19 (13.1%)	1.26 (86.9%)

It can be clearly seen in Table 6.6 that the number of total basic sites increases with the increase of Mg content in the sample. Regarding the strength of basic site, weak or strong, it can be observed that the proportion of strong sites is slightly higher for the samples containing Mg. In the case of Mg-Al mixed oxides the active basic sites are associated to Mg²⁺-O²⁻ acid-base pairs [7]. Noticeably, it can be observed that the samples containing only Mn present also an important number of basic sites that could be related to the presence of Mn⁴⁺ - O²⁻ acid-base pairs. Concerning the number of sites per square meter the trends observed is the same. Remarkably, for the sample containing only Mn/Al prepared under sonication the number of sites is higher, this result is expected considering that Mn₆Al₂HT_US sample with lower crystal size possess higher concentrations of Mn⁴⁺-O²⁻ acid-base pairs. The determination of surface basicity is in accordance with the catalytic results in which the formation of byproducts was related to the presence of basic sites. However, for the samples containing only Mn/Al, it was shown that the redox properties prevails over the basic properties since CO₂ and H₂O are the only products observed during the reaction.

Table 6.7. Summary of main properties and catalytic performance different manganese based materials prepared during this thesis.

Catalyst	Quantity of Catalyst	Reaction Mixture	SSA (m ² /g)	Mn AOS _{XPS}	Mn AOS _{TPR}	T ₅₀ (°C)
Chapter 4						
Pure manganese oxides						
MnO _x C	200mg	HCOH= 500ppm O ₂ = 20% vol and He	31	2.8	2.8	180
MnO _x SC	200mg	HCOH= 500ppm O ₂ = 20% vol and He	20	2.9	3.0	150
MnO _x C_TA	200mg	HCOH= 500ppm O ₂ = 20% vol and He	121	3.2	3.2	110
MnO _x SC_TA	200mg	HCOH= 500ppm O ₂ = 20% vol and He	90	3.4	3.4	90
Calcined (n)MnO _x -(1-n)CeO ₂						
n = 1	200mg	HCOH= 500ppm O ₂ = 20% vol and He	20	2.9	-	155
n = 0.75	200mg	HCOH= 500ppm O ₂ = 20% vol and He	91	2.9	-	130
n = 0.5	200mg	HCOH= 500ppm O ₂ = 20% vol and He	100	2.8	-	135
n = 0.25	200mg	HCOH= 500ppm O ₂ = 20% vol and He	130	2.8	-	125
n = 0	200mg	HCOH= 500ppm O ₂ = 20% vol and He	73	-	-	165
Acis treated (n)MnO _x -(1-n)CeO ₂						
n = 1	200mg	HCOH= 500ppm O ₂ = 20% vol and He	82	3.4	-	90
n = 0.75	200mg	HCOH= 500ppm O ₂ = 20% vol and He	160	3.2	-	105
n = 0.5	200mg	HCOH= 500ppm O ₂ = 20% vol and He	112	2.8	-	155
n = 0.25	200mg	HCOH= 500ppm O ₂ = 20% vol and He	137	2.8	-	185
n = 0	200mg	HCOH= 500ppm O ₂ = 20% vol and He	75	-	-	200
Chapter 5						
MnO _x 9	200mg	HCOH= 170ppm O ₂ = 20% vol and He	70	3.0	3.1	90
Chapter 6						
Mg ₆ Al ₂ HT_US	200mg	HCOH= 170ppm O ₂ = 20% vol and He	220			145
Mg ₄ Mn ₂ Al ₂ HT_US	200mg	HCOH= 170ppm O ₂ = 20% vol and He	177			105
Mg ₂ Mn ₄ Al ₂ HT_US	200mg	HCOH= 170ppm O ₂ = 20% vol and He	170			98
Mn ₆ Al ₂ HT_US	200mg	HCOH= 170ppm O ₂ = 20% vol and He	140	3.4	3.1	85
Mn ₆ Al ₂ HT_Conv	200mg	HCOH= 170ppm O ₂ = 20% vol and He	120	3.3	3.0	90

6.4 Conclusions

In this chapter, Mg-Mn-Al hydrotalcites with different composition were prepared by a coprecipitation method using ultrasound. The results confirm the success of synthesized hydrotalcites as mixed oxides precursors using ultrasound as an ageing method. Moreover, it has been found that the sample prepared under sonication presents homogeneous morphology and much highly dispersed particles in only 2 h of treatment time when compared to the sample prepared by conventional method (24 h treatment).

The thermal decomposition at 500°C leads to the formation of mixed oxides with high specific surface area. It has been shown that mixed oxides derived from hydrotalcites synthesized under sonication have larger specific surface area and improved redox properties. The resulting mixed oxides were tested in the formaldehyde catalytic oxidation. The catalysts containing Mg presents the lowest catalytic activity towards CO₂, and the formation of by-products is evidenced in these materials. The catalytic result also shows the beneficial effect of Mn addition in the hydrotalcite precursors. Furthermore, the highest catalytic activity is found for samples containing only Mn/Al. It is also found that the catalytic activity of sample prepared using ultrasound is slightly better compared to that of the sample prepared by the conventional method. Finally, it can be concluded that the Mn-Al hydrotalcite used as precursor for obtaining mixed manganese oxides is an excellent catalyst in the formaldehyde oxidation reactions, showing that ultrasound is an effective technique to obtain solids with better properties in reduced time.

6.5 References

- ¹ Y. Seida, Y. Nakano, Y. Nakamura, *Clays Clay Miner.* **2002**, *50*, 525
- ² J.F. Lamonier, A. B. Boutoundou, C. Gennequin, M.J. Perez-Zurita, S. Siffert, A. Aboukais. *Catal. Lett.* **2007**, *118*, 165.
- ³ Hao, Ruixia; Peng, Shenglin From Chinese Journal of Geochemistry. **1999**, *18*, 80-86.
- ⁴ S. Fritsch, J. Sarrias, A. Roussel, G. Kumkarni. *Mater Research Bull.* **1998**, *33*, 1185.
- ⁵ F. Cavani, F. Trifiro, A. Vaccari. *Catal Today.* **1991**, *11*, 173.
- ⁶ X.D. Peng, M. A. Barteau, *Langmuir.* **1989**, *5*, 1051.
- ⁷ M. J. Climent, A. Corma, S. Iborra, K. Epping, A. Velty. *J. Catal.* **2004**, *225*, 316.



CONCLUSIONS AND PERSPECTIVES

CONCLUSIONS AND PERSPECTIVES

Considering previous studies concerning total catalytic oxidation, usually involving BTX and chlorinated compounds, the catalytic oxidation of formaldehyde has not been extensively studied up to now. Nevertheless, the literature review shows that this reaction can be performed at RT on noble metal based catalysts. However, the development of less expensive active phase is needed for a large-scale industrial development. Manganese oxides based nanomaterials are described as the most promising catalysts. The main objective of the present study is to develop the synthesis of manganese based nanomaterials with improved textural, structural and redox properties devoted to formaldehyde catalytic oxidation.

In the first part of the thesis, the surfactant assisted synthesis followed by chemical activation (acidic treatment) is proposed for the synthesis of high active mesoporous manganese oxide materials. It is shown that, the structural, textural and redox properties of MnOx samples are deeply modified when the chemical activation was carried out after the calcination step: (i) Mn₃O₄ is transformed to Mn₅O₈ phase, (ii) the surface specific area is increased in 75% by the decrease of the crystal size and the formation of small pore diameter, and (iii) the redox properties are enhanced at low temperatures due to the oxidation of Mn³⁺ into Mn⁴⁺. As a result, high formaldehyde catalytic performance is observed after the chemical activation: a decrease of 60°C of the T₅₀ value when compared to the calcined sample. The same synthesis protocol is followed including cerium in the system. For calcined samples, the substitution of Ce⁴⁺ by Mn species in the fluorite structure to form the solid solution is shown, resulting in an increase of the surface area of the mixed oxides and an enhancement in the redox properties at lower temperatures. Consequently, the catalytic activity in formaldehyde oxidation of calcined Mn/Ce mixed oxides is higher when compared to pure MnOx. However, the chemical activation of mixed oxides is positive only for samples with high manganese content. Additionally, it is shown that after acidic treatment the formation of solid solutions is strongly affected. This results in lower catalytic activity for mixed oxides with respect to the chemically activated pure manganese oxide. The adsorption and transformation of formaldehyde in this chemically activated manganese oxide is studied by different characterization techniques. The results clearly show the participation of oxygen from manganese oxide since oxidation products are observed, while the formation of formate and methoxy species as intermediate are suggested.

The interaction of surfactant with the manganese precursor in the first part of the thesis is not clearly shown. Indeed, considering the concentration of surfactant employed during the preparation, the formation of mesostructure manganese oxides is not achieved. In the second part of the thesis, a novel synthetic route to obtain highly ordered manganese based layered mesostructure material as precursors for the achievement of high surface area manganese oxide is proposed. Several factors relevant to the formation of mesostructured materials are investigated. However, the control of manganese oxidation states in the inorganic precursor $[\text{Mn}(\text{OH})_2]$, as a result of its interaction with the surfactant molecule, is the basis for the development of this synthesis. The textural properties of the resulting manganese oxides after calcination reveal a remarkable enhancement when compared to the calcined sample prepared in the first part of the thesis (prepared under similar composition). The redox properties of the material are also improved by a more complete oxidation in the presence of surfactant molecule. The optimized catalyst (MnO_x 9) presents a $T_{50} = 90^\circ\text{C}$.

Finally, the use of ultrasound as an ageing method to synthesize Mg-Mn-Al hydrotalcites precursors with different compositions is suggested to obtain high surface area mixed manganese oxide. Sonication not only reduces the preparation time but also presents high homogeneous morphology and more highly dispersed particles when compared to the sample prepared by the conventional method. As a consequence, high surface area mixed oxides are obtained after thermal decomposition. The presence of Mg and the increase of the basic sites result in lower catalytic activity towards CO_2 and the formation of by-products. However, the highest catalytic activity is found for samples containing only Mn/Al ($T_{50} = 85^\circ\text{C}$). It is also found that the catalytic activity of samples prepared using ultrasound is slightly better when compared to that of the sample prepared by the conventional method.

Among the large variety of gaseous indoor pollutants, formaldehyde has an exceptional position, and there is no reason to believe that this view will change in the near future. Formaldehyde is (1) a high reactive aldehyde; (2) an important chemical feedstock; (3) a constituent of many industrial products, and (4) omnipresent in outdoor and indoor environments due to natural and anthropogenic processes. Despite the great progress in the achievement of active catalysts for formaldehyde catalytic oxidation, there are still many challenges for the development of an efficient process. As already stated in the first chapters, typical formaldehyde concentrations used in academic studies are around ppm level. However, the commonly used values are far from those encountered in indoor environments

(ppb level). Future researches will reasonably focus on the formaldehyde remediation at low concentration levels. Under these constraining conditions, original technological approaches have to be proposed. Hybrid system combining selective formaldehyde adsorption followed by its selective destruction by catalytic oxidation can be an attractive alternative to solve the problem of formaldehyde concentration at indoor level. We have shown that manganese oxide based materials are promising catalyst to oxidize formaldehyde at low temperature. Therefore in order to develop a manganese based hybrid material for HCHO removal, the formaldehyde adsorption capacity of these materials must be studied.

The stability of these materials is also another important factor determining their use at large scale; one interesting perspective could be to evaluate the HCHO conversion with time on stream of the most active catalyst obtained in this work. Moreover, it is well known that moisture in indoor air is one of the major reasons causing the dramatic loss in the catalytic activity through strong adsorption of water on the active sites, especially at low temperatures [1]. The effect of H₂O on the complete oxidation of HCHO over the manganese based materials approaches the study towards more realistic conditions. For this reason, the effect of water addition on the HCHO oxidation over manganese based catalyst developed in this work would be also interesting to investigate. Finally, it is shown in this thesis that the specific surface area, porosity, and surface reducibility greatly influence the catalytic performance of HCHO oxidation. These results offer interesting perspectives for future works in the synthesis of manganese oxide based materials with originally improved physical properties and morphologies.

¹M. Date, M. Haruta, *J. Catal.* **2001**, *201*, 221.

OXYDATION CATALYTIQUE DU FORMALDEHYDE SUR DES MATERIAUX MESOPOREUX A BASE DE MANGANESE

Résumé :

La qualité de l'air intérieur est une préoccupation majeure de notre société. Le formaldéhyde (HCHO) est un polluant atmosphérique important et présent dans divers environnements intérieurs comme la maison, le bureau et l'industrie. L'oxydation catalytique complète du formaldéhyde est une voie prometteuse pour convertir ce polluant en produits inoffensifs. Les catalyseurs à base d'oxydes de métaux de transition sont décrits comme les plus prometteurs. Parmi ces oxydes, ceux à base d'oxydes de manganèse sont peu coûteux, non toxiques et peuvent être efficaces pour convertir le formaldéhyde à basse température. Ce travail vise à développer des catalyseurs mésoporeux à base d'oxydes de manganèse pour l'élimination catalytique à basse température du formaldéhyde. Des oxydes de manganèse mésoporeux contenant des teneurs variables en cérium ont tout d'abord été obtenus par activation chimique (traitement acide). L'optimisation de la synthèse du matériau mésoporeux sous atmosphère contrôlée a ensuite conduit à l'obtention d'une mésostructure lamellaire d'oxyde de manganèse. Le délaminage de cet oxyde, après calcination, a produit un oxyde de manganèse ayant des propriétés texturales très intéressantes et redox grandement améliorées. Le catalyseur le plus actif a pu oxyder complètement HCHO en CO₂ et H₂O à 110 °C. Finalement, des hydrotalcites à base de Mg, Mn et Al, activées par ultrasons, ont été synthétisées pour être employées en tant que précurseurs d'oxydes mixtes de manganèse de grandes surfaces spécifiques. L'effet de l'apport des ultrasons et de la composition en éléments du matériau (Mg/Mn) sur les propriétés structurales, texturales, basiques et catalytiques des oxydes mixtes a plus particulièrement été étudié.

Mots-clés : Composés Organiques Volatils (COV), Oxydation Catalytique, Formaldéhyde, Oxydes de Manganèse, Matériaux Mésoporeux, Pollution Intérieur.

FORMALDEHYDE CATALYTIC OXIDATION OVER MESOPOROUS MANGANESE BASED MATERIALS

Abstract:

Indoor air quality is currently a societal concern. Formaldehyde is an important air pollutant in various indoor environments, including houses, offices and industries. The catalytic complete oxidation of formaldehyde is a promising way to convert this pollutant into harmless products. Transition metal oxides based catalysts are described as the most promising catalysts. Among these oxides, manganese oxide based materials are promising, cheap, non-toxic and effective catalysts to convert formaldehyde at low temperature. The present work aims to develop a novel mesoporous manganese oxide based catalyst for low temperature formaldehyde catalytic removal. Mesoporous manganese oxides containing variable amounts of cerium were first obtained by chemical activation (acid treatment). The optimization in the synthesis of mesoporous manganese oxide under controlled atmosphere produces a layered mesostructure manganese oxide. The delamination of this layered mesostructure oxide, after calcination, produces high surface area manganese oxides with improved redox properties and the most active catalyst completely oxidizes HCHO into CO₂ and H₂O at 110 °C. Finally, Mg Mn and Al hydrotalcites based compounds, activated by ultrasound, are employed as precursors to obtain high surface area mixed manganese oxide. The effect of ultrasound contribution and the elemental composition of the material (Mg / Mn) on the structural, textural, basic and catalytic properties of the resulting mixed oxides have been particularly studied.

Keywords: Volatile organic compound (VOC), Catalytic Oxidation, Formaldehyde, Manganese Oxides, Mesoporous Material, Indoor Pollution.